Novel Luminescence Centres in Cadmium-Lithium doped Silicon

A thesis submitted for the degree of
Doctor of Philosophy

Presented to
DUBLIN CITY UNIVERSITY

By
Catherine Anne Frehill B.Sc.

Research Supervisor
Professor Martin O. Henry
School of Physical Sciences
Dublin City University

January 2001

Declaration

I hereby certify that this material, which I now submit for assessment on the programme of study leading to the award of Doctor of Philosophy is entirely my own work and has not been taken from the work of others save and to the extent that such work has been cited and acknowledged within the text of my work

Signed: Catherine Frehill . ***ID No.:*** *94971129*

Candidate

Date: 31st January 2001 .

Dedication

This thesis is dedicated to my parents, Martin and Elizabeth,
and to my sisters, Louise and Fiona.

“If we are going to stick with this dammed quantum-jumping,
then I regret that I ever had anything to do with quantum theory ”
- E Schrodinger (quoted by W Heisenberg),
Niels Bohr and the Development of Physics (edited by W. Pauli, 1955)

Table of Contents

Chapter One ***Introduction***

Chapter Two ***Perturbation Techniques***

Chapter Three *Novel Luminescence Defects in Cadmium Doped Silicon*

Chapter Four *Uniaxial Stress Perturbation*

Chapter Five Isotope Substitution and Magnetic Field Perturbation

Chapter Six Discussion

Abstract

Photoluminescence measurements of three cadmium related defects are presented in this thesis. Group I consists of five zero-phonon lines with the minimum energy line observed at ~1058.1 meV. A second group of lines, labelled group II is found to be broadly similar to group I and is centred at ~1068 meV. Group III consists of three zero-phonon lines, labelled α_1, α_2 and α_3 with α_1 observed at ~1083.3 meV. Temperature dependence, uniaxial stress, isotope substitution studies and Zeeman measurements were performed on the three defects reported.

In the case of groups I and II, temperature measurements have shown excited state manifolds with thermalisation occurring to a single ground state. For group III thermalisation data show that both the ground and excited states are manifolds of three levels each, with strong selection rules governing the transitions. Uniaxial stress measurements reveal trigonal (C_{3V}) symmetry for groups I and II. Group III is assigned to monoclinic I symmetry.

Cadmium isotope substitution experiments reveal that all three centres contain at least one cadmium atom. The diffusion of lithium into cadmium-doped silicon enhances the luminescence of all three defects. For group II, lithium isotope substitution studies indicate the involvement of two Li atoms in the defect.

Zeeman measurements show the excited state manifolds consist of both singlet and triplet states for the three centres, with isotropic triplet state g values close to 2.

List of Publications

Cadmium-Lithium defects in silicon,
Frehill C A , Henry M O , McGlynn E , Lightowlers E C and Safanov A , Materials science and Engineering, B58, 159-162, (1999)

Isotope effects in the study of some impurity centres in silicon,
Henry M O , Frehill C A , McGlynn E and Lightowlers E C , Semiconductor Science and Tech , **7**(4) 128 - 134, (1998)

Novel Luminescent Centres in Cadmium Doped Silicon,
Frehill C A , Henry M O , McGlynn E , Daly S E , Deicher M , Magerle R , McGuigan K G , Safanov A and Lightowlers E C , Materials Science Forum, **258-263**, 521-526, (1997)

The Chemical Identification of Defect Impurities Using Radioactive Isotopes Materials,
Daly S E , Henry M O , Frehill C A , Frietag K , Vianden R and Forkel D , Materials Science Forum, **196-201**, 1497-1502, (1995)

List of Figures

List of Tables

Overview

The number of transistors on a silicon chip has doubled every 18 months, and many believe that conventional semiconductor technology will reach its limit in the next decade Integrated circuits (ICs) have evolved from large scale (LSI) to very large scale (VLSI) structures in the past few decades, while research in ultralarge scale integration (ULSI), where the interconnect features are in the sub-micron (<1 μm) range, is being undertaken at present The majority of ICs are manufactured using silicon as the semiconducting material, and in the interest of device performance, reliability and reproducibility a basic understanding of the material, including the effects of host defects, foreign impurities and complexes involving both defects and impurities is necessary In 1995, 98% of the commercial electronics business was based on silicon technology and it is predicted that the interaction between dopants and silicon defects would "*cause the breakdown of next-generation devices*" (Poate, 1995) Only by the continued study of the properties of semiconductor materials can microelectronics progress as continued advances in the industry depend on the ability to further reduce the size of an IC

The work presented in this thesis is concerned with the characterisation of three defects produced in cadmium-implanted silicon Photoluminescence (PL) spectroscopy used in conjunction with the perturbation techniques of uniaxial stress and Zeeman measurements, and with isotope and temperature dependence experiments are used to investigate the properties of the defects

In chapter one the properties of silicon are introduced, with possible impurity configurations and recombination mechanisms Brief reviews of the Group I impurity lithium and Group II impurities beryllium, zinc and cadmium are given Three previously unreported PL systems are introduced and are tentatively assigned to Cd-Li complexes The theory governing the 'tools' of the investigation, i e spectroscopic and perturbation techniques, are presented in chapter two Three defects, labelled group I, II and III, which are the subject matter of this thesis, are introduced in detail in chapter three and their behaviour as a function of temperature studied Chapters four and five contain new data obtained during the course of this work, giving information on the symmetry, the spin states and chemical constituents of the defects Conclusions drawn from the data obtained and suggestions for further work are presented in chapter six

Chapter One

Introduction

1.1 Introduction

Impurities may be introduced into a semiconductor intentionally (by doping) or unintentionally (by contamination) During the crystal growth process, some trace impurities e g carbon and oxygen are always present in the starting material, as described in section 1 2 The conductivity type and electrical behaviour of the material can be controlled by the introduction of impurities The deliberate addition of chemical impurities such as boron or phosphorous during the growth process will produce p-type or n-type material respectively Silicon is one of the most heavily studied semiconductors due to the highly advanced state of silicon technology, which makes silicon available in large volumes with a range of controlled dopants During semiconductor device fabrication, silicon is subjected to various thermal anneals during which impurities can diffuse in from the surface Depending upon their concentration, these impurities can be beneficial or destructive, as they can give rise to defect structures, and it is the behaviour of these defects in silicon, which are of interest In this chapter the properties of silicon are introduced, with possible impurity configurations and recombination mechanisms The present state of knowledge of beryllium, zinc, cadmium and lithium related defect structures already characterised in silicon are presented In the final section, three cadmium-lithium defects, which are the subject matter of this thesis, are introduced

1.2 Silicon

Silicon has a diamond crystal structure for which the space lattice is face-centred cubic (fcc). The diamond structure can be viewed as two fcc structures displaced from each other by one-quarter of a body diagonal. The basis of the lattice consists of two identical silicon atoms at (000) and (¼ ¼ ¼). The tetrahedral bonding characteristic of the silicon structure is shown in Figure 1.1(a), where each atom has four nearest neighbours and 12 next nearest neighbours. At room temperature the interatomic spacing of silicon is 0.234 nm, the lattice parameter is 0.543 nm and the density is 2330 kg/m^3.

Single-crystal silicon is generally grown from the molten state using the Czochralski (CZ) method. A seed crystal is dipped into a crucible of the molten silicon, then slowly withdrawn and new lattice layers solidify on the crystal surface. During the crystal growing process, impurities from the crucible, carbon and oxygen may contaminate the crystal. The impurity concentration can be reduced by using the float-zone (FZ) technique where a small region of polycrystalline rod is melted. Due to the higher solubility of impurities at high temperatures, they remain in the molten zone as it is moved through the rod. Thus, the impurities are swept to one end of the rod. This sweeping process is repeated several times resulting in very high purity material in the bulk of the sample. Typical concentrations of oxygen in CZ silicon are ~10^{18} atoms/cm^3 and < 10^{16} atoms/cm^3 in FZ silicon.

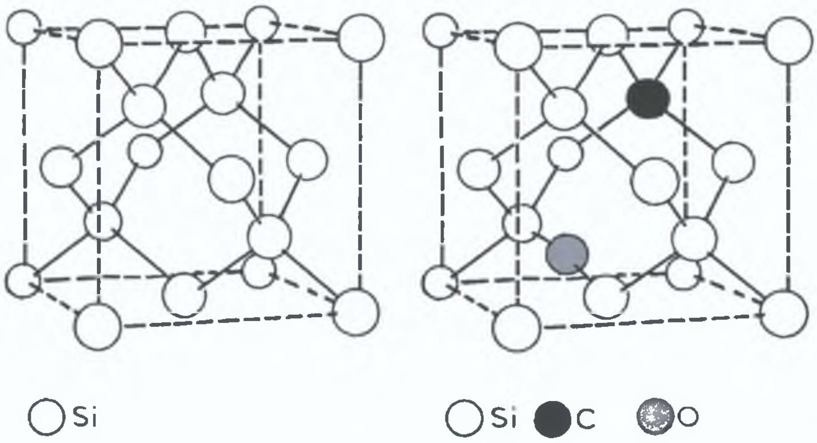

Figure 1.1(a) Crystal structure of silicon showing the tetrahedral bond arrangement and (b) interstitial oxygen defect connected to two nearest neighbour silicon atoms and substitutional carbon (adjusted from Kirshan *et al*, 1990).

An ideal silicon crystal contains no defects or imperfections, however a real crystal may contain dislocations, grain boundaries, strains and point defects Common point defects in real crystals are chemical impurities, vacant lattice sites (the removal of an atom from an atomic site) or atoms in interstitial sites (an extra atom in a non-regular atomic site) Impurity atoms in a crystal can either occupy a normal atomic site in the parent lattice (a substitutional impurity) or a non-regular atomic site (an interstitial impurity) Usually oxygen atoms in silicon occupy interstitial sites, while carbon atoms occupy lattice sites forming a substitutional carbon impurity, both types of impurity are shown in Figure 1 1(b) The presence of defects in a crystal usually introduces energy levels in the forbidden energy bandgap

1.3 Direct and Indirect Semiconductors

The energy gap is the energy difference between the upper edge of the filled valence band and the lower edge of the empty conduction band, with the zero of energy conventionally taken as the top of the valence band Semiconductors are classified into two types, according to whether the bandgap is direct or indirect In a direct gap semiconductor, e g GaAs, the lowest conduction band minimum and the highest valence band maximum are at the same wavevector, $\vec{k}$ in the Brillouin zone Optical transitions across the bandgap conserve total crystal momentum Figure 1 2 (a) shows a direct transition where there is no appreciable change in $\vec{k}$ in going from the valence band to the conduction band Figure 1 2 (b) represents an indirect transition as the lowest point of the conduction band is separated in $\vec{k}$ space from the valence band edge This radiative transition only occurs if accompanied by the absorption or emission of a phonon (or other scattering mechanisms) in order to conserve momentum A phonon is a quantum of vibrational energy, $\hbar\omega$, where ω is the angular frequency of the phonon Since this process involves electron-radiation and electron-phonon interactions, it has a smaller transition probability than the direct transition

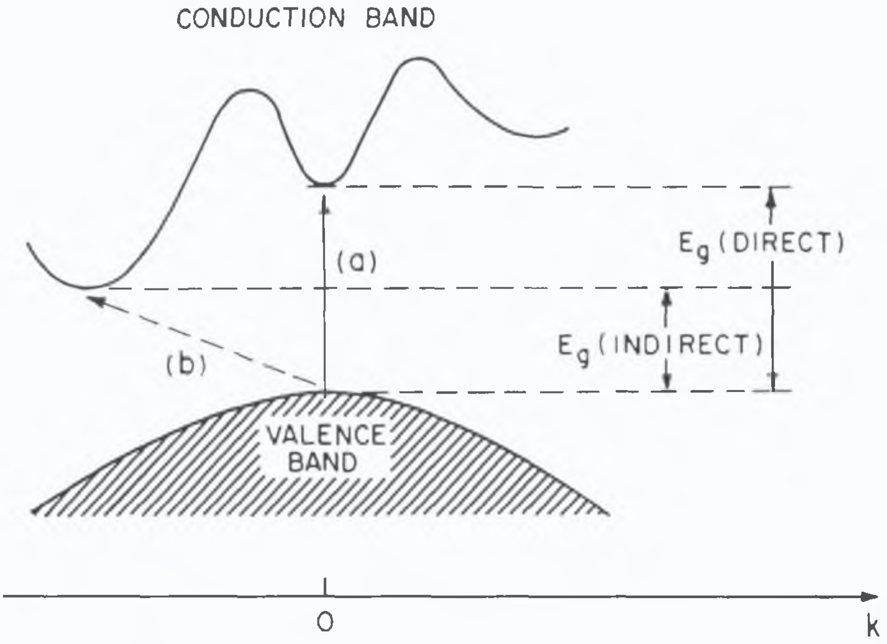

Figure 1.2 Optical transitions (a) direct transitions and (b) indirect transitions involving phonons to conserve momentum (Sze, 1981).

Silicon is an indirect gap semiconductor. The highest occupied valence band state lies at Γ ($\vec{k} = 0$) but the lowest unoccupied conduction band state is close to the X point (along the <100> axis), as shown in figure 1.3(a). Silicon thus has six equivalent conduction band minima corresponding to the six equivalent <100> directions. The energy gap E_g for silicon is 1.17 eV close to 0 K, decreasing to 1.12 eV at room temperature. To excite an electron at the upper valence band at wavevector $\vec{k} = 0$ to the conduction band minimum at $\vec{k}_0$, where $\vec{k}_0 = 0.80\ (\pm\ 0.05)\ \vec{k}/\vec{k}_{MAX}$ for silicon along the <001> axis as shown in figure 1.3(b), only those phonons with the same wavevector $\vec{k}_0$ as the conduction band minimum can take part in the process. The phonon dispersion relation for silicon in the [100] direction is shown in figure 1.3 (b). For each direction the dispersion relation contains two branches, known as the acoustic and optic branches. Labelled in the figure are the longitudinal LO and transverse optic TO modes, and longitudinal LA and transverse acoustic TA modes. Three luminescence bands are observed associated with the TO, LO and TA phonons. The first experimental observation, using a wavelength-derivative absorption technique, of the 55.3 meV LO phonon in silicon was by Shaklee *et al.* (1970). The emission of an 18.2 meV TA and 57.3 meV TO phonon were reported previously (McLean, 1960 and Dean *et al.*, 1969).

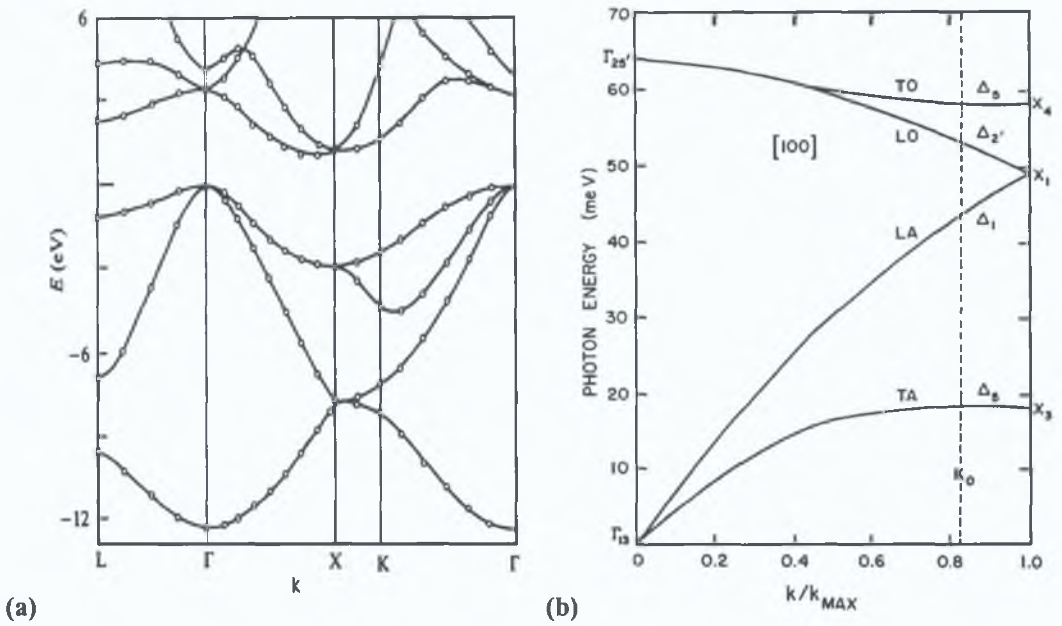

Figure 1.3(a) The energy band structure of silicon, an indirect semiconductor (Myers, 1997) and (b) the vibration spectrum in [100] direction (Reynolds *et al.*, 1981).

1.4 Exciton Recombination

The optical spectra studied in this thesis are produced by transitions between electronic states. In a semiconductor, the transition usually involves the recombination of electrons and holes, from an excited state to a lower energy state or from internal transitions at a defect. The excitation of silicon with photons of energy greater than the bandgap results in the formation of electron-hole pairs. The electrons and holes become bound together as pairs by their mutual Coulombic attraction and they represent a state of energy lower than the unbound electrons and holes, the electron-hole pair is known as a (free) exciton. As the excitation intensity increases the density of the electron-hole pairs increases and the number of excitons formed increases. The electron-hole pairs can recombine via several decay processes which can be radiative, giving rise to luminescence, or non-radiative where the energy goes into lattice vibrations. Lightowlers (1990) gives a detailed review of the possible decay processes. The Auger effect is a non-radiative process in which the exciton energy can be transferred to a third particle without the emission of light.

In an indirect gap semiconductor, momentum-conserving phonons with the same wavevector as the conduction band minimum are emitted with the recombination of the exciton. The energy of the transition, E_T is:

$$E_T = E_g - E_x \pm \hbar\omega \tag{1.1}$$

where E_g is the energy gap of the indirect semiconductor, E_x is the exciton binding energy and $\hbar\omega$ is the energy of the momentum conserving phonon. The + sign implies phonon absorption and the - sign implies phonon emission.

Excitons in a high purity material are free to move through the crystal and they are described as free excitons (FE). The FE is a hydrogen-like bound pair, the hole is from the top of the valence band and the electron from the bottom of the conduction band. The binding energy of the exciton, E_x is 14.7 ± 0.04 meV (Shaklee *et al.*, 1970).

A bound-exciton (BE) complex is formed by the binding of a free exciton to a host lattice defect or to a chemical impurity atom(s). If the material contains donors and acceptors with concentrations $>10^{15}$ cm^{-3} then at low temperatures nearly all of the free-excitons are captured giving rise to impurity specific BE luminescence. The BE spectral lines are impurity specific for silicon and can occur with or without the emission of phonons. The spectral lines are sharp with photon energy:

$$E_T = E_g - E_x - E_B(\pm\hbar\omega) \tag{1.2}$$

where E_B is the binding energy of the exciton to the neutral donor or acceptor, and the other symbols are given as above. The ground state in the case of donors and acceptors already contains one bound particle, an electron in the case of a donor and the hole in the case of an acceptor. In the case of neutral centres (isoelectronic) the ground state of the excitation is the bare defect. The localisation of an additional electron-hole pair to the defect creates the BE excitation, which may be regarded as containing two electronic particles for a neutral defect and three particles for a donor or acceptor (if single donors or acceptors are considered). The binding energy of shallow BE donors and acceptors is weak compared to the FE binding energy and is impurity specific e.g. 3.8 meV for B and 4.7 meV for P (Davies, 1989 and ref. therein). The spectral lines are sharp in comparison to the FE line, which follows a Boltzmann distribution. It is this narrow line shape which allows small shifts in energy from isotope experiments, Zeeman and stress measurements to be observed thereby helping to identify the impurity involved in the defect Dean and Herbert (1979) and Monemar *et al* (1987) give detailed review papers on the structure of BEs

At increased excitation densities a series of sharp lines at energies below an associated BE luminescence can be observed The luminescence lines show a strong dependence on the excitation density and are due to the binding of more than one exciton at the donor or acceptor trap A detailed review of these so-called bound multi-exciton complexes (BMEC) is given by Thewalt (1977, 1982a) and a review of the shell model by Kirczenow (1977)

1.4.1 Isoelectronic Bound Excitons

An isoelectronic centre has the same number of valence electrons as the atoms it replaces and is electrically neutral The neutral ground state of the defect possesses a local potential due to electronegativity differences or a local strain field about the defect site, which can tightly bind a particle (primary particle) with typical binding energies of a few hundred meV A second particle of the opposite charge is then bound via the Coulomb potential of the primary particle, with binding energies of a few tens of meV The secondary particle is in a shallow effective-mass orbit according to the Hopfield-Thomas-Lynch (1966) model The term isoelectronic bound exciton (IBE) is used to describe the excited state of the defect Isoelectronic centres can consist of substitutional impurity atoms with the same number of valence electrons as Si, e g Ge, C, or molecular type defects which consist of impurity-impurity and impurity-intrinsic defect complexes Weber *et al* (1979, 1980) first reported IBEs in silicon and Davies (1989) gives an extensive report of IBEs in silicon Isoelectronic defects can be classified as either acceptors or donors depending upon which particle, electron or hole, is bound to the defect first

The centre acts as an acceptor if the electron is the tightly bound particle which can now capture a hole by its Coulomb attraction The angular momentum of the electron is $j_e = \frac{1}{2}$, while the angular momentum of the hole is $j_h = \frac{3}{2}$ The bound exciton state will split into a J = 1 and J = 2 state under the electron-hole exchange interaction Electron attractive core defects, such as the

ABC centre (Weber *et al*, 1980, Davies *et al*, 1994) and the Be-pair (Thewalt *et al*, 1982b) in silicon are isoelectronic acceptors A schematic diagram of an isoelectronic acceptor is shown in figure 1 4 (a)

In an isoelectronic donor the hole is the tightly bound particle and the electron is bound via the Coulomb attraction The angular momentum of the electron is $j_e = \frac{1}{2}$, and the angular momentum of the hole is quenched giving $j_h = \frac{1}{2}$ Thus both particles have s-like wavefunctions and the electron-hole exchange interaction will split the bound exciton state into S = 1 and S = 0, triplet and singlet states These electron attractive defects for example the C-line (Thonke *et al*, 1985) and the P-line (Wagner *et al*, 1985) in silicon are called isoelectronic donors and can be represented schematically, figure 1 4 (b)

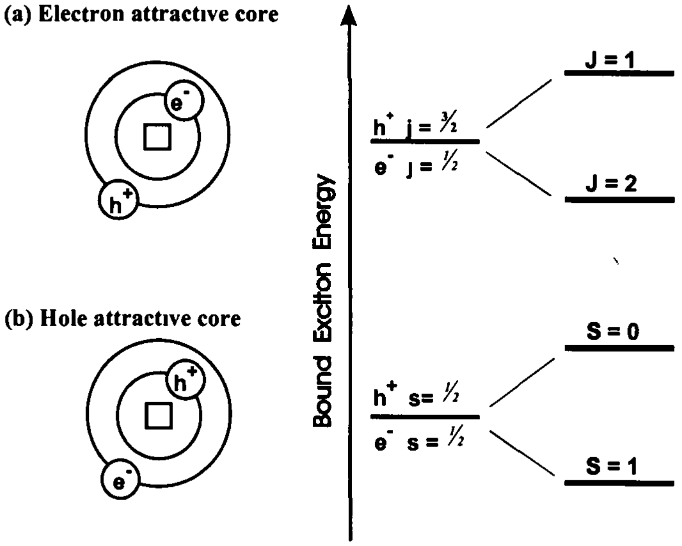

Figure 1.4. (a) Isoelectronic acceptor and (b) isoelectronic donor defect centres.

Exciton recombination is highly efficient at an isoelectronic centre, as no particles are available for Auger-type non-radiative recombination processes The identification of donor and acceptor BE luminescence can be straightforward due to deliberate doping with various donors and acceptors When other impurities are introduced by contamination during growth or complexes are formed by radiation damage or thermal treatment the identification of the impurities responsible is complicated

1.5 Electronic and Vibrational Elements of Optical Transitions

If an electron is excited from a low energy state to an excited state of an isolated atom, it will eventually undergo a transition from the higher energy state to the lower state, with the emission of radiation exactly equal to the energy difference of the two states As the atom is not isolated but is present in a crystal lattice, as a defect centre, the electronic and lattice systems are coupled together The transition of the electron from the higher energy state to the lower state may cause the lattice around the centre to relax to a new equilibrium position All optical centres have atomic vibrations about equilibrium positions in different electronic states, the coupling of the electronic states to the vibration of the centre is referred to as electron-phonon coupling Electron-phonon coupling was first considered by Born and Oppenheimer (1927) and Born and Huang (1954) It has been reviewed in detail recently by for example, Henderson *et al* , (1989) and Davies (1999) In the following, the case of an optical centre with just one vibrational degree of freedom (configurational co-ordinate) and non-degenerate electronic states which are well separated in energy from all other electronic states will be considered, in the case of linear electron-phonon coupling

To represent electronic coupling to a single vibrational mode a configurational co-ordinate (CC) diagram is drawn The diagram, as shown schematically in figure 1 5, relates the total energy of the centre to Q, the distance of the defect atom(s) to its nearest neighbour The centre in the ground state (g) vibrates harmonically around the equilibrium position $Q = Q_g = 0$ with angular frequency, $\omega = \sqrt{k/m}$, where k is the effective "spring constant" and m is the mass The angular frequency of the excited state (e) is the same as the ground state, but vibrates at equilibrium position $Q = Q_e$, where $Q_e > Q_g$ The difference in the average value of Q arises because of the difference in coupling, the larger the difference in coupling the larger $Q_g - Q_e$ The relaxation energy E_r defined in figure 1.5, is a measure of the difference in coupling

$$E_r = S\hbar\omega \qquad (1\ 3)$$

where S the Huang-Rhys parameter, represents the difference in coupling between the initial and final states of a transition The Frank-Condon approximation states that the nuclei can be considered to be stationary during the course of transitions, as the timescale of the electronic transitions is short compared to that of nuclear vibrations On the CC diagram as shown in figure 1 5 the electronic transitions can be represented by vertical lines

According to the Born-Oppenheimer approximation the total wave-function of a centre can be considered to consist of an electronic part $\phi(r)$, which depends on the electronic co-ordinates r, and a vibrational part $\chi(Q)$ The total wavefunctions of the ground and excited electronic states are

$$\psi_{g,n} = \phi_g(r)\chi_n(Q-Q_g) \qquad (1\ 4)$$

$$\psi_{e,N} = \phi_e(r)\chi_N(Q-Q_e) \qquad (1\ 5)$$

where n, N are the quantum states of the vibration in the ground and excited electronic states, respectively

In the ground state, the vibrational potential energy is

$$V_g = \tfrac{1}{2}m\omega^2(Q-Q_g)^2 \qquad (1\ 6)$$

When the electrons are excited through energy E, the potential energy of the excited state is

$$V_e = E + \tfrac{1}{2}m\omega^2(Q-Q_e)^2 - E_r \qquad (1\ 7)$$

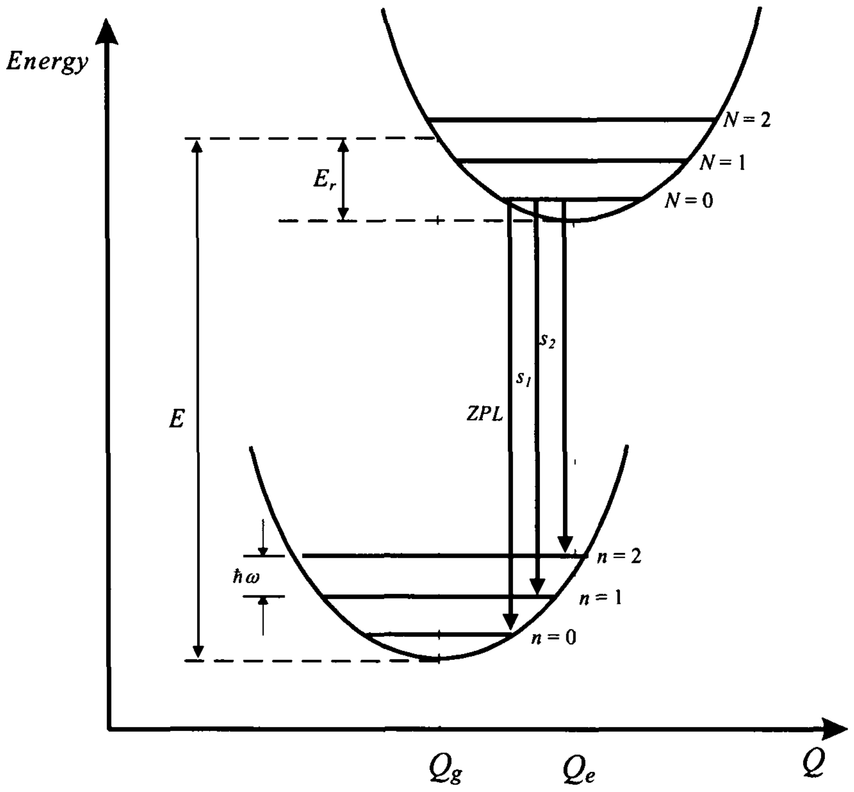

Figure 1.5 Configurational co-ordinate diagram showing ground (*g*) and excited (*e*) states of a defect. The line $N = 0$ to $n = 0$ is the zero-phonon line (ZPL) and the first two sidebands s_1, $N = 1$ to $n = 0$ and s_2, $N = 2$ to $n = 0$ are shown in the diagram.

The linear electron-phonon coupling term written in terms of the excited state equilibrium position is

$$a = -m\omega^2(Q_e - Q_g) \tag{1.8}$$

The potential energy of the excited state can be rewritten in terms of a as

$$V_e = E + \tfrac{1}{2}m\omega^2(Q - Q_g)^2 + a(Q - Q_g) \tag{1.9}$$

The change in equilibrium position and relaxation energy E_r are given by

$$\left|Q_e - Q_g\right| = \frac{a}{m\omega^2} \tag{1.10}$$

$$E_r = \frac{a^2}{2m\omega^2} \tag{1.11}$$

Absorption and emission transitions between states can be analysed from the CC diagram; the observed spectra will depend upon the difference in electron-phonon coupling between the two states. The probability of absorption from electronic-vibrational state g, n to electronic-vibrational state e, N depends on (Davies 1999):

$$I_{eN,gn} = \left[\int dr\phi_e^*(r)r\phi_g(r)\right]\left[\int dQ\chi_N(Q-Q_e)\chi_n(Q-Q_g)\right]^2 \qquad (1.12)$$

The first integral is the purely electronic transition probability, P_{ge} and is the same for all vibrational states n, N. The second integral determines the overlap integral between states of the form $\chi_N(Q-Q_e)$ and $\chi_n(Q-Q_g)$ which are generally non-zero. The transition probability $W_{gn\text{-}eN}$ is then:

$$W_{gn-eN} = P_{ge}\left[\int dQ\chi_N(Q-Q_e)\chi_n(Q-Q_g)\right]^2 \qquad (1.13)$$

At low temperatures, T ~ 0 K only the $n = 0$ vibrational state in the lower state is occupied. The probability of an absorption transition to the N^{th} vibrational level in the excited state varies as the square of the overlap integral, which is called the zero-temperature Frank-Condon factor, $F_N(0)$ (Henderson *et al.*, 1989):

$$F_N(0) = \left|\int dQ\chi_N(Q-Q_e)^*\chi_0(Q-Q_g)\right|^2 = \frac{S^N exp(-S)}{N!} \qquad (1.14)$$

At T ~ 0K the absorption band shape is given by:

$$I_{ge}(E) = I_0\sum_N\frac{exp(-S)S^N}{N!}\delta(E_0 + N\hbar\omega - E) \qquad (1.15)$$

where E_0 is the energy of the transition between the zero vibrational levels of both final and initial states, this is the energy of the zero-phonon line (ZPL) and I_0 is the intensity of the full band. The ZPL has intensity $I_0\, exp(-S)$ and if $S = 0$ all the intensity is contained in the line. For $S = 0$, $Q_g = Q_e$ and the excited and ground state parabola are identical As S increases the intensity of the zero-phonon line decreases with the appearance of vibrational sidebands which are observed at energies $N\hbar\omega$ above the zero-phonon line. The intensity of the full band, I_0 is independent of S, thus the sideband intensity is obtained at the expense of zero-phonon line The zero-phonon transition, $0 \rightarrow 0$ is a transition between pure electronic states and is expected to be a sharp line The other transitions $0 \rightarrow N$, occurring at higher energies involve the creation of n phonons, which appear as sidebands along with the zero-phonon line The bandshapes, which are drawn to have the same maximum intensity for different values of S, are shown in figure 1 6

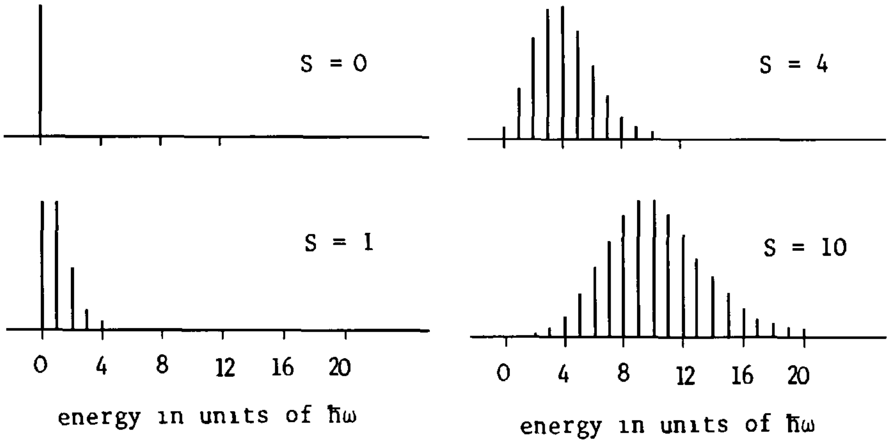

Figure 1.6 The variation of sideband intensity for various Huang-Rhys values (Henderson *et al.*, 1989).

As the value of the Huang-Rhys parameter increases, sidebands appear as continuous bands with the relative intensities of the different transitions changing with the strength of the coupling Only sharp electronic zero-phonon transitions would occur if there were no lattice vibrations However, due to lattice vibrations, sidebands occur

When the electronic-vibrational system is raised to some higher vibrational level in the excited electronic state, g, it decays quickly by multiphonon emission to the ground vibrational level of the excited state ($N = 0$) Radiative decay returns the system to the vibrational level, n, of the ground electronic state

The shape of the emission band at low temperature, T = 0 K is

$$I_{ge}(E) = I_0 \sum_n \frac{exp(-S)}{n!} \delta\left(E_0 - n\hbar\omega - E\right) \tag{1 16}$$

Absorption and emission transitions are shown in figure 1 7 The zero-phonon transitions for absorption and emission occur at the same frequency, with the emission band at lower energy The shapes of the emission and absorption bands are mirror images if the excited- and ground- state parabolas are identical, the energy separation between the peaks of the bands is known as the Stokes shift, and has a value $(2S - 1)\hbar\omega$ When the spring constant k differs in the excited and ground states, $\hbar\omega_e \neq \hbar\omega_g$, the parabola are no longer identical and the mirror symmetry does not occur, thus the energy shift between the zero-phonon line and the Stokes (emission) and anti-Stokes (absorption) shift will vary

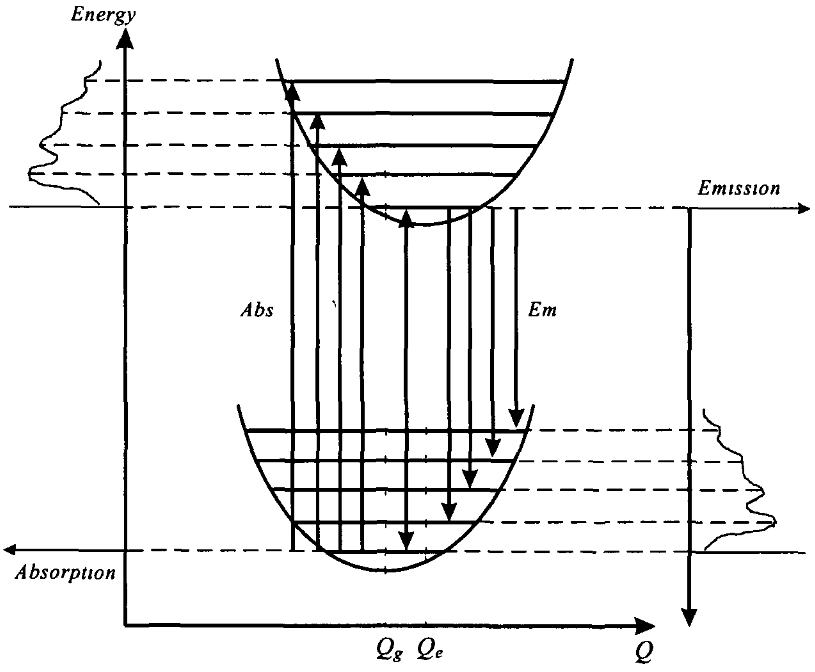

Figure 1.7 Low temperature absorption and emission between two states. The zero-phonon line will occur at the same frequency in emission and absorption (adjusted from Henderson *et al.*, 1989). The energy axes are reversed for absorption and emission.

Only electronic coupling to a single vibrational mode has been considered However, in a real system there are more than a single CC hence an optical centre has a large number of vibrational modes, and the potential energy of the ground and excited state for the i^{th} mode are generalised as

$$V_g = \tfrac{1}{2}\sum m_i \omega_i^2 (Q - Q_g)_i^2 \qquad (1\ 17)$$

$$V_e = E + \tfrac{1}{2}\sum m_i \omega_i^2 (Q - Q_e)^2 + \sum a_i (Q - Q_g)_i \qquad (1\ 18)$$

The vibrational modes do not mix in the linear coupling approximation and the multi-phonon sideband of any particular transition may be estimated provided an accurate one-phonon sideband is known The spectrum of the n-phonon sideband $I_n(v)$ is given by (Davies 1999)

$$I_n(v) = \int_o^{\omega_m} dx I_1(x) I_{n-1}(v - x) \qquad n > 1 \qquad (1\ 19)$$

where ω_m is the maximum vibrational frequency in the defect and $I_1(x)$ is the one phonon sideband

1.6 Group II in Silicon

The group II impurities on substitutional silicon sites, lacking two electrons to form four covalent bonds, behave as double acceptors When the group II impurities are incorporated on an interstitial site the two outer electrons are ionised and the impurity acts as a double donor The group II elements, which have received particular attention in previous studies, are Be, Cd and Zn A summary of the main findings of each of these elements will be discussed in the following sections

1.6.1 Beryllium Doped Silicon

Beryllium doping produces p-type silicon and mobile interstitial atoms are believed to become trapped at vacancies thus producing substitutional acceptor impurities Crouch *et al*, (1972) suggest that a line spectrum, which they labelled Be-I, is due to single beryllium atoms occupying substitutional silicon lattice sites with the ground state binding energy of 191 9 meV An acceptor level at E_V + 145 8 meV, labelled BE-II, is believed to involve two Be atoms on nearest neighbour sites with trigonal symmetry (Crouch *et al*, 1972, Heyman *et al*, 1991, 1992) The diffusion of lithium into beryllium-doped silicon produces two new acceptor levels at 106 and 81 meV above the valence band These new levels are due to lithium forming a complex with the defects responsible for the Be-I and II levels, respectively (Crouch *et al*, 1972) Beryllium-doped silicon samples which were heated in an hydrogen environment revealed acceptor levels at about 91 and 73 meV These acceptor levels are due to beryllium-hydrogen pairs, a direct analogy to the beryllium-lithium pairs (Crouch *et al*, 1974)

Infrared absorption studies of the lines around 83 meV, labelled Be-IV, indicates the creation of the centres is due to the decomposition of the beryllium pairs, Be-II Two additional lines around 190 meV which are due to a different acceptor are labelled Be-III (Ho *et al*, 1995) On the higher energy side of the Be-IV centres, several absorption lines have been identified and are due to another beryllium centre, labelled Be-V The Be-I and Be-II centres have been studied since the early '70s, however, the III to V centres need further study to be fully understood (Ho *et al*, 1997)

An isoelectronic centre observed at ~1077 meV is identified as a double donor-double acceptor pair formed by a substitutional Be^{2-} next to an interstitial Be^{2+} in a <111> geometry (Killoran *et al*, 1982, Henry *et al*, 1981, 1990, Thewalt *et al*, 1982)

A number of recombination centres with ZPLs at ~1138 and ~1053 meV, are not exhibited by oxygen-lean FZ material and are attributed to the complexing of O with Be (Gerasimenko *et al*, 1985) Further PL studies have revealed the behaviour of the ~1138 meV line to be consistent with a pseudo-donor model with rhombic I (C_{2V}) symmetry (Daly *et al*, 1996). A complicated band of lines was observed in the range 650-900 meV in silicon irradiated with beryllium ions annealed at 400-600°C. The energy positions of over thirty lines were in agreement with those calculated on the assumption that one component was a beryllium atom or pair at the nearest lattice sites (acceptors with E_A = 191 and 145 meV, respectively) and the second in a donor site (Gerasimenko *et al.,* 1985). Table 1.1 summarises the beryllium acceptor levels and PL centres.

Line (meV)	Name	Element(s)/ identity	Symmetry (if known)	Ref.
Acceptor Levels				
E_V + 191.9	Be-I	Be subs		Crouch *et al*, 1972
E_V + 145.8	Be-II	2 Be n.n.	Trigonal	Crouch *et al*, 1972
E_V + 106	Be-I + Li	Be subs + Li		Crouch *et al*, 1974
E_V + 81	Be-II + Li	2 Be n.n. + Li		Crouch *et al*, 1974
E_V + 91	Be-I + H	Be subs + H		Crouch *et al*, 1974
E_V + 73	Be-II + H	2 Be n.n. + H		Crouch *et al*, 1974
E_V + 190	Be-III			Ho *et al.*, 1995
E_V + 83	Be-IV			Ho *et al.*, 1997
PL Centres				
1076		Be pair	Rhombic I	Henry *et al.*, 1981,1990
1138	Be_A	Be + O	Rhombic I	Daly *et al.*, 1996
1052.8		Be + O		Gerasimenko *et al.*, 1985

Table 1.1 Be acceptor levels and PL centres (subs = substitutional, n.n. = nearest neighbour).

1.6.2 Zinc Doped Silicon

Zinc is firmly established as a substitutional double acceptor impurity, confirmed by Hall effect (Fuller *et al.*, 1957), photothermal ionisation (Grimmeiss *et al.*, 1975) and infrared absorption experiments (Merk *et al.*, 1989, Dörnen *et al.*, 1989). Infrared absorption studies have yielded the most accurate values for the ionisation of neutral zinc and are given as $E_{0/-} = E_V$ + 319.53 meV (Merk *et al.*, 1989) or E_V + (319.1 ± 0.3) meV (Dörnen *et al.*, 1989).

An investigation of zinc-diffused CZ silicon that failed to produce any evidence of bound exciton recombination at zinc double acceptors revealed two systems with zero-phonon transitions observed at 1129.57 meV and 1090.47 meV, labelled the Zn_A and Zn_B systems (Henry *et al.,* 1989, 1994). In subsequent investigations two other zinc related systems were observed labelled Zn_C and Zn_D. Zn_C consists of two thermalising lines at 1050.31 and 1051.24 meV, and Zn_D has a zero-phonon line at 1100.42 meV (McGuigan *et al.*, 1996). The behaviour of all four zinc-related systems under uniaxial stress was almost identical. Zn_A defects are found to possess rhombic I symmetry with Zn_B, Zn_C and Zn_D possessing monoclinic I symmetry. All four defects are believed to be due to the complexing of zinc with oxygen and are pseudo-donor in nature. A brief summary of zinc luminescence centres and acceptor levels is given in table 1.2 below.

Line (meV)	Name	Element(s)/ identity	Symmetry (if known)	Ref.
Acceptor Levels				
E_V + 319.53				Merk *et al.*, 1989
E_V + 319.1				Dörnen *et al.*, 1989
PL Centres				
1129.57	Zn_A	Zn + O	Rhombic I	Henry *et al.*, 1989,
1190.44	Zn_B	Zn + O	Monoclinic I	1994
~1051	Zn_C	Zn + O	Monoclinic I	McGuigan *et al.*,
1100.42	Zn_D	Zn + O	Monoclinic I	1996

Table 1.2 Zinc acceptor levels and PL centres as described in the text.

1.6.3 Cadmium Doped Silicon

The substitutional single cadmium impurity in silicon introduces two acceptor levels. Hall effect and photoconductivity measurements place the levels at E_V + 550 meV for $Cd^{0/-}$ and E_C - 450 meV for $Cd^{-/2-}$ (Gulamova *et al.*, 1971). The technique of DLTS on Radioactive Impurities (DLTS-RI) has identified the singly and doubly charged state of the isolated Cd double acceptor in Si and placed the level for $Cd^{0/-}$ at E_V + 485 (± 27) meV and $Cd^{-/2-}$ at E_C - 450 (± 20) meV (Lang *et al.*, 1991,1992). The level observed at E_V + 485 meV is attributed to CdFe pairs (Lang *et al.*, 1992) where interstitial Fe atoms slowly diffuse in the silicon lattice at room temperature and form pairs with isolated Cd atoms. Hall measurements have revealed two levels placed at E_C - 330 and E_C - 540 meV (Dyunaidov *et al.*, 1981). These two levels have been attributed to substitutional cadmium, which suggests a double acceptor nature in silicon similar to zinc. At high temperatures a third level was observed located between E_C - 330 and E_C - 540 meV Dyunaidov and his co-workers suggest this is the level at E_C - 450 meV observed previously In B- and Al-doped silicon two Cd-impurity related levels were observed, labelled Cd-B1 and Cd-Al1 Both centres act as a single acceptor and contain one Cd atom complexing with an unknown impurity Their ground states were located in the bandgap, Cd-B1 at E_V + 200 (±10) meV and Cd-Al1 at E_V + 205 (±10) meV The precise values and identification of Cd-related states observed in the band gap varies from one report to another

The structural and electronic properties of Cd were studied by Electron Paramagnetic Resonance (EPR) The Cd(1) centre was identified showing an angular dependence suggesting a single tetrahedrally co-ordinated Cd atom is involved A substitutional lattice site is suggested with the Cd(1) spectra due to the isolated Cd^+ donor state with a singlet ground state (Naser *et al*, 1998) Naser tentatively assigned Cd(1) to an energy level at E_V + 200 (±10) meV which is in disagreement with the acceptor-like Cd-B1 centre observed previously (Lang *et al*, 1991)

Perturbed Angular Correlation spectroscopy (PAC) of Cd-H complexes in silicon have identified an acceptor energy level at $E = E_V + 60$ meV (Gebhard *et al*, 1991) A first principles investigation of the possible neutral complexes of Cd-H in silicon revealed the energetically favourable configuration is one where the Cd atom and the nearest silicon suffer relaxation along the [111] direction (Caravaca *et al*, 1998)

Three pseudo-donor type Cd-related defects in CZ Si were observed in photoluminescence studies with zero-phonon lines at 935, 983 and 1026 meV, labelled Cd_B, Cd_A and the 1026 meV defect, respectively (McGlynn *et al*, 1996) Isotope substitution experiments show all three defects contain one Cd atom and probably involve one or more impurity atoms McGlynn and his co-workers reported no definite links between the defects observed in DLTS and PL could be established due to the low thermal binding energy found in the PL measurements Cd_A defects have rhombic I symmetry with very similar stress parameters as the Zn_A defects, as are the stress parameters of the monoclinic I Cd_B and Zn_B defects Regardless of the chemical identities of the impurities in the defects, the basic symmetry and geometry is similar in all cases Due to the close parallels with zinc and beryllium, the pairing of cadmium with oxygen was proposed to account for these defects Table 1 3 compares the acceptor levels and summarises the information known to date on cadmium related luminescence centres

Line (meV)	Name	Element(s)/ identity	Symmetry (if known)	Ref
Acceptor Levels				
$E_V + 550$	Cd$^{0/-}$			Gulamova *et al* , 1971
$E_C - 450$	Cd$^{-/2-}$			
$E_V + 485$	Cd$^{0/-}$	CdFe pairs		Lang *et al* , 1991, 1992
$E_C - 450$	Cd$^{-/2-}$			
$E_C - 330$		Cd subs		Dyunaidov *et al* , 1981
$E_C - 540$		Cd subs		Dyunaidov *et al* , 1981
$E_V + 200$	Cd-B1	Cd + B ?		Lang *et al* , 1991
$E_V + 205$	Cd-Al1	Cd + Al ?		Lang *et al* , 1991
$E_V + 200$	Cd1	Cd subs		Näser *et al* , 1998
$E_V + 60$		Cd-H		Gebhard *et al* , 1991
PL Centres				
935	Cd$_B$	Cd + O	monoclinic I	McGlynn *et al* , 1996
983	Cd$_A$	Cd + O	rhombic I	McGlynn *et al* , 1996
1026		Cd + O	rhombic I	McGlynn *et al* , 1996

Table 1.3 Previously reported luminescence centres and acceptor levels of cadmium related centres.

A comparative study of PL spectra of silicon doped with group II impurities Be, Cd and Zn in oxygen-rich and oxygen-lean silicon have shown the defects are not observed in oxygen-lean silicon (Daly *et al* , 1995a, b) The defects are attributed to the complexing of the impurities with oxygen Under uniaxial stress and Zeeman measurements the zero phonon lines have shown near identical behaviour and are all believed to be pseudo-donor in nature

1.7 Lithium in Silicon

The process of passivation is important in the development of devices as it suppresses the concentration of deep level impurities in the active region of the device. Previous work has concentrated on the passivation of shallow impurities with hydrogen. The introduction of hydrogen during silicon device processing forms complexes with defects and impurities. It is traditionally thought of as a passivating element, able to diffuse rapidly through the lattice and terminate dangling bonds associated with other point defects resulting in electrically inactive complexes. Lithium, another group I impurity has received much attention in recent years due to its ability to passivate defects and impurities. A detailed comparison of the passivation of impurities by hydrogen and lithium shows similarities for shallow acceptor passivation. However, while shallow donors in Si and GaAs are not passivated by lithium, deep donor levels are passivated (Gislason, 1997).

The excitation spectra of lithium were studied by far infra-red techniques and the spectra revealed both isolated lithium and lithium-oxygen complexes (Aggarwal *et al.*, 1965). Lithium, a fast interstitial diffuser, as a singly ionised donor is normally observed at the tetrahedral interstitial site acting as a shallow donor with a level at E_C - 33.8 meV (Watkins *et al.*, 1970, Aggarwal *et al.*, 1965). The general behaviour of shallow donors can be described by effective mass theory (EMT) (Kohn 1957). If an impurity centre has a sufficiently delocalised wavefunction the energy of an eigenstate can be calculated by a hydrogenic model where the macroscopic properties of the host lattice dominate. The conduction band edge of silicon has six equivalent minima along the <100> axis in k-space and for simple substitutional donors of T_d symmetry this leads to a reduction for the s_0 and p_0 states into the A_1, E and T_2 irreducible representations of T_d. The valley orbit-splitting of the shallow T_d donor ground state is expected to lead to a lowering of the A_1 (singlet) with respect to the T_2 (triplet) and E (doublet) states. However, for the interstitial lithium donor the A_1 state was found to lie above the (E+T_2) state, Aggrawal proposed the interstitial lithium donor must have “inverted valley-orbit splitting”. The ground state of the lithium donor is unusual, as it is five-fold degenerate, the singlet A_1 state is 1.8 ±

0 1 meV above the $(E+T_2)$ ground state This unusual ground state has prompted detailed studies of lithium and lithium-related defects

Photoluminescence spectra due to lithium interstitial donors in oxygen-rich and -lean silicon were first reported by Kosai *et al*, (1974) At least seven lithium related lines were observed and they were attributed to recombination within complexes of several excitons bound to a single impurity, a bound multi-exciton complex High resolution spectra reported a number of new lines and were interpreted as excited states of the BE and BMEC (Lyon *et al*, 1978, Thewalt 1978) Figure 1 8 shows the TO and LO phonon assisted lines at 4 2K which are accompanied by multi-exciton lines The 1093 2 meV no-phonon line (labelled BE_{TO}) is associated with emission from an exciton bound to a Li donor with the creation of one TO phonon The lines labelled b_i are accepted as being due to electron-hole recombination in complexes containing more than one electron-hole pair bound to neutral impurities as reported previously by Kosai The lines labelled BE_1^*, b_1^* and b_3^* are excited states of the BE and BMEC, m=2 and m=4, respectively

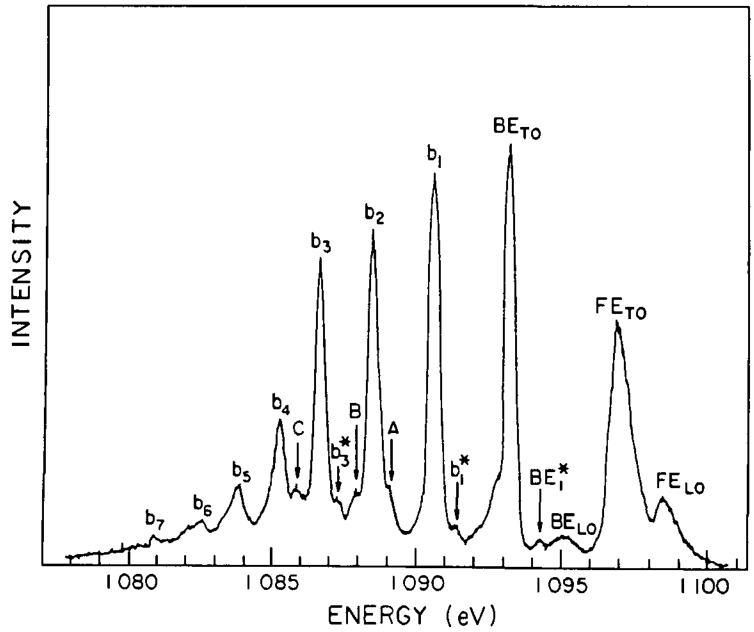

Figure 1.8 Photoluminescence spectra of Si:Li in the TO and LO phonon assisted spectral region. The lines labelled BE_1^*, b_1^* and b_3^* are excited states of the BE and m=2 and m=4 BMEC, respectively (Lyon *et al.*, 1978).

Isotope substitution experiments (section 2.6) have proven to be crucial in the identification and determination of the number of Li-atoms present in defects. The lithium saturated vacancy, Li_4-V, also known as the Q centre, with three thermalising lines at ~1045 meV is observed in irradiation damaged lithium-doped silicon. Isotope substitution data and uniaxial stress measurements indicate four-Li atoms replace a single silicon atom at a substitutional site, producing a molecular isoelectronic trap with a trigonal distortion (Davies *et al.*, 1984, Lightowlers *et al.*, 1984). A centre known as the S centre with ZPLs at ~1082 meV is enhanced in FZ silicon with a high carbon concentration. This centre is similar to the Q centre, with four-Li atoms replacing the substitutional silicon atom and complexing with a near-neighbour carbon atom. Zeeman measurements suggest both centres are isoelectronic donors (Lightowlers *et al.*, 1984).

Two gold-lithium centres, identified as an orthorhombic Au-Li pair and a trigonal Au-Li_3 complex have been identified from EPR and double ENDOR studies. The Au-Li_3 complex has a single donor level within the bandgap above E_C - 400 meV (Alteheld *et al.*, 1994). Using DLTS two different complexes between gold acceptors and lithium were observed (Sveinbjörnsson *et al.*, 1995). One is most likely an electrically passive Au-Li pair while the other complex, labelled L1, contains one gold atom and one or more lithium atoms, has a deep level within the silicon bandgap and is possibly the Au-Li_3 complex previously reported by Alteheld. The passivation of the Au-Li complex in n-type silicon can be reversed provided there is enough lithium present in the crystal. A comparison of the concentration of electrically inactive Au-Li complexes and the intensity of a zero-phonon line observed at 1122.3 meV suggests the two are correlated (Gislason *et al.*, 1995). Thus the 1122.3 meV line can be attributed to an exciton bound to an electrically inactive complex of Li and Au, the product of lithium passivation of the Au acceptor. Gislason and his co-workers suggest that the centre which produces a PL spectrum with two zero phonon lines at 765.4 and 766.4 meV are due to transitions from a split excited state to a single ground state of a neutral Au-Li related acceptor at E_V + 760 meV observed from DLTS.

Recent PL work on Au-Li doped silicon has concentrated on three complexes known as the L, H and O systems. The L system involves one or more Au atoms with at least two atoms in inequivalent sites, suggesting a trigonal symmetry or three lithium atoms in equivalent sites with a lower symmetry Both the H and O system have been shown from isotopic shifts to be lithium-related, however, other impurities are, at present, unidentified (Zhu, 1998)

Trigonal Au-Li$_3$ and orthorhombic Pt-Li centres were investigated by EPR and ENDOR techniques From total energy calculations only trigonal defect clusters with the lithium interstitial at the nearest neighbour or next-nearest neighbour positions agrees with experimental results (Alteheld *et al*, 1994)

The formation of centres in lithium-doped silicon by variation of lithium concentration and annealing temperature studied by PL, can reveal the passivation processes of centres The C centre at 789 6 meV, involving a carbon and oxygen interstitial is passivated by lithium (Rodriguez *et al*, 1997a) In the same study, ZPLs D1 and D2 at 1106 9 and 1107 7 meV respectively, known to be due to an isoelectronic centre of trigonal symmetry, (Canham, 1983), are shown to be very efficiently passivated at a concentration of lithium lower than required to passivate the C centre

The isotope structure of a new lithium complex with zero-phonon line at 1133 meV reveals seven non-thermalising lines with a large isotope shift A tentative model to explain the isotope data, suggests a four-atom Li defect with two inequivalent sites (Rodriguez *et al*, 1997a) A new deep centre at 879 3 meV in irradiated FZ C- and Li-doped silicon appears to be passivated upon prolonged annealing at room temperature (Rodriguez *et al*, 1997b) The presence of oxygen inhibits the formation of the defect and the intensity dependence of the line with variations in carbon concentration suggests it is involved in the defect Lithium isotope substitution experiments reveal only one Li-atom is involved in the complex Recently the symmetry of the defect has been determined as monoclinic I (Rodriguez *et al*, 2000) Table 1 4 summarises the main findings of the lithium acceptor and photoluminescence centres

Line (meV)	Name	Element(s)/ identity	Symmetry (if known)	Ref.
Acceptor Levels				
E_V + 760		Au + Li		Gislason *et al.*, 1995
PL Centres				
1093.2		BE_{TO}		Kosai *et al.*, 1974
		BMEC		Lyon *et al.*, 1978
1045	Q	Li_4-V	trigonal	Davies *et al.*, 1984
1082	S	Li_4-C	trigonal	Lightowlers *et al.*, 1984
1122.3	Au-Li	Au + Li		Gislason *et al.*, 1995
~766		Au + Li		Gislason *et al.*, 1995
1133		Li_4 - related		Rodriguez *et al.*, 1997a,
879.3		Li + C		1997b
763.6	O_1	Li-related		Zhu., 1998
764.2	L	Au-$Li_{3\ \mathrm{or}\ 2}$	trigonal	Zhu., 1998
1121.2	H	X-Li_n		Zhu., 1998

Table 1.4 Summary of the main lithium acceptor levels and PL centres.

1.8 Cadmium-Lithium related defects in Silicon

Substitution of stable isotopes enables the chemical identity of defect impurities to be determined. Different isotopes of an element have the same number of protons, however they are distinguished by their nuclear mass and some isotopes have different nuclear spins. When the effect of different isotopes of a suspected impurity are observed in an associated line shift or broadening of the line the chemical identity and the number of atoms present in the defect can be estimated (this technique is described in detail in the next chapter). In the absence of stable isotopes the availability of radioactive isotopes where the disappearance or appearance of a spectral feature at a rate equal to the half-life of the isotope can help identify the constituent of a defect. A study of a high purity FZ silicon sample implanted with the radioactive isotope ^{111}In was undertaken to determine the feasibility of using radioactive isotopes in photoluminescence spectroscopy (Daly *et al.*, 1994, 1995c). ^{111}In was chosen as it has a half-life of 2.8 d and the PQR centre, which has one of the most intense PL emissions for silicon, was chosen to produce good quality data

(Thewalt *et al* , 1981, Weber *et al* , 1981) Three days after implantation the samples received a rapid thermal anneal, 10 s at ~ 1100°C and a rapid quench to room temperature which produced the PQR luminescence The free-exciton (FE), boron bound-exciton line (B) and the neutral In acceptor bound-exciton line were also observed in the spectrum which was dominated by the P line Spectra were recorded approximately every eight hours and after only one day the P line was no longer observed The P line and its associated sidebands, which dominate the spectrum, recorded two hours after quenching is shown in figure 1 9 (a)

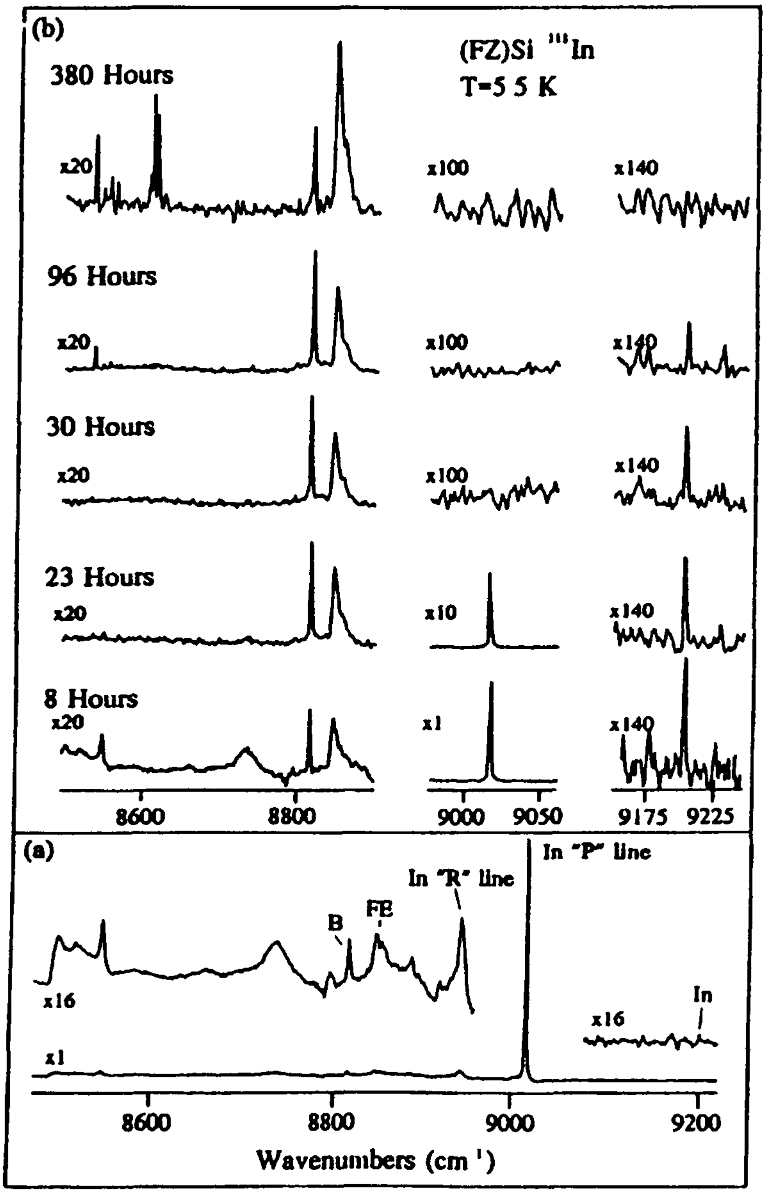

Figure 1.9 (a) PQR In related spectrum, (b) PQR system as it evolved over 16 day period. Two new systems were observed at 5.5 K after 16 days (Daly *et al.*, 1994).

The decay of the P line which occurs rapidly compared to the decay of the of the In acceptor BE line is clear in figure 1 9 (b) The acceptor bound-exciton intensity decayed as expected, with a 2 8 d half-life The luminescence intensity of the PQR centre decayed non-exponentially at a higher rate than the expected half-life of ^{111}In

The most interesting result of the experiment was the observation of a number of previously unreported spectral lines The lines can be divided into three groups, the first group centred near 8550 cm^{-1} (~1060 meV) appeared after one half-life, while the second centred near 8610 cm^{-1} (~1070 meV) appeared clearly after ten days Both of these groups are shown clearly in figure 1 9 (b) 380 hours after annealing The third system, in the range 8680 - 8780 cm^{-1} (1070 - 1090 meV) were not observed in spectra recorded at ~ 5 5 K but were evident at temperatures of 10 K and above From figure 1 10, the complexity of the line structure is evident and due to inadequate signal levels reliable thermalisation data could not be developed A comparison of the rate of growth of the new lines with the rate of decay of ^{111}In suggested the rate of evolution was below that expected for the direct indium to cadmium transition The relative intensities of the three groups indicates the three are unrelated, thus suggesting different defects are involved

Daly *et al* (1994) attributed these centres to the complexing of cadmium atoms in the crystal when stored at room temperature Substitutional cadmium is expected to produce double acceptor bound exciton recombination which is unobserved in silicon and the complexity of the line structure may be consistent with such recombination However, no two-hole or two-electron satellites were observed due to weak PL signals and the assignment could not be confirmed Cd-diffused and implanted samples which were annealed by a similar method to produce the PQR centre revealed the three groups of lines and a subsequent anneal in the temperature range 100 - 200^{o}C for 30 min was found to enhance defect production This indicated a fast diffusing impurity, possibly a transition element was also involved in the formation of the defects These three defect systems have formed the basis of this research and results confirming the identity, temperature dependence, symmetry and spin states are reported for the first time in this thesis

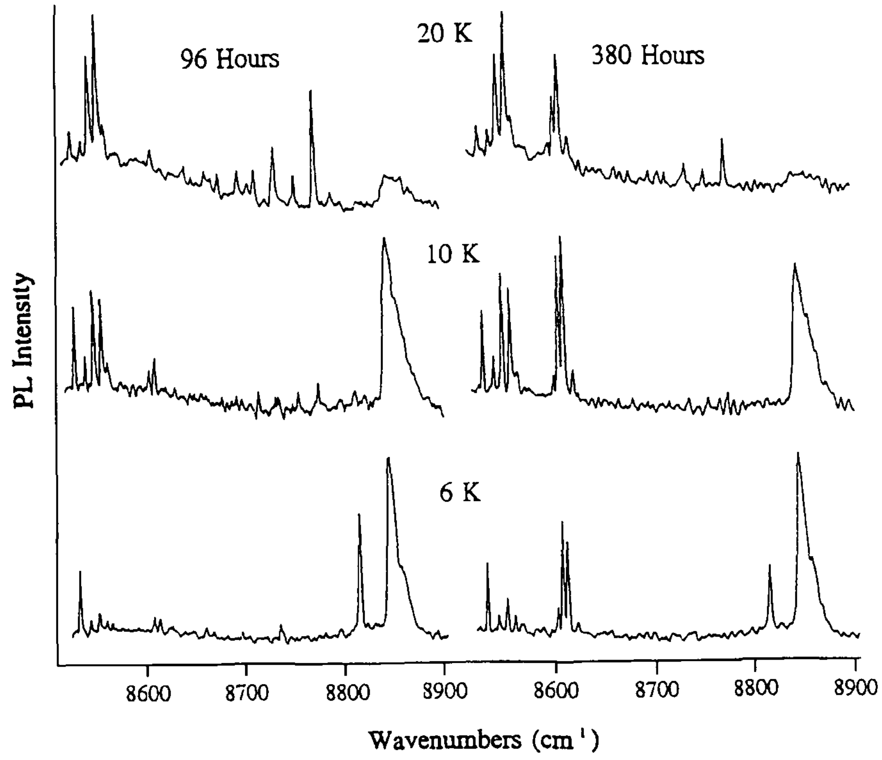

Figure 1.10 Preliminary temperature dependence of the new PL spectra observed in Si:^{111}In following the decay of ^{111}In to ^{111}Cd (Daly *et al.*, 1994).

1.9 Conclusion

The introduction of defects in silicon can introduce energy levels in the forbidden energy gap which can allow control of the optical and electronic properties of the host material which may be tailored for specific technological purposes The details of the electronic and optical properties of the beryllium, zinc and cadmium, group II elements and of lithium, a group I element in silicon were presented Three defect structures likely to contain cadmium and lithium were introduced and are the subject of this thesis The optical technique of photoluminescence is the primary tool used to probe these defects, and in the next chapter perturbation techniques of uniaxial stress, Zeeman and isotope experiments are described However, in the first section of chapter two, the effect of temperature variation on optical spectra is described

References

Aggarwal R L , Fisher P , Mourzine V and Ramdas A K , Phys Rev **A** 882-893, (1965)

Alteheld P , Greulich-Weber S , Spaeth J -M , Overhof M and Hohne M , Mater Sci Forum, **143-147**, 1173-1178, (1994)

Born M and Oppenheimer J R , Ann Phys , **84**, 457, (1927)

Born M and Huang R , “Dynamical Theory of crystal lattices”, Clarendon Press, Oxford, (1954)

Canham L T , PhD Thesis, University of London, (1983)

Caravaca M A , Casali R A and Rodriguez C O , Phys Rev **B57**, 14580-14583, (1998)

Crouch R K , Robertson J B and Gilmar Jr T E , Phys Rev **B5**, 3111-3119, (1972)

Crouch R K , Robertson J B , Morgan H T , Gilmar Jr T E and Franks R K , J Phys Chem Solids **35**, 833-837, (1974)

Daly S E , Henry M O , Freitag K and Vianden R , J Phys Condens Matter **6** L643-L650, (1994)

Daly S E , McGlynn E , Henry M O , Campion J D , McGuigan K G , Do Carmo M C. and Nazare M H , Mater Sci Forum, **196-201**, 1303-1307, (1995a)

Daly S E , Campion J D , McGlynn E , Henry M O , Do Carmo M C and Nazare M H , Solid State Commun , **93**, 454, (1995b)

Daly S E , Henry M O , Frehill C A , Frietag K , Vianden R , Rohrlack G and Forkel D , Mater Sci Forum, **196-201**, 1497-1502, (1995c)

Daly S E , Henry M O , McGuigan K G , Do Carmo M C , Semicond Sci Technol, **11**, 7, 996-1001, (1996)

Davies G , Rep Prog Phys , **44**, 787-830, (1981)

Davies G , Canham L T and Lightowlers E C , J Phys **C17**, L173-L178, (1984)

Davies G , Zafar Iqbal M and Lightowlers E C , Phys Rev **B50**, 11520-11530, (1994)

Davies G , “The Optical Properties of Luminescence Centres in Silicon”, Physics Reports **176**, 3&4, (1989)

Davies G , Chapter one in “Identification of Defects in Semiconductors”, edited by Stavola M , Academic Press, (1999) Dean P J , Yafet Y and Haynes J R , Phys Rev **184**, 837-843, (1969)

Dean P J and Herbert D C , Chapter three in "Excitons", edited by Cho K , Springer-Verlag, (1979)

Dornen A Kienle R , Thonke K , Stolz P , Pensl G , Grunebaum D and Stolwijk N A , Phys Rev **B40**, 12005-12008, (1989)

Dyunaidov S S , Urmanov N A and Gafurova M V , Phys Stat Sol **A66**, K79-81, (1981)

Fuller C S and Morin F J , Phys Rev , **105**, 379-384, (1957)

Gebhard M , Achtziger N , Baurichter A , Forkel D , Vogt B and Witthuhn W , Physica **B170**, 320-324, (1991)

Gerasimenko N N, Zaltsev B A, Safronov L N and Smirnov L S , Sov Phys Semicond , **19**(7), 762-765, (1985)

Gislason H P , Kristjansson S and Sveinbjornsson E Ö , Mater Sci Forum , **196-201**, 695-700, (1995)

Gislason H P , Physics Scripta **T69**, 40-51, (1997)

Grimmeiss H G and Ledebo L A , J Phys **C8**, 2615-2626, (1975)

Gulamova M A , Karimova I Z and Knigin P I , Sov Phys -Semicond **5**, 687-689, (1971)

Henry M O , Campion J D , McGuigan K G , Thewalt M L W and Lightowlers E C , Mater Sci Eng **B4** , 269-272, (1989)

Henry M O , McGuigan K G , do Carmo M C Nazare M H and Lightowlers E C , J Phys , Condens Matter, **2**, 9697-9700, (1990)

Henry M O , Campion J D , McGuigan K G , Lightowlers E C , do Carmo M C and Nazare M H , Semicond Sci Technol **9**, 1375-1381, (1994)

Henry M O , Lightowlers E C , Killoran N , Dunstan D J and Cavenett B C , J Phys **C14**, L255-261, (1981)

Heyman J N , Giesekus A and Haller E E , Mater Sci Forum **83-87**, 257-262, (1992)

Heyman J N , Haller E E , and Giesekus A , Phys Rev **B44**, 12769-75, (1991)

Henderson B and Imbusch G F , "Optical Spectroscopy of Inorganic Solids", Clarendon Press, Oxford, (1989)

Ho L T and Lin F Y , International Journal of Infrared and Millimeter Waves, **18**, 463-473, (1997) Ho L T , Lin F Y and Lin W J , International Journal of Infrared and Millimeter Waves, **16**, 339-348, (1995)

Hopfield J J, Thomas D G and Lynch R T, Phys Rev **B17**, 312, (1966)

Killoran N , Dunstan D J , Henry M O , Lightowlers E C and Cavenett B C , J Phys **C15**, 6067-6085, (1982)

Kirczenow G , Can J Phys **55**, 1787, (1977)

Kirshan K , Stout P J and Watanabe M , Chapter six in "Practical Fourier Transform Infrared Spectroscopy", Academic Press, (1990)

Kohn W , Solid State Phys **5**, 257, (1957)

Kosai K and Gershenzon M , Phys Rev **B9**, 723-736, (1974)

Lang M , Pensl G , Gebhard M , Achtziger N and Uhrmacher M , Appl Phys **A53**, 95-101, (1991)

Lang M , Pensl G , Gebhard M , Achtziger N and Uhrmacher M , Mater Sci Forum, **83-87**, 1097-1102, (1992)

Lightowlers E C , "Growth and Characterisation of Semiconductors", edited by Stradling R A and Kipstein P C , Adam-Hilger, (1990)

Lightowlers E C , Canham L T , Davies G , Thewalt M L W and Watkins S P , Phys Rev **B29**, 4517-4523, (1984)

Lyon S A , Smith D L and McGill T C , Solid State Commun , **28**, 317-320, (1978)

McGlynn E , Henry M O , McGuigan K G and Do Carmo M C , Phys Rev **B54**, (20) 14494-14503, (1996)

McGuigan K G , Henry M O , Campion J D , Daly S E , McGlynn E and Do Carmo M C , Semicond Sci Technol **11**, 930-934, (1996)

McLean T P , "Progress in Semiconductors", edited by Gibson A F , Burgess R E and Kroger F A , Wiley, New York, 1960 Vol V , and references therein

Merk E , Heyman J and Haller E E , Solid State Commun , **72**, 851-854, (1989)

Monemar B , Lindefelt U and Chen W M , Physica **146B**, 256-285, (1987)

Myers H P , "Introductory Solid State Physics", second edition, Taylor & Francis Ltd , 282, (1997)

Naser A , Gehlhoff W , Overhof H and Yankov R A , Phys Stat Sol (b) **210**, 753-757, (1998)

Poate J , Physics World, 8(11), 15-16, (1995) Rodriguez F , Davies G and Lightowlers E C , Mater Sci Forum **258-263**, 635-640, (1997a)

Rodriguez F , Davies G and Lightowlers E C , Mater Sci Forum **258-263**, 411-416, (1997b)

Rodriguez F , Davies G and Lightowlers E C , Phys Rev **B62**, 6180-6191, (2000)

Reynolds D C and Collins T C , "Excitons-their properties and uses", Academic Press Inc , 101, (1981)

Shaklee K L and Nahory R E , Phys Rev Lett , **24**, 942-945, (1970)

Sveinbjornsson E Ö , Kristjansson S And Gislason H P , J Appl Phys **77**, 3146-3154, (1995)

Sze S M, "Physics of Semiconductor Devices", John Wiley & Sons, 41, (1981)

Thewalt M L W , Can J Phys , **55**, 1463-1480, (1977)

Thewalt M L W , Solid State Commun , **28**, 361-364, (1978)

Thewalt M L W , Ziemelis U O and Parsons R R , Solid State Commun , **39**, 27, (1981)

Thewalt M L W , "Excitons", edited by Rashba E I and Sturge M D , Amsterdam North Holland, 393-485, (1982a)

Thewalt M L W , Watkins S P , Ziemelis U O , Lightowlers E C. and Henry M O , Solid State Commun , **44**, 573-577, (1982b)

Thonke K , Hangleiter A , Wagner J and Sauer R , J Phys **C18**, L795, (1985)

Wagner J , Dornen A and Sauer R , Phys Rev **B31**, 5561, (1985)

Watkins G D and Ham F S , Phys Rev **B10**, 4071, (1970)

Watts R K , Chapter three in "Point Defects in Crystals", John Wiley & Sons, (1977)

Weber J, Schmid W and Sauer R , J Lumin **18/19**, 93, (1979)

Weber J, Schmid W and Sauer R , Phys Rev **B21**, 2401, (1980)

Weber J, Sauer R and Wagner P , J Lumin **24/25**, 155, (1981)

Zhu M , PhD Thesis, University of London, (1998)

Chapter Two

Perturbation Techniques

2.1 Introduction

The relevant theoretical and experimental techniques that are used in the analysis of the defects are outlined in this chapter. The technique of photoluminescence is used in association with perturbation techniques of temperature dependence, uniaxial stress and magnetic field perturbations and isotope substitution experiments to discover the symmetry, electronic structure, spin states and chemical constituents of the defects under study. The technique of PL spectroscopy is outlined in the first section. The second section explains the wealth of information available about the energy levels from temperature dependence experiments. In the third section the experimental technique and the effect of applying stress to defects in crystals is discussed. The two main symmetry types of interest in this thesis are monoclinic I (C_{1h}) and trigonal (C_{3V}). The relevant equations and the expected number of stress split components for monoclinic I symmetry will be considered. In the fourth section, magnetic field perturbation effects will be discussed and in the final section a discussion of the method of chemical identification of defect constituents by isotope substitution is outlined.

2.2 Photoluminescence Measurement

All of the spectroscopic measurements in this thesis are carried out at low temperatures. Illumination by light with photon energies greater than the bandgap creates excitons, which can be captured at defect centres, and their recombination may subsequently produce luminescence. The measurements are performed at low temperatures to prevent excitons being thermally dissociated from defect centres, to reduce thermal broadening of the luminescence features due to lattice vibrations and also to reduce the role of non-radiative paths for recombination The optical transition occurs from an excited electronic state to a lower electronic state, which is usually the ground state Only a transition from the lowest lying excited states to the ground state are observed at low temperatures, and as the temperature is increased higher energy excited states can become populated as will be explained in detail in the next section

The source of excitation used for the work in this thesis was an argon ion laser operating on its (green) 514 nm line Silicon, which is an indirect gap semiconductor has poor PL efficiency and laser powers of typically 100 mW are necessary in order to observe PL signals with reasonable signal to noise ratio During temperature dependence measurements a major problem is heating of the sample due to the heating effect of the laser beam A high intensity focused beam can cause damage and annealing of the sample An unfocussed laser beam of diameter ~ 3 mm which caused negligible heating was used Figure 2 1 shows schematically the main elements of the experimental set-up

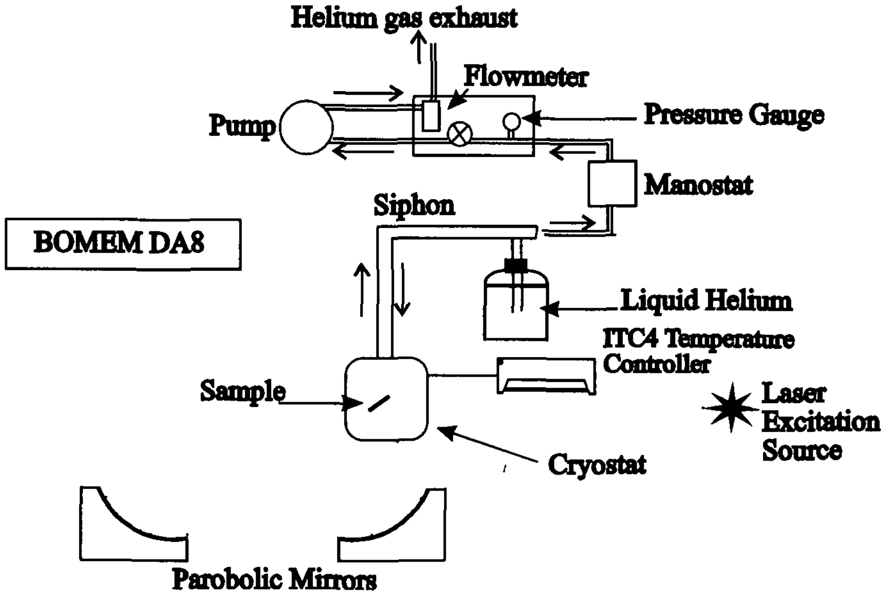

Figure 2.1 Schematic diagram of apparatus to achieve 4.2 - 300K temperature range.

The PL signal from the sample passes via two parabolic mirrors through a BOMEM DA8 Fourier transform spectrometer to the detector The Michelson interferometer is the main element of a Fourier transform (FT) spectrometer, shown in figure 2 2 The ultimate resolution of the system is determined by the range of the moving mirror of the Michelson interferometer and by the size of the aperture The maximum optical path difference of the mirror is 2 5 m corresponding to a maximum resolution of 0 004 cm^{-1}, for this work typical resolutions of 1 cm^{-1} and 0 15 cm^{-1} were used The beamsplitter of the interferometer was BK5 glass, which had a transmission curve of 3,500 to 30,000 cm^{-1} Several accounts of the advantages and disadvantages of FT spectroscopy have been compiled (Horlick 1968, Thewalt *et al*, 1990, Birch *et al*, 1995 and Lightowlers 1990)

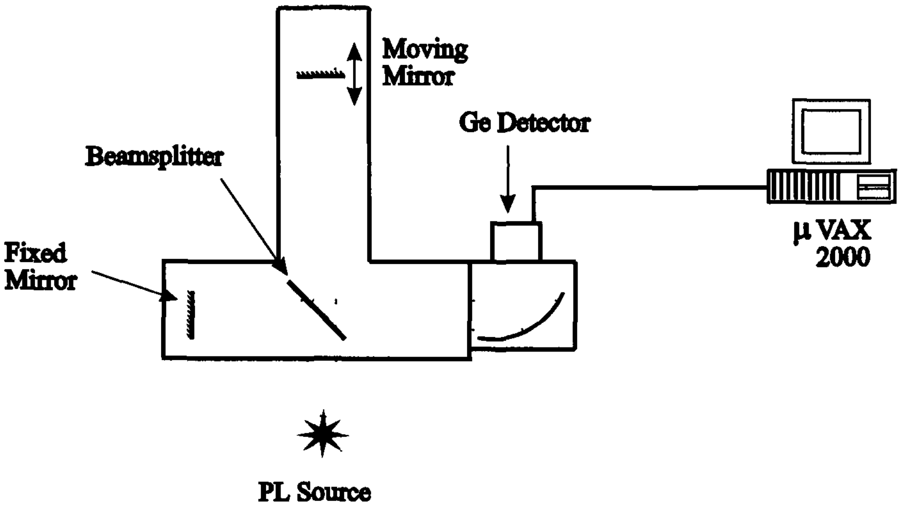

Figure 2.2 Schematic diagram of a Michelson interferometer based Fourier transform spectrometer.

The detector used was a North Coast cooled germanium diode detector (model EO817L-ED2) which set the limits of the spectral range as 6,000 to 10,000 cm^{-1} The germanium detector, the feedback resistor and the FET of the preamplifier were cooled to 77 K using liquid nitrogen This provided a highly sensitive, low noise performance detector in the 0 8 μm to 1 8 μm wavelength range In operation, the output from the detector is not a spectrum, but an interferogram, by performing a Fourier transform on the interferogram the spectrum is obtained The data handling, control and monitoring of the stability of the instrument was managed by a DEC μVAX 2000

To achieve the low temperatures necessary to acquire high resolution spectra three different types of cryostat were used to cool the samples In preliminary measurements, temperatures of 10 to 20 K were sufficiently low and a JANIS closed cycle refrigeration cryostat (model CCS-500) was used The samples were cooled by mounting them on a sample rod which was suspended inside the exchange gas tube, helium exchange gas was used as the thermal link between the samples and the refrigerator For temperature measurements in the range 4 2 to 300 K, the samples were cooled in an Oxford Instruments flow cryostat (model CF 1204) To obtain a temperature of 4 2 K the samples were immersed in liquid helium Changing the liquid helium or helium gas flow rate and using a heater on the sample holder the temperature within the cryostat can be varied An Oxford Instruments ITC4 temperature controller was used to monitor the temperature and the power supplied to the heater within the cryostat An Oxford Instruments germanium resistance temperature sensor was used for accurate temperature control below 40 K An Oxford Instruments manostat was used to control the flow of coolant from the dewar to the cryostat and to maintain a constant pressure within the cryostat

In the temperature dependence experiment, the temperature of the sample was reduced to ~2 K by reducing the vapour pressure over the liquid helium in an Oxford Instrument bath cryostat (model MD3) The bubbling of the helium was eliminated below the lambda point and the temperature of the sample was estimated from the pressure in the cryostat as no sensor was available on the sample holder The thermal broadening of the lines was expected to be of the order of only ~ 0 15 meV at ~ 2 K (Perkowitz 1993)

2.3 Temperature Dependence

Information about the energy level structure of a defect and the exciton binding energy to the defect may be obtained by studying the luminescence intensity of the defect as a function of temperature The total luminescence increases with temperature up to a maximum and above this temperature the luminescence is rapidly quenched At low temperatures excitons are trapped in the lowest energy excited states and transitions are only possible from these low energy excited states to the ground states As the temperature increases new lines may be observed in the spectra as their associated states are populated by excitons freed from other traps in the sample

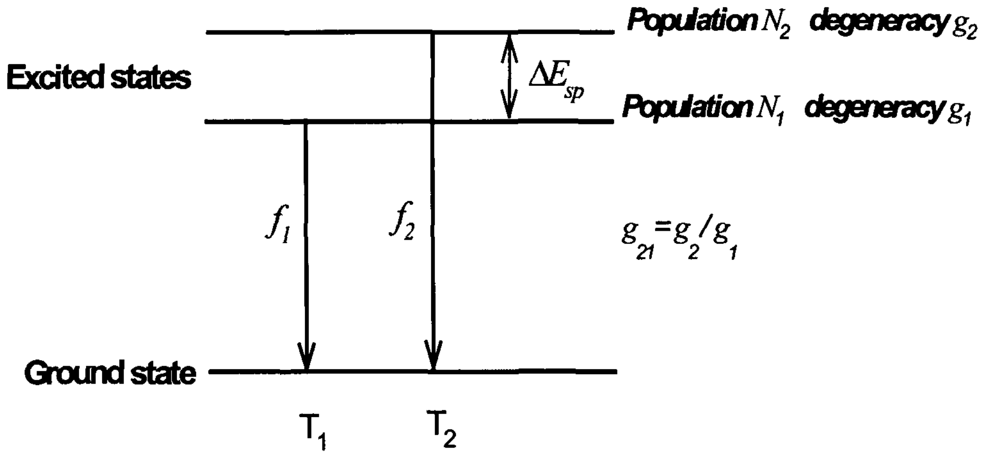

Figure 2.3 Energy level diagram of two zero-phonon lines thermalising to the same ground state, where f_i is the probability of radiative recombination and ΔE_{sp} is the spectral separation of the two lines.

The energy level diagram in figure 2 3 describes a PL centre consisting of two zero-phonon lines At low temperature only the transition from the lowest energy excited state to the ground state is observed, T_1, and its intensity can be expressed as

$$I_{tot} = N_1(0) f_1 \tag{2 1}$$

where $N_1(0)$ is the population of the first excited state at $T \sim$ 0K and f_1 is the probability of radiative recombination As the temperature is increased a second line may be observed and the total intensity of the two transitions, T_1 and T_2 is

$$I_{tot}(T) = N_1(T) f_1 \left[1 + (f_2/f_1) g_{21} \exp\left(-\Delta E_{sp}/kT\right)\right] \tag{2 2}$$

Rearrangement of the equation, assuming $N_1(0) = N_1(T) + N_2(T)$, leads to

$$I_{tot}(T) = \frac{I(0)\left[1 + (f_2/f_1) g_{21} \exp\left(-\Delta E_{sp}/kT\right)\right]}{\left[1 + g_{21} \exp\left(-\Delta E_{sp}/kT\right)\right]} \tag{2 3}$$

The natural log of the relative intensities of the two zero phonon lines as a function of inverse temperature yields a graph of slope $-\Delta E_{th}/k$ and intercept $\ln(f_2 g_{21}/f_1)$ ΔE_{th} is the activation energy calculated from the graph and a linear graph indicates two thermalising lines A calculated activation energy in good agreement with the spectral separation (ΔE_{sp}) of the two lines indicates that both excited states depopulate into the same ground state as shown in figure 2 3 If the calculated activation energy does not equal the spectral separation this indicates transitions are from excited states to a split ground state The total luminescence intensity arising from impurity levels created by the defect as a function of temperature can be rewritten as

$$I_1(T) = \frac{I(0)\left[1+\sum_{i>1}(f_i/f_1)g_{i1}\, exp\left(-\Delta E'_{sp}/kT\right)\right]}{\left[1+\sum_{i>1} g_{i1}\, exp\left(-\Delta E'_{sp}/kT\right)\right]} \tag{2 4}$$

where the i^{th} level is thermalising with respect to the first excited state and $\Delta E'_{sp}$ is the spectral separation between the levels assuming a common ground state

The increase in luminescence as a function of temperature can vary in different samples due to different concentrations of traps and different impurities introduced into the samples during defect production processes These shallow traps may have excitons weakly bound to them and as the temperature increases the excitons, which decay from these traps become available for capture at the defect This will cause an increase in luminescence as the temperature rises, dependent upon the energy position and the number of shallow traps, which will vary from sample to sample Schematically these shallow traps can be represented by a single trap, with population N_t and a binding energy of ΔE_t, as shown in figure 2 4 The conduction band acts as a source of excitons available for capture at either the shallow traps or at the deeper defect levels As the temperature increases the fraction of excitons trapped at the shallow traps decreases as the excitons are released almost immediately and are available for capture at the deeper defect The fraction of traps, which can compete with the deeper, centres for the capture of the available excitons is (Davies 1989)

$$f = 1/\left[1 + G_t T^{3/2} \exp\left(-\Delta E_t/kT\right)\right] \qquad (2\ 5)$$

where the $G_t T^{3/2}$ term describes the temperature dependent ratio of the band state concentration to the trap concentration The total luminescence resulting from the release of excitons and their capture as a function of temperature can be written as

$$I_2(T) = \frac{I(0)}{1 + rf} \qquad (2\ 6)$$

where r is the branching ratio of capture at trap centres relative to capture at the defect centre of interest

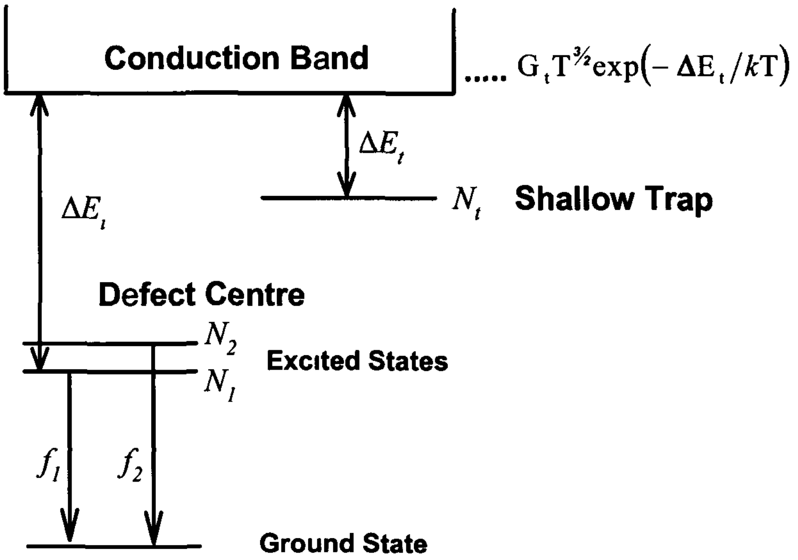

Figure 2.4 Shallow trap and defect centres compete for excitons.

At higher temperatures the luminescence is quenched rapidly The excitons may dissociate to the band, with dissociation energy E_i before they recombine at the defect centre The luminescence in this high temperature regime can be described by

$$I_3(T) = \frac{I(0)}{1 + G_d T^{3/2} \exp\left(-\Delta E_i/kT\right)} \qquad (2\ 7)$$

where G_d is the ratio of the conduction band density of states to the defect density of states The total luminescence of the defect centre as a function of temperature can be described by

$$I_{TOT}(T) = I(0)\; I_1(T)\; I_2(T)\; I_3(T) \qquad (2\ 8)$$

This equation when fitted to the experimental data will yield values for E_i, E_t, r, G_t, G_d and ΔE_{sp} E_i provides information about the thermal dissociation energy of the defect and can be compared to the spectroscopic binding energy of the defect

2.4 Uniaxial Stress Technique

The technique of applying stress to solids, which may cause any defect or impurity zero-phonon lines to split or shift in energy, is widely used to determine the symmetry of the defect or impurity A perfect silicon lattice has cubic symmetry and defects or impurities can only be arranged in the crystal in a certain number of inequivalent ways Applying a compression along the major symmetry axes of the crystal may remove the degeneracy of the defect states, this degeneracy may be orientational and/or electronic which will cause the lines to split The symmetry of the defect and the electronic nature of the transition can then be determined from the number, shift rate and polarisation intensities of the stress-split components The theory concerning the interpretation of stress splitting patterns and the number of expected lines has been well documented by Kaplyanskii (1964a, 1964b), Hughes and Runciman (1967) and Mohammed *et al* (1982) Once the symmetry of the defect has been determined, a model of the defect can be proposed, as there is a limit to the number of inequivalent orientations of the defect for each particular symmetry

For uniaxial stress measurements the samples are cut into rectangular parallelepipeds (12 x 4 x 2 mm) with the long axis along <001>, <111> and <110> directions The stress apparatus used and experimental set-up are outlined in appendix A There are a number of difficulties involved in taking reliable stress measurements. Great care must be taken when aligning the samples, as misalignment of the sample or applied stress will result in additional line splitting complicating the assignment of shift rate equations. To reduce the possibly of errors due to sample misalignment great care was taken during the alignment and measurements for each stress direction were repeated at least twice, both in Kings College London and Dublin City University. The most reliable data is presented in this thesis. The expected number of components under an applied stress is identical for several symmetries, further complicating the stress analysis. Both trigonal A-E and monoclinic I defects have a splitting pattern with two components in <001>, three in <111> and four in <110> stress directions (Mohammed *et al.*, 1982). Polarisation intensities of the stress components can help in identifying the symmetry but in PL measurements polarisation data is often very poor due to multiple internal reflections which depolarise the PL signal. In the absence of polarisation data, absolute intensities can aid the symmetry identification, however, this can also be complicated due to other stress induced effects; for example interactions with higher excited states may cause the component intensities to change (Mohammed *et al.*, 1982, McGuigan *et al.*, 2000). Three defects are considered in this thesis, groups I and II will be shown to have trigonal symmetry with transitions between A and E states and group III will be shown to exhibit monoclinic I symmetry. The application of stress to a monoclinic I centre results in the removal of orientation degeneracy only. For transitions between a doubly degenerate E state and a single A state in trigonal defects both the orientational and electronic degeneracy may be removed. The addition of electronic degeneracy further complicates the stress splitting pattern. Hughes and Runciman (1967) have treated this electronic degeneracy for trigonal centres in detail. The shift rate equations relevant to monoclinic I centres are considered in the next section.

2.4.1 Uniaxial Stress Technique - Monoclinic I Centres

Monoclinic centres have one C_2 axis or symmetry plane σ_h giving rise to two possible classifications. For monoclinic centres of type I, C_2 coincides with <110> or σ_h with {110}, for centres of type II the C_2 axis coincides with <100> or σ_h with {100} (Mohammed *et al.*, 1982). Monoclinic centres of type I are discussed here as they are relevant to this thesis. The symmetry operations of a monoclinic centre are the identity operation E, which corresponds to doing nothing to the defect, and a reflection plane σ_h. The primary axis (Z) of the optical centre is chosen normal to the reflection plane and is directed along a <110> direction in the lattice. A typical monoclinic defect is shown in figure 2.5.

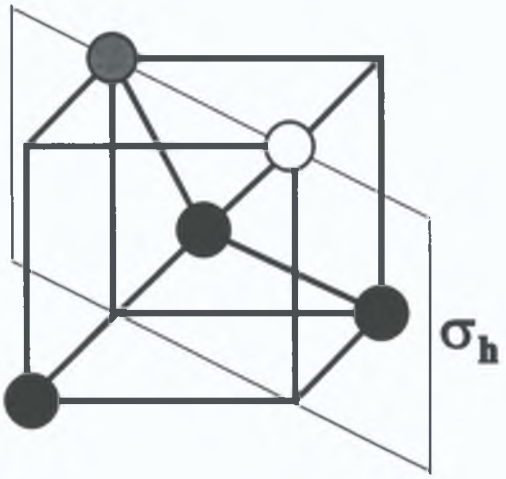

Figure 2.5 Schematic diagram of a monoclinic I defect.

The point group of the monoclinic centre in silicon is C_{1h} and the character table is shown in table 2.1 where the columns are labelled according to the number and type of operations forming each class. The labels of the irreducible representations are *A* and *B* for non-degenerate irreducible representations. Electric dipole transitions can occur between different *A* states, different *B* states or between an *A* and *B* state. For more details of character tables see Tinkham (1964).

C_{1h}	E	σ_h	
A	1	1	x^2, y^2, z^2, xy, x, y
B	1	-1	xz, yz, z

Table 2.1 Character table of a monoclinic I (C_{1h}) centre.

The number of inequivalent orientations *N*, of a monoclinic defect, or of any defect is given by $N = G/g$ where *G* is the order of the point group of the host lattice and *g* is the order of the defect group. The point group of silicon is octahedral of order 48, but each element is paired with another by the inversion operator of the silicon lattice. Uniaxial stress cannot distinguish between these pairs and the point group of silicon is effectively tetrahedral with *G* = 24. In the case of monoclinic I, $g = 2$ and there are twelve inequivalent orientations of a monoclinic defect and these inequivalent orientations are listed in table 2 2

Orientation Number	X axis	Y axis	Z axis
1	00**1**	**1**10	110
2	**1**00	0**1**1	011
3	0**1**0	10**1**	101
4	001	110	**1**10
5	100	011	0**1**1
6	010	101	10**1**
7	0**1**0	**1**01	**1**0**1**
8	00**1**	1**1**0	**11**0
9	**1**00	01**1**	0**11**
10	100	0**11**	01**1**
11	001	**11**0	1**1**0
12	010	**1**0**1**	**1**01

Table 2.2 Twelve possible orientations of a monoclinic I centre where the bold font indicates -1.

In the absence of stress the energy levels that arise about a defect correspond to the wavefunctions that will satisfy the Schrodinger wave equation

$$H_0\Psi = E\Psi \tag{2 9}$$

where

$$H_0 = H_C + H_i \tag{2 10}$$

H_C is the Hamiltonian operator of the pure crystal and H_i is the perturbation operator of the Hamiltonian due to the impurities in the crystal A transition between two energy levels about an axial defect with group symmetry g in a crystal of symmetry G has a transition energy E_T

$$E_T = E_2 - E_1 \tag{2 11}$$

where E_2 and E_1 are the energies of the excited state and ground state respectively By applying a stress, the energy of the transition, E_T may change as shown in figure 2 6 and the energy of the perturbed transition, E_S is

$$E_S = E_2 - E_1 + \Delta E \tag{2 12}$$

where the shift rate, ΔE of the transition is the difference of two terms, $\langle E_2|\overline{V}_S|E_2\rangle - \langle E_1|\overline{V}_S|E_1\rangle$ For the application of stress which is significantly small, first order perturbation theory is used and the Hamiltonian can be re-written as

$$H = H_0 + \overline{V}_S \tag{2 13}$$

where H_0 is the Hamiltonian for zero stress and $\overline{V}_S$ is the stress operator

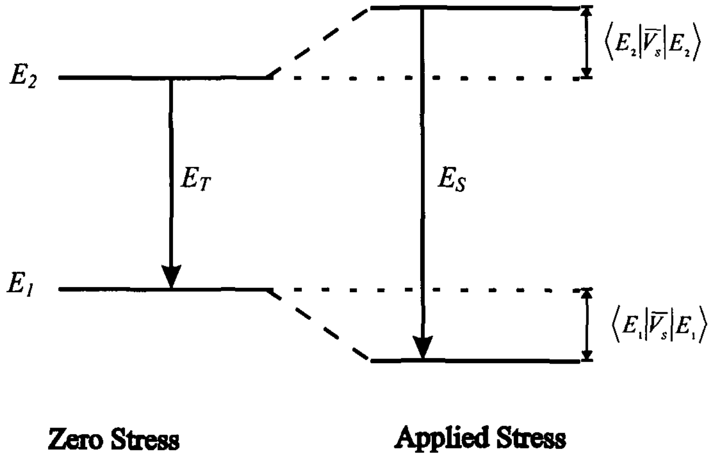

Figure 2.6 When stress is applied to a transition E_T the energy levels may shift giving new transition energy E_S

Following the notation of Kaplyanskii (1964) the stress operator is

$$\overline{V}_S = \sum_{i,j} \overline{a}_k S_{ij} \tag{2 14}$$

where i, j = X, Y, Z are the defect co-ordinates, S_{ij} is the strain tensor and $\overline{a}_k$ (k = 1, , 6), are sub-operators of the stress operator $\overline{V}_S$, such that

$$\overline{V}_S = \overline{a}_1 S_{XX} + \overline{a}_2 S_{YY} + \overline{a}_3 S_{ZZ} + \overline{a}_4 S_{XY} + \overline{a}_5 S_{XZ} + \overline{a}_6 S_{YZ} \tag{2 15}$$

From group theory, the only elements of the potential $\overline{V}_S$ which contribute to the shift in energy, ΔE are those elements transforming as the A irreducible representation. Further details of this general theorem for non-degenerate states can be found in Tinkham (1964). For a monoclinic centre only the terms XX, YY, ZZ and XY will be retained in equation 2.15, and the stress operator $\overline{V}_S$ for a monoclinic defect has the form:

$$\overline{V}_S = \overline{a}_1 S_{XX} + \overline{a}_2 S_{YY} + \overline{a}_3 S_{ZZ} + \overline{a}_4 S_{XY} \tag{2.16}$$

Substituting this equation into equation (2.13), solutions for each term $\langle E_2 | \overline{a}_x | E_2 \rangle + \langle E_1 | \overline{a}_x | E_1 \rangle$ are found to be real constants and are termed stress parameters, a_x where $x \in$ 1,2,3,4. Thus a general expression for the shift rate is obtained:

$$\Delta E = a_1 S_{XX} + a_2 S_{YY} + a_3 S_{ZZ} + a_4 S_{XY} \tag{2.17}$$

Solving for two defects, each with different chemical configurations, we would expect the stress parameters a_1, a_2, a_3 and a_4 to be different for each type of monoclinic defect; thus, the defect dependent stress parameters can be used as a tool to identify defects.

The shift in energy due to an applied stress for the twelve orientations can be derived. To meet the experimental conditions the defect co-ordinates must be transformed to crystal co-ordinates. Defining the crystal co-ordinates as:

$$x = (100) \qquad y = (010) \qquad z = (001) \tag{2.18}$$

and considering defect 1 in table 2.2:

$$\mathrm{X} = 001 \qquad \mathrm{Y} = 110 \qquad \mathrm{Z} = 110$$

The defect co-ordinates in terms of crystal co-ordinates are

$$\mathrm{X} = y \qquad \mathrm{Y} = \frac{-x + y}{\sqrt{2}} \qquad \mathrm{Z} = \frac{x + y}{\sqrt{2}} \tag{2.19}$$

The tensors S_{ij} from equation (2.17) can now be re-written in terms of crystal co-ordinates as:

$$
\begin{aligned}
S_{XX} &= S_{zz} \\
S_{YY} &= \tfrac{1}{2}\left(S_{xx} + S_{yy} - 2S_{xy}\right) \\
S_{ZZ} &= \tfrac{1}{2}\left(S_{xx} + S_{yy} + 2S_{xy}\right) \\
S_{XZ} &= \tfrac{1}{\sqrt{2}}\left(S_{xx} - S_{yz}\right)
\end{aligned} \tag{2.20}
$$

By defining the stress parameters as $A_1 = a_1$, $2A_2 = a_2 + a_3$, $2A_3 = a_2 - a_3$ and $2A_4 = a_4/\sqrt{2}$ and by substitution into equation (2.17) the shift rate can be written as:

$$\Delta E = A_1 S_{zz} + A_2\left(S_{xx} + S_{yy}\right) - 2A_3 S_{xy} + 2A_4\left(S_{xz} - S_{yz}\right) \tag{2.21}$$

The shift in energy for the twelve orientations can be re-written in the form given by Kaplyanskii (1964), and are summarised in table 2.3.

Orientation Number	Shift in Energy
1	$\Delta E = A_1 S_{zz} + A_2\left(S_{xx} + S_{yy}\right) - 2A_3 S_{xy} + 2A_4\left(S_{xz} - S_{yz}\right)$
2	$\Delta E = A_1 S_{xx} + A_2\left(S_{yy} + S_{zz}\right) - 2A_3 S_{yz} + 2A_4\left(S_{xy} - S_{xz}\right)$
3	$\Delta E = A_1 S_{yy} + A_2\left(S_{xx} + S_{zz}\right) - 2A_3 S_{xz} + 2A_4\left(S_{yz} - S_{xy}\right)$
4	$\Delta E = A_1 S_{zz} + A_2\left(S_{xx} + S_{yy}\right) + 2A_3 S_{xy} + 2A_4\left(S_{xz} + S_{yz}\right)$
5	$\Delta E = A_1 S_{xx} + A_2\left(S_{yy} + S_{zz}\right) + 2A_3 S_{yz} + 2A_4\left(S_{xy} + S_{xz}\right)$
6	$\Delta E = A_1 S_{yy} + A_2\left(S_{xx} + S_{zz}\right) + 2A_3 S_{xz} + 2A_4\left(S_{xy} + S_{yz}\right)$
7	$\Delta E = A_1 S_{yy} + A_2\left(S_{xx} + S_{zz}\right) - 2A_3 S_{xz} + 2A_4\left(S_{xy} - S_{yz}\right)$
8	$\Delta E = A_1 S_{zz} + A_2\left(S_{xx} + S_{yy}\right) - 2A_3 S_{xy} + 2A_4\left(S_{yz} - S_{xz}\right)$
9	$\Delta E = A_1 S_{xx} + A_2\left(S_{yy} + S_{zz}\right) - 2A_3 S_{yz} + 2A_4\left(S_{xz} - S_{xy}\right)$
10	$\Delta E = A_1 S_{xx} + A_2\left(S_{yy} + S_{zz}\right) + 2A_3 S_{yz} - 2A_4\left(S_{xy} + S_{xz}\right)$
11	$\Delta E = A_1 S_{zz} + A_2\left(S_{xx} + S_{yy}\right) + 2A_3 S_{xy} - 2A_4\left(S_{xz} - S_{yz}\right)$
12	$\Delta E = A_1 S_{yy} + A_2\left(S_{xx} + S_{zz}\right) + 2A_3 S_{xz} - 2A_4\left(S_{xy} + S_{yz}\right)$

Table 2.3 The shift rates of the twelve orientations of a monoclinic I defect in terms of crystal co-ordinates. The four parameters A_1, A_2, A_3 and A_4 give the perturbations of the centres.

The strain tensors S_{ij} are calculated along the three principal crystal directions The strain tensor is

$$S_{ij} = |\overline{P}|Cos(\overline{P},i)Cos(\overline{P},j) \qquad (2\ 22)$$

where $(\overline{P},i)$ is the angle between the stress direction $\overline{P}$ and the i^{th} axis, $|\overline{P}|$ is the magnitude of the applied stress Since $S_{ij} = S_{ji}$ there are only six components of the stress tensor, S_{xx}, S_{yy} and S_{zz} are the normal components while S_{xy}, S_{yz} and S_{xz} are the shear components

For example a stress applied down the <111> axis of a cubic crystal gives

$$S_{xx} = |\overline{P}|Cos((100)\ (111))Cos((100)\ (111))$$

$$= \overline{P}\frac{1}{\sqrt{3}}\frac{1}{\sqrt{3}} = \frac{\overline{P}}{3}$$

All the tensor components for each direction of stress can be calculated and are listed below ($\overline{P} = 1$)

$$\overline{P} \| <001> \qquad \begin{matrix} S_{zz} = 1 \\ S_{yy} = S_{xx} = S_{xy} = S_{yz} = S_{xz} = 0 \end{matrix} \qquad (2\ 23)$$

$$\overline{P} \| <111> \qquad S_{ij} = \tfrac{1}{3} \qquad (2\ 24)$$

$$\overline{P} \| <110> \qquad \begin{matrix} S_{xx} = S_{yy} = S_{xy} = \tfrac{1}{2} \\ S_{zz} = S_{xz} = S_{yz} = 0 \end{matrix} \qquad (2\ 25)$$

By substituting these strain tensor, S_{ij} values into the twelve shift rate equations for each orientation of a monoclinic I defect, the shift rates for each direction of applied stress are obtained as in table 2.4, below.

Orientation Number	$\bar{P}\|<001>$ ΔE	$\bar{P}\|<111>$ ΔE	$\bar{P}\|<110>$ ΔE
1	A_1	$(A_1+2A_2-2A_3)/3$	A_2-A_3
2	A_2	$(A_1+2A_2-2A_3)/3$	$(A_1+2A_2+2A_4)/2$
3	A_2	$(A_1+2A_2-2A_3)/3$	$(A_1+2A_2-2A_4)/2$
4	A_1	$(A_1+2A_2+2A_3+4A_4)/3$	A_2+A_3
5	A_2	$(A_1+2A_2+2A_3+4A_4)/3$	$(A_1+2A_2+2A_4)/2$
6	A_2	$(A_1+2A_2+2A_3+4A_4)/3$	$(A_1+2A_2+2A_4)/2$
7	A_2	$(A_1+2A_2-2A_3)/3$	$(A_1+2A_2+2A_4)/2$
8	A_1	$(A_1+2A_2-2A_3)/3$	A_2-A_3
9	A_2	$(A_1+2A_2-2A_3)/3$	$(A_1+2A_2-2A_4)/2$
10	A_2	$(A_1+2A_2+2A_3-4A_4)/3$	$(A_1+2A_2-2A_4)/2$
11	A_1	$(A_1+2A_2+2A_3-4A_4)/3$	A_2+A_3
12	A_2	$(A_1+2A_2+2A_3-4A_4)/3$	$(A_1+2A_2-2A_4)/2$

Table 2.4 Shift in energy for each of the twelve orientations of a monoclinic centres for stress applied in the <001>, <111> and <110> directions.

From the above table, under a <001> applied stress the zero-phonon line is expected to split into two components with shift rates described by stress parameters A_1 and A_2 A <111> stress will split the zero-phonon line into three components with shift rates given in the above table while a stress applied parallel to the <110> direction will split the zero-phonon line into four components The intensity ratio and polarisation content of each stress-split component can be calculated This additional data allows one to identify a particular stress split component with a particular equation

2.4.2 Intensity and Polarisation

The relative intensities and polarisation of the components can be calculated by assuming the electric dipole of the transition lies along a particular direction This is usually along the defect axis of highest symmetry, the defect Z-axis The intensity observed is proportional to the square of the projection of the electric dipole vector ($\bar{E}$) of the luminescence onto the direction ($\bar{X}$) parallel or perpendicular to the stress direction, in a plane perpendicular to the viewing direction, thus

$$I \propto \left|\cos(\bar{E}\ \bar{X})\right|^2 \qquad (2\ 26)$$

π polarised luminescence is emitted when the electric vector is parallel to the stress direction, whereas, σ polarised luminescence has the electric vector perpendicular to the stress direction

For [110] stress, there are two inequivalent perpendicular viewing axes, <001> and <110> that will give two sets of inequivalent σ polarisation data The polarisation intensities and shift rates for monoclinic I symmetry are summarised in table 2 5 Each shift rate equation for each stress direction can be identified from the polarisation intensities If the predicted intensities do not match the experimental results then possibly the choice of dipole vector is incorrect, for example the electric dipole could be aligned perpendicular to the Z-axis of the defect. Fitting of the nine shift rate equations for monoclinic symmetry to experimental data will yield values the four stress parameters A_1, A_2, A_3 and A_4.

Stress Direction ($\overline{P}$)	Energy Shift	A to B Intensity and Polarisation			A to A, B to B Intensity and Polarisation		
		$E\parallel\overline{P}(\pi)$	$E\parallel\overline{P}(\sigma)$		$E\parallel\overline{P}(\pi)$	$E\parallel\overline{P}(\sigma)$	
<001>	A_1	0	1		0	1	
	A_2	2	1		2	1	
<111>	$(A_1 + 2A_2 - 2A_3)/3$	8	2		0	6	
	$(A_1 + 2A_2 + 2A_3 - 4A_4)/3$	0	3		4	1	
	$(A_1 + 2A_2 + 2A_3 + 4A_4)/3$	0	3		4	1	
<110>		$E\parallel\overline{P}(\pi)$	$E\parallel\overline{P}_{001}(\sigma)$	$E\parallel\overline{P}_{1\bar{1}0}(\sigma)$	$E\parallel\overline{P}(\pi)$	$E\parallel\overline{P}_{001}(\sigma)$	$E\parallel\overline{P}_{1\bar{1}0}(\sigma)$
	$A_2 - A_3$	2	0	0	0	0	2
	$(A_1 + 2A_2 + 2A_4)/2$	1	2	1	1	2	1
	$(A_1 + 2A_2 - 2A_4)/2$	1	2	1	1	2	1
	$A_2 + A_3$	0	0	2	2	0	0

Table 2.5 Intensity, polarisation and energy shift rate equations of zero-phonon lines in a monoclinic I centre.

2.4.3 Interaction of States

In the previous section the shift rate equations to describe the effect of an applied stress on transitions between non-degenerate states in a monoclinic I defect were outlined. In the discussion above it was assumed that the shift rates were linear as a function of stress, however at high stresses non-linear shift rates are often observed and can be due to excited states interacting with the observed transition. Many defects have a series of closely spaced excited states and under the application of a uniaxial stress these states can interact with each other, causing a non-linear shift rate. Due to selection rules, transitions from the excited state causing the interaction may be forbidden and not observed in the photoluminescence measurement. Consider the case of a monoclinic I centre consisting of two closely spaced excited states and an isolated ground state. The interaction matrix for the two excited states, labelled E_1 and E_2, can be written in the form of a secular matrix as:

$$\begin{array}{c|cc} \overline{V}_S & E_1 & E_2 \\ \hline E_1 & \langle E_1|\overline{V}_S|E_1\rangle & \langle E_1|\overline{V}_S|E_2\rangle \\ E_2 & \langle E_2|\overline{V}_S|E_1\rangle & \langle E_2|\overline{V}_S|E_1\rangle \end{array}$$

If the levels interact, the off-diagonal elements will be non-zero and a non-linear shift rate will be observed. The matrix elements [1,1] and [2,2] may be replaced by terms, which are similar to the terms describing non-degenerate states:

$$[1,1] \qquad a_1 S_{XX} + a_2 S_{YY} + a_3 S_{ZZ} + a_4 S_{XY} \tag{2.27}$$

$$[2,2] \qquad b_1 S_{XX} + b_2 S_{YY} + b_3 S_{ZZ} + b_4 S_{XY} + \Delta E \tag{2.28}$$

where a_i, b_i are the stress parameters and ΔE is the energy separation between the interacting levels. The form of the off-diagonal elements will depend on the transformation properties of the interacting states. Figure 2.7 shows four possible cases for a defect of monoclinic I symmetry, with all transitions to a ground A state. Similar transitions are also possible to a ground B state.

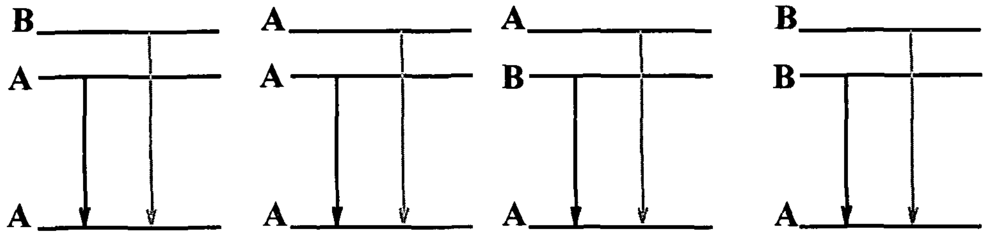

Figure 2.7 Possible excited state structures for A to A and B to A transitions at a monoclinic I defect. The black line indicates an allowed transition while the grey line represents a forbidden transition.

Using the Wigner-Eckhart theorem (Tinkham 1964) the elements of the stress potential can be determined and are summarised in table 2 6 There are only two interaction elements necessary to describe all eight possible cases as $\langle A|\overline{V}_S|B\rangle = \langle B|\overline{V}_S|A\rangle$

Interacting States E_1	 E_2	Matrix Element $\langle E_1\|\overline{V}_S\|E_2\rangle$
A (B)	*A (B)*	$c_1S_{XX}+c_2S_{YY}+c_3S_{ZZ}+c_4S_{XY}$
A	*B*	$c_1S_{XZ}+c_2S_{YZ}$

Table 2.6 The possible interaction elements for a monoclinic I symmetry.

The matrix must be diagonalised to fit the data to the theoretical model allowing the stress parameters a_i, b_i, c_i and the energy separation ΔE to vary A custom-built optimisation tool TRANID (McCarren *et al*, 1994) which determines the elements of the matrix by performing a least squares fit to the data is used in the analysis of the stress data in this thesis Analysis of the stress data in the low stress regime can aid in the fitting procedure, as initial values for a_i can be determined For certain stress directions the interaction may have no effect on the shift rates, that is the shift rate is linear even in the high stress regime Thus the off-diagonal elements of the matrix are equal to zero in the direction of the linear shift rate This information can help in the identification of the transitions as shown in chapter four for the monoclinic I defect studied in this thesis

2.5 Magnetic Field Perturbation

A magnetic field perturbation reveals information about the spin states and possibly the symmetry of the defect under consideration, in contrast to a uniaxial stress perturbation, which gives information only about the symmetry The behaviour of the zero phonon lines as a function of an applied external magnetic field along each crystallographic direction is studied The rate of splitting and the number of split components of a line gives information about the spin states, energy level structure and the binding of the excitons to the defect

In the case of an isoelectronic donor (pseudo-donor), the hole is the primary bound particle and the electron is loosely bound The electron, from the bottom of the conduction band has angular momentum $j = \frac{1}{2}$, and the hole, from the top of the valence band has angular momentum $j = \frac{3}{2}$ The localised nature of the bound hole makes it very sensitive to the symmetry of the local defect potential In the case of a compressive axial strain the angular momentum of the hole is quenched, thus changing the hole from p-like, to s-like, behaving to a good approximation as an isotropic $j = \frac{1}{2}$ particle The electron remains spin-like as it is weakly perturbed by the local field These two states couple, resulting in a J = 1 triplet and a J = 0 singlet state with the J = 1 state usually lower in energy As the orbital angular momentum is quenched, the observed splitting involves only pure spin states, under the application of an applied magnetic field the S = 1 triplet state splits into three components, as shown in figure 2 8, whereas the S = 0 singlet state is unaffected by the magnetic field The energy shift due to the magnetic field is

$$\Delta E_j = \mu_B m_j g\vec{B} \qquad (2\ 29)$$

where μ_B is the Bohr magnetron, $\vec{B}$ is the applied magnetic field and g is the Landé g-factor

The selection rule ΔS = 0 ensures transitions from the triplet state to the crystal ground state are dipole forbidden when the particles are purely spin like Several reports have revealed isotropic triplet splitting of the exciton ground state to the crystal ground state (Jeyanathan *et al*, 1995, Lightowlers *et al*, 1984) For transitions between triplet-singlet states, the Landé g-factor is 2 A g-factor, $g \neq 2$ suggests the hole angular momentum is not completely quenched, thus the states are not purely spin-like and the Δm_j (0 to 0 forbidden) selection rule is relaxed and the transition becomes weakly allowed

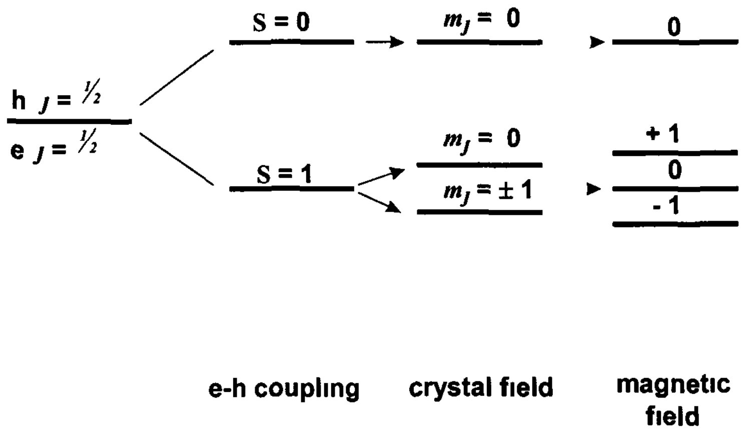

Figure 2.8 Schematic of the energy level structure of a triplet-singlet bound exciton system. The axial field is compressive and as the hole is the tightly bound particle it is more sensitive to the local symmetry field.

If the $j = \frac{1}{2}$ electron is the tightly bound particle, as in the pseudo-acceptor model, and the $j = \frac{3}{2}$ hole the secondary bound particle, in the absence of an internal strain they can couple to form excitonic states of total angular momentum of J = 1 or J = 2, with the J = 2 level lying lower in energy In the presence of an tensile axial strain the J = 2 exciton level splits into $m_j = \pm 2$, ± 1 and 0 sublevels and the J = 1 level splits into $m_j = \pm 1$ and 0 The application of a magnetic field removes the remaining degeneracy of the levels The optical selection rules apply and transitions from one state to another are only allowed if the change in the orbital angular momentum number, l, increases or decreases by 1, while the orbital magnetic quantum number, m_j, remains constant or increases or decreases by 1 Thus, transitions from the $m_j = \pm 2$ and $m_j = 0$ sublevels to the crystal ground state remain dipole forbidden and the $m_j = \pm 1$ are allowed The application of a magnetic field on a pseudo-acceptor model is shown in figure 2 9 Examples of an electron attractive neutral IBE exhibiting quintet-triplet transitions include the β Cu^* line (McGuigan, 1989) and the TI system in silicon (Watkins, 1985)

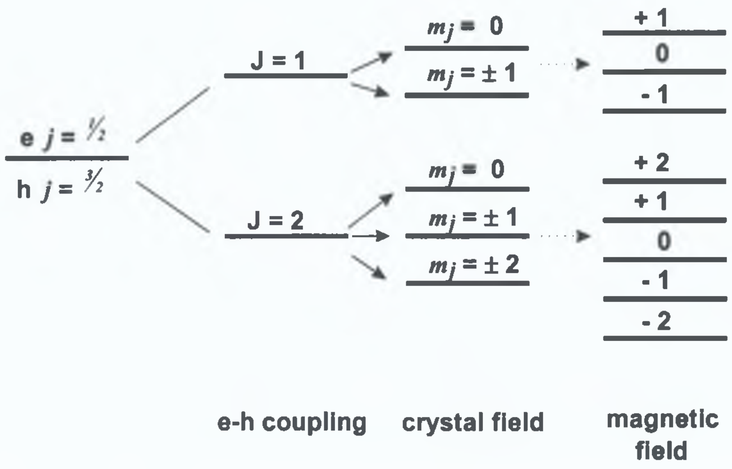

Figure 2.9 Schematic of the energy level structure of quintet-triplet system due to a tensile axial strain and magnetic field acting on an exciton with the electron as the tightly bound particle.

Observing the splitting of the spectral lines as the defect centre is rotated in the magnetic field can reveal centres with anisotropic behaviour. By rotation of the sample the differently oriented centres in the crystal will make different angles relative to the magnetic field and experience different perturbations thus revealing any anisotropy. As we will see in chapter five the defects studied within this thesis do not reveal any anisotropy.

2.6 Isotope Substitution Experiments

The chemical make-up of a defect is of interest and may be predicted from circumstantial evidence, such as controlling the concentration of the suspect impurity and correlation of the optical signal with the measured concentration. One major drawback is an internal calibration of the intensity is necessary as the luminescence signal is not absolute and varies with position of the sample with respect to the spectrometer, excitation power etc. However, isotope substitution experiments, where the effects of different isotopes of a suspected impurity are observed, can determine the defect constituents unambiguously. Different isotopes of an element have the same number of electrons, however they are distinguished by their nuclear mass and some isotopes have different nuclear spins. As the electronic states of the defect are influenced by the components of the defect and its surrounding lattice, there are two possibilities, either the isotopic mass of the constituent impurity can be varied or the isotopic mass of the host crystal can be varied Changing the isotope of a constituent of the defect and its effect on the associated zero-phonon transitions will be outlined as this method is relevant to the work presented in this thesis

As shown in section 1 5, the vibrational potential energy of the ground state, V_g, and the potential energy of the excited state, V_e are

$$V_g = \tfrac{1}{2} m\omega^2 (Q - Q_g)^2 \qquad (2\ 30)$$

$$V_e = E + \tfrac{1}{2} m\omega^2 (Q - Q_g)^2 + a(Q - Q_g) \qquad (2\ 31)$$

and may be represented by a CC diagram as shown in figure 2 10 The zero-phonon line is defined as the transition from the lowest vibrational level $N = 0$ of the excited state to the $n = 0$ state of the ground state

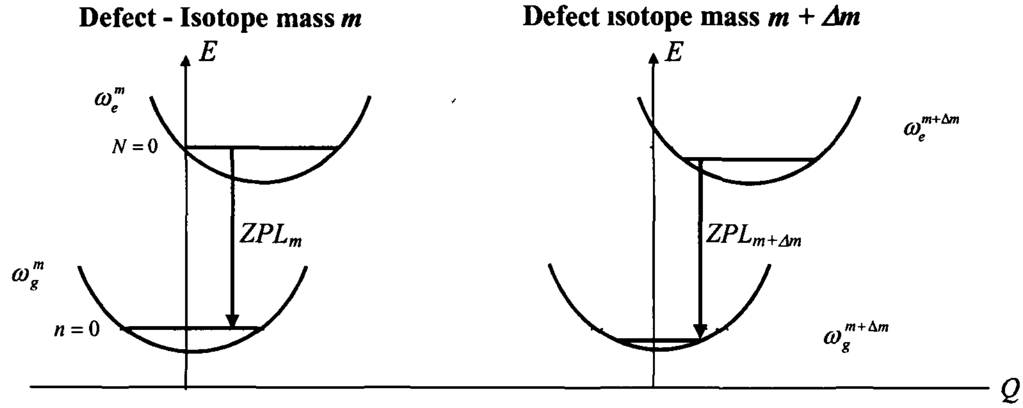

Figure 2.10 Comparison of the configuration co-ordinate models for an isotope of mass *m* and mass *m*+*Δm*.

If it is assumed the vibrational mode of the defect is due to the vibration of the atomic species of interest of mass m, against a restoring force of effective spring constant, k_i ($i = e$, g for the excited and ground state respectively), the normal vibration frequency of the mode neglecting vibrations of other defect constituents is

$$\omega_i^m = \sqrt{\frac{k_i}{m}} \qquad (2\ 32)$$

Replacing the impurity of mass m with an isotope of the impurity with mass $m + \Delta m$, the vibrational frequency will be

$$\omega_i^{m+\Delta m} = \sqrt{\frac{k_i}{m+\Delta m}} \tag{2 33}$$

The frequency shift for the excited state will be

$$\begin{aligned}\Delta\omega_e = \omega_e^{m} - \omega_e^{m+\Delta m} &= \sqrt{\frac{k_e}{m}} - \sqrt{\frac{k_e}{m+\Delta m}} \\ &= \sqrt{\frac{k_e}{m}}\left(1 - \sqrt{\frac{m}{m+\Delta m}}\right)\end{aligned} \tag{2 34}$$

Following the same method, the frequency shift of the ground state is

$$\Delta\omega_g = \sqrt{\frac{k_g}{m}}\left(1 - \sqrt{\frac{m}{m+\Delta m}}\right) \tag{2 35}$$

The ZPL energy shift between the two isotopes, in terms of frequency change is

$$\Delta = \Delta\omega_e - \Delta\omega_g = \left[\sqrt{\frac{k_e}{m}} - \sqrt{\frac{k_g}{m}}\right]\left[1 - \sqrt{\frac{m}{m+\Delta m}}\right] \tag{2 36}$$

and the shift in zero-phonon line energy can be written as

$$E_m - E_{m+\Delta m} = \tfrac{1}{2}\left[\hbar\omega_g - \hbar\omega_e\right]\left[1 - \sqrt{\frac{m}{m+\Delta m}}\right] \tag{2 37}$$

The magnitude of the isotope shift depends on Δm and the difference between the effective spring constant for the ground and excited state, $k_e - k_g$ The greater the difference in mass Δm, the better resolved the isotope shift would be Depending on the magnitude and sign of $k_e - k_g$ the isotope shift is in the positive or negative direction. As $k_e - k_g$ tends to zero, the isotope shift tends to zero. Consequently, in this model there is no change in zero-phonon energy when the isotopes are changed.

To obtain isotope effects, higher order electron-phonon coupling and anharmonic vibrational potentials must be considered. To allow for a different frequency in the excited state we rewrite equation (2.31) as:

$$V_e = E + \tfrac{1}{2}m\omega^2(Q-Q_g)^2 + a(Q-Q_g) + b(Q-Q_g)^2 \qquad (2.38)$$

$$= E + \tfrac{1}{2}m(\omega_g^2 + \frac{2b}{m})(Q-Q_g)^2 + a(Q-Q_g) \qquad (2.39)$$

The vibrational frequency of the excited state is:

$$\omega_e^2 = \omega_g^2 + \frac{2b}{m} \qquad (2.40)$$

and the shift in energy of the zero-phonon line can be expressed as:

$$\Delta E = \tfrac{1}{2}\hbar\left[\omega_e^m - \omega_g^m\right] - \tfrac{1}{2}\hbar\left[\omega_e^{m+\Delta m} - \omega_g^{m+\Delta m}\right] \qquad (2.41)$$

Information on the chemical constituents of the defect can also be obtained from the isotope shift of the phonon sideband. The ratio of the frequency shift to the normal vibration frequency of the excited state (equations 2.23 and 2.34) may be written as:

$$\frac{\Delta\omega_e}{\omega_e} = 1 - \sqrt{\frac{m}{m+\Delta m}} \qquad (2.42)$$

Thus, the phonon energy shift only depends on the change of the mass and is independent of the coupling states and the electronic states with which the mode is coupled. Defects can show isotope shifts in their phonon sidebands with are not present in the ZPL (Kurner *et al.*, 1989).

For nearly all of the experimentally reported isotope shifts of zero-phonon lines, the lower mass line falls at lower energy, indicative of a negative value for $k_e - k_g$, $k_e < k_g$ For these cases, the spring constant of the excited state is smaller than the ground state, indicating the excited state mode has been softened However, there are exceptions to this general trend, as we will see in chapter five

Isotope studies on the energy shift of zero-phonon lines may provide proof, not only of the involvement of a given impurity, but also on the number of impurity atoms present Considering the case of a single cadmium atom, samples implanted with ^{106}Cd are expected to show zero-phonon lines at lower energies than samples implanted with ^{116}Cd In a dual implant sample, the zero-phonon line will be expected to split into two components Depending upon the resolution, no splitting of the zero-phonon line may be observed, the line may only be broadened

The splitting of zero-phonon lines and their relative intensities in dual implant samples can provide information on the number of constituent atoms in defects If more than one atom is present the number of split components observed depends upon whether the atoms occupy equivalent or inequivalent sites in the centre Consider a centre containing two cadmium atoms which occupy equivalent sites, three types of centre will be produced when doped with both isotopes as the atoms can be interchanged Considering a centre containing two cadmium atoms occupying inequivalent sites, since the ^{116}Cd and the ^{106}Cd isotopes have different vibrational energies, due to their mass dependence, they are not interchangeable, thus four different types of centre can be produced

In this thesis, the results of lithium and cadmium isotope substitution experiments are described Since the defects are produced in cadmium implanted silicon, cadmium is the primary defect candidate Samples are implanted with ^{106}Cd, ^{116}Cd or a mixture of ^{106}Cd and ^{116}Cd isotopes to determine if cadmium is a constituent of the defects Lithium may be a catalyst in the formation of the defects or a constituent element, and it is shown in chapter three that introducing lithium during defect production enhances the defect luminescence The two stable isotopes of ^{7}Li and ^{6}Li were used for isotope studies

2.7 Summary and Conclusion

In this chapter the techniques and experimental apparatus used to investigate the defects presented in this thesis were outlined The main perturbation techniques of uniaxial stress, Zeeman and isotope substitution experiments were outlined The primary aim of chapter three is to introduce each of the defects in detail, provide details of their formation techniques and discuss the behaviour of the zero-phonon lines of each defect as a function of temperature The results for each perturbation technique applied to each defect are reported in chapters four and five

References

Birch J R and Clarke F J J , Spectroscopy Europe, **7**, (4), (1995)

Davies G , Physics Reports, **3&4**, 83, (1989)

Horlick G , Applied Spectroscopy, **22**, 6, 617, (1968)

Hughes A E and Runciman W A , Proc Phys Soc , 90, 827, (1967)

Kaplyanskii A A , Opt Spectrosc 16, 329, (1964a)

Kaplyanskii A A , Opt Spectrosc 16, 557, (1964b)

Jeyanathan L , Ph D thesis, King's College London, (1994)

Jeyanathan L, Davies G, and Lightowlers E C , Phys Rev **B52**, 10923, (1995)

Kurner W , Sauer R , Dornen A and Thonke K , Phys Rev B39, 13327, (1989)

Lightowlers E C , Canham L T , Davies G , Thewalt M L W and Watkins S P , Phys Rev **B29**, 4517, (1984)

Lightowlers E C , "Growth and Characterisation of Semiconductors", edited by Stradling R A and Kipstein P C , Adam-Hilger, (1990)

McCarren A L , Ruskin H J , McGuigan K G and Henry M O , IEE Proc Sci Meas Technol , **141**, 185, (1994)

McGlynn E , Henry M O , McGuigan K G and Do Carmo M C , Phys Rev **B54**, (20) 14 494-14 503, (1996)

McGuigan K G , PhD Thesis, Dublin City University, (1989)

McGuigan K G , McGlynn E , O'Cairbre F , Love J and Henry M O , J Phys Condens Matter **12**, 7055-7068, (2000)

Mohammed K , Davies G and Collins A T , J Phys C Solid State Phys , **15**, 2779-2788, (1982)

Perkowitz S , "Optical Characterisation of Semiconductors", Academic Press, (1993)

Thewalt M L W , Nissen M K , Beckett D J S and Lundgren K R , Mater Research Symp Proc 163, 221-232, (1990)

Tinkham M , Group Theory and Quantum Mechanics, McGraw-Hill, (1964)

Watkins S P and Thewalt M L W , Can J Phys **63**, 1074, (1985)

Chapter Three

Novel Luminescence Defects in Cadmium Doped Silicon

3.1 Introduction

As highlighted in section 1 8, the implantation of ^{111}In ions in silicon led to the observation of three previously unreported defects after several half-lives The decay of ^{111}In to its ^{111}Cd daughter atom was suspected to contribute to the formation of these new defects which were first reported by (Daly *et al*, 1994) This chapter is concerned with the detailed introduction of these three defects, labelled group I, II and III The term 'group' is used as each defect contains several zero-phonon lines and associated sidebands It will be shown in section 3 2 that cadmium is involved in the formation of these defects and the defects can be produced in non-radioactive samples Thus, the problems associated with using radioactive isotopes, such as the relatively short lived half life of the radioactive samples, (^{111}In has a 2 8 day half-life), and their hazardous nature can be overcome A detailed spectroscopic description of each defect and its associated phonon sidebands is given in section 3 3 The temperature dependence of each defect is discussed in subsequent sections An initial comparison of the defects indicates that defects I and II are similar in nature while group III must be treated separately

A typical photoluminescence spectrum of cadmium implanted FZ silicon obtained at 13 K, using 514 5 nm Ar$^+$ laser excitation is shown in figure 3 1 Three very strong luminescence systems are observed in the range 1055-1090 meV These systems are observed in samples implanted with cadmium only, which received a high temperature anneal at ~1100°C and quench with a subsequent anneal for 30 min at 100°C The cadmium implantation energy and dose were 200 keV and 1x10^{14} cm^{-2} Lithium contamination very likely came from the quartz tubing during the high temperature treatment, and indeed this will be shown to be the case in the subsequent section Similar lithium contamination has been reported in the formation of Au-Li defects (Zhu, 1997) The insets in figure 3 1 shows groups I, II and III Group I is centred at ~ 1061 meV, group II is centred at ~ 1068 meV and the lowest energy zero-phonon line of group III is at 1083 3 meV The spectral features of each group will be outlined in section 3 4 Two Cu-related lines at 943 7 and 944 2 (±0 1) meV, labelled $^{*}\mathrm{Cu}_0^{0}$ and $^{*}\mathrm{Cu}_1^{0}$ (McGuigan *et al*, 1988), and their Stokes sidebands are also observed Two low intensity zero-phonon lines observed at ~ 778 9 and 779 8 (±0 1) meV are attributed to a silver-related centre in the literature (Olajos *et al*, 1988, Zhu *et al*, 1997) A very weak zero-phonon line is observed at ~ 920 meV, which is a radiation damage centre involving C (Davies *et al*, 1984) Zero-phonon lines are observed at ~ 880 8, 825 4 and 813 7 (±0 1) meV and another doublet is observed at 867 28 and 868 21 (±0 1) meV, these lines have not been reported in the literature to date A previously unreported series of very closely spaced zero-phonon lines have been observed very close to the group I lines, not shown in figure 3 1 The principal lines are at energies 1055 06, 1055 5, 1055 94 and 1056 69 meV and may be silver-related lithium defects as the ~779 meV silver centre is also observed in the spectrum A series of lines with the principal zero-phonon line at ~ 996 meV has been observed in samples with groups I, II and III, this series of lines is not observed in the spectra shown in figure 3 1 No further study of this system has been reported, however, this centre has been observed previously in annealed CZ Cd-doped material (McGlynn *et al*, 1996)

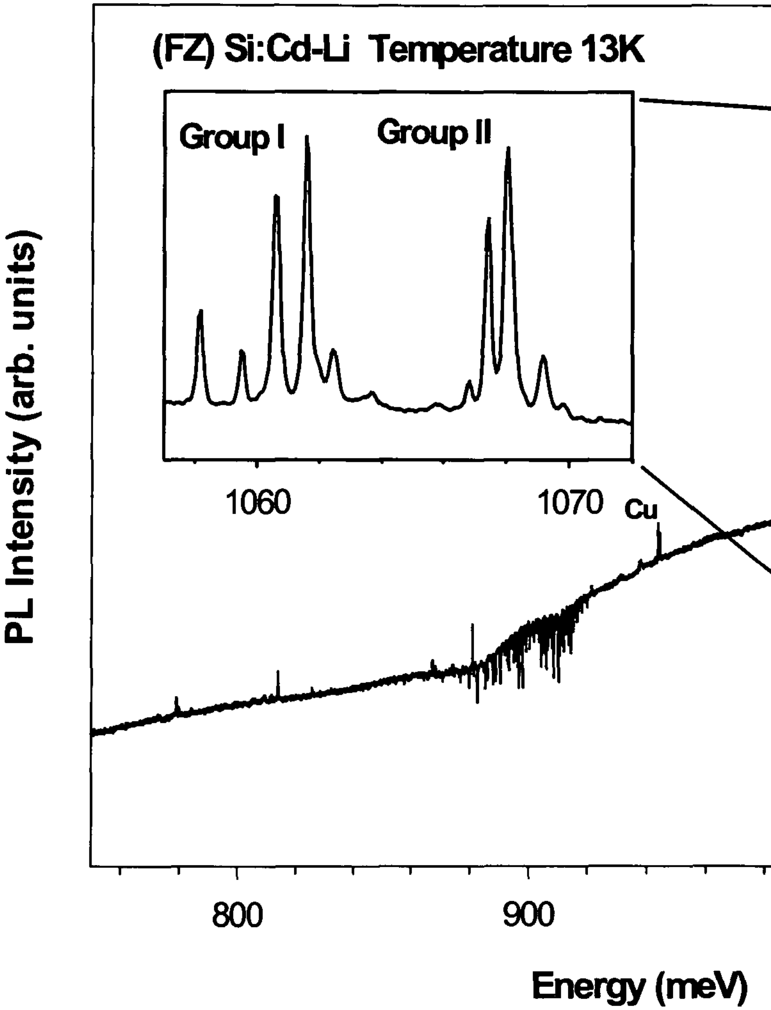
(FZ) Si:Cd-Li Temperature 13K
Group I
Group II
1060
1070
Cu
PL Intensity (arb. units)
800
900
Energy (meV)

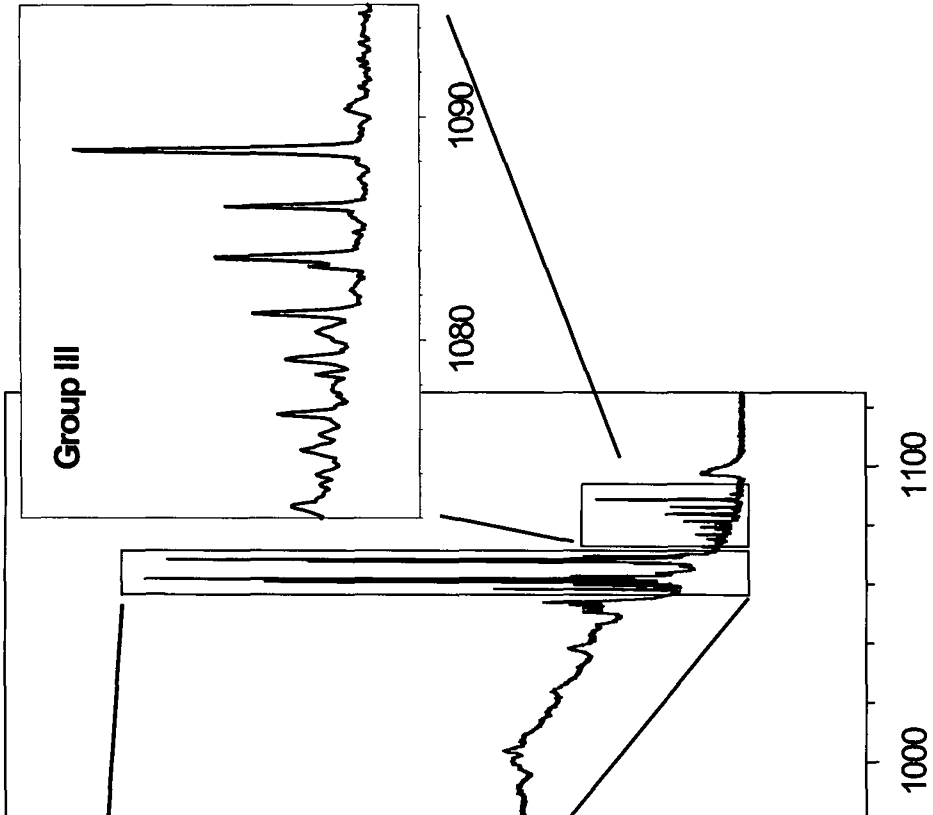
Group III
1080
1090
1000
1100

3.2 Defect Production

Samples used in preliminary experiments, temperature dependence experiments and isotope studies were all produced in cadmium implanted material by a high temperature anneal and rapid quench followed by a low temperature anneal, which is discussed in detail in this section The samples used in uniaxial stress measurements and magnetic field perturbation studies, which were prepared by cadmium diffusion, are described in chapter four, section 4 1

A number of samples were prepared by cadmium implantation or diffusion into high resistivity silicon, both oxygen-rich and oxygen-lean, and of both conductivity types For implantation, the typical ion implantation energy and dose were 200 keV and 1×10^{14} ions cm^{-2}, respectively To remove surface organics and metal contamination the samples were RCA cleaned before all heat treatments The RCA clean is the most widely used wet chemical clean in the IC industry and was initially developed by Kern *et al*, (1970) An outline of an RCA clean is given in Appendix B The RCA cleaned samples were placed in an RCA cleaned quartz tube which was heated rapidly to ~ 1100°C for 10s and quenched to room temperature in an isopropanol water (6 4) mixture The isopropanol and water mixture gives a slower quench rate than water alone, this reduces the risk of sample fracture The defect centres were produced by a subsequent anneal All subsequent isochronal annealing treatments were carried out in a furnace, where the samples were placed in a quartz tube in a flowing Ar atmosphere The samples were withdrawn slowly from the furnace and allowed to cool to room temperature without any quenching process to optimise the signal to noise ratio

Figure 3 2 shows spectra obtained from a Cd-implanted FZ p-type silicon sample which received a high temperature anneal at ~ 1100°C for 10 s and rapidly quenched followed by successive isochronal anneals for a duration of 15 min From this series of heat treatments the optimum defect formation conditions were obtained In figure 3 3 the photoluminescence intensity normalised to the maximum intensity for each group as a function of anneal temperature is illustrated The most favourable annealing temperature after the high temperature anneal and quench for each defect is evident

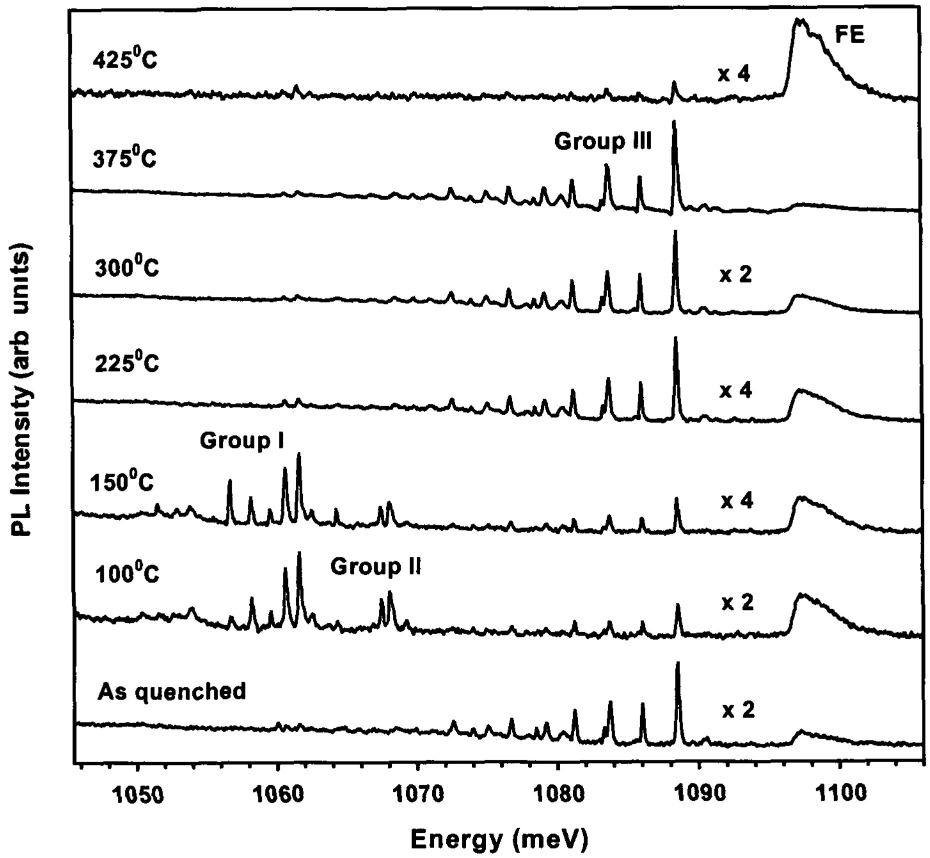

Figure 3.2 Effect of isochronal anneals on $Si:^{116}Cd$ FZ p-type sample subsequent to a high temperature anneal and quench. The spectra were recorded at a nominal temperature of 15K.

An anneal temperature of ~ 150°C optimises group I, for group II the optimal defect production temperature is ~ 100°C, whereas annealing at ~ 375°C optimises group III Annealing above 425°C causes all three groups of spectra to vanish

The production of the three defects was found to be dependant upon the cooling rate during the rapid quench to room temperature, which can be affected by the sample dimensions The smaller the sample dimensions the faster the rapid cool from ~ 1100°C to room temperature, resulting in optimal signals, while in a large sample with a slower cooling rate the intensity of the luminescence from the defects diminishes

On leaving the samples at room temperature for several weeks, the relative intensity of the defect photoluminescence was reduced or had completely vanished Subsequent to this discovery, all samples were stored at liquid nitrogen temperatures

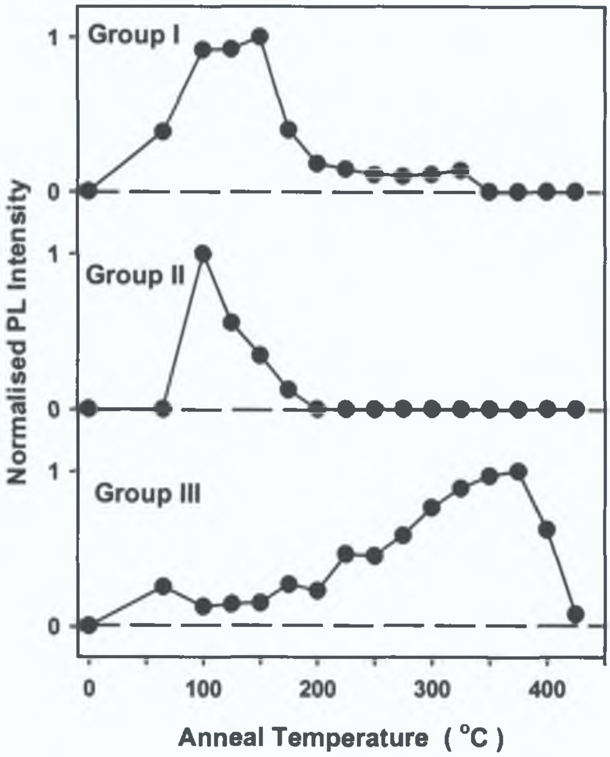

Figure 3.3 Normalised photoluminescence intensity of defects annealed in the range 0 - 425^{0}C.

Four representative spectra are shown in figure 3.4 from four different samples. All samples were treated by a high temperature anneal and rapid quench to room temperature. Groups I and III are observed in (a) where the sample received a subsequent anneal at 200^{o}C whereas in (b) that was annealed at 125^{o}C, group II dominates the spectrum and in (c) annealed at 225^{o}C, group III dominates. The relative intensity of each group is dependent upon the annealing conditions. The observation of each defect independently and the variation in the relative intensity between defects suggests they are not related directly. Thus, depending upon the annealing all three defects (d) or any one defect can be observed. The spectrum shown in (d) where all three defects are observed was obtained from a sample which received a subsequent anneal at 275^{o}C. The observation of all three defects after annealing at 275^{o}C was unexpected. Group II is not expected to be observed above an anneal of 200^{o}C as shown in figure 3.3. This highlights the important role the size of the sample plays in the formation of the defects. The quench rate of the sample after the high temperature anneal will be reduced in a large sample. Due to the difficulty involved in actually measuring the quench rate a quantitative analysis of the effect of sample size on the quench rate and defect formation was not undertaken

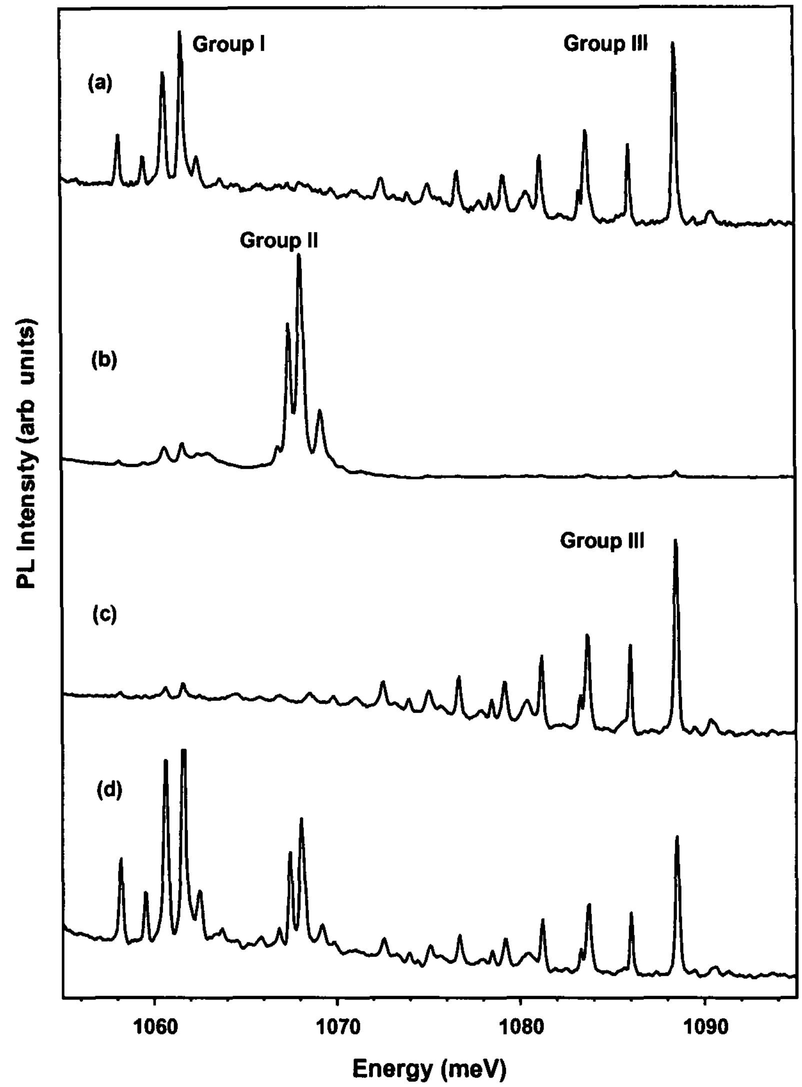

Figure 3.4 Photoluminescence spectra from FZ Si implanted with Cd showing: (a) Group I and III, (b) Group II, (c) Group III and (d) all three groups. Four different samples were used which indicates that the three groups are independent. All spectra were recorded at a nominal temperature of ~ 15 K.

Annealing an FZ silicon sample implanted with cadmium by flame heating at ~ 950°C and rapid quench did not create the three defects of interest A centre at 1093 2 meV was observed as shown in figure 3 5(a), which is assigned by Thewalt (1978) as emission from exciton bound to the lithium donor, thus suggesting the involvement of lithium in the defect production A Cu-related line at 943 7 meV is observed and is attributed to an isoelectronic Cu-Cu defect (McGuigan *et al*, 1988) Cu, one of the transition metals (TMs), has a large diffusion coefficient in silicon at high temperatures. Like other TM defects, the defects may impair the electric and optical properties of silicon and may impair the formation of any defects of interest. When preparing a sample that requires heating, care must be taken to prevent Cu contamination if possible.

The lithium contamination may be due to the out-diffusion of lithium from the quartz tubing during the high temperature anneal. The involvement of lithium in the generation of the three defects or as a catalyst in the creation of the defects was confirmed by placing lithium pellets in the quartz tube in the proximity of the samples which were annealed at ~ 1100°C and quenched. The luminescence from the three defects was enhanced greatly, as shown in figure 3.5(b). A line at ~ 919 meV was observed and is a radiation damage centre involving C (Davies *et al.*, 1984). A lithium pellet was placed in the quartz tube during the high temperature anneal and quench of all subsequent samples to optimise defect photoluminescence.

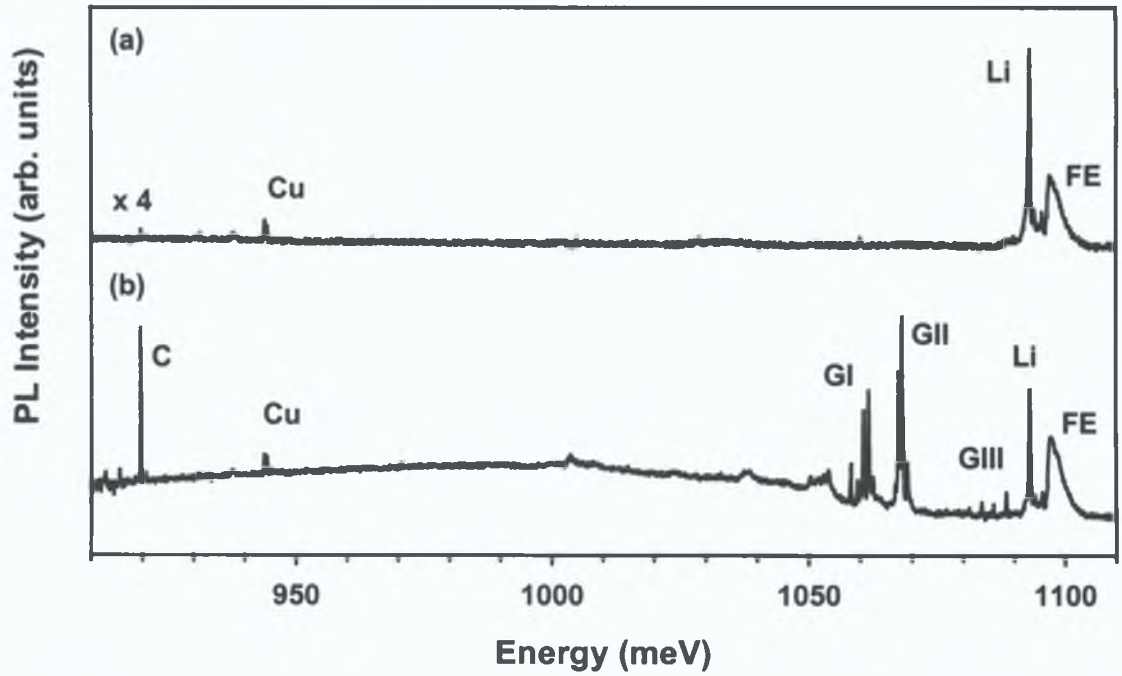

Figure 3.5 (a) Lithium bound exciton luminescence created by a high temperature anneal and quench of Si:^{116}Cd sample (b) Luminescence from the three defects is enhanced by the introduction of a lithium pellet in the quenching process.

Samples of CZ material that has a high oxygen concentration and FZ material that has a relatively low oxygen concentration were prepared. Both samples received the same heat treatment and figure 3.6 shows all three groups are observed in both spectra. The relative intensity of group III in (b) is low compared to the other two groups, this is believed to be due to the heat treatment and sample size rather than the oxygen content of the sample This evidence, although circumstantial, suggests oxygen is not involved in these defects as the groups are observed in FZ samples

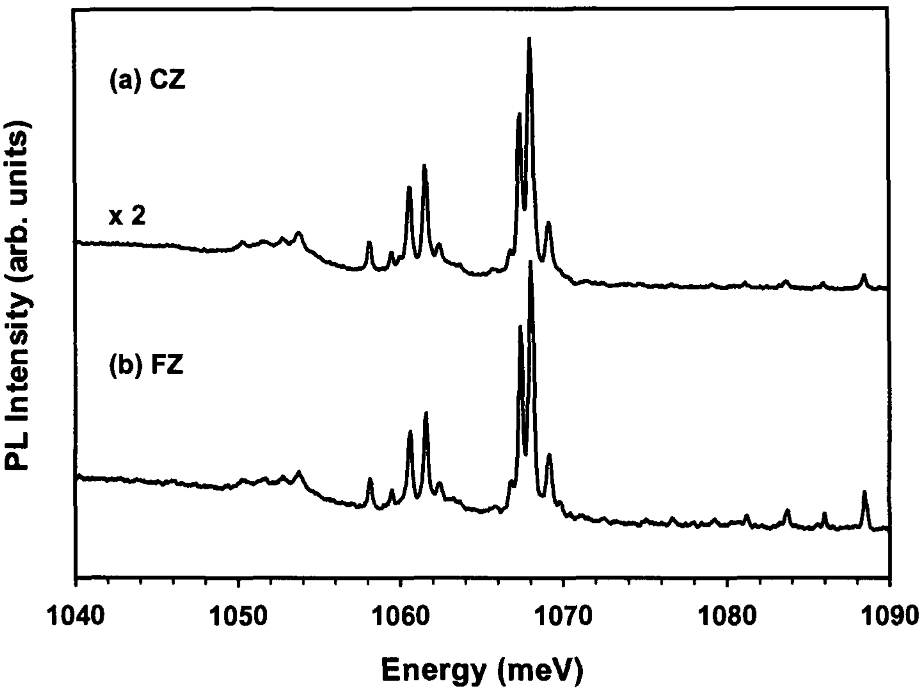

Figure 3.6 Comparison of (a) CZ and (b) FZ Cd implanted silicon samples, which received the same heat treatments to produce, group I, II and III. The spectra were recorded at T ~ 10 K.

In an effort to maximise the luminescence of the defects a series of samples of both conductivity types, p-type and n-type, were prepared by cadmium diffusion All samples were FZ material and RCA cleaned before each treatment and the samples and treatments are listed in table 3 1 Cadmium was diffused into the samples either in vacuum, air or at a pressure of 500 mbar in a helium atmosphere Several samples were subjected to post diffusion treatments as either hydrogen or lithium were introduced into the quartz tubing during the subsequent anneal For hydrogen diffusion the samples were annealed at 200°C for 10 min while samples with lithium diffusion were subjected to an anneal at 415°C for 10 min Table 3 1 lists which of the three groups, if any, were observed in the luminescence spectra Also included is the observation of a cadmium-related line at 1026 meV (McGlynn *et al.*, 1996) and the 1014 meV Cu related centre, indicating copper contamination Group III has been observed in cadmium diffused samples regardless of conductivity type, with and without hydrogen and lithium diffusion It is difficult to identify which conductivity type material favours the production of the defect However, groups I and II are only observed in samples which are lithium diffused Figure 3 7 shows spectra of p-type and n-type Cd- and Li-diffused material The production of groups I and II is favoured in p-type material Ratioing the intensities associated with group II zero-phonon lines and the W line at ~ 1018 meV, in both types of material revealed a ratio of ~ 24 in p-type material and ~ 0 5 in n-type material

Starting Material FZ Si	Resistivity Ω cm	Treatment Cd 1100°C 2 hr	Post anneal	Group I	Group II	Group III	1026 meV Cd line	1014 meV Cu line
n- type	1-10	Control						*
		vac				*	*	
		air				*	*	*
		500mbar He				*	*	*
		vac	H			*	*	
		500mbar He	H			*	*	*
		vac	Li					
		500mbar He	Li	*	*			
p-type	10 k	Control						*
		air				*		*
		vac	275°C 30 min			*		*
		vac	H			*		
		500mbar He	H					*
		vac	Li	*	*	*		
		500mbar He	Li	*	*			
	500	air				*		*
		500mbar He				*	*	*
	12	air						

Table 3.1 n-type and p-type FZ silicon samples prepared by cadmium diffusion and subsequent treatments. The observation of each group, the 1026 meV Cd centre and the 1014 meV Cu centre is indicated for each sample

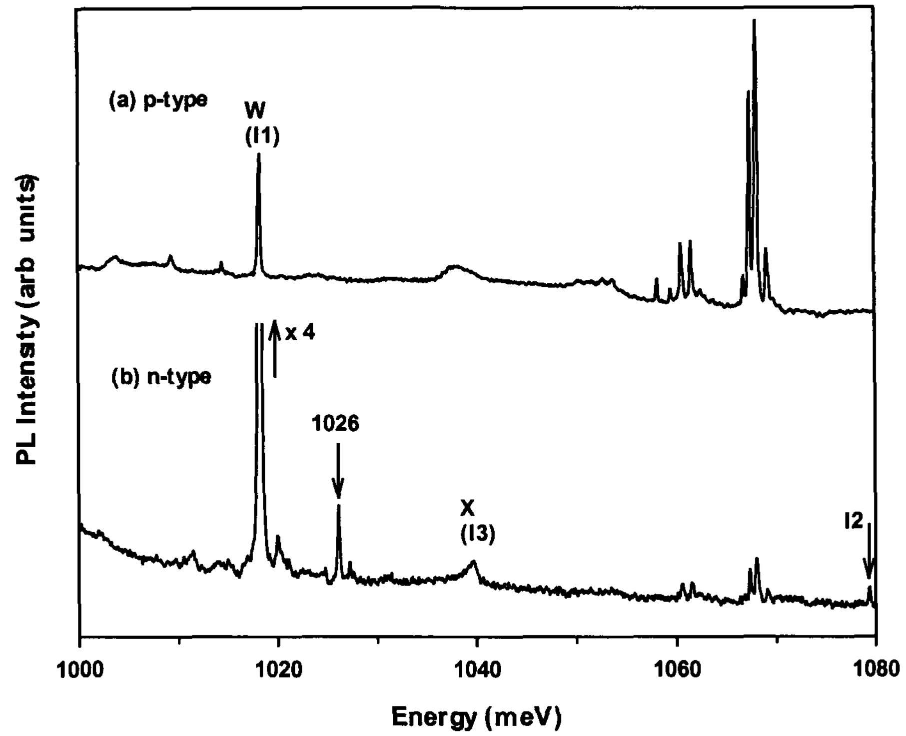

Figure 3.7 Comparison of groups I and II in p-type and n-type material. The labelled lines, W, X (or I3) and I2 are all damage related lines (Davies 1989). The cadmium related 1026 meV line and its first local mode at ~ 1020 meV (McGlynn *et al.*, 1996) were also observed

3.3 Spectral Features

3.3.1 Group I

A luminescence spectrum obtained at ~ 18 K of FZ silicon implanted with ^{116}Cd, which received a high temperature anneal and quench, followed by a 50^{0}C anneal for 30 min is shown in figure 3 8 The spectrum consisting of the three defects is dominated by group I and a detailed sideband is observed Group I consists of zero-phonon transitions, labelled A to E$_*$, in the range 1058 - 1064 meV, the details of which shall be given in the next section The zero-phonon lines couple to an in-band local mode phonon of energy ~ 7 8 (±0 1) meV, with one phonon replicas labelled A^1 E_*^1 in the spectrum A two phonon sideband, D^2 at energy ~ 15 5 (±0 1) meV from the most intense line, D, is observed Unfortunately this assignment cannot be fully confirmed by the observation of any other two-phonon features due to overlap with the transverse acoustic (TA) mode of the zero-phonon lines Additional peaks are observed in the sideband at ~ 1037 8 and 1023 4 (±0 2) meV which coincide with a local mode of group II (L^3_{GII}) and a density of states peak (DOS_{GII}), identified with group II as will be discussed below The O^{Γ} cut-off of group I can be seen at ~ 995 9 (±0 1) meV

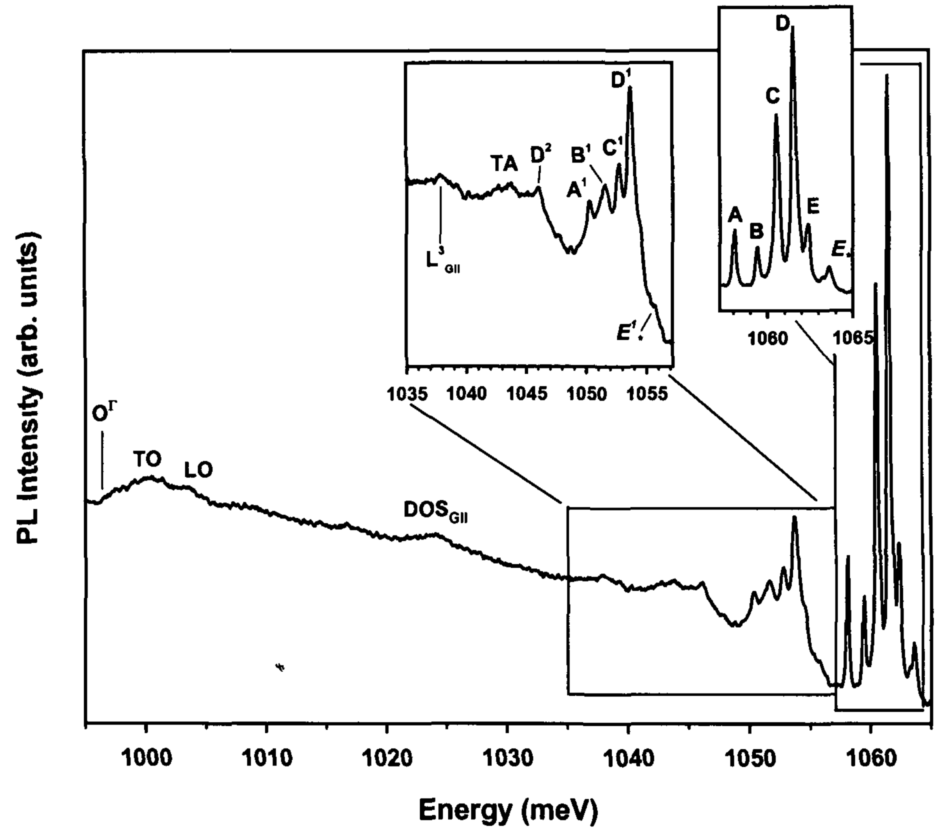

Figure 3.8 Photoluminescence spectrum showing position of group I and sideband.

At low temperature, T ~ 4 K, only the zero-phonon line A and its local mode A^1 are observed and the Huang-Rhys factor can be estimated from the luminescence spectrum using the equation

$$S = \frac{I(localmode)}{I(ZPL)} \qquad (3\ 1)$$

where I is the intensity The estimated Huang-Rhys parameter, S_A is 0 356 This compares favourably with a value of 0 31 calculated from

$$S = \ln\left(\frac{I(totalband)}{I(ZPL)}\right) \qquad (3\ 2)$$

As the temperature is increased, the local modes of lines B to D appear and their S values can be estimated. For example at 10 K, $S_A \sim 0.55$, $S_B \sim 1.37$, $S_C \sim 0.27$ and $S_D \sim 0.56$. A Huang-Rhys value, $S \sim 0.43$ was estimated from the ratio of the total band area to the zero-phonon line area. The high value of S_B when compared to the other Huang-Rhys values may be attributed to the broad nature of the B^1 local mode and any error in estimating the underlying baseline will contribute a large experimental error to S. S_E was not estimated as the area of the E^1 mode is unreliable due to its low intensity. The relative intensity of the n^{th} local mode is given by

$$S^n \frac{\exp(-S)}{n!} \qquad (3.3)$$

Using S_A estimated from the spectrum the estimated value for a second local mode is 0.035, this relatively small value can account for the difficulty in confirming the existence of any second local mode.

For a weakly bound exciton, the luminescence spectrum is expected to be characterised mainly by contributions from wavevector conserving, TA, LO and TO phonons. This is not the case for group I defects. When luminescence occurs the exciton is annihilated and this induces a relaxation of the defect with the lattice. The concept of a relaxation energy was introduced in section 1.5. The relaxation energy can be defined as the difference between the zero-phonon energy E_z and the energy E_c of the centroid of the luminescence band

$$E_r = E_z - E_c \qquad (3.4)$$

The centroid energy obtained by integration of the entire luminescence band, while ignoring features not related to group I is $E_c \sim 979$ meV. Taking $E_z \sim 1065.9$ meV, as the average zero-phonon line energy, the relaxation energy is $E_r \sim 86.9$ meV. Several sources of error which limit the reliability of the value obtained for the relaxation energy must be taken into account. The largest source of error to be considered is the estimation of all features of the band which are unrelated to group I, including the background luminescence and water absorption features. The resolution of the spectrum and the system response must also be considered. Including these errors the relaxation and centroid energy, ~ 87 and 979 meV respectively can only be estimated within ± 20 meV (McGlynn 1996) What is important is from a comparison of the relaxation energy and the spectroscopic binding energy, which is calculated from the energy gap of silicon and the position of the minimum energy zero-phonon line, ~ 1169 9 - 1058 16 meV i e ~ 111.74 meV the relaxation energy accounts for ~ 77% of the binding energy This indicates a self binding exciton similar to the ABC centre (Iqbal *et al* 1994, Davies *et al*, 1994) and Li-related centres (Lightowlers *et al*, 1984)

3.3.2 Group II

A low resolution spectrum at ~ 4 2 K dominated by three group II zero-phonon lines labelled F, H and J, is shown in figure 3 9 Two Local modes are identified, L^1 at ~ 7 3 (±0 1) meV and L^3 at ~ 30 meV below the zero-phonon lines The feature marked H^2, ~ 15 8 meV below the H line, is possibly another local mode of line H However, this cannot be confirmed due to the overlap of the transverse acoustic (TA) mode with the lower energy phonons A peak in the phonon sideband at ~ 1024 meV labelled DOS in the figure, can be identified with a peak in the phonon density of states for silicon The lines labelled Cu and Cu^1 are due to copper contamination The TO, LO DOS peaks and the O$^\Gamma$ cut-off are clearly identified in the spectrum

At 4 2 K, ratioing the intensity of F^1 with the corresponding zero-phonon line F gives a Huang-Rhys factor S_F of ~ 0 03 which is confirmed by relating the total area of the band to the total area of the zero-phonon lines The estimated values of S_H and S_J are ~ 0 02 and 0 05, respectively

The centroid energy was obtained from the luminescence spectrum following the method outlined as for group I and is estimated to be ~ 944 meV Figure 3 10 (a) shows the luminescence spectrum of group II while (b) shows the corrected spectrum Corrections have been made for water vapour absorption, unrelated luminescence features and background intensity Using an average zero-phonon line energy of 1067 4 meV the relaxation energy is estimated to be ~ 73 meV With the number of corrections made to the spectrum, the effects of resolution and system response these values are only approximations From the similarity of the binding energy ~ 87 meV and the relaxation energy, at least a large fraction of the binding energy arises from the relaxation energy and the exciton is self-trapped

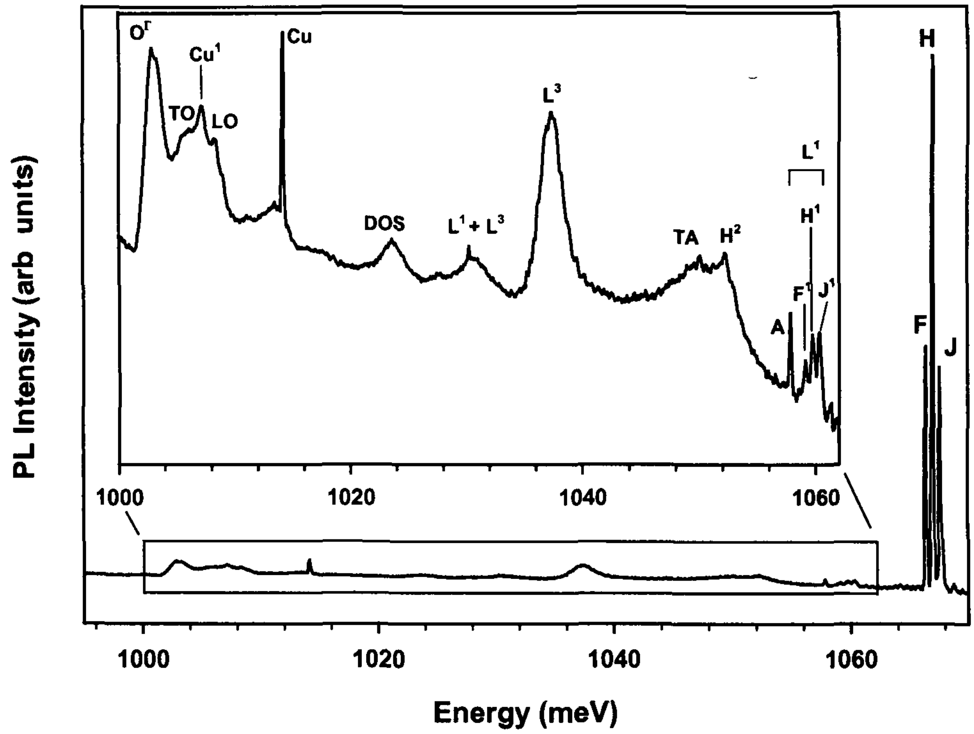

Figure 3.9 Photoluminescence spectra showing group II and its related sideband. The sample was prepared by a high temperature anneal and quench, followed by a 175°C anneal for 30 min.

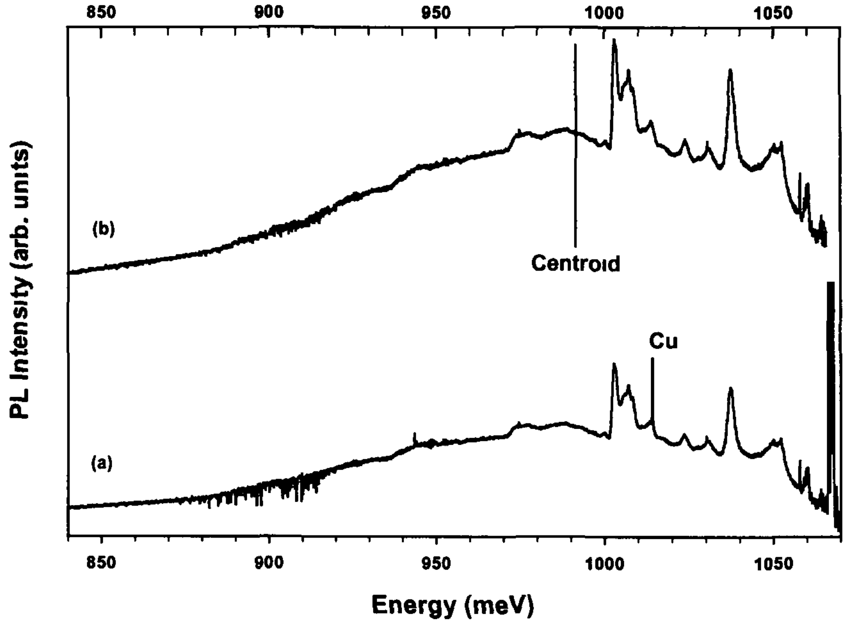

Figure 3.10(a) Group II and its related sideband and (b) corrected spectrum indicating the estimated centroid energy.

The energy shift from the zero-phonon line and the identification of the spectral features of groups I and II are compared in figure 3.11. The O^{Γ} cut-off in each spectrum has been aligned to coincide. The group II local mode and associated sideband are readily identified as intense group II luminescence was observed with a H line signal to noise ratio > 1000. Both group I and II are present in the lower spectrum, with group I dominating, however both L^3 and DOS_{GII} due to group II are observed in the sideband. The second local mode of each group has not been labelled in figure 3.11 due to the tentative nature of the assignments.

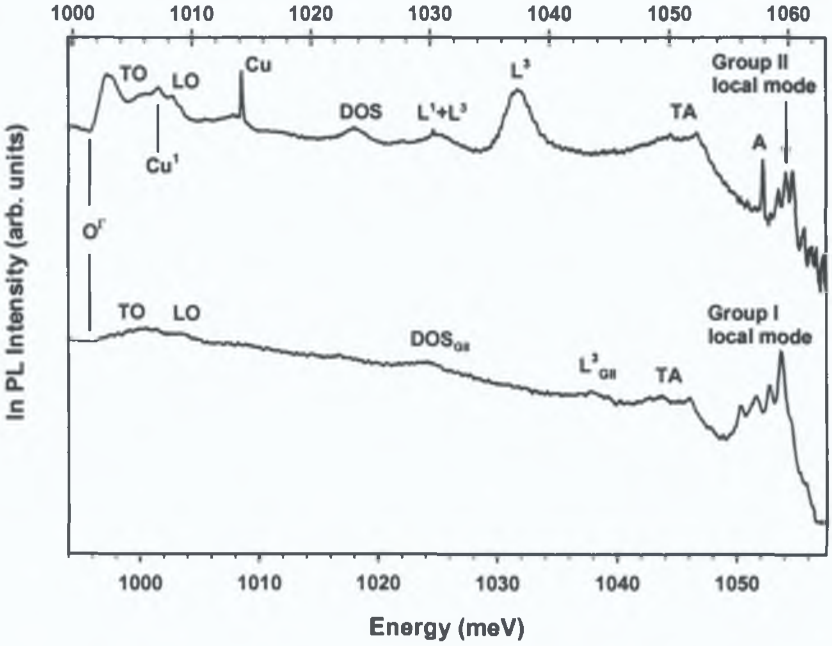

Figure 3.11 Comparison of group I and II phonon sidebands, with the group I sideband shown on the bottom. The group II local modes at ~ 7.3 meV are expected to coincide with the group I zero-phonon lines which will effect temperature dependence measurements.

3.3.3 Group III

Representative spectra of group III at various temperatures recorded using a Fourier transform spectrometer are shown in figure 3.12. At 4.2 K only the lowest energy zero-phonon line at 1083.32 (±0.05) meV, labelled α_1 and its sidebands are observed. Three local modes can be identified, β_1 at a lower energy of 1078.48 (±0.05) meV, γ_1 at 1073.97 (±0.05) meV and δ_1 at 1069.83 (±0.05) meV. From the line energies values of 4.84, 9.35 and 13.49 (±0.07) meV are associated with the emission of one, two and three phonons, respectively indicating the frequency mode of the vibronic series is slightly anharmonic The successive phonon replica energy decreases with increasing number These phonon energies simplify the analysis and interpretation of the higher temperature spectra

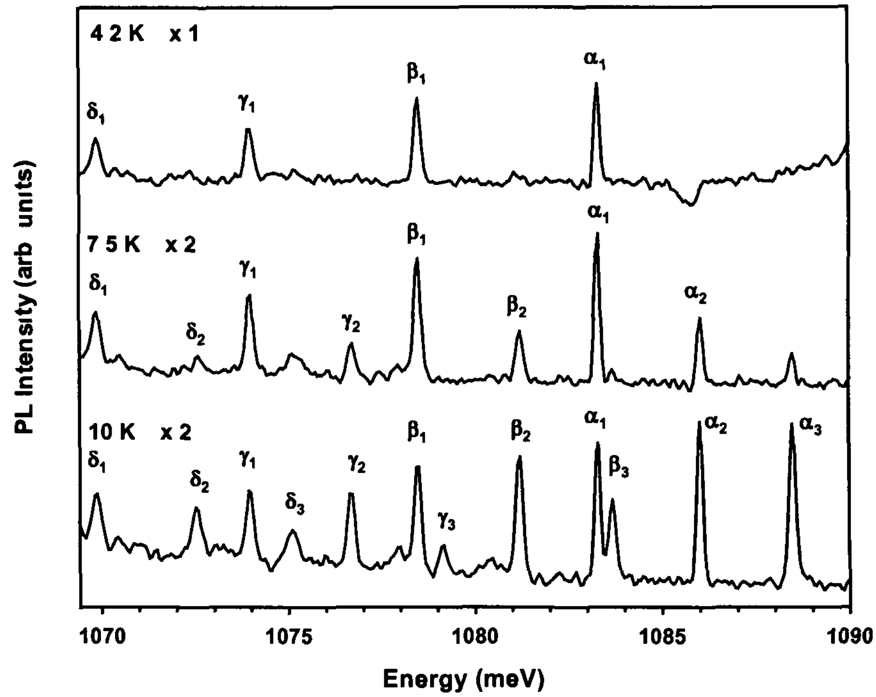

Figure 3.12 Representative spectra of group III at 4.2, 7.5 and 10 K at a resolution of 1 cm^{-1}.

A similar luminescence spectrum dominated by a single vibrational mode of ~ 7 meV has been reported (Canham *et al*, 1985) Up to 11 phonon replicas were observed related to an optical centre thought to be an intrinsic defect that has complexed with lithium and possibly carbon Figure 3 13 shows the first five replicas labelled L1 to L5 of the zero-phonon line LO Similar to group III the frequency mode is anharmonic but in this case the successive phonon replica energies increase with quantum number

As the temperature is increased there is a dramatic change in the spectrum, a second zero-phonon line labelled as α_2 at 1086 02 (±0 05) meV and its related sideband appears At higher temperatures a third zero-phonon line, α_3 at 1088 53 (±0 05) meV and its associated sideband are observed The separations of the zero-phonon lines are close to the phonon energy, which accounts for the complexity seen in the spectrum

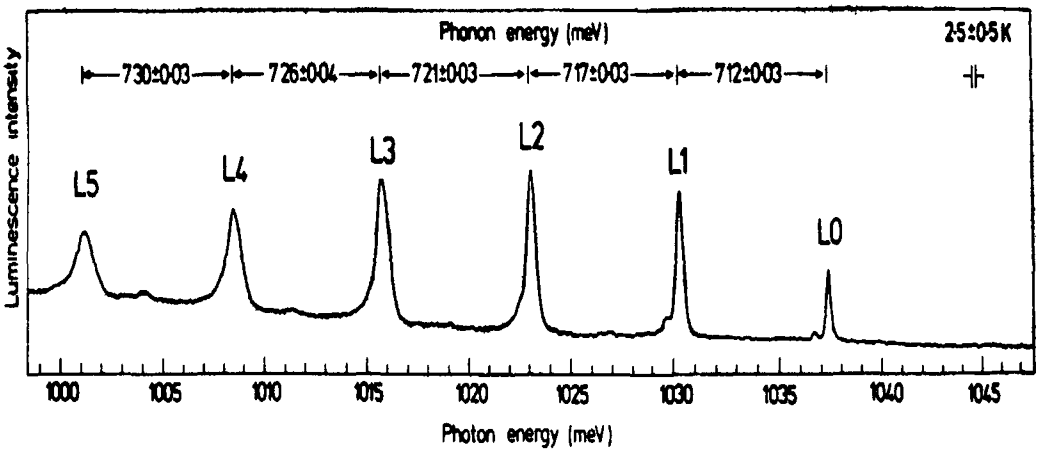

Figu

Figure 3.13 Photoluminescence from FZ silicon containing 2x10^{17} cm^{-3} Li and [C] ~ 2x10^{17} cm^{-3} and [O] < 10^{16} cm^{-3}. The zero-phonon line, L0 lies at 1037.3 ± 0.1 meV. The phonon frequencies of L1 to L5 increase with quantum number (Canham *et al.*, 1985)

At low temperatures the Huang-Rhys parameter, S_l associated with the emission of one phonon is estimated to be ~ 1 by obtaining the ratio of the area of β_1 to the zero-phonon line area, α_1 By the same method the second and third Huang-Rhys parameters for α_2 and α_3, S_2 and S_3 are calculated to be ~ 0 7 and ~ 0 6 respectively The Huang-Rhys parameter S, can also be calculated from obtaining the natural log of the ratio of the total luminescence intensity of the band to the intensity of the zero-phonon lines and the calculated parameters for $S^l{}_l$, $S^l{}_2$ and $S^l{}_3$ are ~ 1 2, 0 7 and 0 3 The values for the one- and two- phonon Huang-Rhys parameters are in agreement within experimental error, however a large discrepancy exists between the two values of S_3 and $S^l{}_3$ This may be attributed to the background and the increasing width of the δ phonon-line making a reliable estimate of the intensity of the line difficult The total calculated value of the Huang-Rhys parameters yields a value of ~ 2 1 which is almost in agreement with the sum of individual modes, $S_l + S_2 + S_3$, of ~ 2 3

Using two sets of Huang-Rhys parameters at T ~ 8 K, estimated as outlined above and the full-width of the lines at half maximum (FWHM) from the observed spectrum the predicted band shapes for group III are shown in figure 3 14 In (a) using $S^l{}_l$ $S^l{}_2$ and $S^l{}_3$ ≅ 1 2, 0 7 and 0 3 respectively, the band shape agrees well with the experimental spectrum (c) for the third-phonon sideband, however for the one- and two-phonon region it underestimates the ratio of intensities The opposite case is observed in (b) where the experimentally obtained values of S_1 S_2 S_3 $\cong$ 1, 0 7 and 0 7 respectively, were used

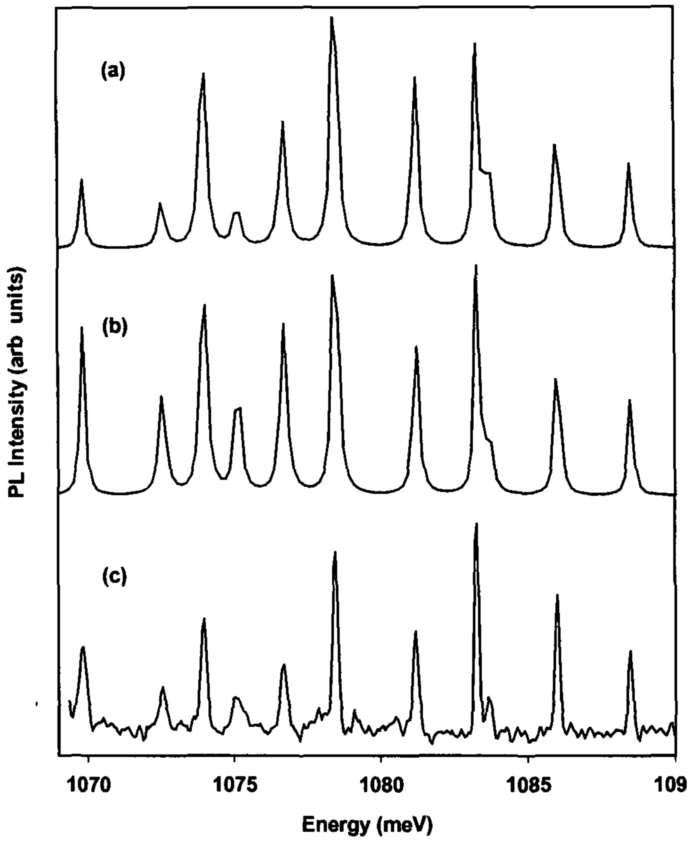

Figure 3.14 Comparison of the estimated group III phonon sideband with Huang-Rhys factor, S calculated by (a) ratio of areas ($S^1_{1,2,3}$), (b) ratio of total sideband area ($S_{1,2,3}$) and (c) experimental spectra observed at T ~ 8 K.

The centroid energy of group III is estimated to be ~ 993 5 meV with a relaxation energy of ~ 83 meV using an average zero-phonon line energy of 1076 5 meV Corrections were made to the spectrum for background intensity, water vapour absorption and non-related spectral features These corrections introduce errors in the estimation of the centroid and relaxation energy ~ ± 20 meV The relaxation energy, 83 (± 20) meV is comparable to the binding energy of group III, ~ 74 meV indicating most if not all of the spectroscopic binding energy is accounted for by the relaxation energy

3.4 Temperature Dependence of Group I

The photoluminescence spectrum of the 1061 meV centred luminescence band, labelled group I in this work, and its associated sideband, as a function of temperature is shown in figure 3 15 At low temperatures, ~ 4 2 K a single zero-phonon line, A, at 1058 16 (±0 05) meV and its related local mode phonon, A^1 at ~ 7 75 (±0 1) meV is observed with a band extending to lower energies As the temperature is increased the growth of several new lines, labelled B to E, and their related phonon modes are observed in the spectrum

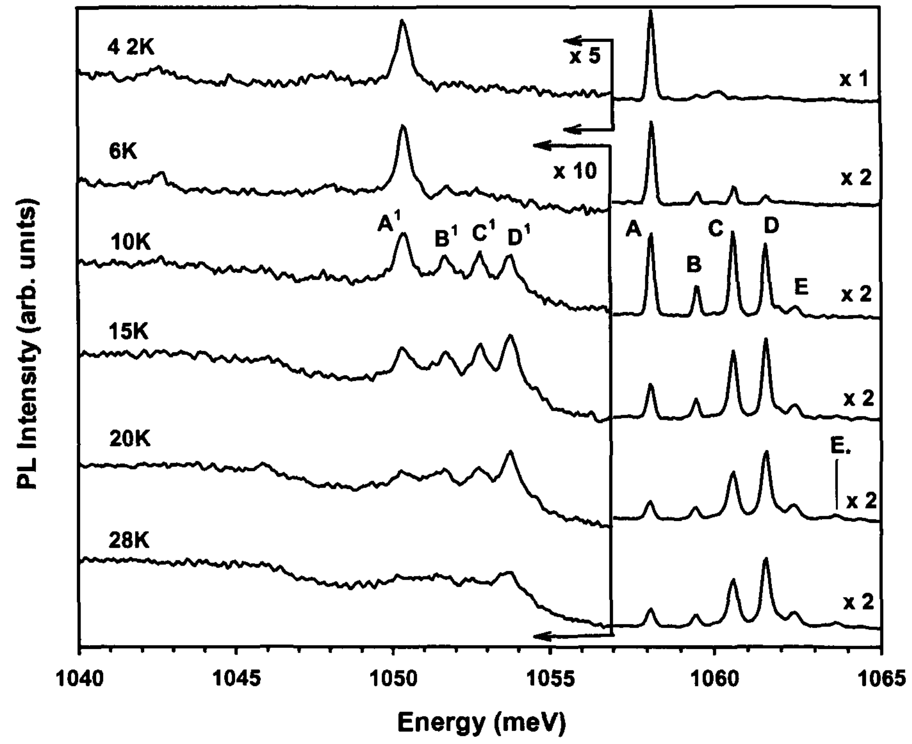

Figure 3.15 Photoluminescence spectrum of group I and phonon sideband as a function of temperature (resolution: 1cm^{-1}).

At high temperatures group I is composed of at least five zero phonon transitions, the labels and energies of the principal zero-phonon lines are given in table 3 2 with their shift from the minimum energy zero-phonon line At temperatures above 15 K a zero-phonon line labelled E* is observed and is attributed to group I, however, due to its low relative intensity, no further work has been undertaken to confirm this identification A plot of the natural log of the intensity ratios of the principal thermally activated lines relative to the minimum energy zero-phonon line versus inverse temperature is shown in figure 3.16.

Spectral Feature	Position (meV) (±0.05)	Energy Shift (meV) ΔE_{sp} (±0.1)	Energy Shift (meV) ΔE_{th}
A	1058.16	0.00	
B	1059.52	1.36	1.27 ± 0.12
C	1060.65	2.49	2.38 ± 0.24
D	1061.64	3.48	2.99 ± 0.31
E	1062.48	4.32	4.01 ± 0.35
E*	1063.74	5.58	unknown

Table 3.2 Spectral features of group I zero-phonon lines.

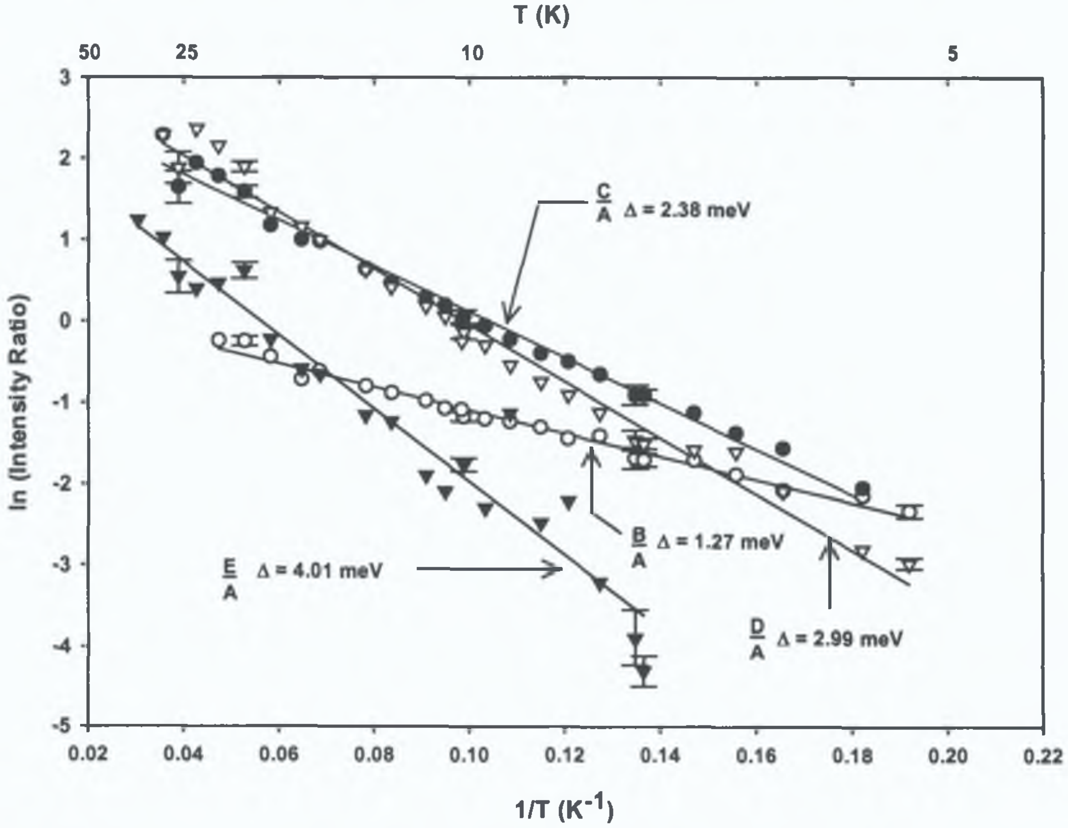

Figure 3.16 Arrhenius plot of the ln of intensities of the principal group I lines with respect to the minimum energy zero-phonon line, A, as a function of reciprocal temperature.

A linear fit to the data for lines B, C, D and E, with respect to A, yields activation energies (ΔE_{th}) of 1.27, 2.38, 2.99 and 4.01 meV, respectively. The deviation from a linear relationship above 17 K and below 8 K is probably due to errors in obtaining the relative intensities due to weak transitions, these intensities are difficult to obtain as they are just above noise levels The appearance of the local mode phonons of group II at the group I line energies, as shown previously in figure 3 9, will contribute to the errors in the intensity ratios, especially at high temperatures The observed spectroscopic separations (ΔE_{sp}) are 1 36, 2 49, 3 48 and 4 32 (±0 1) meV from the A line, respectively, and a comparison of these values to the experimental activation energies indicates these are transitions from five excited state levels to the same final ground state, as illustrated in figure 3 17 The figures indicated below the energy level diagram correspond to the approximate infinite temperature intensity ratios, $f_i g_{iA} / f_A$, where f_i is the probability of radiative recombination of the i^{th} excited state level

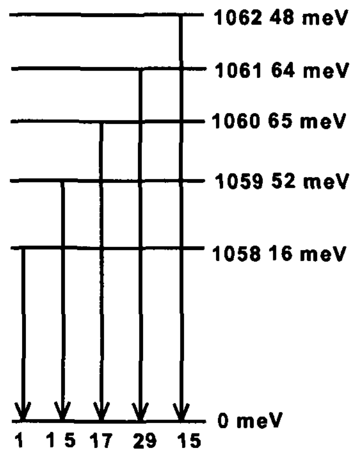

Figure 3.17 Schematic of the predicted energy level diagram of group I. The estimated infinite temperature intensity ratios are indicated below the transitions.

With increasing temperature the total luminescence intensity from the band increases as the higher energy lines become populated, with the intensity growing to a maximum at 14 K Figure 3 19 shows the temperature dependence of the total luminescence from the band At higher temperatures, the intensity decreases by thermal dissociation of the excited states and the intensity becomes undetectable at temperatures >40 K This temperature dependence is not uncommon and has been reported previously for luminescence bands (Nazare *et al*, 1989, McGlynn *et al*, 1996) First, only the rate of decay in the temperature range above 14 K will be considered and an initial value for the thermal dissociation energy will be calculated. The temperature dependence of the decay in luminescence intensity is given by.

$$I(T)=\frac{I(0)}{1+G_d T^{3/2}\, exp\left(-\Delta E_t/kT\right)} \qquad (3\ 5)$$

where G_d is the ratio of the conduction band density of states to the defect density of states and E_t is the dissociation energy of the bound complex The intensity data for T > 14 K is shown in figure 3 18 where the line represents the best fit with a dissociation energy of ~ 10 5 (±2) meV

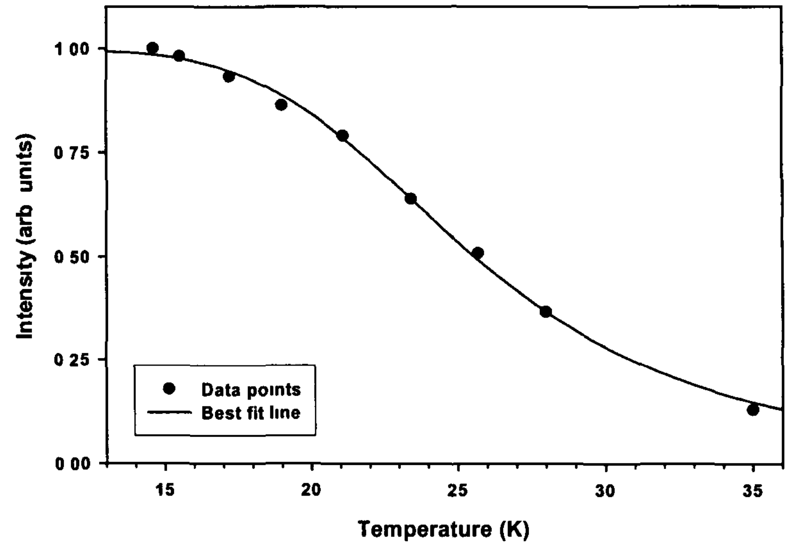

Figure 3.18 Temperature dependence of the luminescence intensity of group I lines above 14 K. The line is the best fit line with a dissociation energy E_t = 10.5 meV and G_d = 0.896.

The thermal dissociation energy is much less than the spectroscopic binding energy ~ 111 74 meV The calculated value of ~ 10 5 (±2) meV is comparable to the binding energy of the exciton, 14 7 ± 0 04 meV (Shaklee *et al*, 1970) suggesting the exciton was captured by the centres through a weak interaction and then relaxes to be localised to the centre If the excited state is a bound exciton, the primary particle is tightly bound, ~ 101 2 (±2) meV and the secondary particle is weakly bound (~ 10 5 (±2) meV)

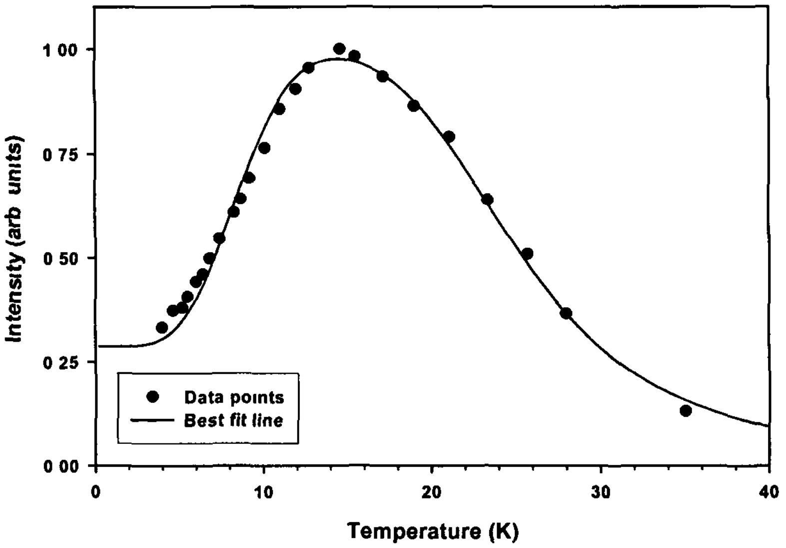

Figure 3.19 Intensity of group I zero phonon lines as a function of temperature with fit parameters: $r = 0.858$, $G_t = 0.0474$, $G_d = 0.896$, $E_t = 10.5$ meV and $E_t = 3$ meV.

The total luminescence of the band as a function of temperature is described by equation 2 8, and using the values of E_t and G_d found above as starting values and the observed activation energies, ΔE_{sp} given in table 3 2, the best fit line shown in figure 3 19 was obtained The shallow traps were found to have a binding energy E_t of ~ 3 meV, and excitons may be released from these shallow traps as the temperature is increased and captured at the group I defect, thus contributing to the increase in luminescence Typically, shallow traps have a binding energy of ~ 4 meV and to date the origin of shallow traps is unknown (Davies, 1999) Figure 3 19 suggests the intensity of group I, has not fully stabilised at 4 2 K suggesting the existence of an energy level below the observed A line from which transitions may be forbidden

Spectra at high resolution have revealed a zero-phonon line on the low energy side of the A line, labelled A* in figure 3 20 This line at ~ 1058 05 meV, which was not observed in the temperature dependence data detailed above due to the relatively low resolution of the spectra, was investigated further in the temperature range ~ 2 - 4 2 K at high resolution (0 15 cm^{-1}) The expected change in relative intensities between 2 and 4 2 K is ~25% Unfortunately, within the signal-to-noise ratio achieved, no thermalisation was observed when the liquid-helium bath temperature was decreased from 4 2 to 2 K, even when the excitation power was reduced to very low levels to avoid sample heating. No local modes of A^* or A were observed at these low temperatures and at present, A* is not included as part of the group I energy level system Further investigation of the A* line is necessary to determine if it is a lower energy line of the group I system as the low temperature data are inconclusive

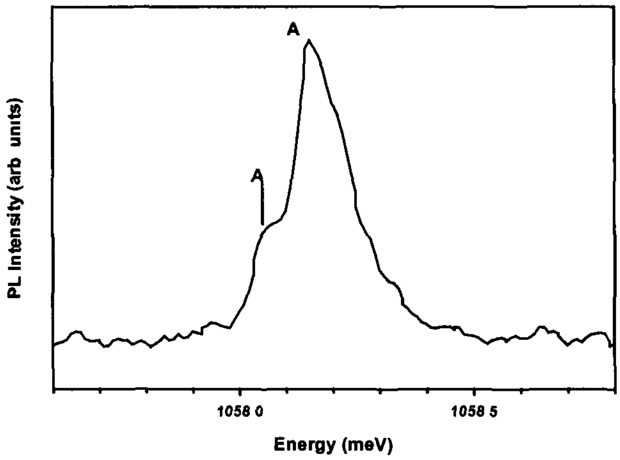

Figure 3.20 At high resolution (0.15 cm^{-1}) A* is observed on the shoulder of the minimum energy A line at 4.2 K.

To summarise, from the thermal data, group I consists of at least five zero-phonon lines due to transitions from a set of thermalising excited states to a single ground state The temperature dependence of the group I luminescence is characteristic of an isoelectronic centre The calculated dissociation energy of ~ 10 5 (±2) meV for group I suggests the exciton was captured by the centres and subsequently relaxes to be localised to the centre

3.5 Temperature Dependence of Group II

A second group of lines, labelled group II is found to be broadly similar to group I and is centred at ~ 1068 meV The minimum energy zero-phonon line, labelled F is at 1066 84 ± 0 05 meV and high-resolution spectra, as shown in figure 3 21(b), reveal at least eight lines, labelled G to M, within a range of 2 4 meV. PL measurements at 4 2 K and below were carried out in a liquid He bath cryostat, with the temperature determined from the He vapour pressure

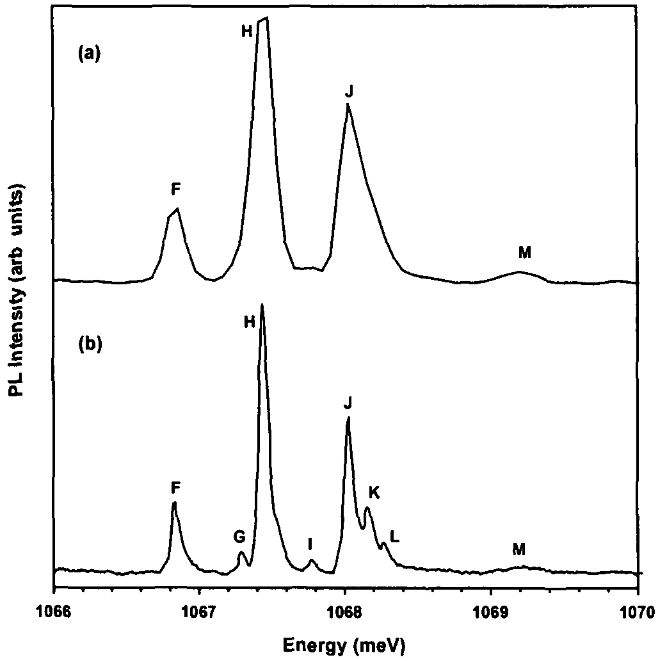

Figure 3.21 The zero-phonon lines of the group II system recorded from a sample at ~5 K with (a) resolution of 1 cm^{-1} and (b) higher resolution of 0.15 cm^{-1}.

As shown in figure 3 22 the minimum energy zero-phonon line is most clearly observed at ~ 2 K with rapid thermalisation of higher energy zero-phonon lines as the temperature is increased At high resolution there is overlapping of different components and using purpose built code (Cafolla, 1998), the overlapping lines were deconvolved using gaussian lineshapes

The intensity ratios of the excited states to the minimum energy state (F) follow an exponential law versus reciprocal temperature, and according to the Arrhenius plots shown in figure 3 23, these lines are interpreted as zero-phonon transitions between excited states of the same defect

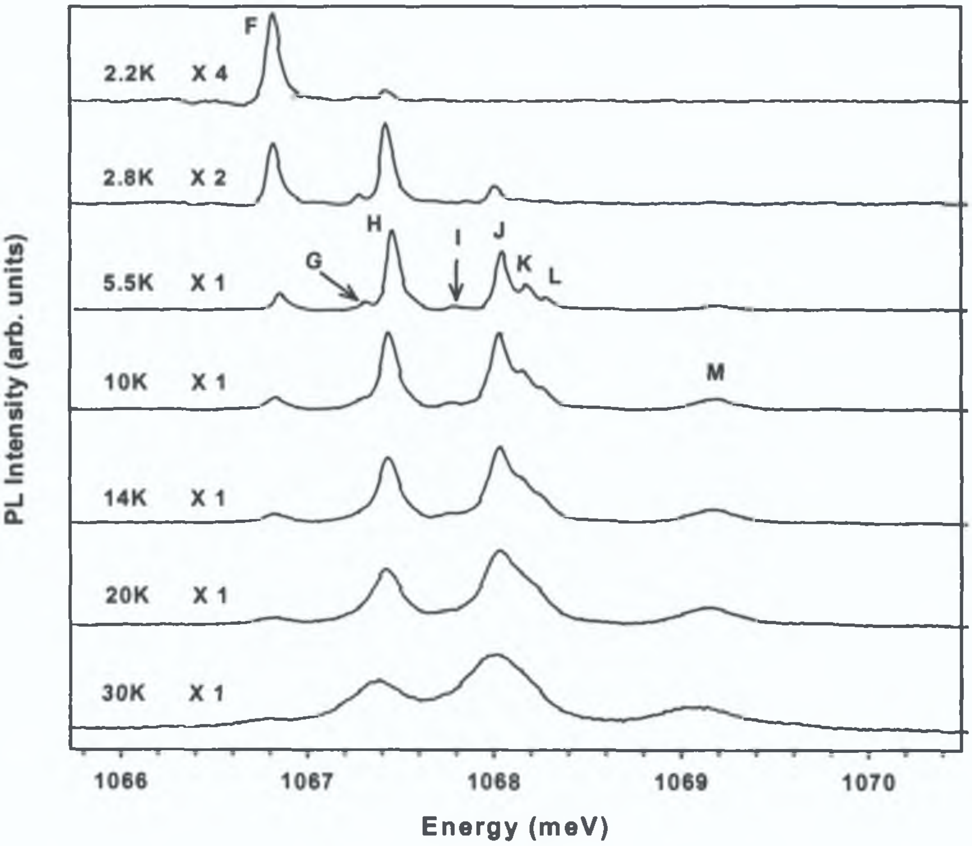

Figure 3.22 Group II as a function of temperature.

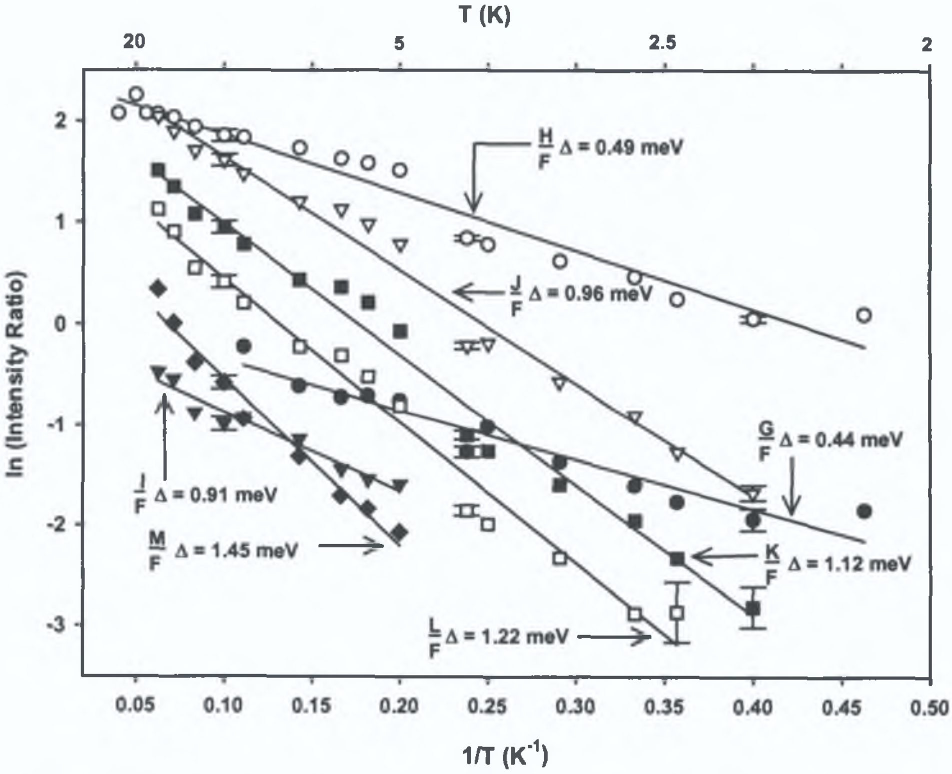

Figure 3.23 Arrhenius plot of the group II zero-phonon lines. The solid lines are the best-fit lines used to calculate the activation energies.

A comparison of the spectroscopic energy splitting, ΔE_{sp}, and the calculated splitting, ΔE_{th}, for each zero phonon line is shown in table 3 3

Spectral Feature	Position (meV) (±0 05)	ΔE_{sp} (meV) (±0 10)	ΔE_{th} (meV)
F	1066 84	0 00	
G	1067 31	0 47	0 44 ± 0 16
H	1067 45	0 61	0 49 ± 0 17
I	1067 78	0 94	0 91 ± 0 20
J	1068 04	1 20	0 96 ± 0 32
K	1068 18	1 34	1 12 ± 0 37
L	1068 28	1 44	1 22 ± 0 37
M	1069 21	2 37	1 45 ± 0 28

Table 3.3 Labelling and energy positions for group II zero-phonon lines.

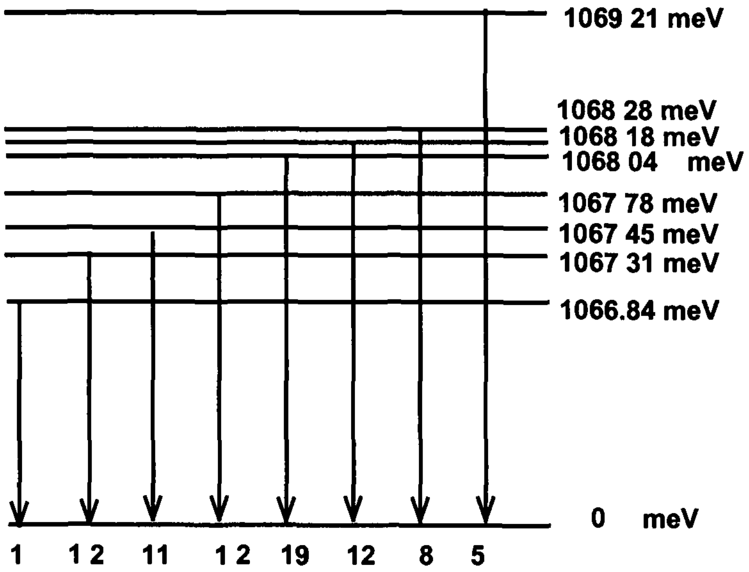

Figure 3.24 Energy level diagram for group II zero-phonon lines thermalising to a single ground state. The infinite temperature ratios are indicated in the diagram.

As indicated in figure 3 24, it is possible that these transitions are from excited state levels to the same final ground state, as the discrepancy in the calculated activation energy (ΔE_{th}) and the spectroscopically determined energy splitting (ΔE_{sp}) is within error limits It is clear from table 3.3 that the activation energy for the highest energy line, M does not agree with the spectroscopic splitting The very broad nature and low intensity of the line, (the full width at half maximum is ~ 0 25 meV compared to ~ 0 12 meV of the F line at ~ 10 K), will contribute large errors in the estimation of the relative intensities of the lines Studying the intensity ratio of the M line with the lowest energy line, F in several samples has revealed that the ratio is independent of sample indicating the zero-phonon line is a group II transition Tentatively the line is included in the energy level diagram as an excited state transition to the same single ground state

The intensity of all eight energy levels were combined together and the total group II intensity shown in figure 3 25 grows rapidly to a maximum at ~ 5 5 K and decays until the luminescence finally disappears at ~ 30 K An initial value for E_t was obtained by a fit to the data in the temperature range 5 5 to 30 K and was used as a starting value to obtain the best fit line shown in figure 3 25 A thermal dissociation energy of ~ 15 (±2) meV and trap energy E_t of ~ 4 meV were calculated This dissociation energy is very close to the energy of the free exciton indicating that an exciton was captured by the centre and is now localised to the centre with energy 88 meV The dissociation energy accounts for approximately one-fifth of the localisation energy At temperatures below 3 K the fit to experimental data is unsatisfactory and values for the dissociation energy, the ratio of the conduction band density of states to the defect density of states and the trap density of states were varied Similar fits were achieved with different values for these three parameters to the best fit shown in figure 3 25 The ability to obtain reasonable fits to the total luminescence data with differing set of parameters indicates there are still some uncertainties

Comparing groups I and II, the total luminescence of each group as a function of temperature are very different (figures 3 19 and 3 25) Group I and (as will be shown in the next section) group III follow the trend which is usually reported in the literature for isoelectronic centres with a maximum at ~ 15 K and with the luminescence observed until ~ 40 K Previously reported cadmium-related defects, Cd$_A$ and Cd$_B$ luminescence intensity reaches a maximum at ~ 13 and 15 K, respectively, and are completely gone at temperatures above 50 K (McGlynn *et al* , 1996) Group II is unusual as it reaches a maximum at 5 5 K and above 25 K the system is no longer observed No explanation can be offered at present for this unusual result However, the calculated thermal dissociation energy of ~ 15 (±2) meV is comparable to the dissociation energy of the free exciton, indicating an isoelectronic centre, where the exciton is captured by the centre and then relaxes and is localised to the centre

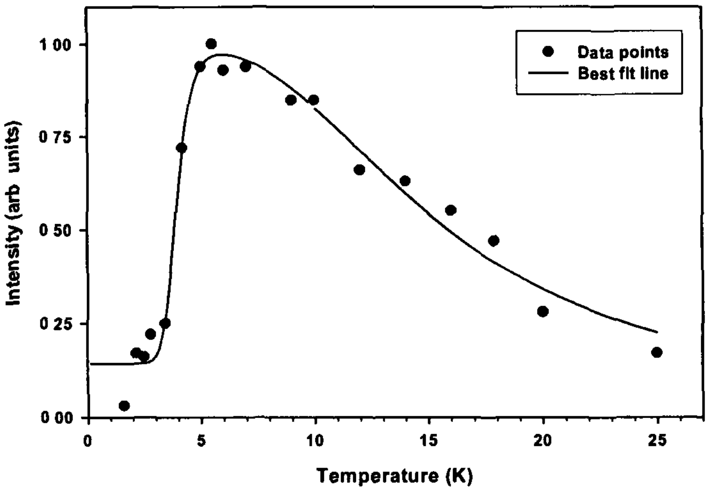

Figure 3.25 Group II intensity as a function of temperature. Best fit line with thermal activation energy E_t ~ 15 meV and E_t ~ 4 meV.

Group II, consists of at least eight zero phonon lines which are tentatively assigned to transitions from thermalising excited states to a single ground state The variation of the total luminescence with temperature indicates the centre is isoelectronic The thermal dissociation energy is estimated to be ~ 15 (±2) meV

3.6 Temperature Dependence of Group III

A typical detailed spectrum of group III is shown below in figure 3 26 at T ~ 15 K Three zero-phonon lines are observed, labelled α_1, α_2 and α_3 As shown previously a complicated sideband structure is observed consisting of three local modes, labelled β, γ and δ Emission is observed from the free exciton (FE) and multi-bound exciton emission involving two excitons on Li donor and TO phonon creation and emission from exciton bound to B acceptor with TO phonon emission, labelled b_1 and B^{TO} respectively (Davies, 1989) Three group I lines, A, C and D are observed and three lines labelled x_1, x_2 and x_3 which coincide with group II line energies are observed, at present these lines appear to be unrelated to group III The remainder of the lines labelled in figure 3 25 will be discussed in detail after initial temperature dependence results are presented

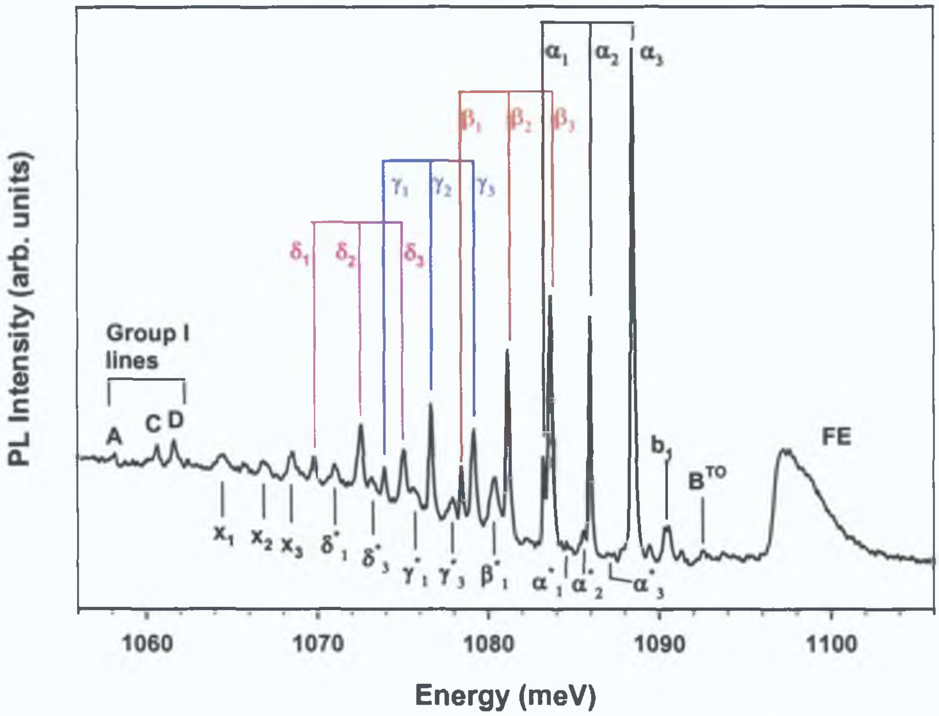

Figure 3.26 The group III zero-phonon lines and complicated sideband structure at T ~ 14 K with labels as explained in the text.

The logarithm of the intensity ratios of α_2 to α_1 and α_3 to α_1 as a function of reciprocal temperature are shown in figure 3.27. A linear fit to the data yields thermal activation energies of 1.49 (± 0.18) and 3.35 (± 0.32) meV for α_2 to α_1 and α_3 to α_1, respectively. These experimental thermal activation energies do not agree with the spectroscopic splitting of the lines, 2.70 and 5.21 (± 0.10) meV, respectively, indicating that both the initial and final electronic states are split. The proposed energy level diagram is shown in figure 3.28 with the infinite temperature ratios relative to α_1 shown below the transitions. Centres where both the initial and final states are split are uncommon for defects that are believed to be electrically neutral. Exceptions to this general rule include the Zn_A and Zn_B defects, which have split ground and excited states (Henry *et al.*, 1994); and the Au-Li at ~ 765 meV and ~ 1121 meV defects (Zhu, 1998). Two well-characterised centres with split states are centres involving In and Tl acceptors in silicon (Thewalt *et al.*, 1982).

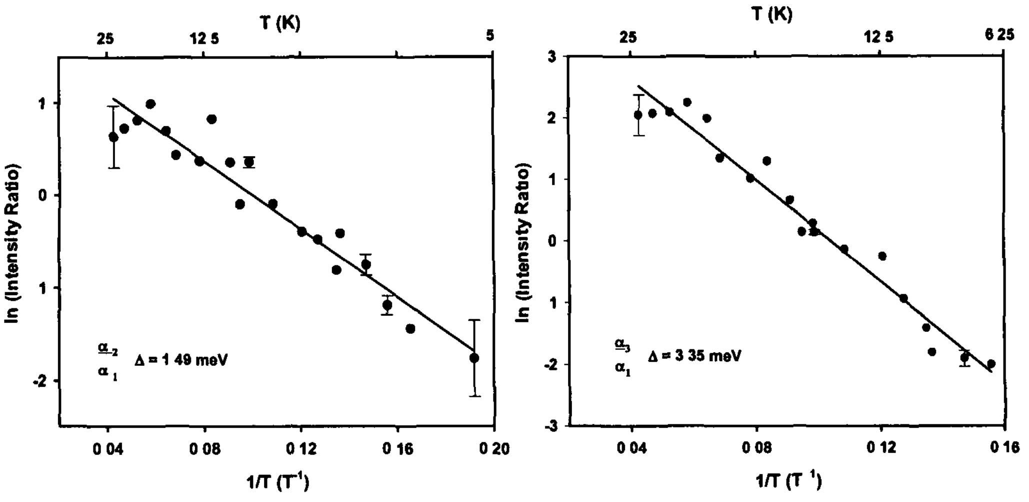

Figure 3.27 Logarithm of the intensities of the α_2/α_1 lines and the α_3/α_1 lines as a function of inverse temperature. Thermal activation energies of ~ 1.49 and ~ 3.35 meV are indicated.

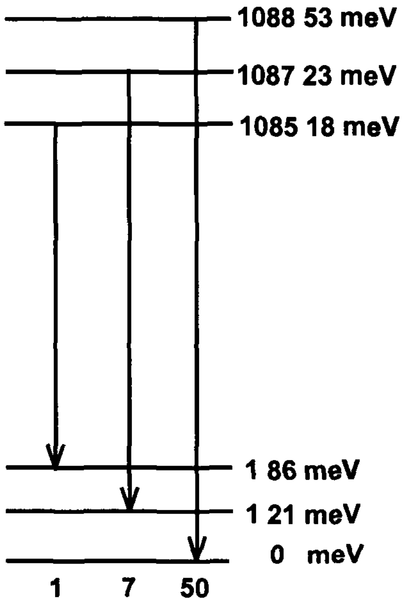

Figure 3.28 Proposed energy level diagram for group III system, the infinite temperature ratios for the α lines are shown.

From the proposed energy level scheme additional features of group III can be identified as (partially allowed) forbidden transitions A complete listing of the zero-phonon lines, phonon sideband, unidentified lines and some largely forbidden transitions are given in table 3 4 and are labelled as shown in figure 3 25 Other forbidden transitions cannot be assigned due to their low intensity and their expected position overlaps with main zero-phonon lines and phonon sideband features

Label	Energy (meV)	Assignment
α_1	1083 32	zero-phonon line
α_2	1086 04	
α_3	1088 53	
β_1	1078 50	one phonon
β_2	1081 22	
β_3	1083 72	
γ_1	1074 01	two phonon
γ_2	1076 02	
γ_3	1079 21	
δ_1	1069 80	three phonon
δ_2	1072 59	
δ_3	1075 07	
x_1	1064 46	unknown
x_2	1066 82	
x_3	1068 54	
β^*_1	1080 47	forbidden transitions
γ^*_3	1077 95	
γ^*_1	1075 87	
δ^*_3	1073 21	
δ^*_1	1071 45	
α^*_1	1083 97	
α^*_2	1085 40	
α^*_3	1086 67	

Table 3.4 Listing of the main lines of the group III system and some very low intensity forbidden transitions observed in figure 3.25.

The total intensity of the group III system (zero-phonon lines and sidebands) as a function of temperature increases to a maximum at ~ 20 K, and then decreases until the luminescence is quenched at temperatures > 40 K The calculated thermal binding energy of the defect centre is ~ 13 (±2) meV deduced from the best fit line obtained, shown in figure 3 29 A shallow trap at energy E_t of ~ 3 meV acts as a trap for luminescence and as the temperature is increased excitons may be released from the shallow level and captured at the defect centre of interest The calculated thermal binding energy accounts for ~ 17% of the spectroscopic binding energy of 73 6 (±2) meV Group III is an isoelectronic centre as in the case of groups I and II

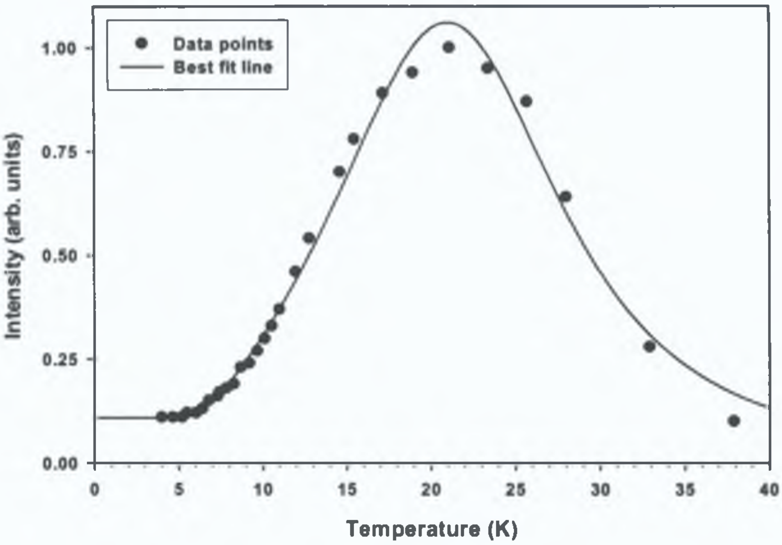

Figure 3.29 Total Intensity of group III zero-phonon lines as a function of temperature. The best-fit line is shown with fit parameters : $r = 1.79$, $G_1 = 4.81$, $E_i = 12.97$ meV and $E_t = 2.89$ meV.

3.7 Conclusions

A detailed introduction has been given of three defects created in Cd doped silicon, labelled groups I, II and III. Although it was initially thought the three defects were related, subsequently it was found that each group of lines can be produced alone or all three defects can be created in the one sample depending upon the heat treatment after the high temperature anneal and quench. The optimum condition for the creation of group I is an anneal at ~ 150°C for about 15 min. The system consists of five zero-phonon transitions with a local mode at ~ 7.8 (±0.1) meV. Temperature dependence shows these are transitions from five excited state levels to the same final ground state. There is a decrease in luminescence intensity above 15 K with a calculated thermal dissociation energy of ~ 10.5 (±2) meV. The low dissociation energy compared to the difference in energy between the zero-phonon line energy and the silicon band gap indicates the self-trapped exciton is captured as a pair and then relaxes after localisation where the primary particle is tightly bound (~ 101.2 (±2) meV). High resolution reveals a zero-phonon line, A^* on the low energy side of the minimum energy line A. This zero-phonon line requires special consideration and further experimental work must be undertaken to determine its origin.

The temperature dependence of group II is complicated as there are at least eight lines within a range of 2 4 meV Evidence is seen of thermalising states and a tentative model suggests all zero-phonon lines are due to transitions from thermalising excited states to a single ground state The intensity grows rapidly to a maximum at ~ 5 5 K and decreases rapidly above this temperature As with group I, the exciton, captured through a weak interaction is then localised at the centre, which relaxes The optimum condition for creating group II is an anneal at ~ 100°C for 15 min following the high temperature anneal and quench The luminescence spectrum contains, as for group I, a detailed phonon sideband on the low energy side of the zero-phonon lines

A comparison of groups I and II shows similar defect formation conditions and similar temperature dependence results, with transitions from thermalising excited states to single ground states Due to their apparently similar nature, it can be suggested that the defect that produces the group I lines are possibly a perturbed version of the group II defect The full nature of this possible link has yet to be studied

Temperature dependence of group III shows three zero-phonon lines with both the initial and final ground states split One, two and three phonon-assisted lines are identified and additional sideband structure is observed from which several lines can be identified as (partially allowed) forbidden transitions The luminescence increases to a maximum at ~ 20 K and decreases above this temperature The calculated thermal binding energy of the centre is ~ 13 (±2) meV indicating a third isoelectronic defect A summary of the main findings of this chapter are compiled in table 3 5

Chapter four will concentrate on further analysis and comparisons of the three defects by uniaxial stress Isotope measurements and magnetic field perturbation studies for each of the defects are considered in chapter five

	Group I	Group II	Group III
Minimum energy ZPL (±0 05) meV	label A 1058 16	label F 1066 84	label α_1 1083 32
No of ZPLs	~5	~8	~3
Ground State	singlet	singlet	multiple
Post Quench Anneal	150°C 30 min	100°C 30 min	375°C 30 min
local modes	~7 8	~7 3 ~30	~4 8 anharmonic
Thermal Binding Energy (± 2 meV)	10 5	15 0	13 0
Spectroscopic Binding Energy (± 2 meV)	101 2	87 2	73 6
Proposed Model	Isoelectronic Centre	Isoelectronic Centre	Isoelectronic Centre

Table 3.5 Comparison of the main findings from the temperature dependence measurements and analysis of spectral features for the three groups.

References

Cafolla A A, Surface Science, 404-404, 561-565, (1998)

Canham L T , Davies G and Lightowlers E C , Proc 17th Intl Conf on the Physics of Semiconductors, 737-740, (1985)

Daly S E , Henry M O , Freitag K and Vianden R , J Phys Condens Matter **6**, L643-L650, (1994)

Daly S E , Ph D Thesis, Dublin City University, (1994)

Davies G , Lightowlers E C , Woolley R A , Newman R C and Oates A S , J Phys **C17**, L499, (1984)

Davies G , "The Optical Properties of Luminescence Centres in Silicon", Physics Reports **176**, Nos 3&4, 83-188, (1989)

Davies G , Chapter one in "Identification of Defects in Semiconductors", editor Stavola M , Academic Press (1999)

Davies G , Iqbal M Zafar and Lightowlers E C , Phys Rev B50, 11 520-11 530, (1994)

Henry M O , Campion J D , McGuigan K G , Lightowlers E C , do Carmo M C and Nazare M H , Semicond Sci Technol , **9**, 1375-1381, (1994)

Henry M O , Campion J D , McGuigan K G , Thewalt M L W and Lightowlers E C , Mater Sci and Eng , **B4**, 201-204, (1989)

Kern W , RCA Rev (USA), **31**, 207-233, (1970)

McGlynn E , PhD Thesis, Dublin City University, (1996)

McGlynn E , Henry M O , McGuigan K G and Do Carmo M C , Phys Rev **B54**, (20) 14 494-14 503, (1996)

McGuigan K G , Henry M O , Lightowlers E C , Steele A G and Thewalt M L W , Solid State Commum, **68**, 7, (1988)

Nazare M H , Do Carmo M C and Duarte A J , Mater Sci and Eng , **B4**, 273-276, (1989)

Olajos J , Kleverman M and Grimmess G , Phys Rev **B38**, 10 633, (1988)

Shaklee K L and Nahory R E , Phys Rev Lett , **24**, 942-945, (1970)

Thewalt M L W , Solid State Commun , **28**, 361-364, (1978)

Thewalt M.L W , Ziemelis U O , Watkins S P and Parsons R R , Can J Phys , **60**, 1691, (1982) Iqbal M Zafar, Davies G and Lightowlers E C , J Lumin, **60/61**, 559-562, (1994)

Zhu M-X , Davies G , Iqbal M Zafar and Lightowlers E C , Mater Sci Forum, **258-263**, 485-490, (1997)

Zhu M-X , PhD Thesis, University of London, (1998)

Chapter Four

Uniaxial Stress Perturbation

4.1 Introduction

Uniaxial stress measurements were recorded along the three major symmetry directions of the crystal <001>, <111> and <110> to reveal the symmetry information of the three defects under study. The interaction of adjacent states at the same centre complicates the splitting patterns of the zero-phonon lines. By studying the stress split patterns and measuring the intensity ratios at low temperatures where only the minimum energy zero-phonon line is observed and at low stresses where the level mixing and thermalisation effects are relatively small it may be possible to identify the transition type. Polarisation data of the stress-split components can be very useful in identifying components with the theoretically derived shift rate equations. Unfortunately, the polarisation of the luminescence signal is generally mixed by internal reflections in the samples and by stress-induced interactions and as a result polarisation intensity measurements were not obtained during the stress measurements reported here.

Possible errors may arise in uniaxial stress measurements in the form of additional lines and stress components, which become broadened with increasing stress. To avoid spurious results, care must be taken to avoid misalignment of the samples in the stress rig and to prepare samples with a uniform cross-sectional area. The uniaxial stress and Zeeman measurements were carried out on x-ray orientated rectangular parallelepipeds, with the sample long axis parallel to one of the crystal axes <001>, <111> and <110>. These stress samples were prepared by diffusion. A cadmium pellet was placed together with samples of orientated ultra high pure silicon of resistivity 3 kΩcm in a quartz ampoule at 0 5 atm of helium and heated to 1100°C typically for two hours The cadmium diffused samples were then subsequently annealed in an ampoule containing a lithium pellet and heated to 850°C for 5 min at 0 5 atm of helium To achieve a rapid quench to room temperature the ampoules were plunged into water To optimise group II without destroying groups I and III, the samples were annealed at 100°C in an Ar atmosphere for 10 min and allowed to cool slowly

In this chapter the variation of the energy and relative intensity of the stress split components with applied stress for group I will be reported first Due to the number of closely spaced zero-phonon lines, group I was studied at low temperature where the symmetry of the minimum energy line A was determined as an A to E transition at a trigonal site Having identified the symmetry of the minimum energy zero-phonon line at low temperatures, the higher energy zero-phonon lines were studied at higher temperatures The number of stress-split components for group II is unambiguous due to the large number of closely spaced zero-phonon lines Preliminary measurements presented below indicate the symmetry is due to A to E transition at a trigonal site Future uniaxial stress measurements at 2 K where only the minimum energy zero-phonon line is observed should confirm this symmetry assignment The behaviour of the group III lines under stress is unusual The number of stress components for the two zero-phonon lines studied varies and in section 4 4 the zero-phonon lines are assigned as an A to B transition at a monoclinic I site

4.2 Group I

The stress data for group I were recorded at both low and high temperatures At low temperatures it was possible to follow the shift and split rates of the minimum energy zero-phonon line A, without the confusion of the higher energy lines Once the symmetry and stress parameters had been determined for the A line at low temperatures the higher temperature data were analysed From this data the shift rates and components of all the group I zero-phonon lines were obtained at low stresses

4.2.1 Low Stress Regime

When stress was applied in the <111> direction the A zero-phonon line split into three components Representative spectra showing the splitting of the line with different values of applied stress are shown in figure 4 1 The higher energy lines B, C and D are also observed in the spectra but will not be analysed in the low temperature regime as reliable data could not be obtained for all three stress directions A fan diagram showing a graph of the shift in energy of the three stress split components of the A line as a function of applied stress is shown in figure 4 2 From the fan diagram it can be seen that the shift rates of the stress-split components for stress applied in the <111> direction are linear

The A zero-phonon line splits into four components for stress applied in the <110> direction Spectra recorded for different values of applied stress are shown in figure 4 3 As in the case of the <111> direction the shift rates for the stress split components for the <110> direction appear to be linear However at high stresses above ~ 80 MPa the shift rates of the two higher energy stress split components are slightly non-linear as observed from the fan diagram shown in figure 4 4

Stress applied in the <100> direction did not split the line, however the line did shift to lower energies and broaden with increasing applied stress Figure 4 5 shows spectra of the A zero-phonon line as a function of applied stress in the <001> direction The fan diagram, figure 4 6, shows the non-linearity of the shift rate for stress applied in the <100> direction above 70 MPa

At low stresses, the response of the components is linear, while at higher stresses the non-linear data dominates These non-linear effects are produced by interactions between nearly degenerate states and both the <001> and <110> data show clear evidence of an interaction effect Because of the interacting states, the predicted shift rates of the lines under stress are no longer described by simple linear relationships

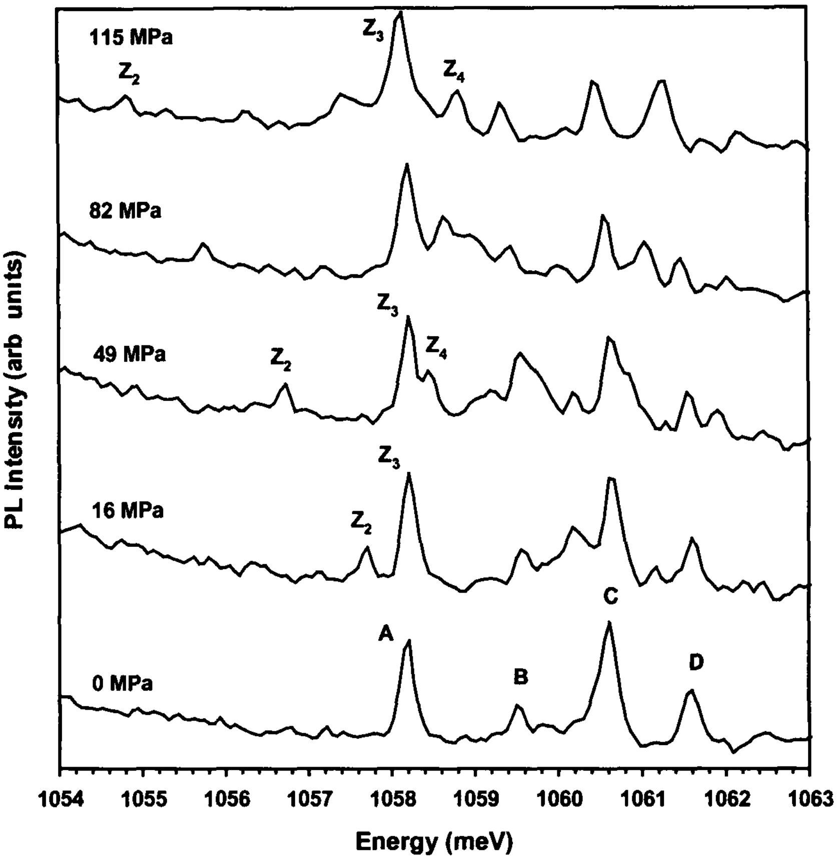

Figure 4.1 Photoluminescence spectra taken at different values of stress in the <111> direction at T ~ 8 K.

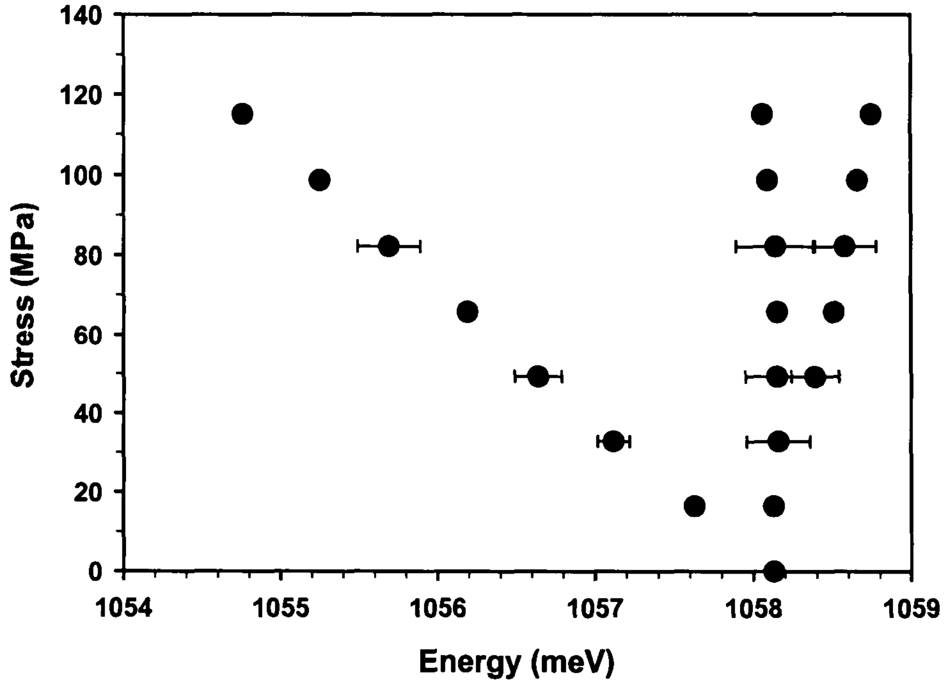

Figure 4.2 Fan diagram for <111> stress of group I A zero-phonon line at T ~ 8 K. The error bars indicate the width of the spectral lines.

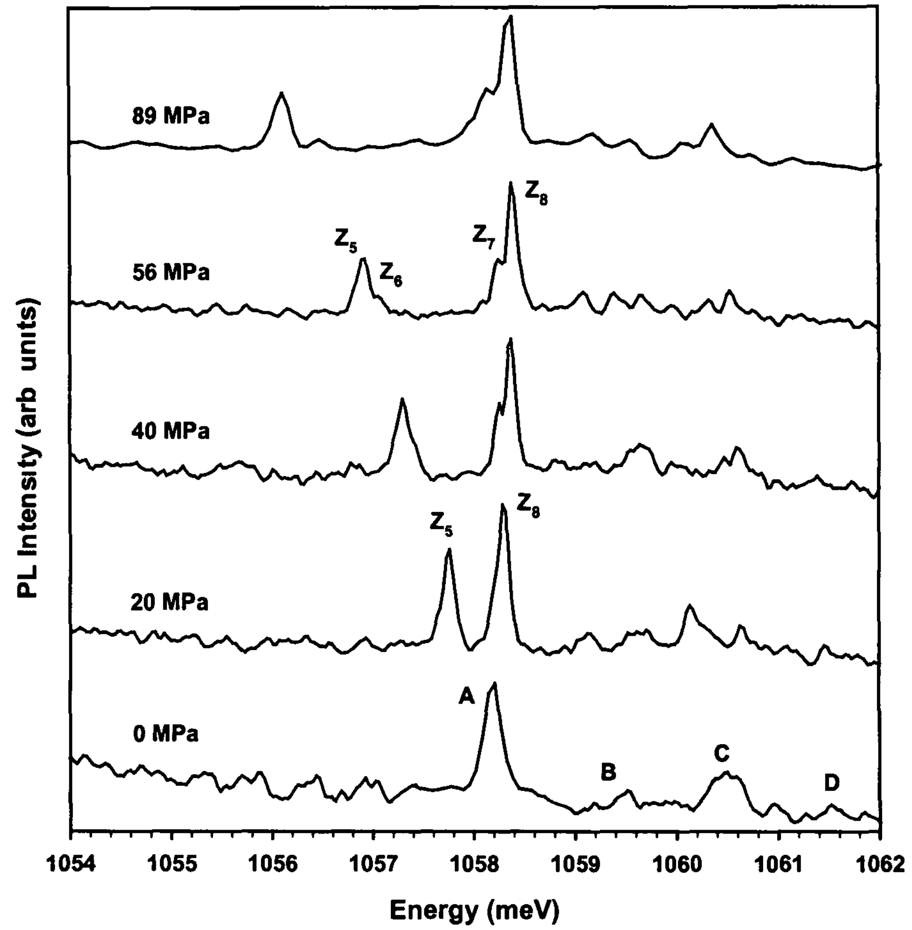

Figure 4.3 Photoluminescence spectra taken at different values of stress in the <110> direction at T ~ 5.5 K.

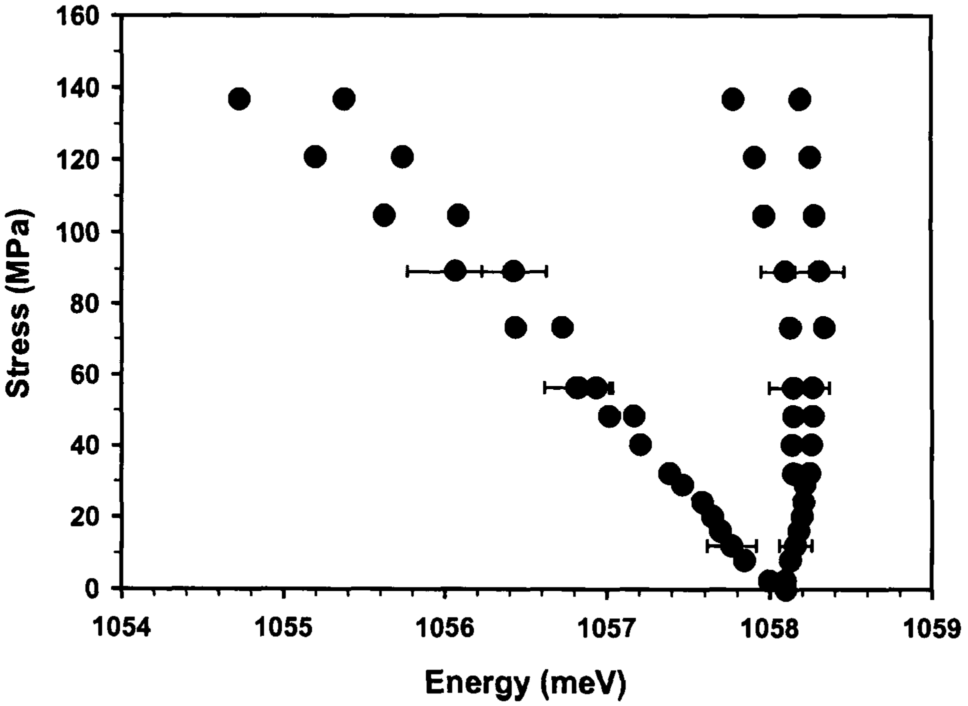

Figure 4.4 Fan diagram for <110> stress of group I A zero-phonon line at T ~ 5.5 K. The error bars indicate the width of the spectral lines.

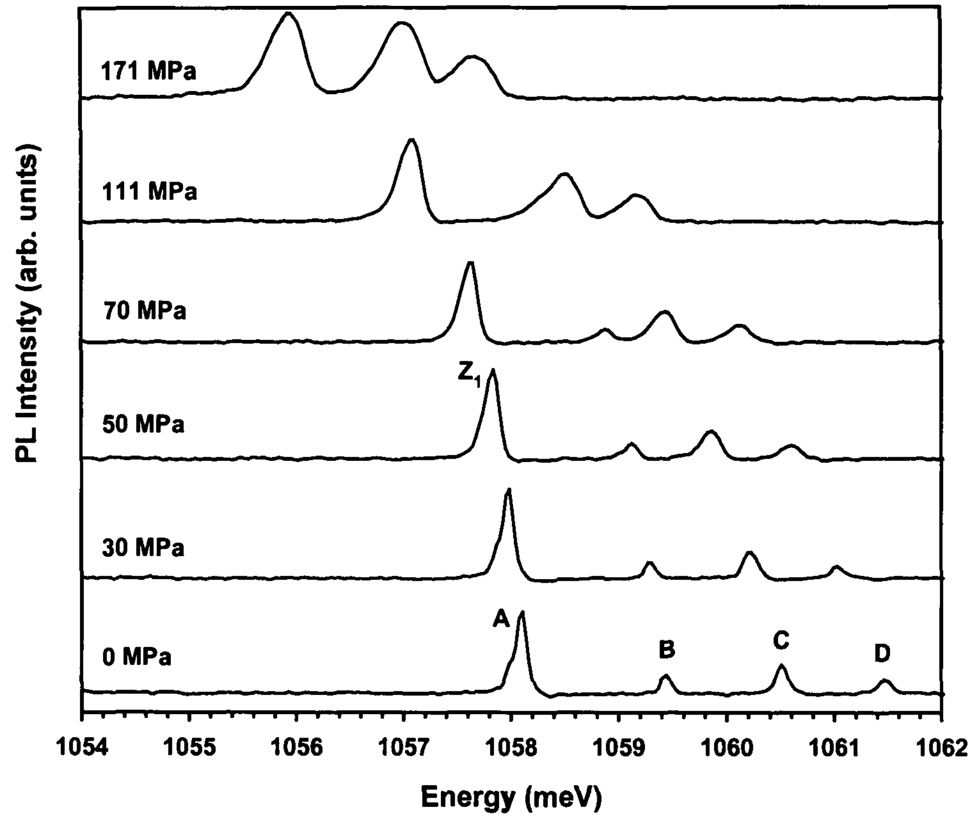

Figure 4.5 Representative spectra taken at different values of stress in the <001> direction for group I minimum energy zero-phonon lines at T ~ 5.5 K.

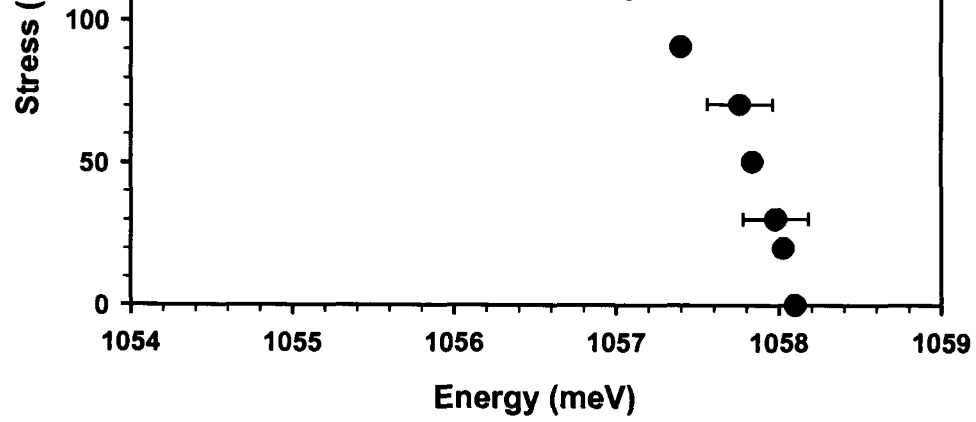

Figure 4.6 Fan diagram for stress in the <100> direction of group I A zero-phonon line at T ~ 5.5 K. The error bars indicate the width of the spectral lines.

In the first instance, the data will be analysed in the low stress regime where the response of the components is linear and can be described by linear equations Once the symmetry and stress parameters have been determined for the linear region the high stress region can be studied by including an interaction to account for non-linear shift rates

A summary of the number of stress split components observed for each stress direction is given in table 4 1 Comparing the number of stress split components - one, three and four for stress parallel to the <001>, <111> and <110> directions - of the A zero-phonon line with the number of components expected for any of the eight possible symmetry types of the cubic crystal, the numbers observed are not consistent with any one of the symmetry structures (Mohammed *et al*, 1982, Kaplyanskii 1964)

Number of Components	<001>	<111>	<110>
A zero-phonon line	1	3	4
Trigonal A to A	1	2	2
Trigonal A to E	2	3	4
Monoclinic I	2	3	4

Table 4.1 Comparison of the number of stress split components observed for each direction of the group I A line with the number of components expected for trigonal and monoclinic I symmetry.

For <100> applied stress, the only symmetry for which the zero-phonon line is not expected to split is trigonal A to A, but the zero-phonon line is expected to split into two components under both <111> and <110> stress The observed number of stress split components, three and four for <111> and <110> directions respectively, rule out trigonal A to A as the symmetry and transition type of the defect Zero-phonon lines of both monoclinic I and trigonal A to E symmetry are expected to split into three components under <111> stress and four components under <110> stress, which are in agreement with the observed number of components for the A line However, as shown in table 4 1 under <001> stress the zero-phonon line is expected to split into two components, which is not observed for the A line

Examining the intensities of the stress-split components should help identify the symmetry of the defect and transition type A comparison of the experimentally observed intensity ratios of the stress-split components in different directions with the expected intensity ratios for an A to A type transition (dipole direction parallel to <110>) and an A to B transition at monoclinic I site and an A to E transition at a trigonal site are listed in table 4 2 An examination of the intensity ratios under <111> stress direction at low stress shows acceptable agreement with both monoclinic I, A to B and trigonal, A to E symmetry In the <110> direction the expected intensity ratios are similar for both symmetries The direction of the electric dipole was varied and the intensity ratio of the stress-split components estimated The best agreement was found with the dipole direction aligned parallel to <110> Due to the absence of polarisation data a symmetry identification based on intensity comparisons alone is unreliable and both symmetries must be considered First the trigonal case shall be examined

<001>		<110>		<111>	
Stress (MPa)	**Ratio**	**Stress (MPa)**	**Experimental**	**Stress (MPa)**	**Experimental**
10	*No splitting observed*	20	1 15	16	1 3
35		40	2 2 3	49	1 4 2
		56	2 1 2 3	66	1 4 2
		89	2 05 2 3	82	1 45 2
Monoclinic	**Theoretical**		**Theoretical**		**Theoretical**
A↔A	1 3		4 2 2 4		5 6 5
A↔B	1 3		4 2 2 4		3 10 3
Trigonal					
A↔E	3 5		4 2 2 4		6 17 9

Table 4.2 Comparison of the experimental A zero-phonon line and theoretical intensity ratios for <110> and <111> stress. No polarisation data was obtained and the theoretical intensity components are the sum of the individual components for the π and σ luminescence directions.

4.2.2 Trigonal fit to Group I

Hughes and Runciman (1967) have described the basic theory for a transition between E and A states at a trigonal centre in detail The stress operator V_S for a trigonal defect has the form

$$V_S = a_1\left(S_{xx} + S_{yy} + S_{zz}\right) + a_2\left(S_{yz} + S_{zx} + S_{xy}\right) + E_x\left(2S_{zz} - S_{xx} - S_{yy}\right)$$
$$+\sqrt{3}E_y\left(S_{xx} - S_{yy}\right) + E_x^{'}\left(2S_{xy} - S_{yz} - S_{zx}\right) + \sqrt{3}E_y^{'}\left(S_{yz} - S_{zx}\right) \qquad (4\ 1)$$

The standard basis vectors for the irreducible E representation are x and y, thus a solution to the secular matrix denoting the effect of V_S on E_x and E_y will reveal the allowed eigenvalues which will describe the allowed splitting and expected energy shift of the zero-phonon lines under stress The a_1 and a_2 symmetry operators cause shifts of the level while the E_x $E_y^{'}$ operators remove the electronic degeneracy The secular matrix that describes the stress perturbation takes the form

V_S	E_x	E_y
E_x	$\alpha - \beta$	γ
E_y	γ	$\alpha + \beta$

where the eigenvalues are obtained from the roots of the matrix α, β and γ describe the first order perturbations of E_x and E_y and are defined in terms of stress tensor components S_{ij} as

$$\alpha = A_1\left(S_{xx} + S_{yy} + S_{zz}\right) + 2A_2\left(S_{yz} + S_{zx} + S_{xy}\right) \qquad (4\ 2)$$

$$\beta = -B\left(S_{xx} + S_{yy} - 2S_{zz}\right) + C\left(S_{yz} + S_{zx} - 2S_{xy}\right) \qquad (4\ 3)$$

$$\gamma = B\sqrt{3}\left(S_{xx} - S_{yy}\right) + C\sqrt{3}\left(S_{yz} - S_{zx}\right) \qquad (4\ 4)$$

The stress parameters A_1, A_2, B and C are defined in terms of the matrix elements of the operators a_1, a_2, E_x and E_y and from Hughes and Runciman (1967) are of the form:

$$\langle E_x | a_1 | E_x \rangle = A_1 \tag{4.5}$$

$$\langle E_x | a_2 | E_x \rangle = 2A_2 \tag{4.6}$$

$$\langle E_x | E_x | E_x \rangle = -B \tag{4.7}$$

$$\langle E_x | E_x' | E_x \rangle = -C \tag{4.8}$$

Calculating the S_{ij} strain tensors for stress applied along each direction the shift rates in the notation of Kaplyanskii (1964 b) are obtained and are listed in table 4.3.

Stress Axis	Eigenvalues
[001]	A_1-2B
[001]	A_1+2B
[111]	A_1+2A_2
[11**1**]	$\frac{1}{3}(3A_1-2A_2-4C)$
[1**11**]	$\frac{1}{3}(3A_1-2A_2+4C)$
[110]	A_1+A_2+C-B
[110]	A_1+A_2-C+B
[**1**10]	A_1-A_2+C+B
[110]	A_1-A_2-C-B

Table 4.3 The results for an A to E transition at a trigonal centre in a cubic crystal (Hughes and Runciman 1967). The bold font indicates -1.

Under <001> stress the zero-phonon line does not split (figures 4.5 and 4.6), however, in the case of an A to E transition at a trigonal centre the zero-phonon line is expected to split into two components with shift rates $A_1 \pm 2B$. Setting stress parameter B equal to zero will result in the observation of only one component with shift rate A_1. The A zero-phonon line shifts linearly only for stresses less than 70 MPa in the <001> direction and the shift rate is set equal to A_1. From a linear least squares fit of the stress versus energy data for the

<110> case, initial values of the stress parameters A_2 and C were obtained By substituting these values into the shift rate equations for stress along the <111> direction and comparing the calculated and actual values the parameter assignments were checked As no polarisation data was available to help identify the stress split components with different shift rate equations several iterations were necessary before a reasonable fit was obtained for the low stress regime The best fit obtained using the stress parameters, A_1 = -6 2, A_2 = -11 8, C = 2 0 and B = 0 meV/GPa is represented by the solid lines of figure 4 7 The experimental shift rates are compared to the estimated shift rates in table 4 4

Stress Direction	Component	Shift Rate (meV/GPa) Experimental (± 0.5)	Shift Rate (meV/GPa) Calculated (± 1.0)
<001>	Z_1	-6 3	-6 2
	Z_1	-6 3	-6 2
<111>	Z_2	-29 1	-29 7
	Z_3	0 0	-0 1
	Z_4	5 4	4 3
<110>	Z_5	-23 9	-19 9
	Z_6	-19 6	-16 0
	Z_7	0 9	3 6
	Z_8	3 1	7 6

Table 4.4 The experimental and least square 'shift rates' of the A zero-phonon line at low stresses, where Z_i is the observed component as labelled in the diagrams.

A reasonable fit has been obtained for trigonal A to E symmetry in the low stress regime The analysis was complicated as there was no reliable polarisation data to assist in the assignment of stress components to shift rate equations In the absence of reliable polarisation data the possibility that the centre could be monoclinic I cannot be excluded The possibility of an A to B transition at a monoclinic I centre is considered in the next section

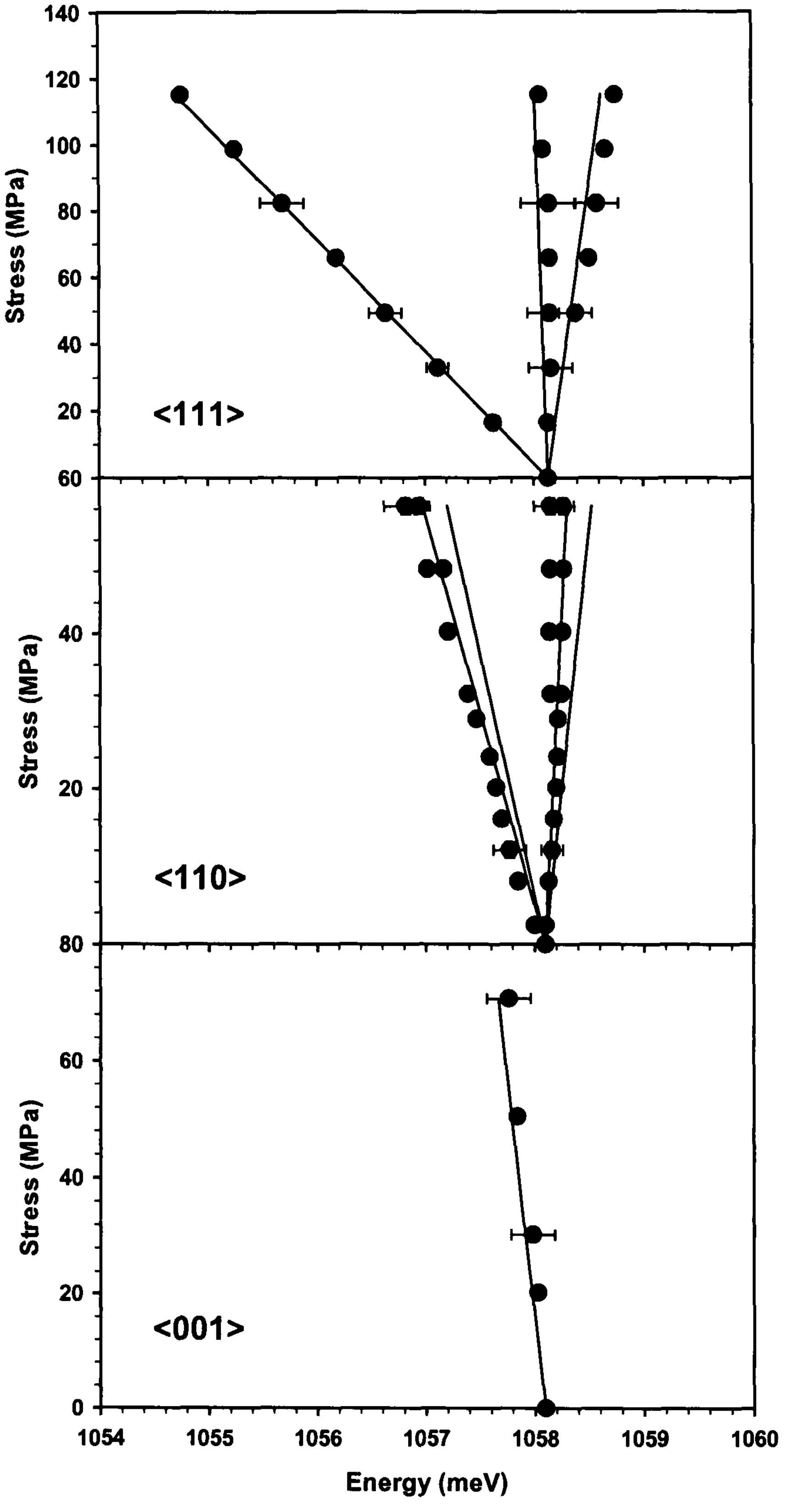

Figure 4.7 Fan diagrams for A zero-phonon line in the linear regime. A trigonal fits using stress parameters A_1 = -6.2, A_2 = -11.8, C = 2 and B = 0 meV/GPa is represented by solid lines.

4.2.3 Monoclinic I fit to Group I

Under <001> stress the zero-phonon line is expected to split into two components for a monoclinic I site described by parameters A_1 and A_2 The observation of only one line under <001> stress is a problem which will be discussed in more detail below A global fit to the data for all three directions was attempted by selecting the observed shift rate under <001> stress as the initial value for A_1 or A_2 , with no constraints on any of the other parameters The best fit was obtained for the following stress parameter values A_1 = -35 4, A_2 = -7 6, A_3 = -7 4 and A_4 = 27 1 meV/GPa The solid lines in figure 4 8 illustrate the quality of the fit to the experimental data

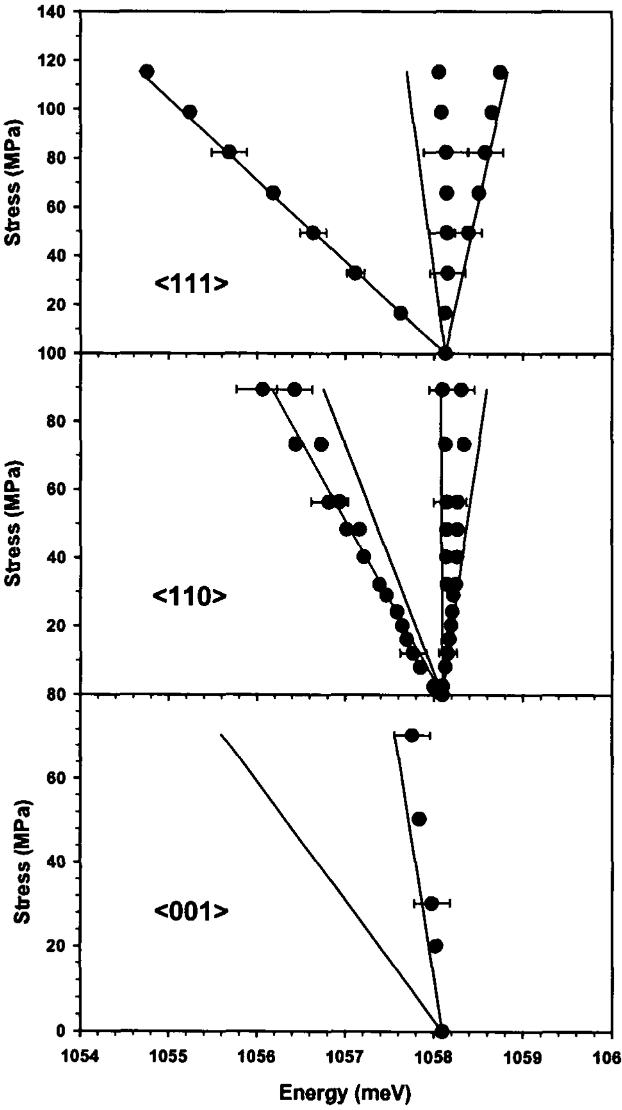

Figure 4.8 Fan diagrams for A zero-phonon line in the linear regime. Fits using the stress parameters A_1 = -35.4, A_2 = -7.6, A_3 = -7.4 and A_4 = 27.1 meV/GPa are represented by solid lines.

The obtained fit is in reasonable agreement with the experimentally observed shift rates in the <111> and <110> directions The line shift observed for the <001> corresponds to the stress parameter A_2 No other assignment of the theoretical expressions to the measured shift rates yields as good a fit A major difficulty with this fit is the absence of any data to support the prediction of two components under <001> stress In particular, the absence of the lower energy component, which would normally be the component observed, presents a challenge to the fit To our knowledge, no centre with an unobserved lowest energy component under <001> stress has been reported The absence of a stress-split component described by shift rate A_1 could arise if the corresponding defects reorient under the application of a <001> stress Orientations 1, 4, 8 and 11 (z-axis is parallel to <001> stress) of the twelve possible orientations of a monoclinic I defect given in table 2 2 contribute to the shift rate A_1 In contrast, the decrease in intensity of components shifting to higher energy, particularly under <001> stress, has been observed for several centres Henry and his co-workers attributed the loss in intensity to a stress-dependant decrease in the excited state binding energy of Zn-related defects (Henry *et al*, 1994) The observed loss in intensity of the Zn_A and Zn_B stress components was in proportion to the shift rate, the components with a higher shift rate showing a more rapid decrease in intensity In the case of Cd-related centres the decrease in intensity was attributed to a stress-induced change in the ability of orientationally inequivalent defects to bind one or both particles at the centre (McGlynn *et al*, 1996) However, the arguments of Henry and McGlynn do not apply to the situation where the stress component is shifting downwards in energy (Henry *et al*, 1994, McGlynn *et al*, 1996)

If we consider the case where the defects are reorientating under stress, we would expect to observe two stress-split components at very low stress As the stress is increased the relative intensity of one component will diminish as the defects reorient In the case of group I under <001> stress the line does not split and the expected lower energy component was not observed even at very low stress In conclusion, the fit to monoclinic I is not adequate to describe the shift rates and number of components of group I Therefore the symmetry assigned is trigonal

4.2.4 High Stress and High Temperature Regime - Trigonal Fit

By considering the low stress regime, an A to E transition at a trigonal centre has been assigned to group I The stress parameters determined yield a set of linear equations which are inadequate to describe the high stress data From the fan diagrams (figures 4 4 and 4 6), under <110> and <001> stress there is evidence of an interaction due to the non-linear shift rate of the data which shall be considered in this section

The downward curvature observed suggests an interaction with an additional excited state at higher energy than the initial state for the observed A zero-phonon line Transitions from a higher energy state will not be observed at low temperatures if the energy separation between the two states is larger than ~ kT since in thermal equilibrium it is not populated When the interacting state is not observed there are more stress parameters than observables and a large number of parameters are required to describe the interaction To avoid unnecessary parameters group I was studied at high temperatures to help identify the interaction state

At high temperatures, ~ 12 K the higher energy zero-phonon lines, dominated by zero-phonon lines labelled C and D were observed in the spectra Applying stress along the <111>, <110> and <001> stress directions all the higher energy lines showed very similar stress splitting data as observed for the minimum energy zero-phonon line at low temperature Figures 4 9 to 4 14 show representative spectra and fan diagrams of all the group I zero-phonon lines

Under <111> stress, zero-phonon lines A, B, C and D split into three stress components with linear shift rates Due to the relatively low intensity of the highest energy zero-phonon line E, it was not possible to observe or confirm the number of stress-split components of this line

Under <110> stress four stress-split components are observed for both the C and D zero-phonon lines Three components instead of four were observed for both A and B zero-phonon lines, this may be attributed to the overlap of lines The energy of the E zero-phonon line shifts to lower energy as the stress increases and no stress-split components were identified due to the low intensity of the line

Figure 4 13 shows representative spectra of the zero-phonon lines under <001> stress Similar to the spectra recorded at low temperatures, the lines do not split but shift with a rapid non-linear shift rate. The lower energy lines A to D shift to lower energy while the highest energy zero-phonon line, E, shifts to higher energy indicating an interaction between the zero-phonon lines. In addition to the group I zero-phonon lines, Z_1^* shifting to higher energy (figure 4.13) was observed. This line may be a stress-induced zero-phonon line of group I which was not observed during temperature dependence analysis due to the broad nature of the D zero-phonon line. This identification cannot be confirmed at present.

A least squares fit to the data in the linear region is represented in the fan diagrams by the solid lines and the shift rates obtained for each component are listed in table 4.5. Comparing the shift rates of the minimum energy zero-phonon line, A, for both high and low temperatures (table 4.4 and 4.5) the shift rates are compatible within experimental error. In all three stress directions, zero-phonon lines A to D show very similar splitting patterns indicating they are due to transitions at trigonal centres. From temperature dependence measurements zero-phonon line E is an excited level of group I and it can be accredited to an A to E transition at a trigonal site. Under <001> stress the E zero-phonon line shifts to higher energy indicating an interaction with the lower energy zero-phonon lines. The matrix to describe the stress perturbation at a trigonal centre given in section 4.2.2 must be extended to include all five zero-phonon lines.

Shift rates <001>	meV/GPa A	meV/GPa B	meV/GPa C	meV/GPa D	meV/GPa E	meV/GPa *
Z_1	-6.8^{i}	-6.6^{ii}	-13.1^{ii}	-18.4^{i}	1.36^{ii}	0.8^{ii}
<111>						
Z_2	-27.7	-27.5	-27.0	-27.0		
Z_3	0.8	0.6	-0.6	0.1	-0.5	
Z_4	6.1	4.5	4.7	4.5		
<110>						
Z_5	-25.3	-25.9	-29.5	-30.7		
Z_6	-20.1	-20.3^{i}	-23.1^{ii}	-24.8		
Z_7			-5.24^{ii}	-8.27^{ii}	-6.21	
Z_8	5.94^{iii}	5.48^{iii}	3.01^{iii}	-2.77^{iii}		

Table 4.5 Least squares fit to group I zero-phonon lines at high temperature in the linear regime as indicated in figures 4.10, 4.12 and 4.14. Unless indicated linear region extends above 90 MPa, ^{i} up to 90 MPa, ^{ii} up to 72 MPa, ^{iii} below 60 MPa.

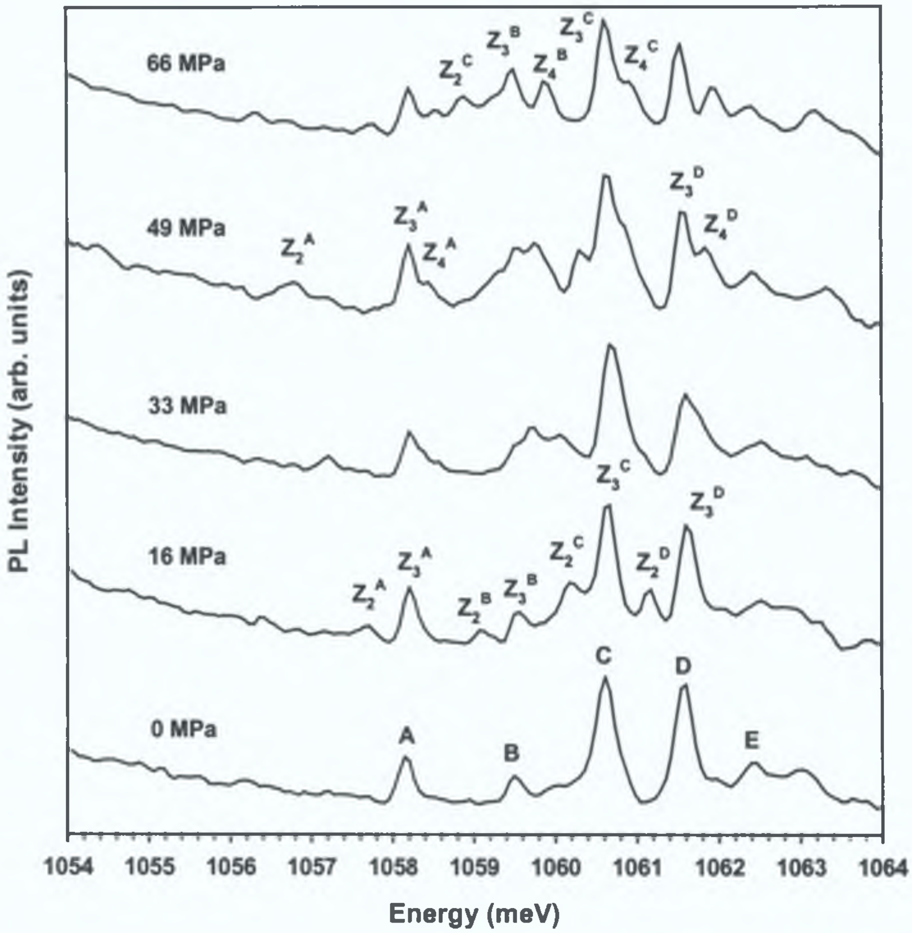

Figure 4.9 Representative spectra taken at different values of stress in the <111> direction for group I zero-phonon lines at T ~ 13 K.

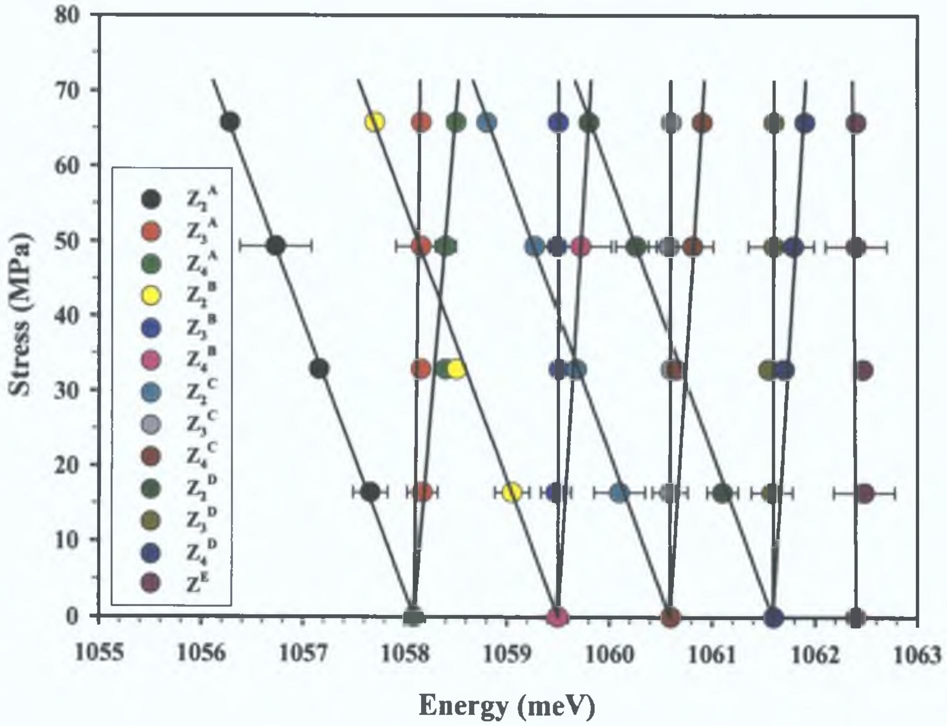

Figure 4.10 Fan diagram for stress in the <111> direction of group I zero-phonon lines at T ~ 13 K. The error bars indicate the width of the spectral lines.

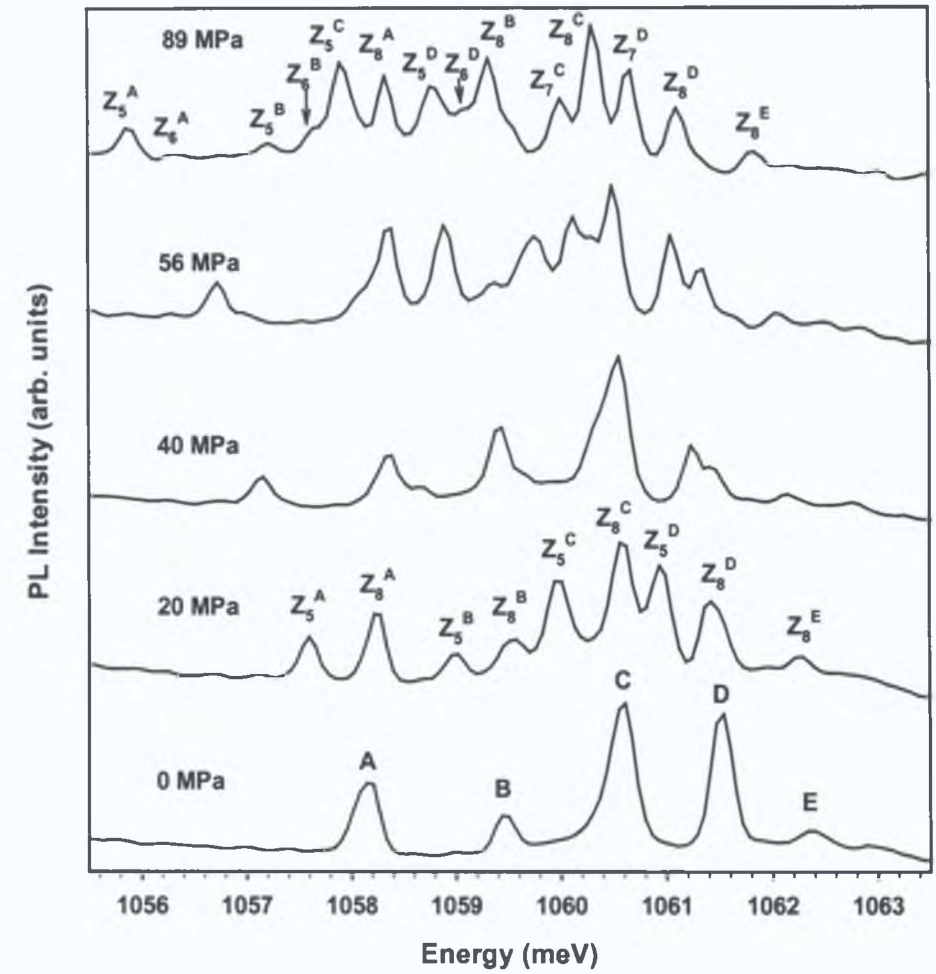

Figure 4.11 Spectra for group I zero-phonon lines under <110> stress at T ~ 12.5K.

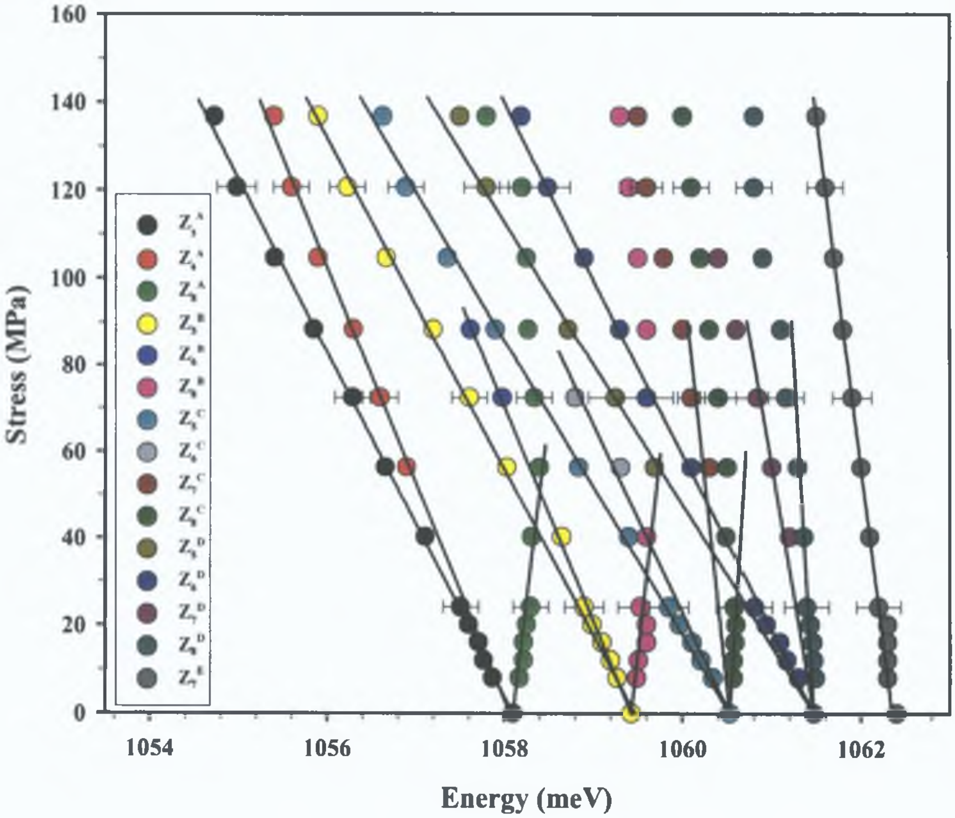

Figure 4.12 Fan diagram of group I zero-phonon lines for stress in <110> direction. The error bars indicate the width of the spectral lines.

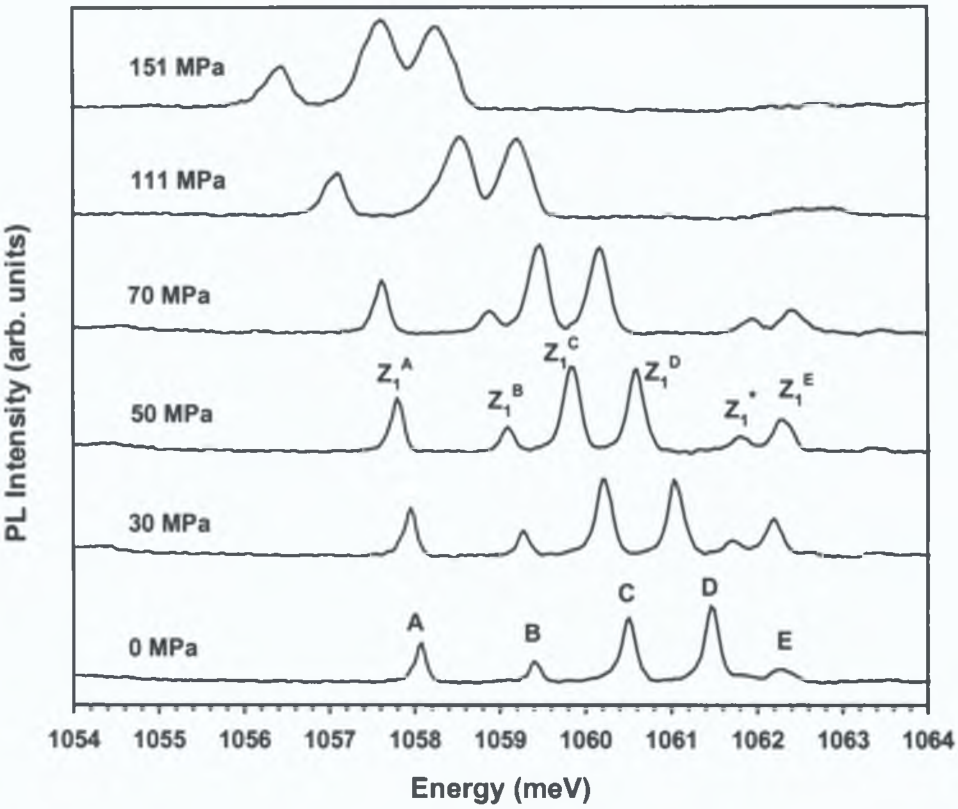

Figure 4.13 Spectra of group I zero-phonon lines taken at different values of stress under <100> stress T ~ 10 K.

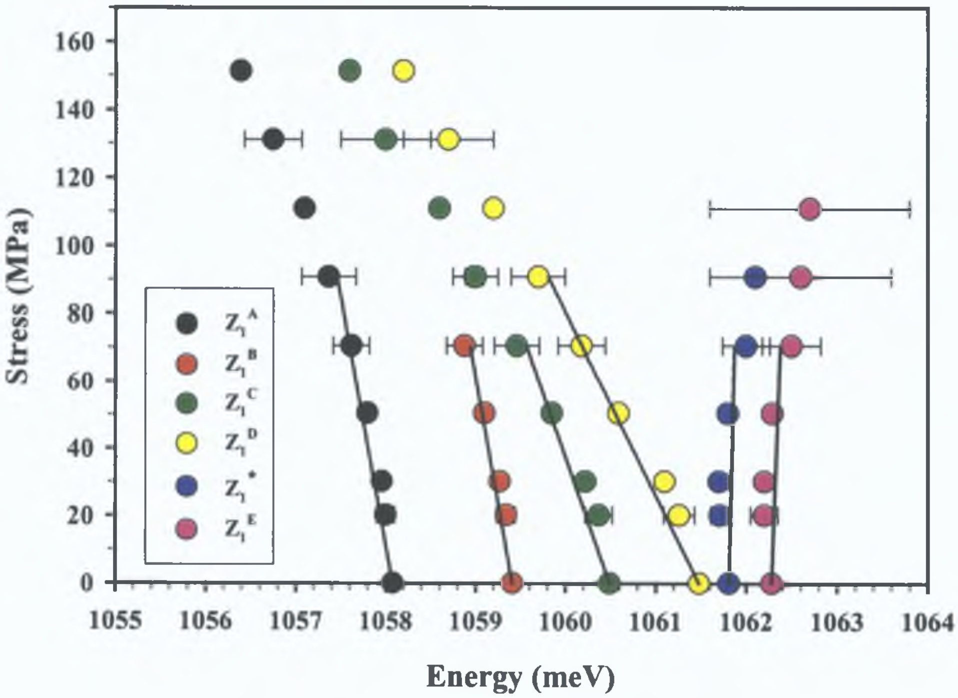

Figure 4.14 <001> fan diagram of group I zero-phonon lines at T ~ 10 K. The error bars indicate the width of the spectral lines.

Expanding this matrix to describe a situation to include all five zero-phonon lines as A to E transitions of trigonal symmetry the matrix would have dimension ten and be expressed in terms of nineteen variables This assumes the interaction is only due to the highest energy zero-phonon line E and there are no interactions between the other four zero-phonon lines At present only three variables are known associated with the transition of the minimum energy zero-phonon line Variables attributed to the higher energy zero-phonon lines are unreliable due to interactions under <001> and <110> at low stresses The signal levels obtained during stress measurements were insufficient for any useful variables to be obtained for the interaction level Further stress measurements should confirm the identification of zero-phonon line E as the interaction state and stress parameters should be obtained

The results described above show that a reasonable fit to trigonal symmetry for group I in the low temperature regime was obtained The existence of an interaction state was particularly evident from the <001> data at high stress where a non-linear shift rate was observed In the high temperature regime, the zero-phonon lines followed the same splitting pattern as the minimum energy line observed at low temperatures This is expected for transitions of the same centre The interaction state was identified as the highest energy zero-phonon line E Due to the complexity of the secular matrix to describe the stress perturbation of all zero-phonon lines and the absence of reliable initial parameter values a reasonable fit was not found for the high temperature data

4.3 Group II

From temperature dependence measurements, group II consists of at least eight zero-phonon lines thermalising to a single ground state These zero-phonon lines are very closely spaced and at ~ 2 K only the lowest energy zero-phonon line is observed Uniaxial stress experiments were performed at ~ 6 K and above Zero-phonon lines labelled F, H and J dominate the spectra recorded The stress-split components of the low intensity G and I zero-phonon lines were not observed in all stress directions The small separation of lines J and K made identification of their stress-split components difficult Indeed, the close proximity of all group II zero-phonon lines made assignment of the stress-split components complicated

4.3.1 Overview of uniaxial stress data

Stresses were applied along the <001>, <111> and <110> directions at ~ 6 and 12 5 K Figure 4 15 shows representative spectra of group II at 12 K under increasing <001> stress The zero-phonon lines split into two components, labelled X_1^i and X_2^i, where i is zero-phonon line, F M The higher energy component of the minimum energy line, X_2^F was only observed at very low stress, as the stress increased it overlapped with X_1^H At ~ 13 MPa both stress-split components were observed for line J while the higher energy component of H, X_2^H, overlaps with X_1^J Only the higher energy split components of lines K, L and M, X_2^K, X_2^L and X_2^L were observed A line, labelled $X_2^?$ was observed shifting to higher energy, this line was not observed at zero-stress and may be a stress induced line of group II Above 18 MPa the data was unreliable due to broadening of the stress components possibly due to sample misalignment Spectra recorded at ~ 6 K for stress above 20 MPa are shown in figure 4 16 The splitting and shift rates were confirmed by repeating the experiments and figure 4 17 shows the shift in zero-phonon line energy as a function of stress For increasing <001> stress the luminescence from X_2^K, X_2^L and X_2^M became weaker and above a certain stress could no longer be distinguished from the broad luminescence band

Figure 4 18 shows representative spectra for group II under <111> stress at ~ 6 K The principal zero-phonon lines are seen clearly to split into two components, labelled X_3^i and X_4^i At high stress the high energy components of the low intensity lines, G and I are observed The shift rates of all the stress induced components are linear, as shown in figure 4 19 indicating no interaction between the lines Spectra recorded at 12 K show similar shift rates and stress splitting pattern

Due to the very closely spaced zero-phonon lines the number and assignment of stress-split components was very difficult under <110> stress

Figure 4 20 shows representative spectra recorded at T ~ 12 K for increasing stress and the splitting pattern is shown in figure 4 21 Despite the total number of components observed, the H line was observed to split into three components, labelled X_5^H, X_6^H and X_7^H Both the J and K lines split into three components, however due to the separation of the lines (~ 0 1 meV) the assignment of stress-split components is unambiguous Only two stress-split components were observed for the F line, this was attributed to the low intensity nature of the stress-split components and inability to resolve these components The stress induced line observed in the <001> data is observed in the <110> spectra, labelled $X_7^?$ Only one component of line M, X_7^M is observed shifting to higher energy at the same rate as $X_7^?$ The high stress component of the minimum energy line F, X_7^F shifts to lower energy at a non-linear shift rate The curvature of the stress components from the centre of the observed zero-phonon lines indicates that the levels are interacting with a level of the centre

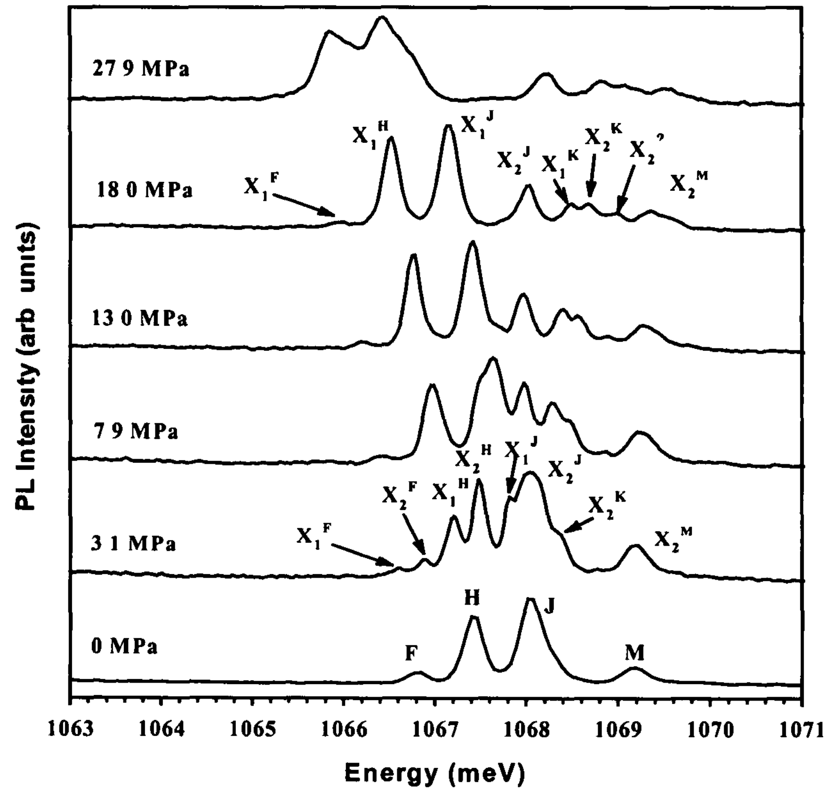

Figure 4.15 Representative spectra of group II at ~ 12 K in the low stress regime under <001> stress.

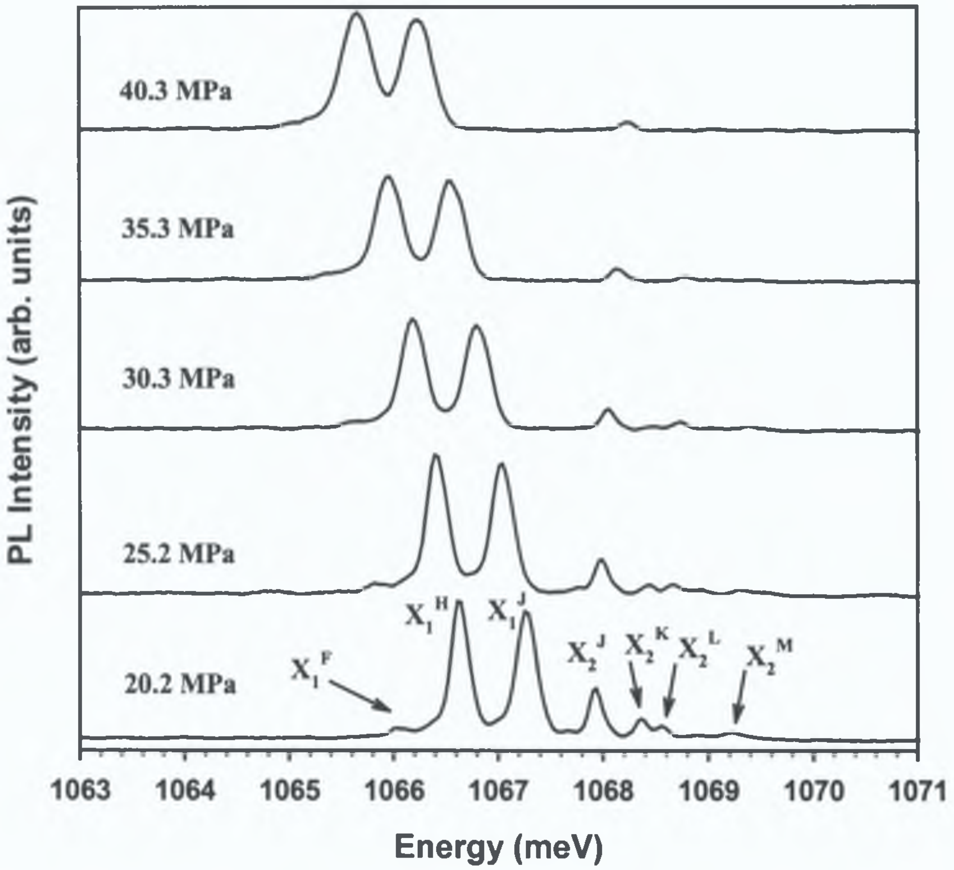

Figure 4.16 Representative spectra of group II under <001> stress above 20 MPa at T ~ 6 K.

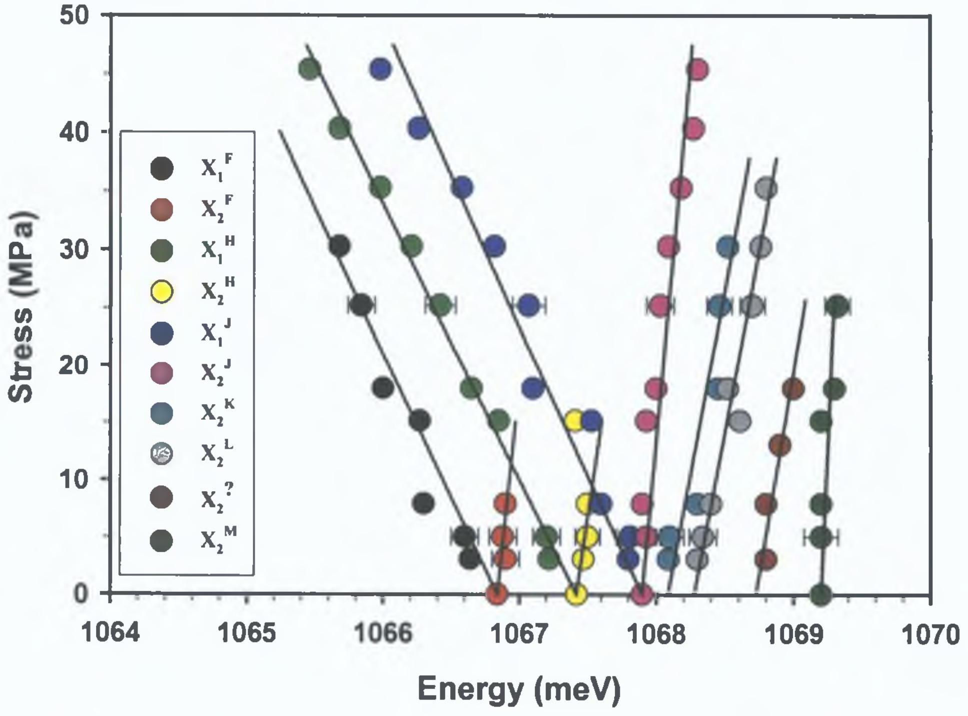

Figure 4.17 A fan diagram of the stress induced splitting of the group II zero-phonon lines under <001> uniaxial stress. Data at ~ 6.5 and 12 K are combined.

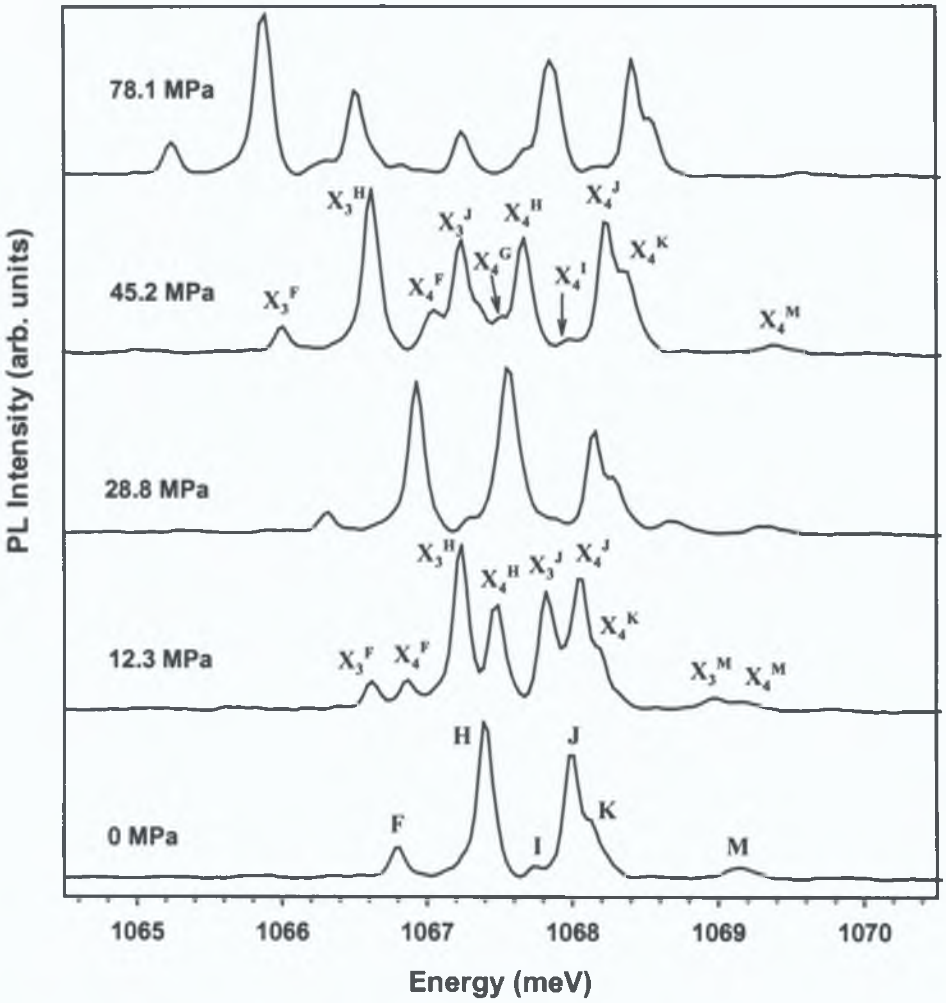

Figure 4.18 Representative spectra of the stress induced splitting for <111> stress at T ~ 6.5 K.

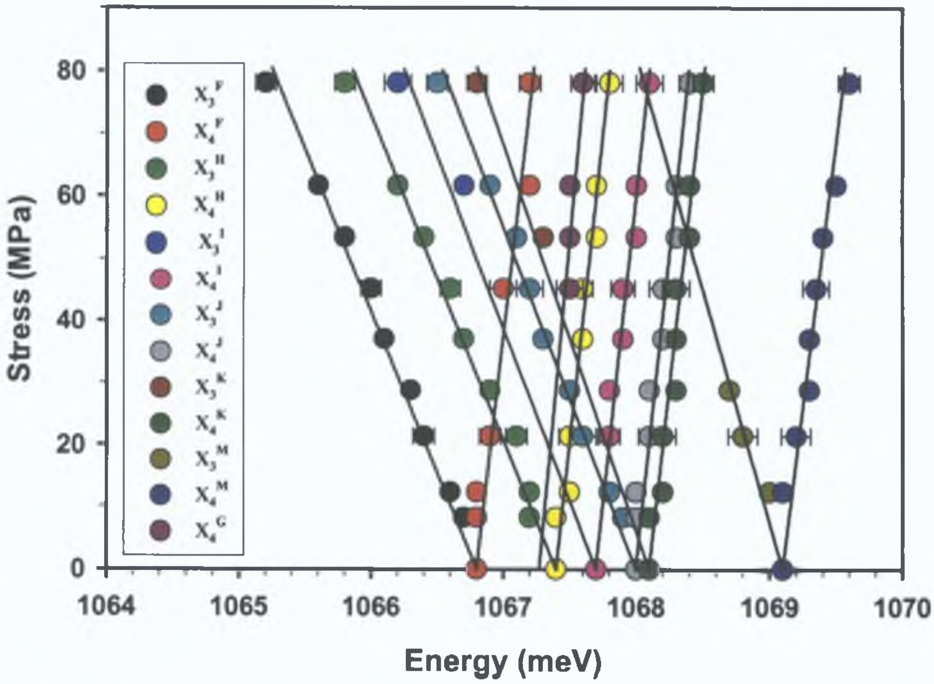

Figure 4.19 Fan diagram showing the <111> stress induced splitting of the group II zero-phonon lines at T ~ 6.5 K.

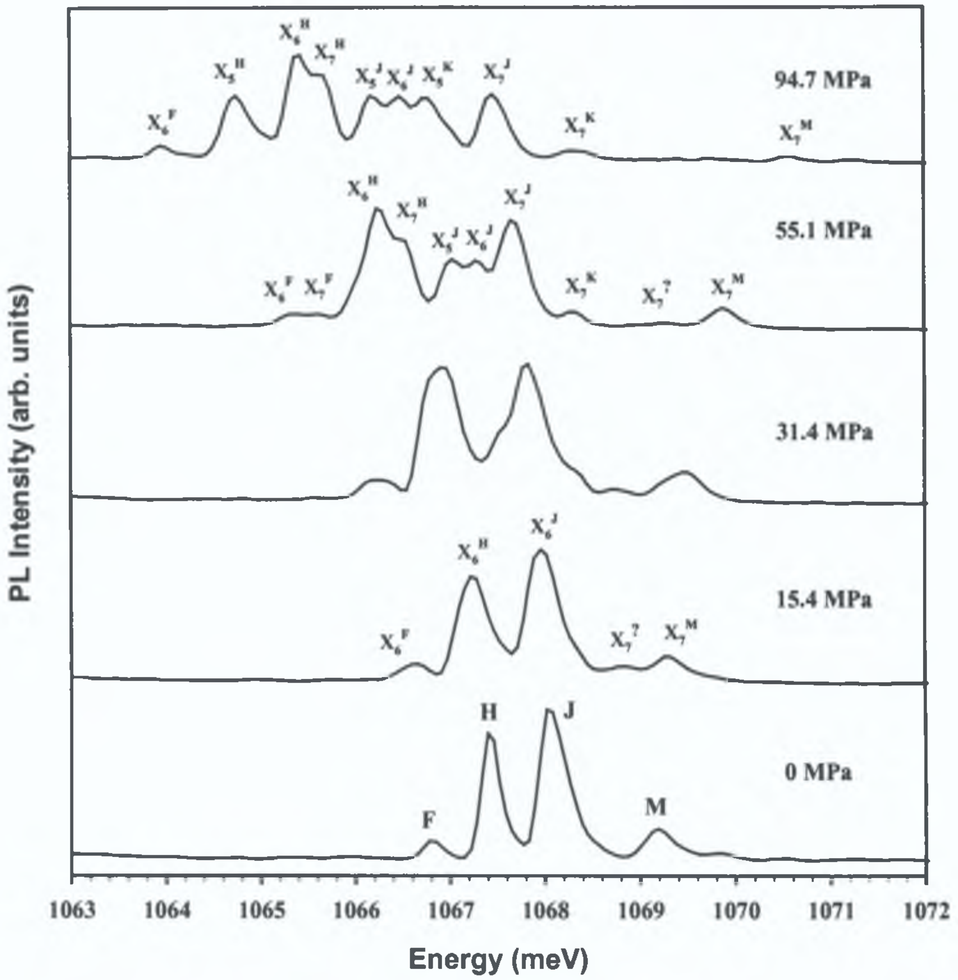

Figure 4.20 Representative spectra of group II zero-phonon line splitting for <110> stress recorded at 12 K.

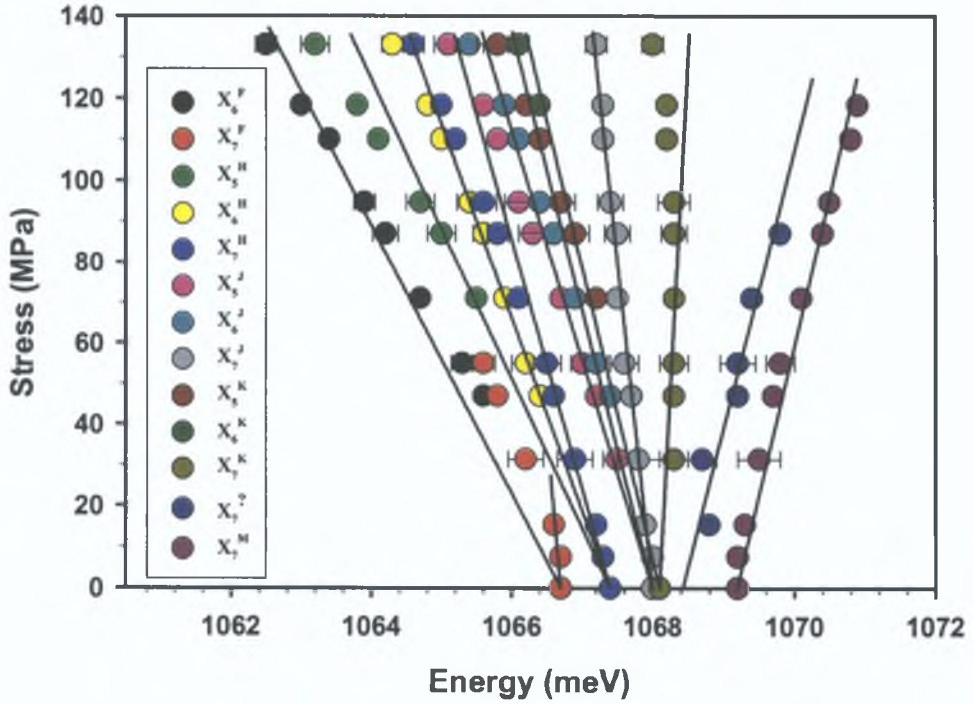

Figure 4.21 A fan diagram of the stress induced splitting of the group II zero-phonon lines under <110> stress.

4.3.2 Analysis of the stress data

If the number of observed splitting are compared with the theoretical splitting calculated by Mohammed *et al*, (1982) and Kaplayanskii (1964) the number of components for several different defect symmetries are identical Taking into account the possibility that some of the stress parameters for the defects are zero then the number of possible symmetries for group II increases There are three candidates, rhombic I, trigonal, and tetrahedral The theoretical shift rate equations for an A to E transition at a trigonal site are given in table 4 3 and the theoretical shift rate equations for rhombic I and tetrahedral are given below in table 4 6

	Tetrahedral T to A	Rhombic I
<001>	A_1+2B A_1-B	A_1 A_2
<111>	$A_1+\frac{2}{3}C$ $A_1-\frac{1}{3}C$	$\frac{1}{3}(A_1+2A_2+2A_3)$ $\frac{1}{3}(A_1+2A_2-2A_3)$
<110>	A_1-B $A_1+\frac{1}{2}(B+C)$ $A_1+\frac{1}{2}(B-C)$	A_2+A_3 $\frac{1}{2}(A_1+A_2)$ A_1-A_3

Table 4.6 Theoretical shift rate equations for a tetrahedral T to A and rhombic I, transitions as calculated by Kaplayanskii (1964) and Mohammed *et al.*, (1982).

In the absence of polarisation data and due to the high number of components observed the splitting cannot be attributed unambiguously to orientational, electronic or both types of degeneracy If the splittings are due entirely to orientational degeneracy the highest symmetry designation that can fit the observed splitting is rhombic I A least squares fit to the experimental data for the H line using a rhombic I model was made The fit while reasonable for both the <001> and <111> direction yielded a large error in the <110> direction The least squares fit of the tetrahedral shift rates yielded a fit which was significantly worse than for the rhombic case

Figure 4 22 shows a least squares for the H zero-phonon line using the shift rate equations for an A to E transition at a trigonal centre Three stress-split components are expected under <111> stress and each group II zero-phonon line splits into two components under <111> stress (figure 4 19) In order for the trigonal model to be correct one of the stress parameters (C) is set equal to zero Four components are expected for this type of transition under <110> stress Due to the bi-axial nature of trigonal centres it is possible for a stress split component not to be observed in photoluminescence under <110> stress (Mohammed *et al*, 1982) The theoretical shift rates and experimental data show good agreement in the <001> and <111> stress directions Under <110> stress interaction effects are observed but were not included in the fitting procedure A trigonal fit which includes interaction effects would be an ideal situation Due to the number of zero-phonon lines - at least eight - the secular matrix would have dimension sixteen The position of the interaction level is unknown The shift rates of both F and M lines indicate the interaction is possibly the H or J zero-phonon line Due to the low relative intensity of several of the zero-phonon lines not all stress split components were observed for each direction These factors contribute to the lack of initial starting values for the stress parameters and experiments where all stress components are resolved are necessary before the matrix could be solved

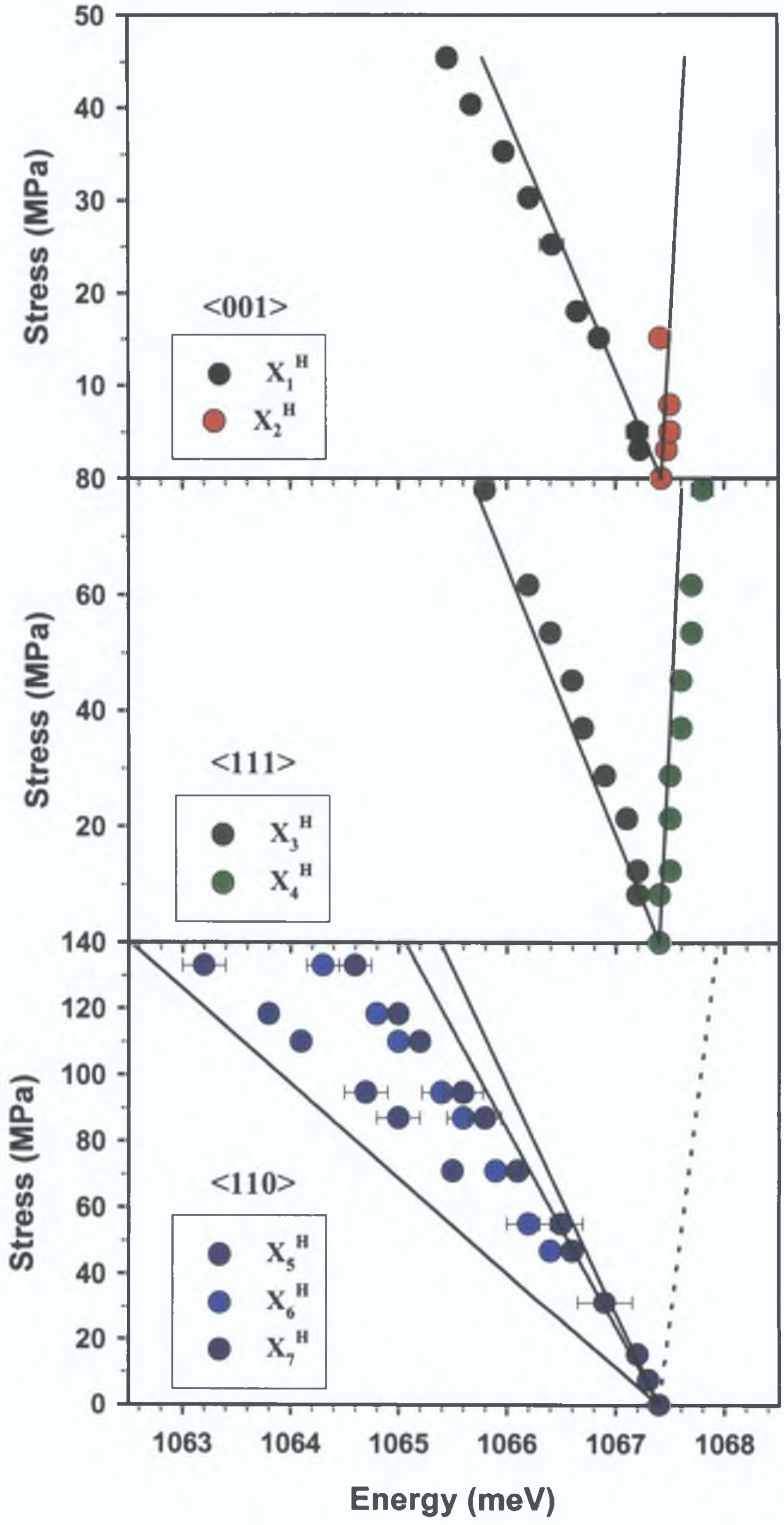

Figure 4.22 Uniaxial stress splitting of H zero-phonon line. The solid lines are theoretical fits to the data for a trigonal (A to E transition) with stress parameters $A_1 = -15.5$, $A_2 = 9.1$, $B = -10.3$ and $C = 0$ meV/GPa. The fourth component under <110> stress predicted from theory is represented by the dotted line.

4.4 Group III

In this section, information about the symmetry of the group III defect complex is discussed The group III luminescence was very weak in all three orientated samples, however, preliminary measurements were made and a symmetry orientation for the defect is presented

4.4.1 Overview of uniaxial stress data

The effect of stress along the three principal crystal (<001>, <111> and <110>) directions on the α zero-phonon lines at ~ 12 K are shown in figures 4 23, 4 25 and 4 27 Unfortunately, the α_1 line cannot be studied as readily as the α_2 and α_3 lines α_1 is observed beside the phonon assisted replica β_3 where even in the absence of stress at high temperatures the stronger β_3 line causes considerable interference This problem is further complicated by phonon broadening and when stress is applied the lines split and it becomes difficult to locate the stress split components This analysis focuses on the higher energy zero-phonon lines α_2 and α_3

Figures 4 24, 4 26 and 4 28 show how the zero-phonon line components vary with increasing stress along <001>, <111> and <110> directions respectively, where the points are the experimental data and the lines represent a least squares fit to the data in the linear region Both α_2 and α_3 split into three components with linear shift rates along the <111> and <110> direction The shift rates of the stress-components in the linear region are listed in table 4 7 The observed splitting under <001> stress appears complicated The α_3 zero-phonon line splits into two components with linear shift rates to ~ 90 MPa, above this the shift rate is highly non-linear Under <001> stress α_2 does not split Similar to the α_3 zero-phonon line, the shift rate of α_2 is linear to ~ 90 MPa before the line shifts rapidly to lower energy with a non-linear shift rate The relative intensity of the zero-phonon lines α_2 to α_3 remained constant as the stress was increased This suggested the intensity of α_2 is due to at least two stress induced components with identical shift rates and thus the components overlap under <001> stress Examining α_1 under <001> stress at 4 2 K at low stress (≤ 20 MPa) the line splits into two components, similar to the α_3 line As the stress was increased the intensity of the α_1 stress-split components decreased and with the signal to noise ratio achieved the shift rates could not be determined

The non-linear shift rates evident under <001> stress are not caused by α zero-phonon line repulsion but from an unobserved excited state Due to the downward curvature of the components under <001> stress, the additional excited must be assumed to exist at a higher energy than the observed state

Stress Direction	Label	Shift Rate meV/GPa (±0 5)	Label	Shift Rate meV/GPa (±0 5)
<001>			α^2_3	-15.4
upto 90 MPa	α^1_2	-6 1	α^1_3	-11 0
<111>	α^3_2	-17 8	α^3_3	-17 4
	α^2_2	3 2	α^2_3	3 8
	α^1_2	11 4	α^1_3	11 3
<110>	α^3_2	-35 3	α^3_3	-41 2
	α^2_2	-13 0	α^2_3	-15 3
	α^1_2	-7 3	α^1_3	-9 7

Table 4.7 The shift rates of the stress split components in the linear regime by least squares fit, as represented by lines in the fan diagrams for stresses along the <001>, <111> and <110> directions.

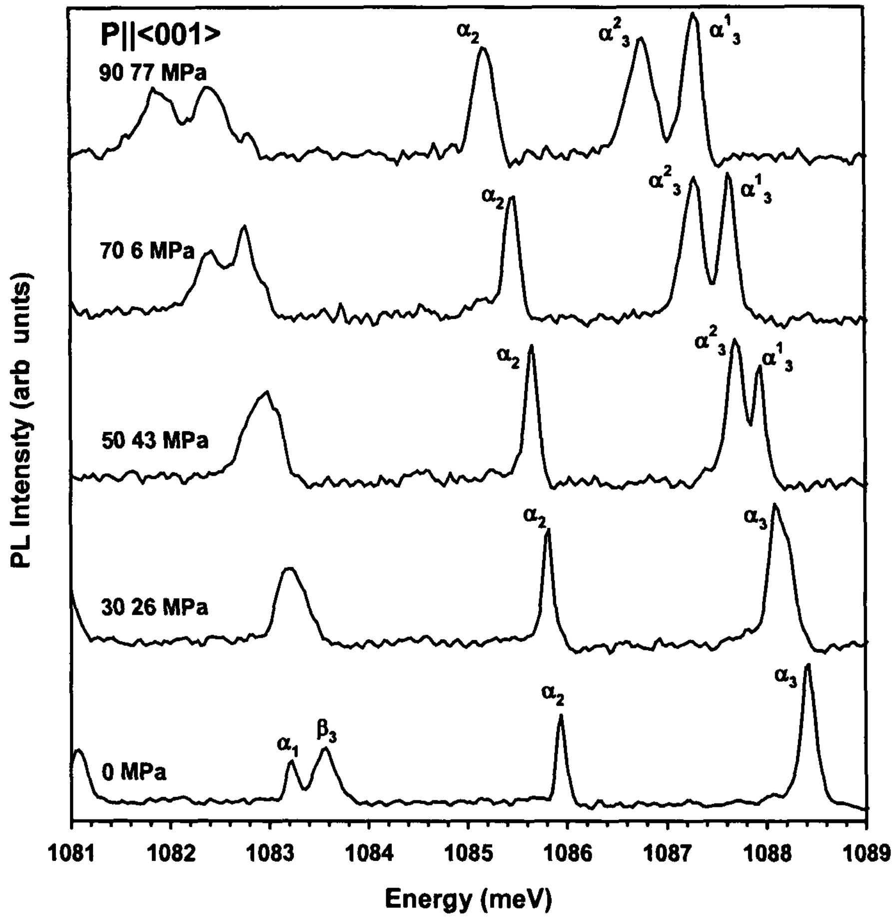

Figure 4.23 Group III α zero-phonon lines under <001> stress at T = ~ 11 K. The higher energy line, α_3 splits into two components under the influence of stress, while the α_2 line does not split.

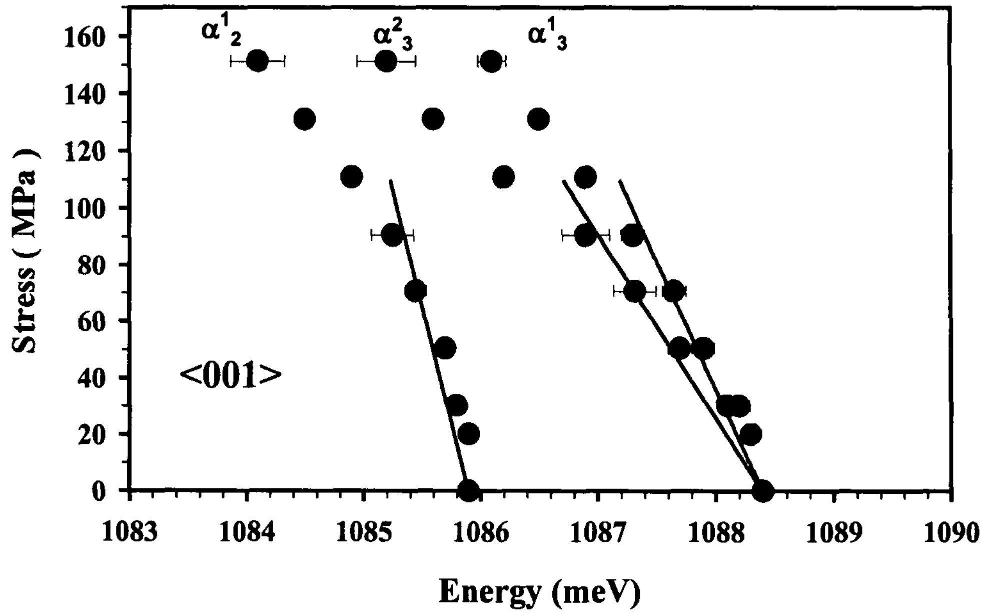

Figure 4.24 Fan diagram of group III α_2 and α_3 splitting under <001> stress. The error bars represent the width of the lines.

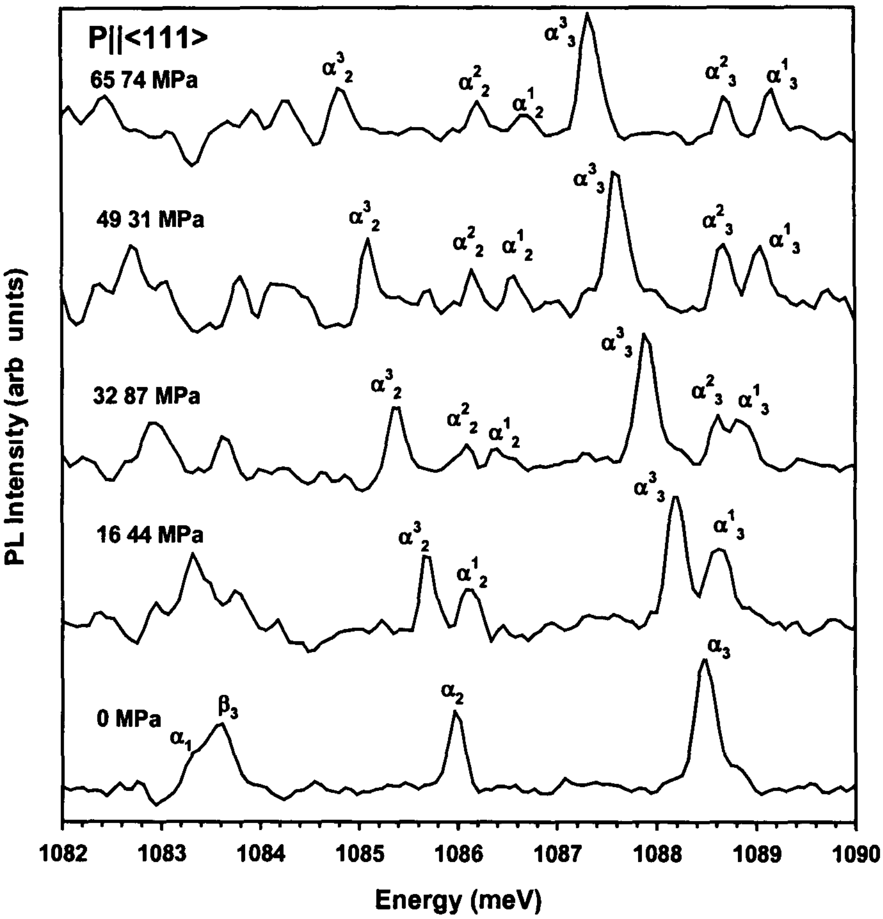

Figure 4.25 Both the α_2 and α_3 lines split into three components under <111> stress at T = ~13 K.

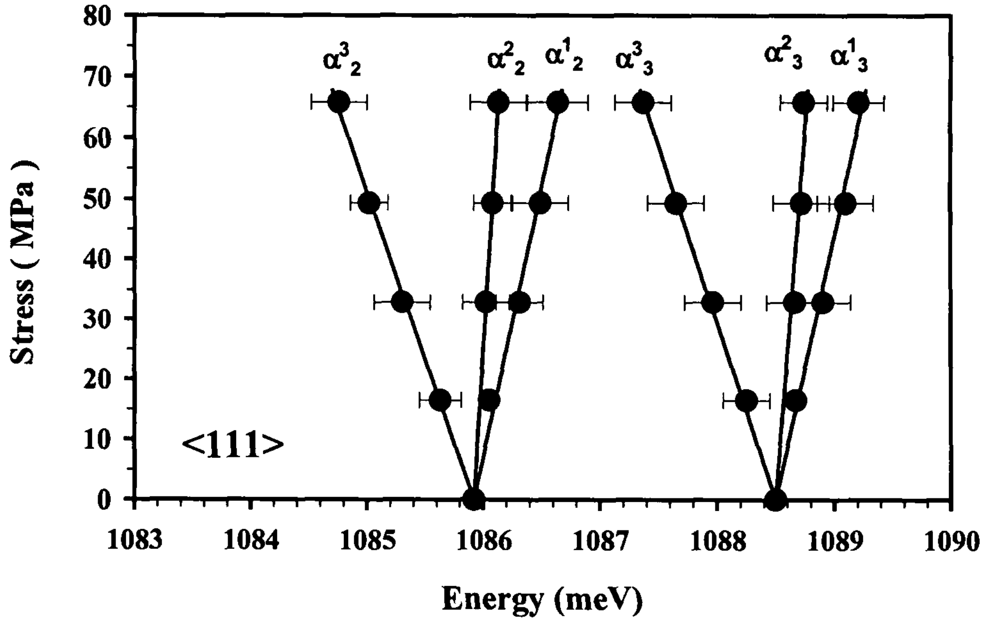

Figure 4.26 Fan diagram of α_2 and α_3 under <111> stress. Each zero-phonon line splits into three components. The error bars indicate the width of the lines.

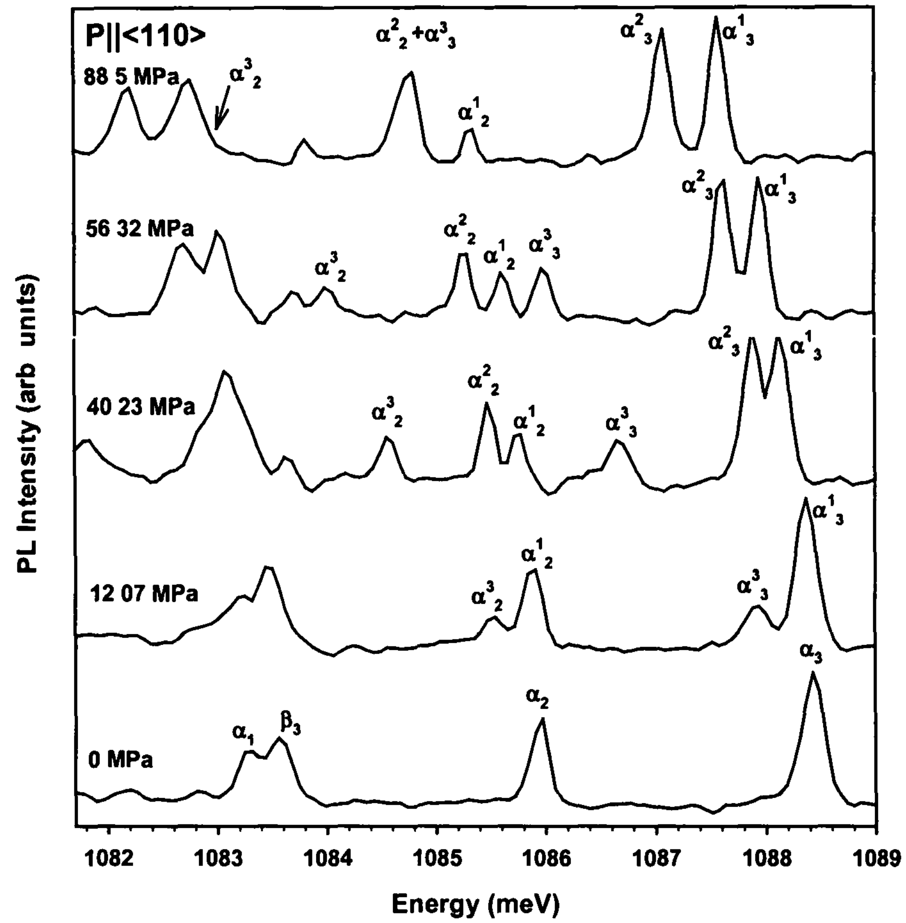

Figure 4.27 Both α_3 and α_2 zero-phonon lines split into three components under <110> stress. Spectra recorded at T = ~12.5 K.

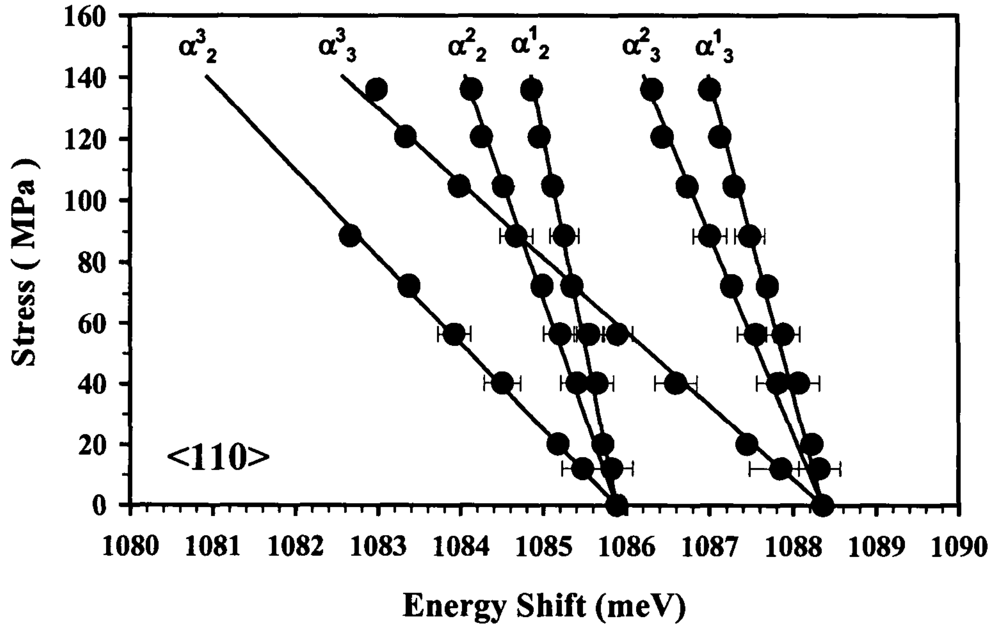

Figure 4.28 Fan diagram of α_2 and α_3 stress-split components under <110> stress. The error bars indicate the width of the lines.

The number of stress split components for either α_2 or α_3 are not consistent with any one symmetry orientation (Mohammed *et al.*, 1982, Kaplyanskii 1964). Under <111> stress zero-phonon lines of both monoclinic I and trigonal (A to E) symmetry are expected to split into three components and into four components under <110> stress. In photoluminescence depending upon polarisation effects only three stress-split components may be observed under <110> stress for both symmetries (Mohammed *et al.*, 1982).

In table 4.2. the expected intensity ratio of each stress-split component for monoclinic I, (A to A and A to B transitions) and trigonal (A to E transition) centres are listed. Comparing the expected intensities with the observed intensities as listed in table 4.8, for both the <111> and <110> directions monoclinic I (A to B) shows good agreement. Applying a stress to monoclinic I centres removes orientational degeneracy only and the intensities of the stress split components are expected to be independent of temperature. The temperature independence of the components cannot be confirmed at present. Only the α_1 line is observed at 4.2 K and at higher temperatures due to overlap of the line with β_3 the intensity of the stress-split components cannot be obtained. In the absence of polarisation data and the temperature dependence of the stress-split components both monoclinic I and trigonal symmetry must be considered. Trigonal symmetry shall be considered in the following section.

Stress Direction	**Stress (MPa)**	**Relative Intensity Ratio**	**Relative Intensity Ratio**
<001>		α^1_2	$\alpha^2_3 : \alpha^1_3$
	0		1
	30.26	*No splitting observed*	1
	50.43		1 : 1.2
	70.60		1 : 1
<111>		$\alpha^3_2 : \alpha^2_2 : \alpha^1_2$	$\alpha^3_3 : \alpha^2_3 : \alpha^1_3$
	0	1	1
	32.87	3 : 1 : 1	2.7 : 1.1 : 1
	65.74	2 .5 : 1.4 : 1	2.5 : 1 : 1
<110>		$\alpha^3_2 : \alpha^2_2 : \alpha^1_2$	$\alpha^3_3 : \alpha^2_3 : \alpha^1_3$
	0	1	1
	12.07	1 : 2.5	1 : 3
	56.32	1 : 2 : 1.5	1 : 3 : 3

Table 4.8 Experimental intensity ratios of α_2 and α_3 stress components as a function of applied stress.

4.4.2 Trigonal fit to Group III

In the first instance the shift rates in the linear regime of the data were considered. The shift rates of the α_3 zero-phonon line were considered as two stress-split components were observed under <001> stress as expected for trigonal symmetry. The fit to the trigonal model did not yield a reasonable fit for all three stress directions. Similar results were obtained for α_2. The shift rates of the stress-split components calculated at low stress do not satisfy the shift rate equations of trigonal symmetry. As no reasonable fit was found in the low stress regime the analysis was not extended to include the higher stress data. This analysis indicated the defect symmetry was monoclinic I and the fit obtained in the next section confirms this assignment.

4.4.3 Monoclinic I fit to Group III

First, the appropriate shift rate equations of an A to B transition at a monoclinic I centre were identified with corresponding stress-split components in the low stress regime where interaction effects are negligible. Initial values for the stress parameters, which yield a set of linear equations, were obtained. The downward curvature observed under <001> stress suggests an unobserved additional excited state exists at a higher energy than the observed zero-phonon lines. Based on the assumption that the observed transition is monoclinic I it is possible to determine the irreducible representation of the interacting excited state. There are several possible transitions which are valid and these were introduced in section 2.4.3.

At zero stress, transitions from the upper excited state are negligible, however as the stress increases the transition is observed through mixing with the observed state. Information from the observed interaction can help in identifying the irreducible representation of the unseen excited state. No interaction was observed under <111> stress, but, it was clearly observed from the non-linear shift rate under <001> stress. In the <110> case at very high stress the shift rates are non-linear. Consider the case where the ground state of the transition is a B state with the observed transition from a higher energy A state. Introducing an additional B state as the unobserved interaction state; the interaction matrix between the two upper levels, will take the form:

$\overline{V}_S$	A	B
A	$\langle A\|\overline{V}_S\|A\rangle$	$\langle A\|\overline{V}_S\|B\rangle$
B	$\langle B\|\overline{V}_S\|A\rangle$	$\langle B\|\overline{V}_S\|B\rangle$

where the perturbation $\overline{V}_S$ associated with a monoclinic I defect was determined in section 2 4 1 The diagonal elements of the secular matrix will take the form

$$\langle A|\overline{V}_S|A\rangle = A_1 s_{zz} + A_2\left(s_{xx} + s_{yy}\right) + 2A_3 s_{xy} + 2A_4\left(s_{yz} - s_{zx}\right) \qquad (4\ 9)$$

$$\langle B|\overline{V}_S|B\rangle = B_1 s_{zz} + B_2\left(s_{xx} + s_{yy}\right) + 2B_3 s_{xy} + 2B_4\left(s_{yz} - s_{zx}\right) + \Delta \qquad (4\ 10)$$

where Δ is the energy separation between the observed excited state, A and the unobserved excited state, B From the character table for monoclinic I, the only terms of the Hamiltonian which can mix A and B states are those which transform with only S_{YZ} and S_{XZ} terms (table 2 6) Calculating all the S_{ij} values for the twelve possible orientations in monoclinic I symmetry (Appendix C) reveals only the S_{YZ} tensor component is zero for stress applied in the <111> direction and non-zero for stress applied in the <001> and <110> direction Therefore it can be concluded that the upper excited state is B as the mixing of the A and B states is zero under <111> stress and the interaction terms of the matrix are of the form S_{YZ} This stress tensor must be transformed from defect co-ordinates to crystal co-ordinates to determine the off-diagonal elements of the matrix Considering defect 1 in table 2 2

$$X = 00\overline{1} \qquad Y = \overline{1}10 \qquad Z = 110 \qquad (4\ 11)$$

the crystal co-ordinates are

$$x = 100 \qquad y = 010 \qquad z = 001 \qquad (4\ 12)$$

and the defect co-ordinates expressed in terms of crystal co-ordinates are

$$X = -z \qquad Y = \frac{-x+y}{\sqrt{2}} \qquad Z = \frac{x+y}{\sqrt{2}} \qquad (4\ 13)$$

The tensor S_{YZ} can now be rewritten as

$$S_{YZ} = \tfrac{1}{2}\left(S_{yy} - S_{xx}\right) \tag{4 14}$$

and the interacting terms of the matrix are

$$\langle A|\bar{V}_s|B\rangle = \langle B|\bar{V}_s|A\rangle = W\left(S_{yy} - S_{xx}\right) \tag{4 15}$$

The general form of the matrix for an A to B transition at a monoclinic I site with an unobserved interaction B state has been discussed This matrix was extended to include both the α_2 and α_3 zero-phonon lines as A to B transitions with an unobserved higher energy B state This matrix takes the form

$$\begin{array}{c|ccc}
 & \alpha_2 & \alpha_3 & \alpha_{FL} \\
\hline
\alpha_2 & \langle\alpha_2|\bar{V}_S|\alpha_2\rangle & \langle\alpha_2|\bar{V}_S|\alpha_3\rangle & \langle\alpha_2|\bar{V}_S|\alpha_{FL}\rangle \\
\alpha_3 & \langle\alpha_3|\bar{V}_S|\alpha_2\rangle & \langle\alpha_3|\bar{V}_S|\alpha_3\rangle & \langle\alpha_3|\bar{V}_S|\alpha_{FL}\rangle \\
\alpha_{FL} & \langle\alpha_{FL}|\bar{V}_S|\alpha_2\rangle & \langle\alpha_{FL}|\bar{V}_S|\alpha_3\rangle & \langle\alpha_{FL}|\bar{V}_S|\alpha_{FL}\rangle
\end{array}$$

where the diagonal elements take the form

$$\langle\alpha_2|\bar{V}_S|\alpha_2\rangle = A_1 s_{zz} + A_2\left(s_{xx} + s_{yy}\right) + 2A_3 s_{xy} + 2A_4\left(s_{yz} - s_{zx}\right) \tag{4 16}$$

$$\langle\alpha_3|\bar{V}_S|\alpha_3\rangle = A_1^1 s_{zz} + A_2^1\left(s_{xx} + s_{yy}\right) + 2A_3^1 s_{xy} + 2A_4^1\left(s_{yz} - s_{zx}\right) + \Delta \tag{4 17}$$

$$\langle\alpha_{FL}|\bar{V}_S|\alpha_{FL}\rangle = B_1 s_{zz} + B_2\left(s_{xx} + s_{yy}\right) + 2B_3 s_{xy} + 2B_4\left(s_{yz} - s_{zx}\right) + \Delta \tag{4 18}$$

Δ is the energy separation between the zero-phonon line and the minimum energy line α_2 The interaction terms equal $W\left(S_{yy} - S_{xx}\right)$, where W is the interaction element between the forbidden level and the zero-phonon lines There are no interactions between α_2 and α_3, thus $\langle\alpha_2|\bar{V}_S|\alpha_3\rangle$ and $\langle\alpha_3|\bar{V}_S|\alpha_2\rangle$ are set equal to zero From the low stress regime initial values for the parameters A_1, $A_1{}^1$ of the observed states were calculated No initial values for the parameters B_1, B_2, B_3 and B_4 of the unobserved state were obtained from the experimental data, but as a first approximation they were initialised to similar parameter values as for the α_3 zero-phonon line The parameters of the matrix were optimised using TRANID (McCarren *et al* , 1994) and figure 4 29 shows the data points and theoretical fit to the lines using the stress parameters listed in table 4 9 The fit obtained where the unobserved level is placed 6 meV above the α_2 zero-phonon line is in good agreement with the observed splitting of the zero-phonon lines

In the <001> direction the α_2 zero-phonon line did not split Intensity measurements indicated that two stress induced components could potentially overlap From the best fit, stress parameters A_1 and A_2 are equal such that only one line is observed at low stresses As the stress increases the lines begin to split due to their interaction with the unobserved excited level The two split components are close together, a line separation of ~ 0 6 meV compared with a line width of ~ 0 5 meV at 150 MPa The stress parameters of the forbidden state cannot be confirmed as no experimental data was available for the state

α_2 Stress Parameter (meV/GPa)		α_3 Stress Parameter (meV/GPa)		α_{FL} Stress Parameter (meV/GPa)	
A_1	-10 0	A_1^1	-20 0	B_1	-35 0
A_2	-10 0	A_2^1	-9 5	B_2	-20 0
A_3	-24 4	A_3^1	-26 3	B_3	-27 4
A_4	5 5	A_4^1	6 4	B_4	7 0

Table 4.9 Stress Parameters for group III, α_2 and α_3 zero-phonon lines obtained using TRANID. The unobserved level is estimated to be ~ 6 meV above the α_2 line and the interaction term, $W = 10$ meV/GPa.

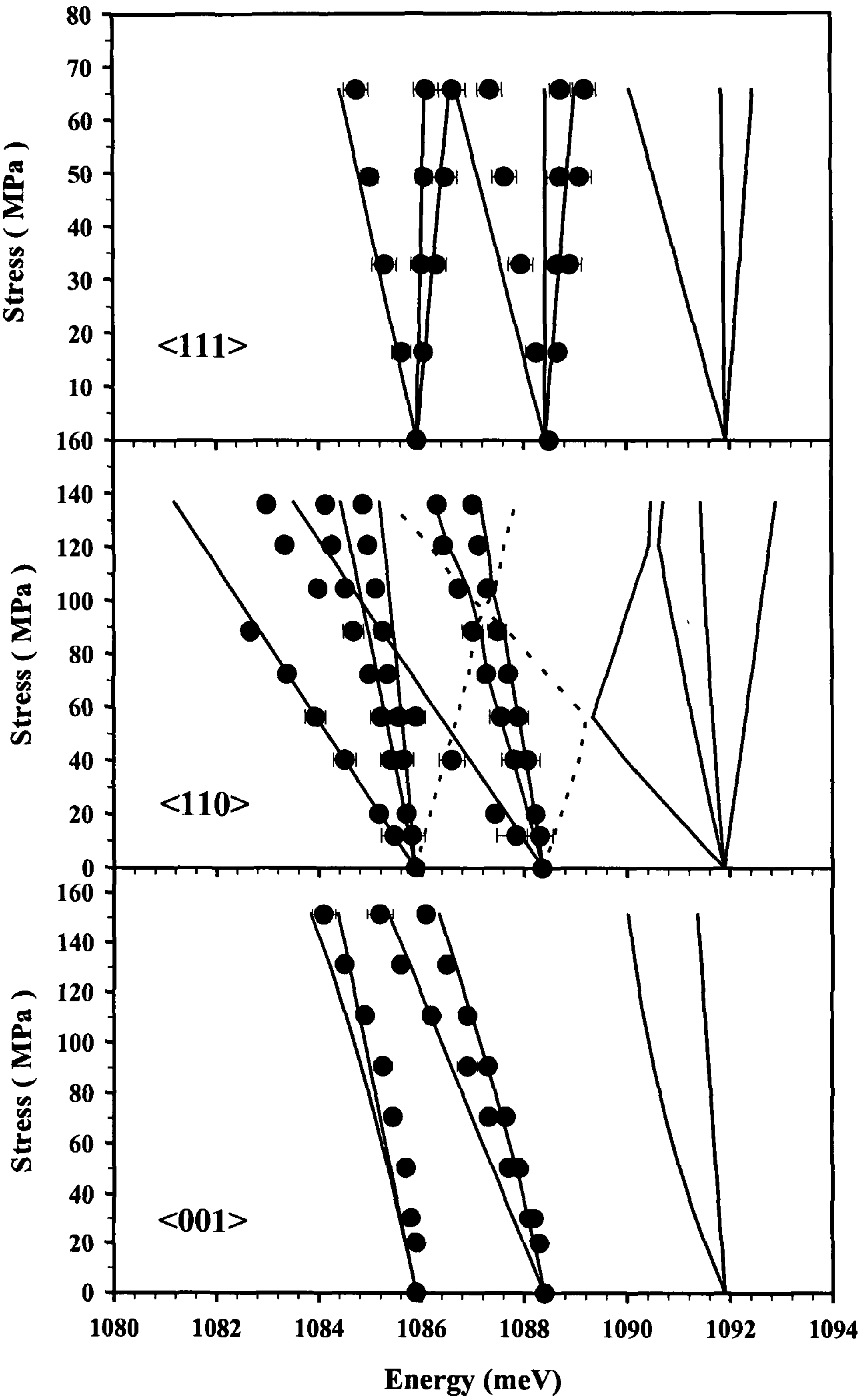

Figure 4.29 Splitting of α_2 and α_3 under <001>, <111> and <110> stress. Points show data, lines are fits to the data with parameters listed in table with an interaction at ~ 6 meV above α_2 line. The dotted line under <110> stress is the unobserved fourth stress-component obtained from the fit.

4.5 Conclusions

In the preceding sections we have shown that almost all of the stress-induced effects in the luminescence spectrum of groups I, II and III can be explained by trigonal and monoclinic I symmetry Spectra recorded at low temperatures indicate that the group I, A zero-phonon line is due to transitions between A and E states at a trigonal defect In the <100> direction at high stress, the shift rate of the line was no longer linear indicating an interaction with a higher energy state Spectra recorded at higher temperatures indicate this interaction is probably due to the highest energy zero-phonon line E For all the directions of stress all of the luminescence lines show splitting which is characteristic of an A to E transition at a trigonal centre Due to the limited data available to describe the upper excited states there is at present no estimation of their stress parameters However, at low stresses the shift rates of zero-phonon lines B, C and D are similar to the shift rates of A indicating the stress parameters should be equivalent

The high number of adjacent zero-phonon lines of group II has led to difficulties in determining the symmetry of the defect Since the spectra can become very complicated when stress is applied it is not always possible to identify the many components and in the <110> case it became very difficult to unambiguously identity the components A fit to one of the most intense zero-phonon lines H has revealed the transition can be tentatively assigned as due to a transition between A and E states at a trigonal defect To establish this symmetry assignment firmly, experiments at ~ 2 K should confirm the number of components for each stress direction This will be one important future study, but several problems associated with this very low temperature must be taken into consideration At 2 K only the lowest energy zero-phonon line will be observed, but at this temperature the intensity of the line is weak As stress is applied the line will split into several components with very low intensity and very high resolution spectra to reduce background luminescence and noise considerations will be necessary At present from the data obtained interaction effects appear to be due to zero-phonon lines H or J The limited data available to describe the curvature of the stress components and excited states means at present the matrix to describe all components of group II cannot be solved

The stress-split components of the higher energy zero-phonon lines α_2 and α_3 of group III were studied and measurements indicate the transitions are A to B transitions at a monoclinic I defect The α_1 line could not be studied due to overlap with β_3 at high temperatures and due to the low intensity of the stress-split components at low temperatures While the fits obtained are in agreement with the experimental data there are several unanswered questions The shift rates and splitting of α_2 and α_3 are equivalent in the <111> and <110> directions Why should the α_2 components under <001> stress be so different from the α_3 components? The fit in the low stress regime is consistent with the observation of two components for α_3 and only one line for α_2 under <001> stress Preliminary measurements of α_1 at very low stress indicate the line splits into two under <001> stress, only when there is conclusive data to confirm the behaviour of this zero-phonon line as a function of stress can we identify the symmetry of this defect unambiguously There is clear experimental evidence of the excited states of the defect interacting with another higher-lying state The absence of any stress induced interaction in the <111> direction indicates the unobserved interaction state is a higher energy B state Table 4 10 summarises the stress parameters found for each defect

	Group I	Group II		Group III	
Stress Parameter (meV/GPa)	A	F	Stress Parameter (meV/GPa)	α_2	α_3
A_1	-6 2	-15 5	A_1	-10	-20
A_2	-11 8	9 1	A_2	-10	-9 5
B	0	-10 3	A_3	-24 4	-26 3
C	2	0	A_4	5 5	6 4

Table 4.10 Stress parameters for the minimum energy lines of groups I and II for trigonal symmetry and for monoclinic I group III zero-phonon lines, α_2 and α_3.

References

Daly S E, Henry M O , Freitag K and Vianden R , J Phys Condens Matter **6,** L643-L650, (1994)

Davies G , Canham L and Lightowlers E C , J Phys C Solid State Phys , **17,** L173-L178, (1984)

Henry M O , Campion J D , McGuigan K G , Lightowlers E C , do Carmo M C and Nazare M H , Semicond Sci Technol , **9,** 1375-1381, (1994)

Hughes A E and Runciman W A , Proc Phys Soc , **90,** 827-838, (1967)

Kaplyanskii A A , Opt Spectrosc **16,** 329, (1964a)

Kaplyanskii A A , Opt Spectrosc **16,** 557, (1964 b)

McCarren A L , Ruskin H J , McGuigan K G and Henry M O , IEE Proc Sci Meas Technol , **141,** 185, (1994)

McGlynn E , Henry M O , McGuigan K G and do Carmo M C , Phys Rev **B54,** 14 494-14 503, (1996)

Mohammed K , Davies G and Collins A T , J Phys C Solid State Phys , **15,** 2779-2788, (1982)

Nazare M H , Duarte A J , Steele A G , Davies G and Lightowlers E C , Mater Sci Forum , **83-87** , 191-196, (1992)

Singh M , Ph D thesis, Kings College London, (1992)

Chapter Five

Isotope Substitution and Magnetic Field Perturbation

5.1 Introduction

In the previous chapter, the symmetry of groups I, II and III were determined In this chapter, the three groups will be investigated further by isotope substitution and magnetic field perturbation experiments To gain an insight of the actual chemical constituents of the defect isotope substitution experiments of the most likely candidates, cadmium and lithium were undertaken The results presented below have established the involvement of cadmium in all three groups and the involvement of lithium in group II The second part of this chapter examines magnetic field perturbation studies, which can reveal information about the spin states of defects The magnetic field perturbations have indicated spin triplet and singlet states for all three groups

5.2 Isotope Studies

Cadmium was suggested as one of the most likely candidates of the three defects as they were first reported after a study of the decay characteristics of radioactive ^{111}In, of which cadmium is the daughter product (Daly *et al*, 1994) Annealing investigations, with a high temperature anneal of cadmium doped silicon in close proximity to a lithium pellet seems to indicate that lithium is favourable for the defects, enhancing their formation Direct proof that cadmium and lithium are incorporated in the centres can be obtained by a corresponding isotope shift

For cadmium isotope substitution studies, isotopes samples of ^{106}Cd and ^{116}Cd were used, implanted either separately into different wafers or together for dual implant studies The total dose of the single isotope samples was ~1 x 10^{14} cm^{-3} while the total dose of the dual implanted samples was 2 x 10^{13} cm^{-3} The lithium isotope samples were prepared in King's College London Four different types of starting materials were prepared

1 1000Ωcm FZ silicon with low [O] and [C] which had been gettered
2 ~60Ωcm n-type FZ silicon with low [O] and [C] ~ 2 x 10^{17} cm^{-3}
3 ~40Ωcm p-type CZ silicon with [O] ~ 1 x 10^{18} and [C] ~ 1 x 10^{15} cm^{-3}
4 ~100Ωcm n-type CZ silicon with [O] ~ 1 x 10^{18} and [C] ~ 1 x 10^{17} cm^{-3}

Four samples of each type were prepared, Cd alone, Cd + ^{7}Li, Cd + ^{6}Li and Cd + ^{6}Li + ^{7}Li The samples were diffused with cadmium at ~ 1100°C for 3h All samples were then coated with lithium (suspended in oil) and were heated to 200°C for 1h to drive off the mineral oil To drive in the lithium the samples were annealed at 400°C for 30min After an RCA clean to remove the lithium source the samples were heated at 600°C for 2h to evenly distribute the lithium and were then lapped and etched to remove surface damage The estimated lithium concentration was ~ 3 x 10^{15} cm^{-3} (Lightowlers, 1997) Further details of this diffusion technique can be found in Zhu (1998)

5.2.1 Group I - Cadmium isotope effects

In samples doped with ^{106}Cd instead of ^{116}Cd, isotope shifts in the zero-phonon lines and local mode, L^{1} were observed and thus the participation of cadmium in the centre was established Preliminary measurements, shown in figure 5 1 show the isotope shift in the zero-phonon lines is small ~ 0 1 meV, with the energy position higher for the lower mass Spectra shown in figure 5 2(a) recorded at 4 2 K at higher resolution, (0 15 cm^{-1}) show that the lowest energy zero-phonon line A, shifted by ~ 0 08 (± 0 02) meV when the mass was reduced from 116 to 106 amu (atomic mass unit) In the case of the dual implant sample a splitting and broadening of the line was observed as shown in figure 5 2(b) The observed lineshape was reconstructed from the superposition of two Lorentzian lines centred at the positions observed for the zero-phonon lines containing only one isotope The estimated relative concentrations of the isotopes ^{116}Cd ^{106}Cd in the dual implant sample was ~ 0 47 0 53 Assuming that two cadmium atoms are incorporated in the defect the observed lineshape could not be reproduced, so we conclude that the defect contains a single cadmium atom The previously reported A* line (section 3 4) observed on the low energy shoulder of the A line, experiences a shift of ~ 0 1 meV when the mass is varied from 116 to 106 amu, similar to the shift observed for the A line The energy position is higher for the lower mass with the isotope shift indicating cadmium involvement The line was not observed in the dual implant sample due to the broad nature of the A zero-phonon line Previously reported isotope shifts for the Cd$_A$ and Cd$_B$ defects have revealed shifts to higher energy of 0 11 and 0 09 meV respectively, when the isotopic mass was varied from 106 amu to 116 amu (McGlynn *et al*, 1996) This isotope behaviour of the group I zero-phonon lines will be discussed later in this section as similar effects were observed for groups II and III

The local mode L^1 energy from the A zero-phonon line was 8 10 (±0 05) meV for ^{106}Cd and 7 83 (±0 05) meV for ^{116}Cd, as shown in figure 5 1 The ratio of local mode frequencies for two different isotope masses can be related to the isotope masses by

$$\frac{\omega_1}{\omega_2}=\sqrt{\frac{m_1}{m_2}} \qquad (5\ 1)$$

This equation holds for an atom vibrating with respect to an otherwise static lattice The ratio expected for a pure cadmium vibrational mode is $\sqrt{106/116}$ = 0 956 and the ratio of the phonon energies is 0 966 This indicates L^1 is primarily due to the vibration of the cadmium atom with respect to the static lattice The data recorded confirmed the involvement of cadmium in local mode L^3, an energy shift of ~ 0 41 (± 0 3) meV was observed when the mass was varied from 116 to 106 amu If the vibration is due only to the vibration of the cadmium atom the expected isotope shift is ~ 1 38 meV The observed shift is ~ 30% of the expected shift for a pure cadmium-like vibration indicating the local mode vibration is only partly due to the vibration of the cadmium atom The clear cadmium isotope shift especially in the local mode L^1 unambiguously confirms the participation of cadmium in the group I defect

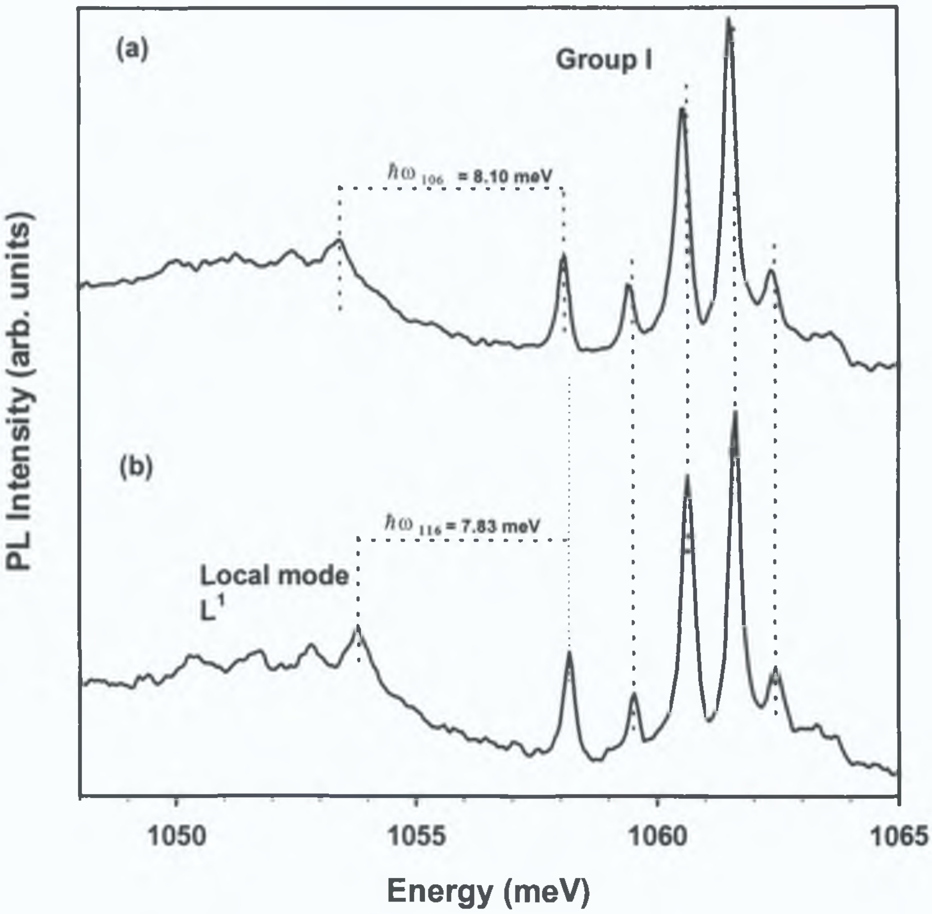

Figure 5.1 Cadmium isotope shifts on group I and L^1 mode at T~ 10 K. (a) ^{106}Cd and (b) ^{116}Cd. Resolution = 1 cm^{-1}.

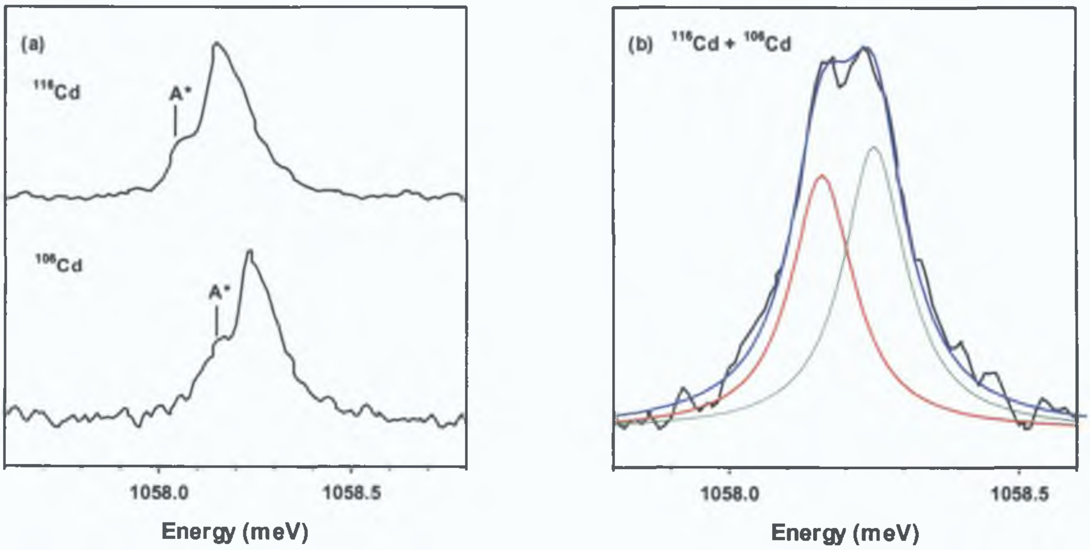

Figure 5.2 High resolution spectra (0.15 cm^{-1}) at ~ 4.2 K of group I minimum energy zero-phonon line A. (a) the isotope shift in the single isotope samples. (b) the width of A has broadened in the dual implant sample. The black line represents the spectrum and the fit (blue) is estimated from the ratio of the ^{106}Cd (red) and ^{116}Cd (green) isotopes.

5.2.2 Group I - Lithium isotope effects

The two stable lithium isotopes, ^{6}Li and ^{7}Li, were diffused either separately or together into Si Cd samples prepared by diffusion These samples received various annealing treatments to enhance the luminescence of the defects, unfortunately, the group I lines were not produced with sufficient intensity to enable isotope effects to be studied Circumstantial evidence as outlined in section 3 2 suggests that lithium is involved in the defect centre The defect formation is enhanced by the introduction of a lithium pellet and the observation of the exciton bound to the lithium donor at 1093 2 meV in samples along with all three groups indicates lithium is diffused into the samples during the high temperature anneal and quench However, at present, direct proof that lithium is incorporated in the centre has not yet been obtained and lithium may be a catalyst in the formation of the defects and not a constituent of the defect To confirm lithium involvement in this defect further samples doped with lithium isotopes and annealing experiments will need to be undertaken to enhance the luminescence of the centre

The involvement of cadmium in the group I defect has been proven The local mode L^1 is due to the vibration of a cadmium atom in an otherwise static lattice and the observed isotope shift of local mode L^3 indicates the vibration of the cadmium contributes to the vibration of the mode However it does not account for the full-expected isotope shift of the mode due to a pure cadmium-like vibration The involvement of lithium in the defect could not be confirmed due to unreliable data An estimate of the change in the silicon lattice parameter that is required to accommodate a Cd atom can be determined For a local mode, the shift Q_0 in equilibrium position is given in terms of the reduced mass μ of the mode and its frequency ω (Davies 1989)

$$Q_0^2 = \frac{2\hbar\omega S}{\mu\omega^2} \qquad (5\ 2)$$

where S is the Huang-Rhys factor for the mode The Huang-Rhys factor S_A for L^1 was estimated as ~ 0 55 in section 3 3 The Huang-Rhys factor for mode L^3 was not estimated due to the broad nature of the mode and the broad background luminescence Considering only local mode L^1, $\hbar\omega = 7\ 8$ meV, $S \sim$ 0 55 and taking the mass of the cadmium atom (116 amu) as the reduced mass, the value of Q_0 is estimated to be ~ 0 00963 nm This is equivalent to a change of ~ 4 1% of the silicon lattice parameter in the presence of this defect This deformation is sufficient to create a local strain field about the defect, which can be either electron or hole attractive In contrast, strains produced in a typical uniaxial stress experiment are < 0 2% of the silicon lattice parameter (Davies, 1989), clearly, the group I deformation is large in comparison

5.2.3 Group II -Cadmium isotope data

To ascertain if cadmium is a constituent of the group II centre, isotope samples doped with ^{116}Cd, ^{106}Cd and both isotopes were treated to optimise group II luminescence A very small isotope shift of ~ 0 06 (± 0 02) meV was observed as the isotopic mass was varied from ^{116}Cd to ^{106}Cd, with the higher energy shift for the lower mass as in the case of the group I isotope shift This is shown in figure 5 3(a) for the minimum energy zero-phonon line F at ~ 4 2 K The same spectral line is shown in figure 5 3(b) for a sample containing both ^{106}Cd and ^{116}Cd isotopes The line, which did broaden but did not split, was reconstructed from the superposition of the two lines centred at the positions observed in the single isotope samples The fit indicates only one cadmium atom is involved in the defect and the relative concentration of the isotopes, ^{116}Cd to ^{106}Cd was estimated to be ~ 30 70 When implanting the dual implant sample the nominal ratio of ^{116}Cd to ^{106}Cd was 50 50, the isotope ratio for group II is not 50 50 as nominally implanted Similar results were observed for Cd$_A$, Cd$_B$ and the 1026 meV defect (McGlynn *et al*, 1996) McGlynn suggests that as the Cd is being implanted it damages the crystal which can reduce or impede the successful implantation of further Cd In the case of group I (section 5 2 1) the ratio is 50 50 A tentative explanation of our result is that the different annealing temperatures during defect production may cause or vary the out-diffusion of Cd Further investigations are necessary to confirm this

The local modes of group II were not observed in the high resolution spectra recorded at 4 2 K In spectra recorded at ~ 10 K the local modes of group II, L^1 at ~ 7 3 meV and L^2 at ~ 15 8 meV were not observed due to overlap with the group I zero-phonon lines and the group II TA mode respectively. However, the L^3 mode at $\hbar\omega \approx 30$ meV was observed. The energy shift expected for L^3 due to a pure cadmium-like vibration in a harmonic-oscillator is $\left(\sqrt{116/106}-1\right)\hbar\omega \cong 1.39$ meV. The observed isotope shift is ~ 0.31 (± 0.2) meV which when compared to the expected shift of a cadmium vibration accounts for ~ 22% of the expected shift, indicating the local mode L^3 is only partly due to the vibration of a cadmium atom.

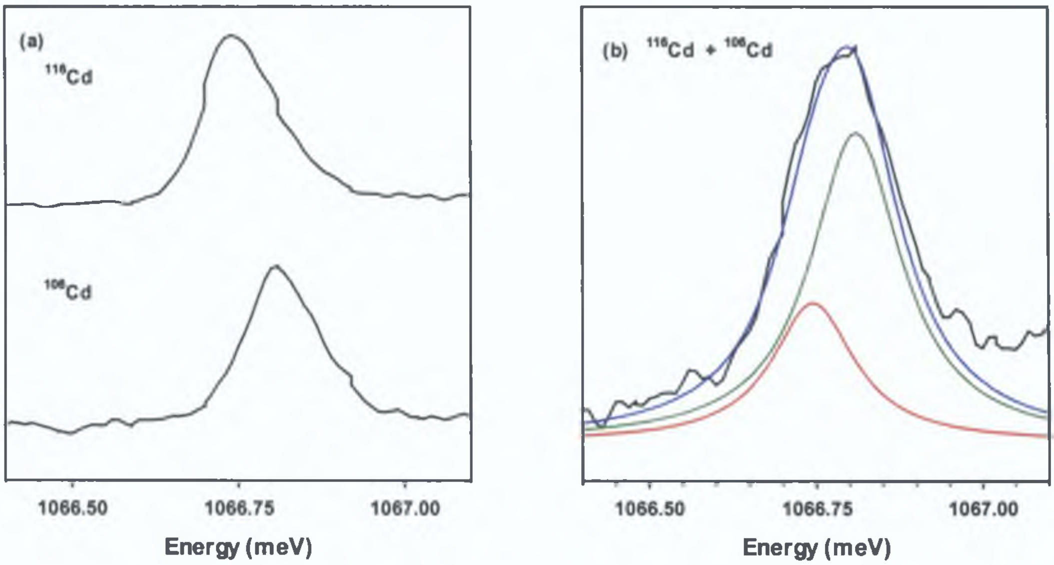

Figure 5.3 Photoluminescence spectra of the lowest energy group II line for samples diffused with (a) one cadmium isotope and (b) both lithium isotopes. In (b) the spectrum is represented by the full black line, the reconstruction by the blue line and position and estimated intensity ratio of the ^{116}Cd (green) and ^{106}Cd (red) lines are shown.

5.2.4 Group II -Lithium isotope data

Group II were the only lines produced in the lithium isotope samples with sufficient intensity to enable isotope effects to be studied. The data recorded show confirmation of the Li involvement in the centre. A shift of ~ 0.1 (± 0.01) meV in the position of the minimum energy zero-phonon line F at ~ 2 K is shown in figure 5.4(a). The higher mass isotope produces the higher energy line position. No splitting of the zero-phonon line was observed in the dual implant sample, but the line did broaden considerably and assuming the involvement of two lithium atoms occupying equivalent sites the lineshape was reconstructed, shown in figure 5.4(b). From the calculated fit, ^{7}Li is the predominant isotope in the dual implant sample as the ratio of isotopes is estimated to be 60 : 40. The isotope shift of ~ 0.1 meV to the high energy side for ^{7}Li is much smaller than the energy shifts observed for most lithium-related centres. Lithium isotope shifts in the range of ~ 1 meV have been reported for the Q, S and a Li_4-related centre (Canham, 1983, Canham *et al.*, 1985, Lightowlers *et al.*, 1984, Rodriguez *et al.*, 1997a, b). Recently lithium-related isotopes shifts in the range of ~ 0.7 meV have been reported for the L and H systems (Zhu, 1998).

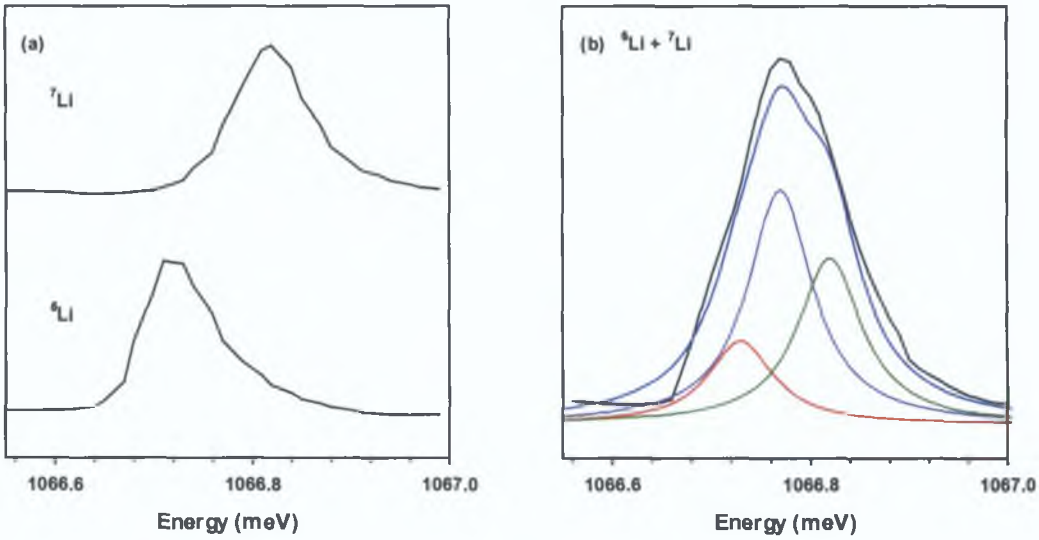

Figure 5.4 Luminescence spectra of the minimum energy line F, for samples diffused with cadmium and (a) one lithium isotope and (b) both lithium isotopes. In (b) the black line represents the spectrum. The blue line represents the fit, the red line ^{6}Li + ^{6}Li, the green line ^{7}Li + ^{7}Li and the purple line ^{6}Li + ^{7}Li.

The phonon sidebands of group II at T ~ 10 K for the ^{6}Li and ^{7}Li isotope samples are shown in figure 5.5. Several additional lines are observed and will be discussed below. The group II local modes L^1 and L^3 are clearly observed and local mode L^2 is observed close to the TA mode of the group. The change in phonon energy from the principal zero-phonon line J, to each local mode for each isotopic sample and the expected isotope shift for each mode due to the vibration of a lithium atom are shown in table 5.1. The L^1 mode does not involve lithium, as the phonon energy is the same for both isotopes. The change in phonon energy that is observed for the L^2 mode is approximately 28% of the expected vibration energy shift of 1.24 meV due to the vibration of a lithium atom. The shift of L^2 directly demonstrates the incorporation of the lithium in the mode, but the vibration of the mode is only partially accounted for by the vibrating lithium atom. The L^3 mode exhibits a large lithium isotopic shift of 2.3

(± 0 3) meV which is in excess of the full size of the expected vibration shift of 2 23 meV The evidence confirms mode L^3 is due to vibrating lithium in an otherwise static lattice

Local Mode	^{6}Li (meV)	^{7}Li (meV)	Phonon energy change (meV)	Expected energy change (meV)
L^1	7 53 (±0 02)	7 53 (±0 02)	0 0	0 6
L^2	15 09 (±0 05)	15 44 (±0 04)	0 35 (±0 07)	1 24
L^3	30 20 (±0 26)	27 90 (±0 2)	2 30 (±0 3)	2 23

Table 5.1 Phonon energy of the group II for the local modes in the lithium isotope samples. If the phonon shift equals the expected vibration shift the mode shift is due to the vibration of the lithium atom only.

The broad feature labelled $L^1 + L^3$ in figure 5 5 was previously ascribed to a combination mode of L^1 and L^3 (section 3 3 2) No isotope shift was observed at $L^1 + L^3$ as the lithium mass was varied but due to the broad nature of the feature it may not be possible to observe the energy change A zero-phonon line (labelled *) at ~ 1030 60 meV with a local mode at $\hbar\omega$ ~7 7 meV (L^*) is not lithium related as no isotope shift was observed as the isotope mass varied No details of this zero-phonon line have been reported in the literature The intensity of the Cu-related line at ~ 1014 meV observed in the ^{6}Li implanted sample is very weak This line is not observed in the ^{7}Li implanted sample, but a broad feature labelled U is observed centred at ~ 1014 meV This feature was not observed with such intensity before and is possibly related to the 1030 6 meV line A doublet at ~ 997 71 and 998 15 meV (labelled **) undergoes an energy shift of ~ 0 18 (± 0 04) meV as the isotopic mass is reduced from 7 to 6 amu indicating the lines are lithium related These lines at present have not been identified from the literature and no further study of these lines was undertaken The lithium related Q-centre (Li_4-V) at ~ 1045 meV and its associated isotope shift are also observed in the spectra but at very low intensity

The group II defect consists of one cadmium and two lithium atoms occupying equivalent sites The Huang-Rhys parameter for the first mode ($\hbar\omega$ = 7 3 meV) is 0 027 (section 3 3) and the calculated shift, Q_0 of the equilibrium position of the mode is ~ 0 00498 nm This ~ 2% change in the silicon parameter in the presence of this defect creates a strain about the defect site which can bind an electron or hole and is comparable to the shift obtained for the group I defect.

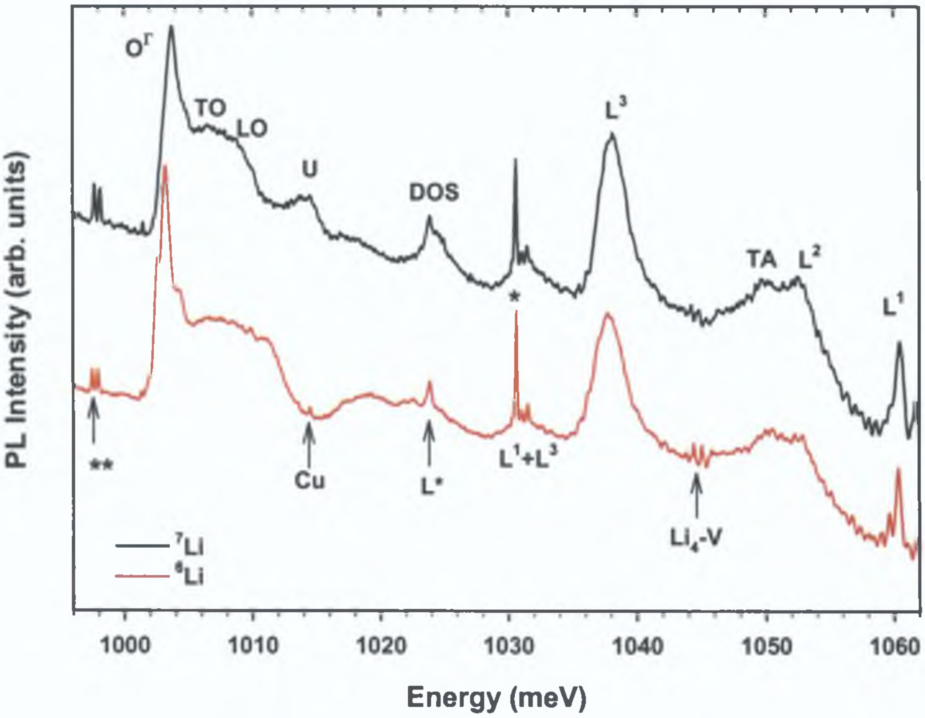

Figure 5.5 Comparison of the phonon sideband of group II in ^{6}Li and ^{7}Li isotope samples.

5.2.5 Isotope splitting data for group III - Cadmium

Cadmium isotope substitution studies have confirmed that cadmium is a constituent of this defect. In figure 5.6 a very small isotope shift is observed in the α_3 zero-phonon line. In (a) where the sample was implanted with ^{106}Cd the α_3 line moved to a lower energy by ~ 0.06 (± 0.02) meV, a smaller shift than observed in group I or II. Spectra of the dual implant sample (c) show the α_3 line is very slightly broadened. The small shift and broadening of the line is too small to indicate how many cadmium atoms are involved in the defect; the only conclusion that can be made is that cadmium is involved in the defect. The isotope shift is more clearly seen in the behaviour of the first local mode, as shown in figure 5.7. In the ^{106}Cd sample, the phonon energy between α_2 and β_2 is ~ 4.99 (± 0.04) meV; when the isotopic mass is increased to ^{116}Cd the phonon energy decreases to ~ 4.76 (± 0.05) meV. The ratio of ~ 0.953 is in excellent agreement with the value of 0.956 expected for a local mode due to the vibration of a cadmium atom against a static defect.

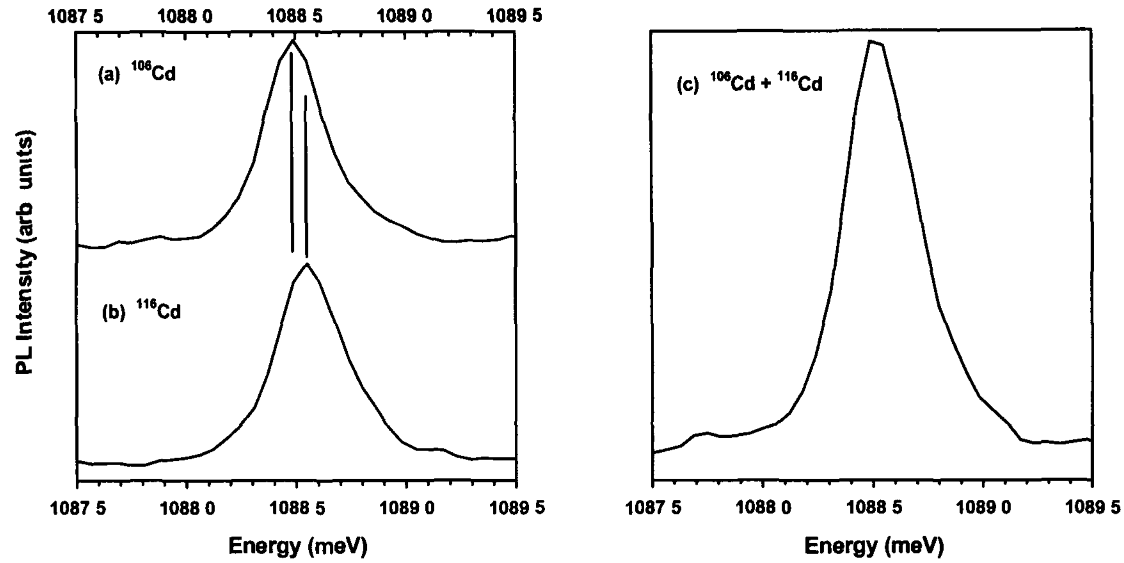

Figure 5.6 Cadmium isotope substitution of α_3 group III zero-phonon line.

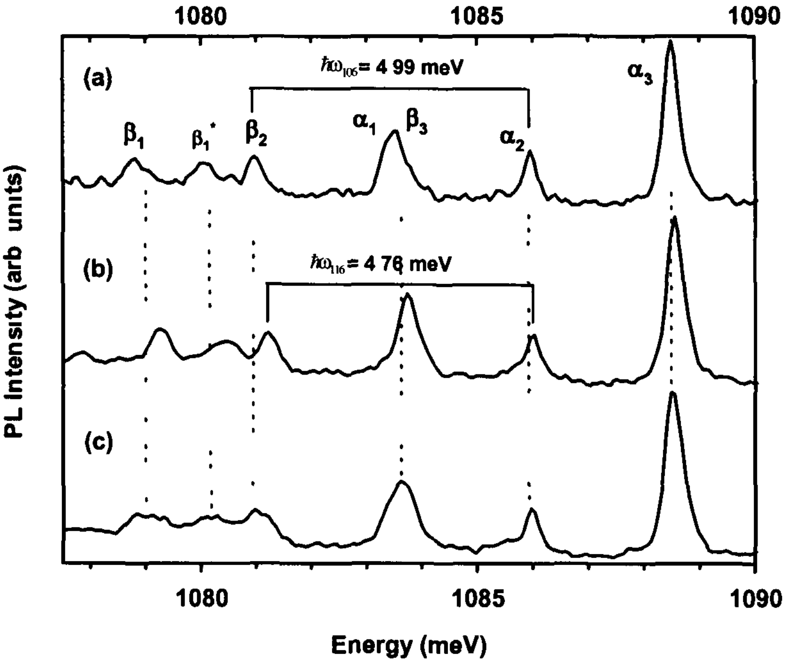

Figure 5.7 The effect of cadmium isotope substitution on the α zero-phonon lines and the first phonon β. (a) sample implanted with ^{106}Cd, (b) ^{116}Cd and (c) dual implant sample. The feature β_1^* was identified in section 3.6 as a (partially allowed) forbidden transition of group III.

The group III system was not observed in the lithium isotope samples and at present, from circumstantial evidence, the enhancement of luminescence from the defect by deliberate lithium contamination can only suggest lithium is a constituent of the defect or is a catalyst in the production of the defect. If we consider the complex to contain one cadmium atom then the reduced mass of this system is 116 a m u Using equation 5 2 and an average phonon energy of 9 19 meV and the calculated total value for *S* of 2 3 (section

3.3.3) the equilibrium position Q_0 for the defect is estimated as ~ 0.001 nm. This is equivalent to a change of ~ 0.6% of the silicon lattice parameter in the presence of this defect. This deformation can produce a strain field about the defect site, which can be attractive to either electrons or holes.

5.3 Zeeman Measurements

Uniaxial stress measurements can only reveal information about the orientational and orbital electronic degeneracy of defects. To reveal any spin degeneracy the three defects of interest were subjected to magnetic fields of up to 5 T. A <110> orientated sample was used as all three major crystallographic directions can be obtained by rotations in a <110> plane. The first section considers the effect of a magnetic field perturbation of group I. This centre consists of triplet-singlet combinations of states. This behaviour was also observed for groups II and III, which are discussed in the following sections.

5.3.1 Zeeman analysis for group I

Representative spectra of the effect of an applied magnetic field on the <110> direction at T ~ 10 K are shown in figure 5.8. There is neither a splitting nor shift in energy for the B, D or E zero-phonon lines, suggesting that the lines are due to transitions between singlet states. However, lines A and C are split into three clearly resolved components. Figure 5.9 shows the variation of the zero-phonon line energies with the increasing magnetic field. There is no variation in energy of the singlet lines (labelled s) and the linear splitting of the triplet lines (t_1 to t_6) reveals there are no magnetically induced interactions between the electronic states. Within the resolution available the triplet splitting is completely isotropic and any zero-field splitting is ≤ 0.1 meV.

The shift rate of the lower energy component of line A, labelled t_1 is smaller than for the higher energy component with corresponding g values of 1.89 (t_1) and 1.94 (t_3) respectively. The g values for the C line were found to be 1.86 (t_4) and 1.90 (t_6) for the low and high energy components, respectively. These values are slightly lower than those of the free electron and also those of groups II and III (next section). This behaviour is consistent with the coupling of two spin ½ particles to form a spin triplet and spin singlet separated by an exchange interaction energy These results are similar to the effect of a magnetic field perturbation on the singlet-triplet lines of the exciton bound to isoelectronic donor centres The orbital angular momentum of the tightly bound

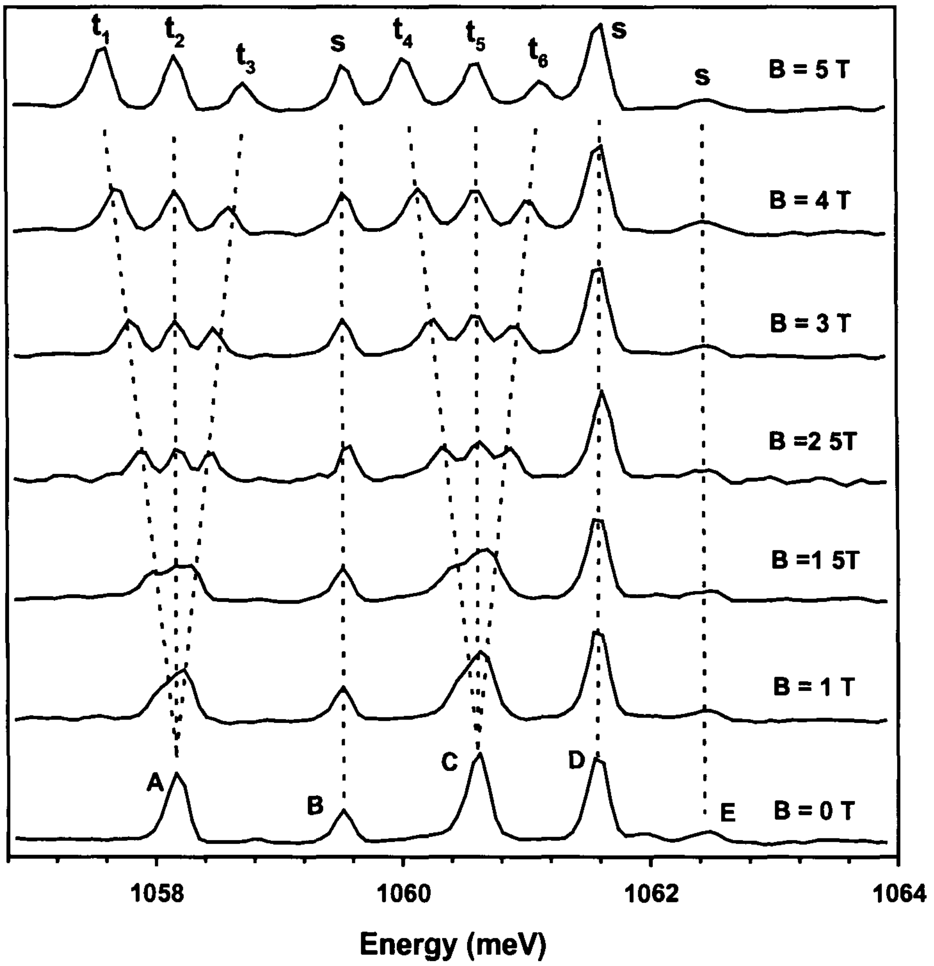

Figure 5.8 Spectra recorded for the group I zero-phonon lines with an increasing <110> magnetic field at a temperature of ~10 K.

hole of the isoelectronic donor is almost quenched so that the bound excitons have two spin like particles - this leaves only the spin state, s = ½ to interact with the loosely bound electron spin states, s = ½ These bound excitons have total angular momentum S = 0 and S = 1 and in the presence of a magnetic field the S = 1 triplet state splits into three components while the S = 0 singlet state is not affected This suggests the group I triplet states with $g \sim 2$ and the unperturbed singlets are most simply regarded as being formed from a spin-½ electron and spin-½ hole, the orbital angular momentum of the hole having being quenched by the axial nature of the defect

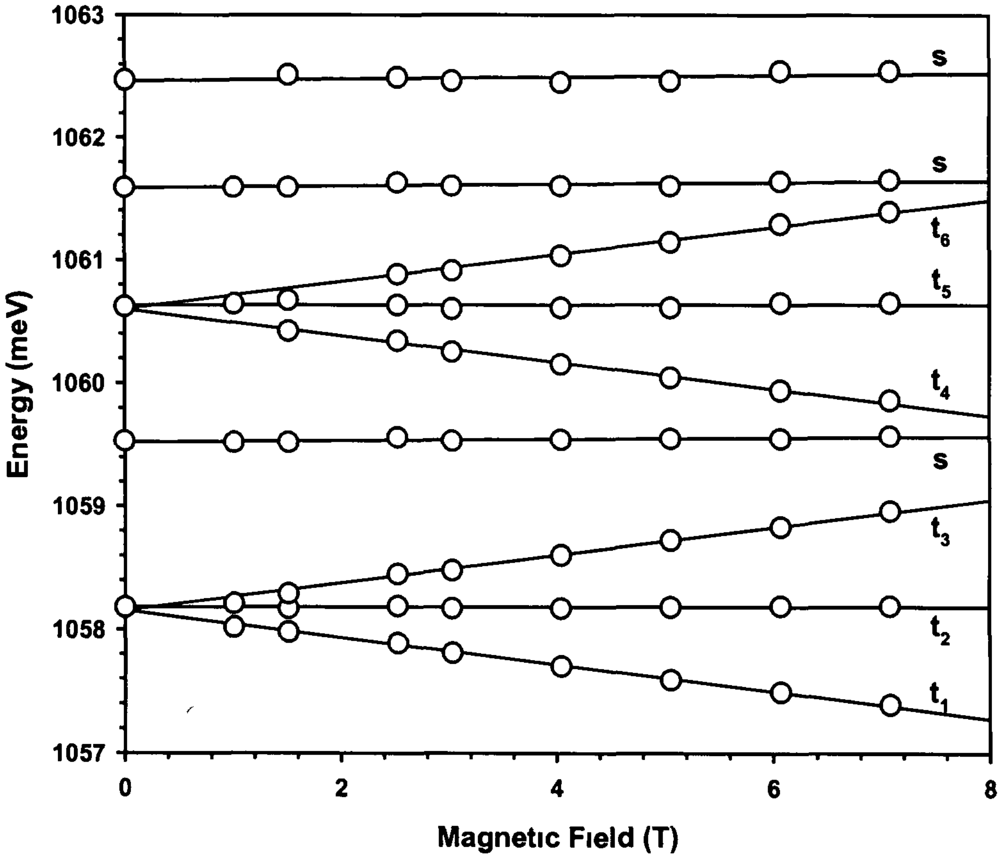

Figure 5.9 Variation of the Group I line energies with the increasing magnetic field along the <110> direction at T ~ 10 K.

The minimum energy zero-phonon line, A was studied at 4 2 K and within the resolution available a zero-field splitting ≤ 0 1 meV was observed, as shown in figure 5 10 This suggests there is a crystal field (T_d) or axial (low symmetry) field splitting similar to the zero-field splittings reported previously for lithium related defects With the application of a magnetic field the ~ 1044 meV Q_L zero-phonon line of the Q centre split into a spin-triplet with a small (< 0 1 meV) zero field splitting (Lightowlers *et al*, 1984) The higher energy lines of the Q centre, Q and Q_H did not split or show any broadening for magnetic fields up to 6 T

Figure 5 11 shows the intensity of the splitting components at 4 2 and 10 K in a magnetic field of 5 T, the relative intensities of the A zero-phonon line are subject to thermalisation The observed splitting therefore occurs in the initial state of the transition

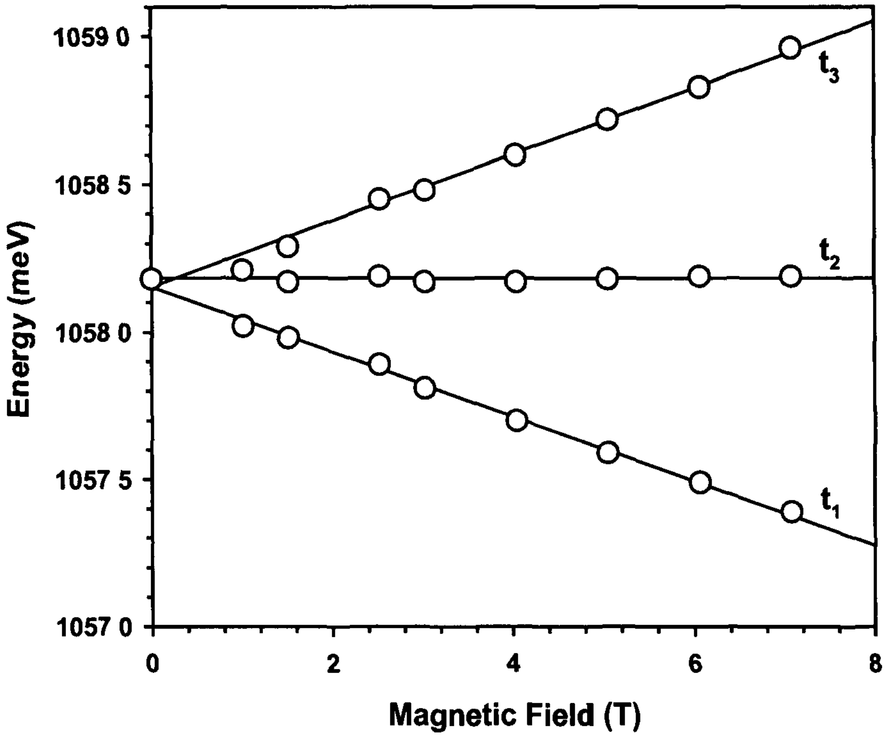

Figure 5.10 The isotropic triplet splitting of the lowest energy A line of group I with increasing magnetic field up to 7 T at a temperature of 4.2 K.

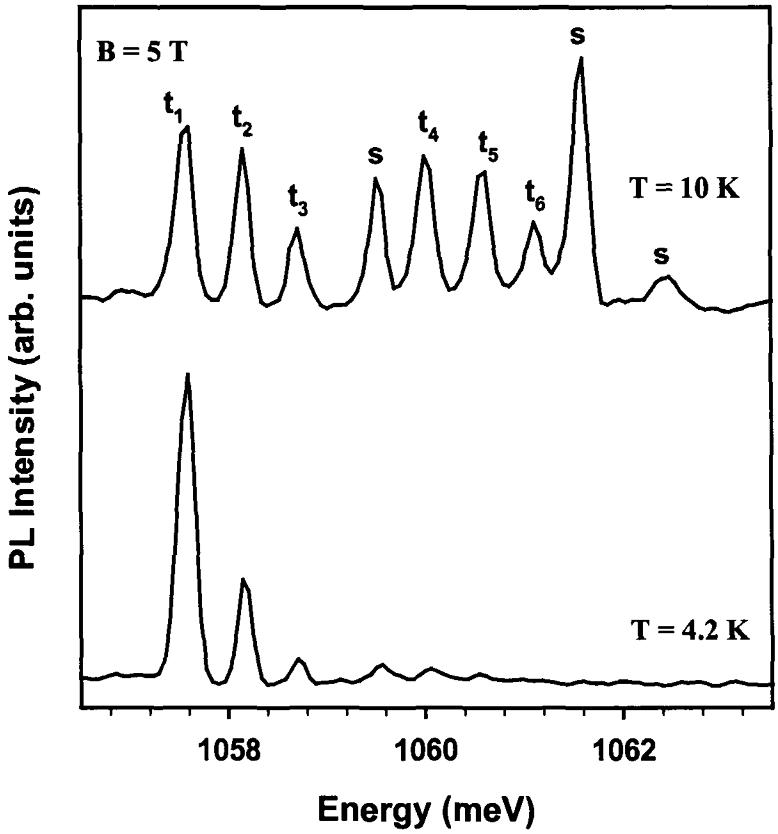

Figure 5.11 Temperature effect of the zero-phonon splitting pattern in a magnetic field of 5 T. The spectra are recorded at 4.2 and 10 K with a resolution of 1 cm^{-1}.

5.3.2 Zeeman analysis for group II

Figure 5 12 shows the effect of the magnetic field applied in the <110> direction on the group II lines at ~4 2 K Within the resolution available identical spectra were obtained for the <001> and <111> directions The lowest energy line F was clearly seen to split into three components (t_1 to t_3) under a magnetic field At high magnetic fields another split component was observed, labelled t_4 in figure 5 12, suggesting zero-phonon line G is spin-triplet Due to thermalisation effects and the low intensity of the G line, the higher energy split component was not observed as it overlapped with line H The higher energy zero-phonon lines do not split, shift or show any broadening under the application of a magnetic field Information on the spin of the highest energy zero-phonon line M was not obtained as the intensity was comparable to the signal to noise ratio obtained during the experimental work The variation of the energy of the lines with increasing magnetic field is shown in figure 5 13 The triplet splitting is linear indicating no magnetically induced interactions between the electronic states and a small zero field splitting of ≤ 0 1 meV is observed for the F line The low energy component of the F triplet has a g value of 2 07 whereas, the higher energy component, t_3 has a g value of 1 92 The higher energy zero-phonon line, G has a g value of 1 95 for the low energy split component with the higher energy component unobserved

The values of g close to 2 indicate that the hole orbital angular momentum is almost quenched so that the bound excitons have two spin-half particles These two combine to give the S = 1 (triplet) and S = 0 (singlet) state which are separated by the electron-hole exchange energy The quenching of orbital angular momentum readily occurs in semiconductors by strong axial low symmetry fields As a result singlet-triplet bound exciton states occur mainly at axial isoelectronic defects with a short-range hole attractive central cell potential This is the case for the group II defect

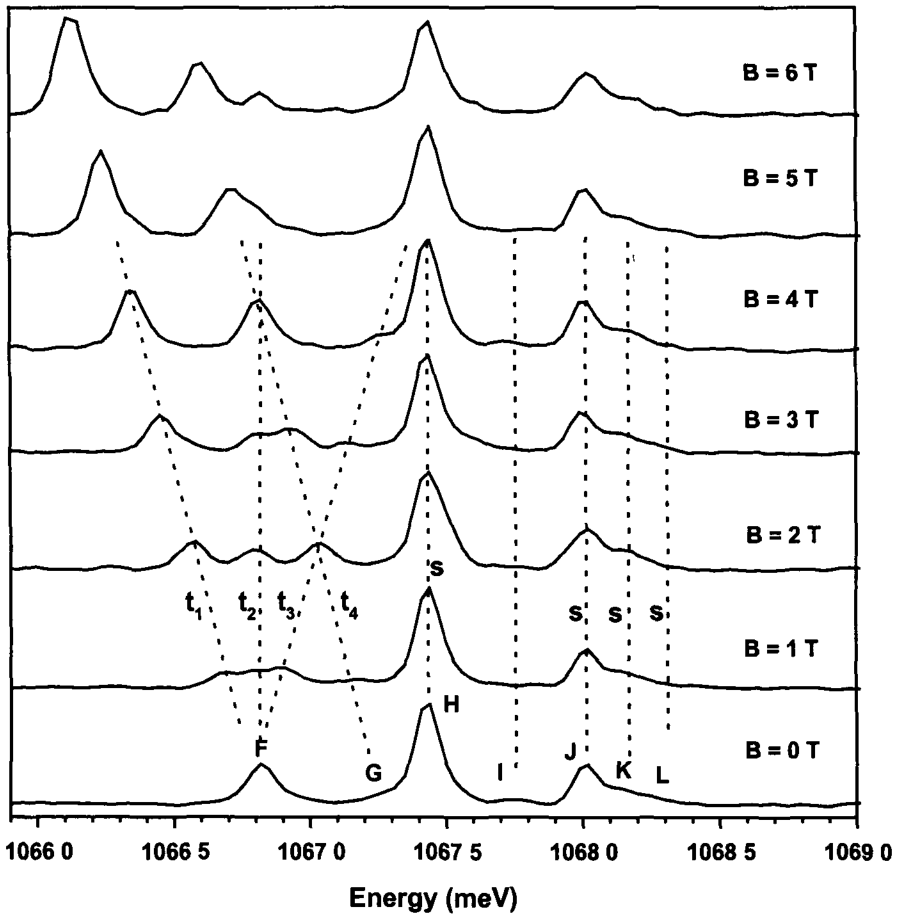

Figure 5.12 The variation of energy of the zero-phonon lines of group II with increasing magnetic field at T ~5 K.

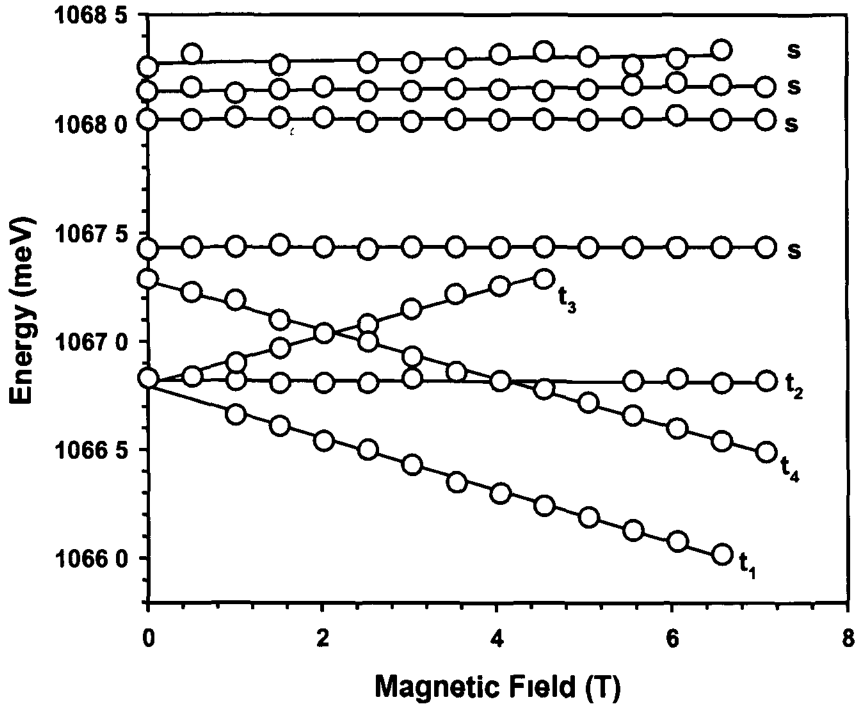

Figure 5.13 Triplet and singlet splitting of the group II zero-phonon lines at ~ 5 K.

The relative intensities of the split components of zero-phonon line F thermalise indicating the observed splitting occurs in the initial state of the transition The intensity of t_4, the lower energy component of zero-phonon line G increases with magnetic field Figure 5 14 shows this increase in intensity is linear as a function of the magnetic field squared, the intensity data are plotted only for values of $\vec{B}$ where the line was clearly observed in the spectra The transition probability is proportional to the square of the matrix element for the transition For a fixed magnetic field, $\vec{B}$ the Hamiltonian takes the form (Anderson E E , 1971)

$$H_O + g\mu_B m_j \vec{B} \qquad (5\ 3)$$

where μ_B is the Bohr magnetron, and g is the Landé g-factor Thus the rate of an induced transition is proportional to B^2 The mixing of t_4 with upper excited states in the applied magnetic field leads to the forbidden transition being allowed with the intensity variation proportional to the square of the magnetic field

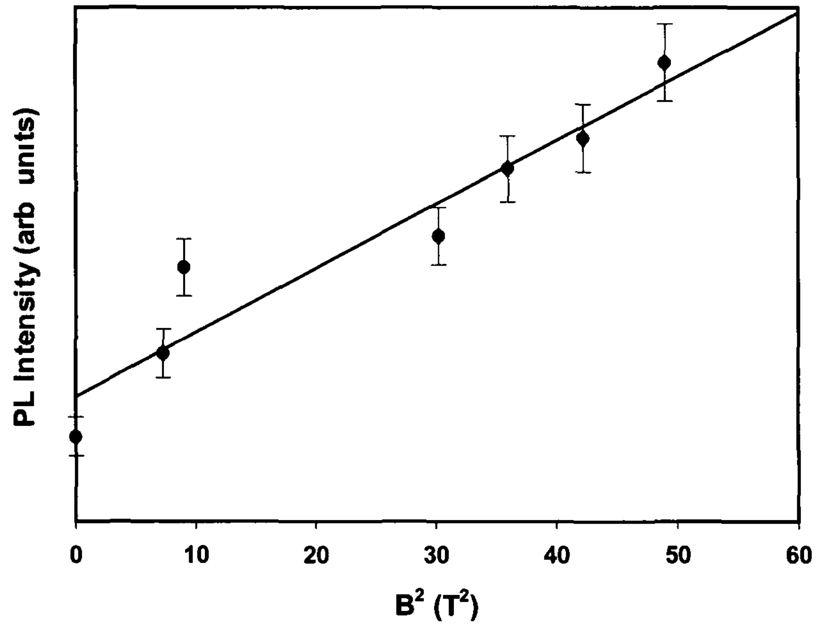

Figure 5.14 The variation in intensity of t_4 as a function of magnetic field squared.

5.3.3 Zeeman Studies for group III

Zeeman measurements were made on the group III, α_1 zero-phonon line at 4 2 K and on the higher energy zero-phonon lines α_2 and α_3 at 10 K Data for an applied magnetic field parallel to the <001> direction at 4 2 K for α_1 is shown in figure 5 15 Under the application of a magnetic field α_1 was split into three thermalising components, as shown in figure 5 16 and by orientation of the sample in the magnetic field, the triplet was found to be isotropic with no zero-field splitting observable The linear splitting of the triplet zero-phonon line indicates there are no magnetically induced interactions between the electronic states Shift rates of 0 116 and 0 117 meV/T for the low- and high-energy components yield *g* values of 2 00 and 2 02 respectively

The fan diagram of the higher energy, α_2 and α_3 zero-phonon lines studied at T ~ 10 K is shown in figure 5 17 The lines do not split or show any energy shift in any crystallographic direction in an applied magnetic field up to 5 T This indicates the higher energy zero-phonon lines are singlet states Also shown is the α_1 triplet state, however the higher energy component is not observed due to overlap with the β_3 phonon replica at this higher temperature

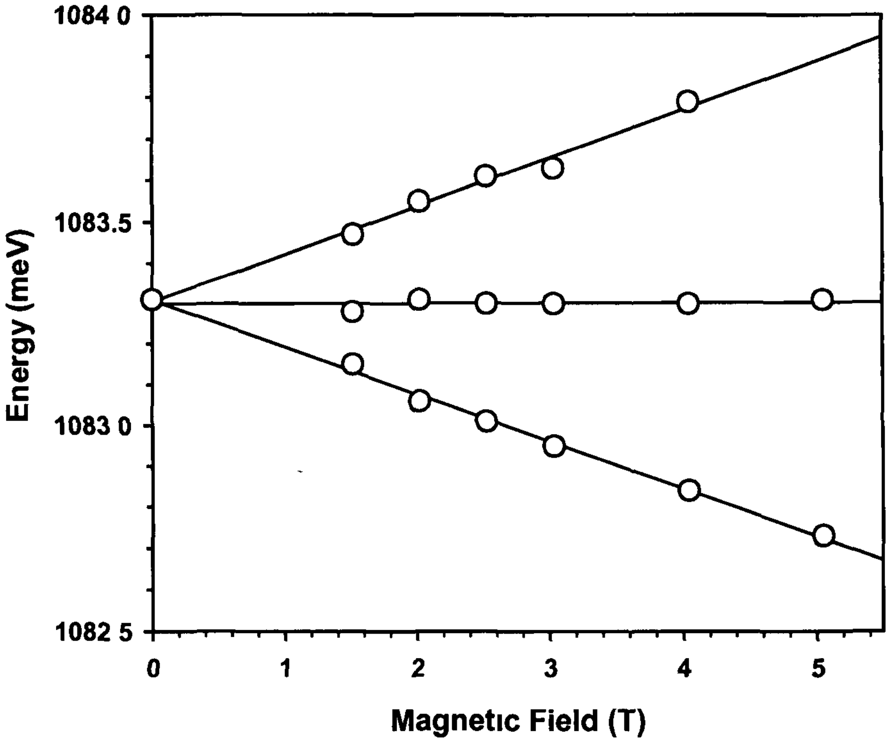

Figure 5.15 The magnetic field splitting of the α_1 line transition for a magnetic field along <001> direction at 4.2 K.

The above results are similar to the results for groups I and II and the singlet-triplet lines of the exciton bound to the isoelectronic donor centres For these centres, the orbital angular momentum of the hole is quenched leaving only its spin state (s = ½) to interact with the loosely bound electron spin (s = ½) (for details see the previous two sections) The α_1 line which originates in the triplet state is weak compared to the singlet line as it is forbidden from the selection rule $\Delta S = 0$ The second singlet state α_3 observed at higher energy may suggest there is a second singlet-triplet pair with the second triplet forbidden Zeeman measurements on the Q luminescence system at ~1045 meV have yielded similar results, a singlet triplet-pair with an additional higher energy singlet state (Lightowlers *et al*, 1984) Lightowlers and his co-workers have suggested a set of two singlet-triplet pairs possibly resulting from two singlet electron states being lowest in energy

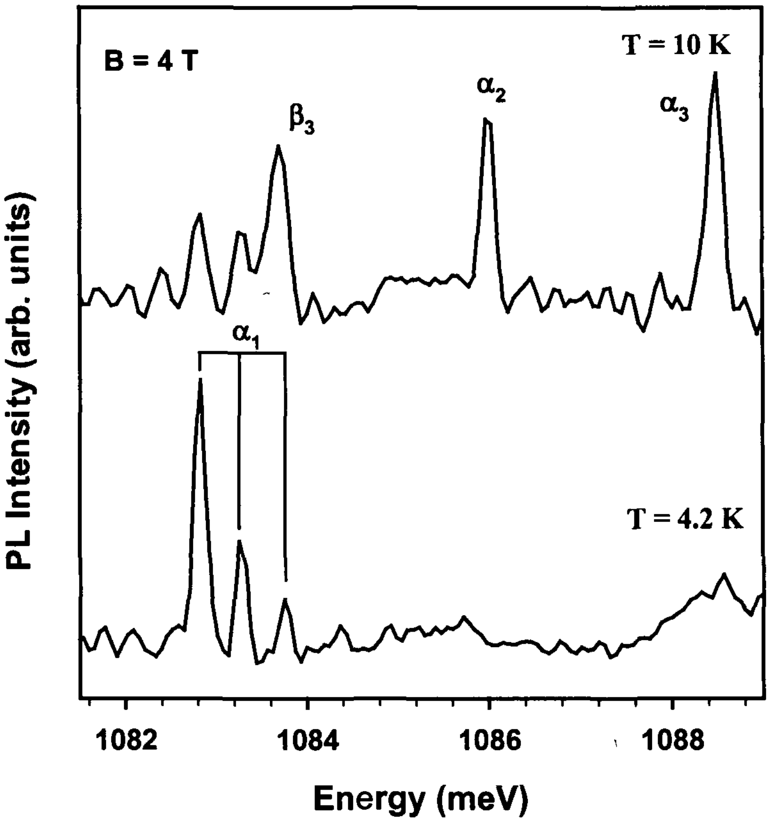

Figure 5.16 Comparison of the intensities of the magnetically split components of α_1 at 4.2 and 10 K in a magnetic field of 4 T.

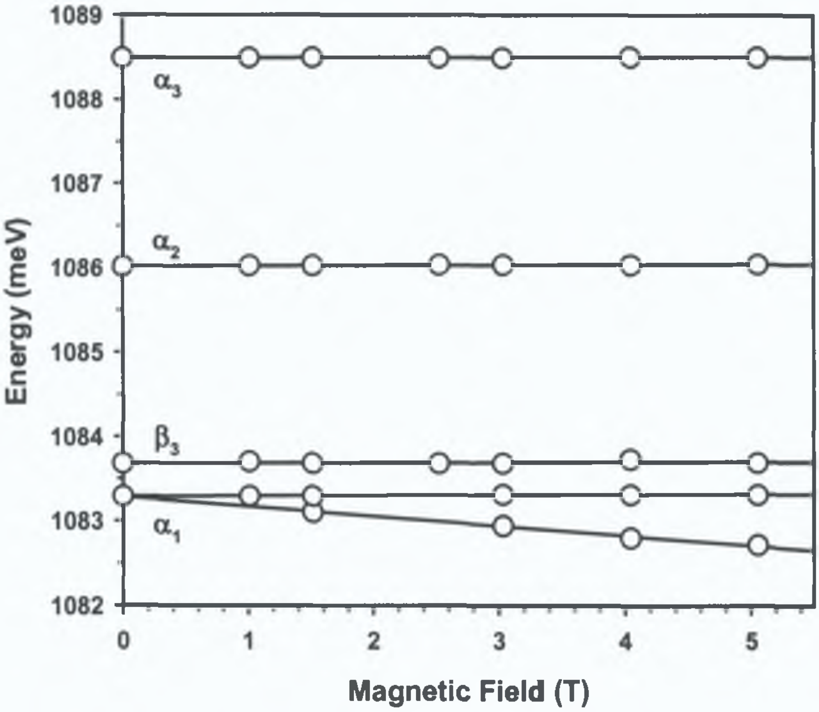

Figure 5.17 The α and β_3 zero-phonon lines of group III as a function of applied magnetic field. The solid lines are a best fit, with $g = 0$ for α_2, α_3 and β_3 indicating singlet states and a g value of 2 for the α_1 low energy triplet component.

5.4 Conclusion

The isotope substitution and Zeeman data presented provide evidence of the chemical constituents and information about the spin states of the defects. Both cadmium and lithium are present in the group II defect - one Cd atom and two Li atoms. It is not yet clear what the full microscopic structure of the group I and III defect complexes are. Cadmium isotope shifts have shown the involvement of cadmium in both defects, but the failure to observe these centres in the samples doped with ^{6}Li and ^{7}Li isotopes means that we have no direct proof of lithium involvement in these defects, the circumstantial evidence outlined (section 3.2) is strong.

In the case of groups I and II, doping the sample with ^{106}Cd instead of ^{116}Cd, the line positions shifted to higher energy for the lighter isotope. When the zero-phonon line is shifted to higher energy for a lighter mass this indicates that $k_e > k_g$, so that the vibrational mode for the ground state is softer than that of the excited state. This suggests that for cadmium dominated vibrations at these centres there is a softening of the forces between the cadmium and the surrounding crystal when the centre is in the excited state. For group III, the forces do not soften between the cadmium atom and the surrounding crystal and the zero-phonon lines shifts to higher energy for heavier mass The shift of the group II zero-phonon lines to higher energies for ^{7}Li compared to ^{6}Li shows the excited state force constant k_e is softer than that of the ground state

From the Zeeman data presented all three defects are similar as they consist of typical triplet-singlet combinations of states produced by isoelectronic centres in semiconductors All three centres may be isoelectronic donors, with the hole being the more strongly bound particle resulting in the quenching of the orbital angular momentum of the hole The two spin-like states interact to form bound exciton states with total angular momentum J = 1 and J = 0 The three defects appear to belong to the family of isoelectronic bound excitons having strong compressive axial strains, similar to the P line (Watkins *et al*, 1985) and the Q line (Lightowlers *et al*, 1984)

The magnetic field perturbation does not affect the highest energy lines for the group I and II systems, but splits the lower energy lines, A and C in the case of group I and zero-phonon lines F and G in group II into three components Within the resolution available all triplet splittings are completely isotropic with g values close to 2 Such an isotropic splitting indicates a total quenching of orbital angular momentum of the hole due to a large compressive axial strain In group III, the lowest energy zero-phonon line is a spin triplet with $g = 2$ and the second singlet state suggests there may be a set of two singlet-triplet pairs From thermalisation measurements the magnetic splitting occurs in the initial state for all triplets

In chapter six, the important results of each defect are summarised and discussed in detail Several models for the defects are considered and a variety of suggestions for future work are made

References

Anderson E E , “Modern Physics and Quantum Mechanics”, W B Saunders Company, (1971)

Canham L T , PhD thesis, University of London, (1983)

Canahm L T , Davies G and Lightowlers E C , in Proc 17th Intern Conf on the Physics of Semiconductors, edited by Chadi J D and Harrison W A , Springer-Verlag, New York, 737, (1985)

Daly S E , Henry M O , Freitag K and Vianden R , J Phys Condens Matter **6** L643-650, (1994)

Davies G , “The Optical Properties of Luminescence Centres in Silicon”, Physics Reports **176**, 3&4, (1989)

Lightowlers E C , Private Communication, (1997)

Lightowlers E C , Canham L T , Davies G , Thewalt M L W and Watkins S P , Phys Rev B **29**, 4517-4523, (1984)

McGlynn E , Henry M O , McGuigan K G and do Carmo M C , Phys Rev **B54**, 14 494-14 503, (1996)

Rodriguez F , Davies G and Lightowlers E C , Mater Sci Forum **258-263**, 635-640, (1997a)

Rodriguez F , Davies G and Lightowlers E C , Mater Sci Forum **258-263**, 411-416, (1997b)

Watkins S P and Thewalt M L W , Can J Phys 63, 1074-1082, (1985)

Zhu M , Ph D thesis, University of London, (1998)

Chapter Six

Discussion

6.1 Introduction

In this thesis three defects observed using photoluminescence in cadmium-doped silicon have been studied. Prior to this study, very little was known about these lines other than they appeared in samples implanted with radioactive ^{111}In ions after several half-lives (Daly *et al.*, 1994). The lines were tentatively assigned to the complexing of ^{111}Cd atoms with impurities in the crystal. When studying the samples after prolonged storage at room temperature, the three defects were not observed. This indicated that at least one of the constituents in the centres responsible was mobile already at room temperature. Since this is a well established property of lithium in silicon, the likelihood that all centres are related to centres that have both cadmium and lithium as constituents was explored in this thesis.

In an attempt to understand the optical properties of these three defects, photoluminescence spectroscopy in conjunction with isotope substitution studies and perturbation techniques of uniaxial stress and magnetic fields have been used. In this chapter we shall gather together all the results of the previous chapters and even though these results have been discussed in each chapter a model, which satisfies all of the observed behaviour of each defect, remains to be established. Groups I and II are very similar in nature and shall be discussed in the next section. The energy level structure deduced for group III indicates that both the initial and final electronic states are split - an uncommon occurrence for defects believed to be electrically neutral; this defect shall be discussed in detail in section 6.3.

6.2 Groups I and II

The group I system can be optimised in cadmium implanted silicon when subjected to a high temperature anneal at ~ 1000°C for 10 s followed by a rapid quench to room temperature and heating at 150°C for about 15 min For group II the optimal defect production temperature (post-quench) is ~ 100°C for 15 min Both groups are observed in FZ and CZ silicon Carbon and oxygen are generally more abundant in CZ silicon and as the groups are more intense in FZ rather than in CZ silicon it seems likely that the defects do not involve carbon or oxygen as constituents The groups were observed in silicon doped with either boron or phosphorous and thus seem to be independent of the common shallow donor and acceptor impurities These observations provide circumstantial evidence that lithium and cadmium are the only impurities involved in the defects Isotope substitution experiments have proven that both cadmium and lithium are present in the group II defect - one Cd atom and two Li atoms Cadmium is a constituent of group I but the involvement of lithium has yet to be proven unambiguously

6.2.1 Group I

The group I luminescence system consists of five zero-phonon lines and temperature dependence measurements have shown these transitions are from five excited state levels to the same final ground state The luminescence is observed up to ~ 40 K and an estimated thermal binding energy of ~ 10 meV suggests the exciton is captured as a pair The exciton once localised on the defect relaxes such that the primary particle is tightly bound and the secondary particle is loosely bound suggesting the centre is isoelectronic in nature The total binding energy of the A excited state is ~ 97 meV and we have found the lattice relaxation has a magnitude E_r ~ 87 (± 20) meV The experimentally estimated relaxation energy is a major contributor to the binding energy of the exciton of the group I centre and the exciton can be considered self-trapped

Within the limits of our uniaxial stress experiment, the pattern and magnitude of the stress induced splittings of all group I zero-phonon lines were identical Interactions between the highest energy zero-phonon line E and the lower energy lines was observed A model that can fit all of the observed splitting and stress induced interactions is still under development, however the group I luminescence centre has been assigned trigonal (C_{3V}) symmetry with transitions between A and E states We have shown from Zeeman studies that the lowest-energy excited state is a spin triplet and that the next highest state is a spin singlet This reveals that the orbital angular momentum of the deeply bound hole is quenched, giving for it s = ½ A second singlet-triplet pair was observed at higher energy This confirms the isoelectronic model proposed from temperature dependence measurements, the optical transition is between a loosely bound electron and a tightly bound hole, a pseudo-donor

6.2.2 Discussion

A Cd-Li-Li defect appears to be an obvious candidate for the isoelectronic centre in question Cd has a relatively low diffusion coefficient indicating that the Cd atoms occupies a substitutional site (Arifov *et al*, 1984), while Li is known to have a very fast diffusion rate in Si which indicates interstitial diffusion (Pell, 1960a, b) Therefore, if we assume that the defect consists of one Cd substitutional atom and two Li interstitial atoms a possible model would be that of the Cd and Li atoms forming an axial defect parallel to a <111> type axis The bonding between the Cd, Li and neighbouring Si atoms must produce an electrically neutral ground state However, confirmation that this centre contains lithium must await isotope experiments on the group I line system

As an isolated impurity, lithium is an interstitial donor in the silicon lattice We would expect lithium to behave as a very shallow donor which can be described by EMT (Kohn 1957) The central cell potential for the lithium interstitial donor is repulsive for electrons thus it seems more likely that the complex binds an exciton with a highly localised hole and an electron in a near-hydrogenic orbit The 1s manifold of a pseudo-donor will have in T_d symmetry three states A_1, E and T_1 Aggrawal proposed that the lithium interstitial donor in silicon has a inverted valley orbit splitting with the 1s(A_1) state lying 1 8 meV above the 1s(E+T_2) state as shown in figure 6 1 (Aggrawal *et al*, 1965) The E and T_2 states are assumed degenerate In the axial C_{3v} symmetry the T_2 level is split further into an A_2 and E state

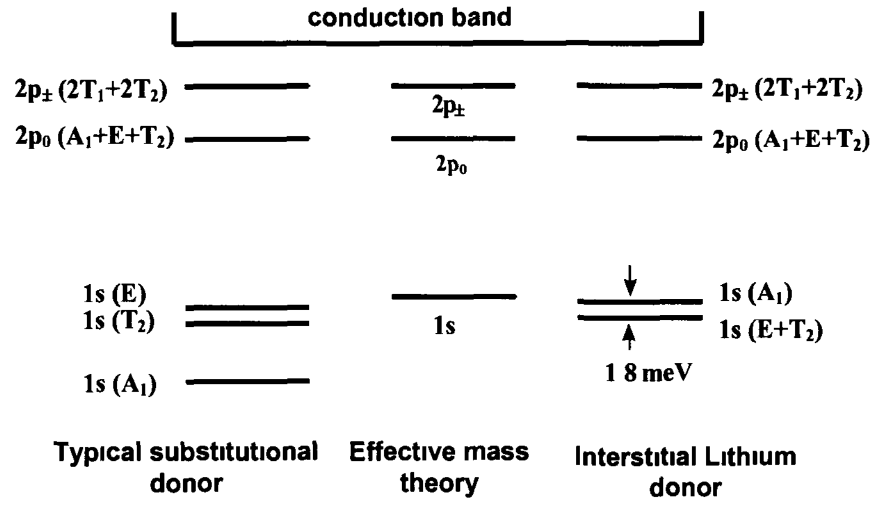

Figure 6.1 The energy level structure of typical substitutional donors compared with that of the interstitial donor.

The Hopfield-Thomas-Lynch model is often used to describe the binding of excitons to isoelectronic impurities (1966) For isovalent donors, a hole is trapped in a non-Coulomb short-range impurity potential of the isovalent complex A bound exciton forms through the long-range Coulomb interaction between the trapped hole and an electron A model based on the ideas of Morgan and Morgan (1970) and developed by Davies (1984) can predict the energy spacing and relevant luminescent intensities of the lowest bound exciton transitions for axial defects in silicon The axial nature of the isoelectronic defect can be represented by a uniform uniaxial internal stress of magnitude S_i (Davies, 1984) For centres with $S_i > 0$ (pseudo-acceptors) this leads to a compression of the defect and an extension of neighbouring silicon atoms Two pseudo-acceptors where the model has predicted the energy spacing and the effects of internal and external stress successfully are the ABC centre and the Be-pair (Davies, 1984) The centres which possess $S_i < 0$ are isoelectronic donors The calculated value of S_i for the 1045 meV defect (the Q-centre) is - 3 6 GPa and the binding energy is 100 meV, which is in close agreement with the electron-phonon relaxation energy (Davies, 1984) The model predicts the separation of the zero-phonon lines of the lowest-energy bound exciton states with two adjustable parameters the internal stress described by S_i and the electron-hole exchange energy, Δ.

The states are formed from a free hole taken from the k = 0 valence band maximum with angular momentum quantum number $j = \frac{3}{2}$ The split-off valence band hole states with k = 0 and j = ½ are included, these holes have an energy ξ = 44 meV larger than the energy of the $j = \frac{3}{2}$ states in silicon The electron states are formed from the conduction minima, found in silicon near the zone boundaries in the <001> direction There are twelve electron states, two spin states for each of the six minima They electron and hole combine to form the J = 1 and J = 2 orbital states when localised on a T_d centre if the electron and hole are bound by a potential weak relative to spin-orbit splitting ξ The J = 1 triplet state and the J = 2 quintet state are separated by the electron-hole exchange energy (Δ), with the J = 2 state being the lower

In the case of an isoelectronic donor ($S_i < 0$) a strong axial field produced by the centre quenches the angular momentum of the tightly bound hole Thus the hole behaves like a spin half particle and couples with the electron to form a spin-triplet, S = 1 state separated from a spin singlet, S = 0 state by energy Δ In group I magnetic field perturbations have revealed the lowest energy line A is a triplet state and B is a singlet state with energy separation Δ = 1 36 (±0 1) meV, and the higher energy triplet singlet states, C and D are separated by $\Delta \approx$ 1 (±0 1) meV Figure 6 2 shows the lower energy bound states as a function of internal stress for a <111> orientated defect in silicon for an electron-hole exchange energy of Δ = 1 36 meV

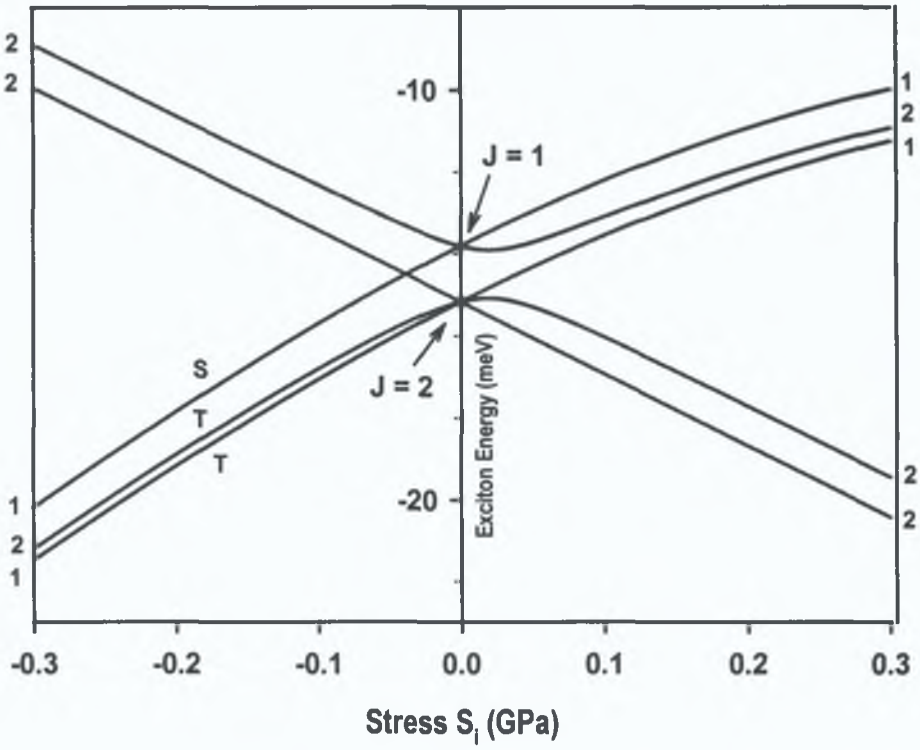

Figure 6.2 The lower bound exciton states as a function of S_i. The degeneracy of each exciton state is shown in the margin. For $S_i < 0$ the states which form the triplet-singlet pair are labelled T and S. Energy separation $\Delta = 1.36$ meV.

A procedure can be undertaken to obtain the best fit parameters for the internal stress (S_i) and the electron-hole exchange energy (Δ). In the group I system the energy spacing of the A-triplet and B-singlet lines is 1.36 meV and this was used as an initial value for the exchange energy. The values of the two parameters $\Delta = 1.5$ meV and $S_i = -0.12$ GPa in the model yield optically allowed transitions at 1.20 and 5.30 meV above the A line, compared to the measured values of 1.36 and 4.32 (±0.1) meV. A state is predicted 0.29 meV below A due to the zero-field splitting of S = 1 and transitions from this state are predicted to be forbidden. Spectra at high resolution revealed a zero-phonon line on the low energy side of A, labelled A^* at ~ 1058.05 meV (section 3.4), it is possible that this is the line predicted 0.29 meV below A, but at present this cannot be confirmed. Transitions from a doubly degenerate state predicted to lie ~ 4.1 meV above A are forbidden as these transitions are from an S = 1 state which are forbidden from the spin selection rule. Figure 6.3(a) shows group I zero-phonon lines at ~ 15 K where (b) shows the energy positions from zero-phonon line A of the predicted levels. The forbidden transitions are represented by the dotted lines.

The second triplet-singlet pair of group I (ZPLs C and D) are separated by Δ ~ 1 0 (±0 1) meV Setting S_i = -0 12 GPa the best fit to the data was obtained for Δ = 1 2 meV The predicted line positions from zero-phonon line C are shown in figure 6 3(c) In this case the forbidden transitions are predicted to lie 0 24 meV below and 4 14 meV above the C line and the allowed transitions at 0 95 and 5 09 meV above C

These calculations show that this model can predict the relative positions of the zero-phonon lines The internal stress is estimated as -0 12 GPa and the electron and hole interact with exchange energies of 1 5 and 1 2 meV The model predicts two levels, 5 3 meV above A and 5 1 meV above C but there is no evidence of these lines in luminescence studies The origin of zero-phonon line E, 4 32 meV above A is not determined from the model The negative sign of the internal stress indicates a compressive local equivalent stress

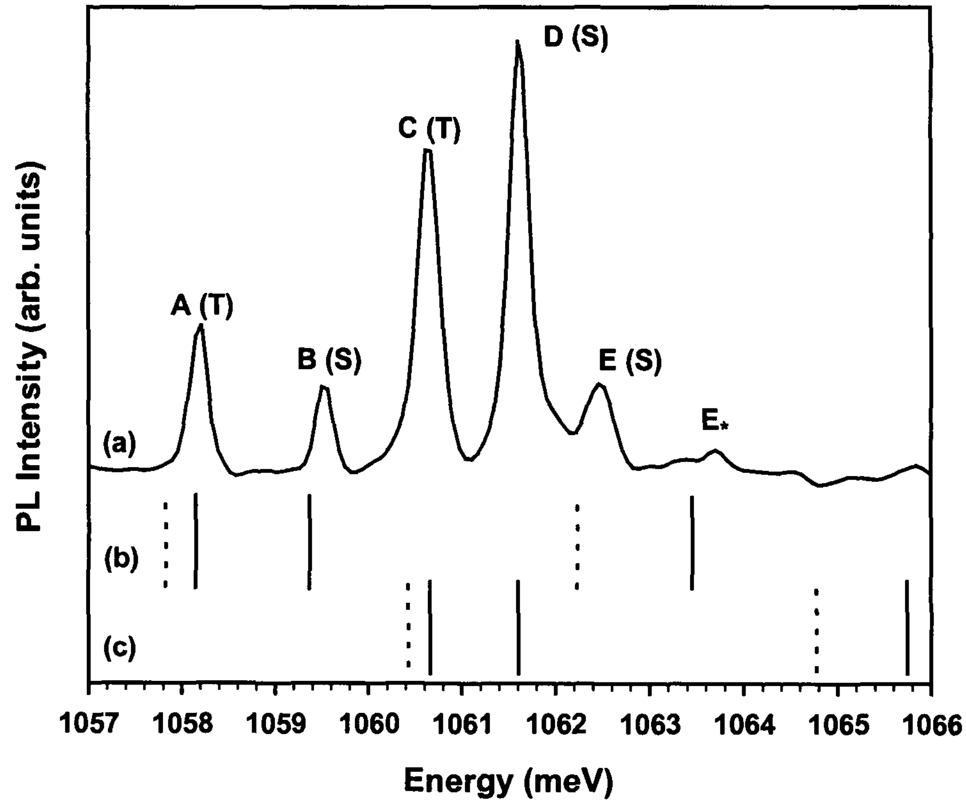

Figure 6.3(a) Group I ZPLs at T ~ 15K. Singlet (S) and triplet (T) states are indicated. Model prediction with internal stress S_i = -0.12 GPa and (b) exchange energy Δ = 1.5 meV. Energy spacing from ZPL A are shown by the vertical lines. (c) exchange energy Δ = 1.2 meV with energy spacing from C. The forbidden transitions are represented by the dotted lines.

For large values of S_l the optical transition from the triplet state is forbidden and as S_l tends to zero transitions from the lowest-energy exciton states are forbidden as they are from the J = 2 state. Figure 6.4(a) shows the ratio of the triplet to singlet transition probabilities as a function of the measured exciton binding energy (Davies, 1984). The exciton binding energy is the difference in energy between the singlet zero-phonon lines and the free exciton energy (1155.2 meV). The value of S_l can be determined from the intensity ratio of the triplet-singlet states. The measured ratios of the transition probabilities for the Y, Z, X, S and Q lithium-related defects at 1131, 1126, 1117, 1082 and 1045 meV respectively, are shown in figure 6.4(a). This graph has been extended to include data from the ratio of the transition probabilities of known singlet/triplet systems in silicon (Davies 1995). Points 2, 4, 6, 8 and 9 in figure 6.4(b) coincide with the X, Y, Z, S and Q lithium-related centres. The line in each graph shows the calculated intensity ratio assuming that the binding energy is produced by the perturbation by the local axial field on the hole.

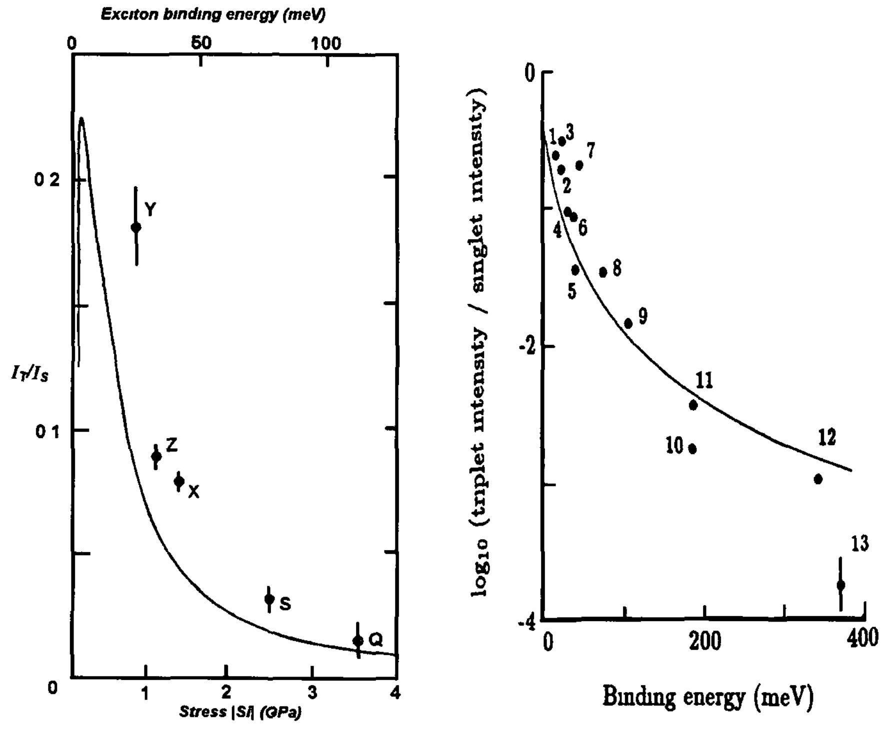

Figure 6.4(a) Ratio of the transition probabilities of the triplet and singlet states as a function of -S_l (Davies 1984). (b) Points show data for triplet/singlet transition probabilities as a function of their exciton binding energies (for details see Davies 1995).

Using the group I infinite temperature ratios determined from temperature dependence measurements the ratio of both singlet-triplet states are ~ 0 6 From figure 6 4(a) the maximum transition probability for singlet-triplet centres I silicon is found to be at most 0 25 In the case of group I the axial binding energy for singlet ZPLs B and D are ~ 95 5 meV and ~ 83 4 meV respectively Clearly, these values are not in agreement with those shown in figure 6 4(a) and in general some of the binding energy is expected to be produced from the binding of the electron For group I the relaxation energy is ~ 87 meV and exciton is self-trapped Using the estimated thermal binding energy of ~ 10 meV and the $\log_{10}$ ratio of the triplet to singlet intensities of ~ -0 22 places the data point in close proximity to point 1, figure 6 4(b) This data point is for the X^{1}_{71} line, a hydrogen related defect in silicon with $\Delta = 0\ 40$ meV and an internal stress of -0 008 GPa (Kaminskii *et al*, 1994, Davies 1995) Thus the model gives a reasonable estimation of the internal stress in comparison to the internal stress for the X^{1}_{71} line using the thermal binding energy

The model developed by Davies is *"a gross oversimplification of reality"* where the large electron-phonon interactions have been ignored (Davies, 1984) The internal stress cannot be determined from spectroscopic data and the general trend of the data as shown in figure 6 4(b) assumes that the local axial field produces all the observed binding This is not the only process operating to bind an exciton and a model has yet to be developed which includes additional binding processes However, despite the limitations this model has predicted within experimental error the energy positions of the zero-phonon lines with only three parameters, the internal stress and the exchange splittings No interactions between the states have been included in the matrix

6.2.3 Group II

Group II consists of at least eight closely spaced zero-phonon lines and a tentative model suggests all zero-phonon lines are from thermalising excited states to a single ground state The intensity grows rapidly to a maximum at ~ 5 5 K and decays until the luminescence finally disappears at ~ 25 K. A thermal dissociation energy of ~ 15 meV is very close to the energy of the free exciton indicating that an exciton was captured by the centre and is now localised to the centre with energy ~ 88 meV. A large fraction of the binding energy arises from the relaxation energy ~ 73 (± 20) meV and the exciton is self-trapped. The symmetry of the centre has been tentatively assigned as trigonal with transitions between A and E states. The high number of closely spaced stress-split components means we are unable to identify which state (A or E), is the excited state and the assignment of the stress components to each zero-phonon line is unreliable. As suggested previously, uniaxial stress measurements at 2 K should confirm this symmetry assignment. Zeeman splittings for group II are very similar to the splittings observed for group I with two triplet-singlet states observed. The minimum energy lines, F and G are triplet states with Landé g-values close to 2, indicating the hole is tightly bound where its angular momentum is quenched by the axial nature of the defect. Thus, similar to group I, the centre is pseudo-donor like.

6.2.4 Discussion

Using the model for excitons bound to an axial isoelectronic defect as outlined in the previous section the energy spacing as shown in figure 6.5 were obtained. From the best fit the internal stress is -31 MPa and the exchange splittings are 0.61 and 0.73 meV for the energy separation between triplet-singlet lines F - H and G - J respectively. Transitions are predicted at 0.61 and 1.59 meV above the F line and 0.72 and 1.69 meV above the G line. The forbidden transitions lie at -0.12 and -0.13 meV below the F and G lines respectively and 0.98 meV above both lines. The group II lines I, K, L and M are not predicted from the model. The $\log_{10}$ ratio of the triplet to singlet intensities is -1.04 and -1.19 for F - H and G - J respectively. Using the thermal binding energy of ~ 15 meV places these data points in close proximity to point 4 on the curve of figure 6.4(b). This point represents the Z-line, a lithium related defect (Lightowlers *et al.*, 1985).

From isotope substitution experiments the defects consists of a Cd-Li complex, most probably one cadmium atom complexing with two lithium atoms to form an isoelectronic defect in the lattice. A tentative assignment of the defect as a Cd-Li-Li complex in a trigonal configuration is proposed. The cadmium atom is proposed to act as a substitutional acceptor with the two lithium atoms in interstitial sites aligned along the <111> axis

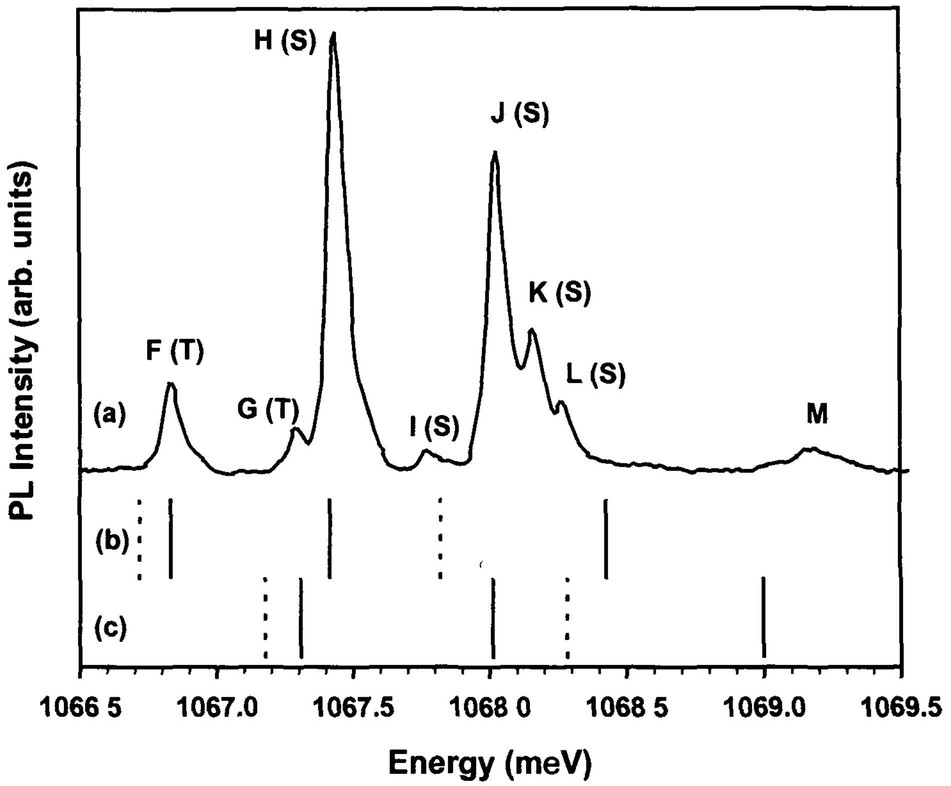

Figure 6.6(a) Group II ZPLs at ~ 5K, with singlet (S) and triplet (T) lines indicated. Model prediction with internal stress S_1 = -31 MPa and (b) exchange energy Δ = 0.61 meV. Energy spacing from zero-phonon line F are shown by the vertical lines. (c) exchange energy Δ = 0.73 meV with energy spacing from G. The forbidden transitions are represented by the dotted lines.

Similarities between groups I and II were discussed The effects of uniaxial stress and magnetic field perturbations on the defects yields similar results, the symmetry of each defect system is assigned as trigonal and both defects have two triplet-singlet pairs indicating the defects are pseudo-donor in nature The centres are cadmium related and the presence of lithium of group I in the defect has yet to be confirmed The luminescence of group I is not seen in all samples produced the same way, the irregular interdependence casts some doubts upon isolated cadmium as the trap but rather indicates a complex centre consisting of more than one impurity most probably two lithium atoms This suggests that the binding centres themselves may be almost identical differing perhaps only the positions of the lithium atoms in the lattice

6.3 Group III

In this thesis comprehensive results on the group III Cd-related defect observed in FZ and CZ silicon have been described The defect is produced by annealing cadmium-implanted silicon at 1000^{0}C and quenching rapidly, followed by an anneal at 375^{0}C for 15 min The defect shows three zero-phonon lines, α_1 at 1083 32, α_2 at 1086 02 and α_3 at 1088 53 (±0 05) meV From an analysis of the phonon sideband one, two and three phonon assisted lines were identified and are labelled β, γ and δ at energies 4 84, 9 35 and 13 49 (±0 07) meV, below α_1 The successive phonon replica energy decreases with increasing phonon number indicating the frequency mode of the vibronic series is slightly anharmonic The energy level structure deduced indicates that both the initial and final electronic states are split The luminescence takes place between three thermalising initial states to three different final states Strong selection rules must govern the luminescence spectrum Temperature dependence studies have shown that the defect consists of one loosely bound particle (with a binding energy of ~ 13 meV) and one tightly bound particle Uniaxial stress measurements establish the symmetry of the defect as monoclinic I with transitions from A to B states The curvature of the stress data indicated a higher energy state, which was identified as a B state The shift rates of the highest energy lines α_2 and α_3 were studied and within experimental error were equivalent in the <111> and <110> directions However, under <001> stress, α_3 split into two components while α_2 did not split Zeeman measurements show no shift or splitting for α_2 and α_3 The lowest energy line α_1 split into three thermalising components with $g = 2$ indicating the orbital angular moment of the hole is completely quenched These results show the triplet-singlet nature of the α_1 and α_2 lines, which are common for excitons, bound to isoelectronic donor centres

Cadmium isotope studies confirm that the defect contains at least one cadmium atom Because the luminescence of the defect is enhanced when the samples are annealed in the presence of lithium (via quartz glass) the circumstantial evidence points to the involvement of lithium in the defect The role of lithium in the defect production cannot be confirmed due to the failure to observe the defect in cadmium implanted samples intentionally doped with ^{6}Li and ^{7}Li Similar to groups I and II, it seems likely that the defect does not involve carbon or oxygen as constituents and appears to be independent of the common shallow donor and acceptor impurities

The energy level structure and vibrational properties of group III are clearly different to those of the other two groups For group III the model used for groups I and II is not adequate and we must look for an alternate description of the luminescence process

6.4 Suggestions for Further Work

We have shown that Li impurities in silicon combine with Cd acceptors to produce at least one Cd-Li-Li defect At present circumstantial evidence exists for the occurrence of two other such defects, which are unstable at room temperature Regarding the formation of such defects from published values of cadmium and lithium diffusion coefficients, lithium is the most mobile It seems probable that the occurrence of several defects corresponds to a lithium atom(s) occupying one of several possible locations in the vicinity of, but not necessarily strongly bonded to a cadmium defect The most immediate investigation that is required is the confirmation of Li in groups I and III

Thermal quenching treatments are necessary to form the defects and to date no explanation has been given as to why this step is crucial in the formation of these defects More work on the formation kinetics of the defects is necessary as the chemistry involved in the creation and destruction of these defects appears to be complicated

Uniaxial stress experiments on the excited states of groups I and II are necessary to confirm the nature of the transitions, that is if they are from A to E states or vice versa Polarisation data for all three defects would aid in the unambiguous identification of the transition types Photoluminescence excitation measurements, with the perturbation techniques of uniaxial stress and Zeeman measurements are required to study the excited state structure of the defects In addition, absorption measurements of group III should confirm the unusual energy level structure proposed

References

Aggarwal R L , Fisher P , Mourzine V and Ramdas A K , Phys Rev **A** 882-893, (1965)

Arifov A A and Rakhimbaev D , Sov Phys J , **27**, 967, (1984)

Davies G , J Phys **C17**, 6331-6348, (1984)

Davies G , Phys Rev **B51**, 13 783-13 785 (1995)

Daly S E , Henry M O , Freitag K and Vianden R , J Phys Condens Matter 6, L643-L650, (1994)

Hopfield J J, Thomas D G and Lynch R T, Phys Rev **B17**, 312, (1966)

Kaminskii A S , Lavrov E V , Karasyuk V A and Thewalt M L W, Phys Rev **B50**, 7338, (1994)

Kohn W , Solid State Phys **5**, 257, (1957)

Lightowlers E C and Davies G , Solid State Commun , **53**, 1055, (1985)

Morgan J van W and Morgan N T Phys Rev **B1**, 739-749, (1970)

Pell E M "Solid State Physics in Electronics and Telecommunications", (Proc I U A P Conf Brussels 1958), Vol **1**, Semic (Part 1), Academic Press, New York, 261, (1960a)

Pell E M , Phys Rev 119, 1222, (1960b)

Appendix A

Stress Rig

The stress rig is designed to fit inside the Oxford Instruments CF 1204 flow cryostat and is made from stainless steel which will minimise heat conduction (O' Morain *et al.,* 1992). There are four apertures in the body of the rig about the sample which allow optical access to excite the sample and collect the luminescence. The samples are mounted in the stress rig such that their long axis is exactly parallel to the vertical axis of the stress cell; this is shown schematically in figure A.1. The samples are held in place by double-sided sellotape on the flat of both small push rods. This is to ensure the stress when applied to the sample is transmitted parallel to the stress direction by compensating for any roughness on the base of the push rods. The stress is transmitted from a steel spring above the load cell to the sample, via a hollow long steel push rod. The force produced by the compressed spring is measured with a Bofors KRA-1 piezoelectric load cell in mV per Kg (0.3 mV per 1 kg load). The actual pressure acting on the sample can be calculated by using the following equation:

$$Stress(MPa) = \frac{9.8(V - V_0)}{A(0.286)} \tag{A.1}$$

where V and V_0 (unit mV) are the load cell voltages at a finite stress and at zero stress respectively, A is the cross-sectional area of the sample (unit mm^2). Stresses of up to 150 MPa can be achieved and the splitting of the stress split components of the zero-phonon lines are generally of the order of a few meV, which at low temperatures are large compared to the zero-phonon line widths.

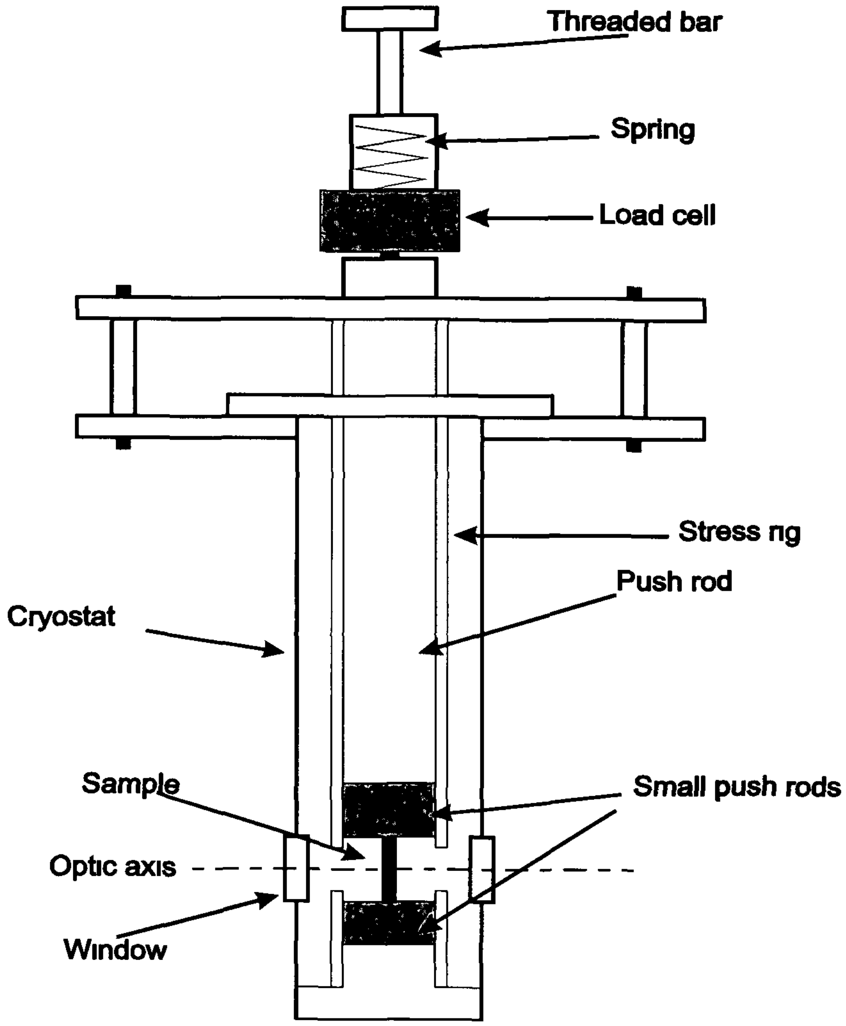

Figure A.1 A schematic diagram of a uniaxial stress cell used in the perturbation technique to determine the symmetry of the defects.

References

Morain C O , McGuigan K G , Henry M O and Campion J D , Meas Sci Technol **3**, 337, (1992)

Appendix B

RCA Clean

Recent developments of the RCA clean are reviewed by (Heyns and Nemanich, 1999), this appendix summarises the critical steps of the clean based on their review The RCA clean removes contaminants, which may be particulate, such as organic molecules and ionic materials, or oxides, which may include other molecular species After the RCA clean, the Si surface is passivated with a chemical oxide layer that protects the Si surface from contamination

The two critical steps of the clean are SC1 (Standard Clean 1) and SC2 The SC1 step removes organic surface films, surface impurities and particles The organic film impurities are removed by oxidation from the peroxide and the solvating effect of NH_4OH dissolves the oxide The metal contaminants are removed by dissolution and complexing with NH_3 The SC2 step removes metallic impurities not removed in the SC1 step The surface is passivated with a hydrated oxide film after SC2

At various stages in the clean, the samples are rinsed in de-ionised (DI) water, to remove any chemical residue on the surface All the steps of the RCA clean are shown in figure B 1

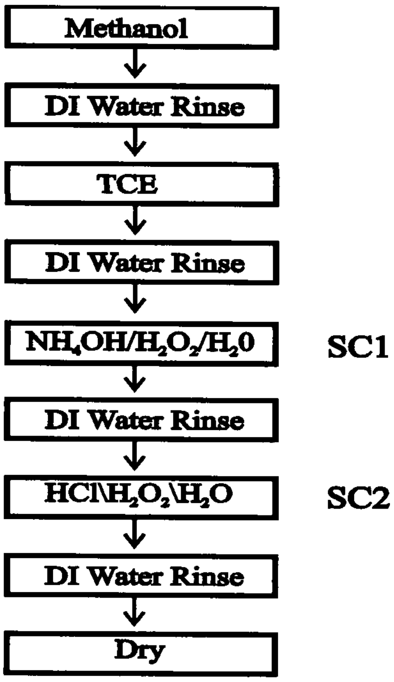

Figure B.1 The main steps involved in an RCA clean.

References

Heyns M M and Nemanich R J , EMIS Datareviews Series, **20**, 219-225, (1999)

Appendix C

Monoclinic I S_{ij} values along the <111> direction

Orientation Number	S_{xx}	S_{yy}	S_{zz}	S_{xy}	S_{yz}	S_{xz}
1	$\frac{1}{3}$	0	$\frac{2}{3}$	0	0	$-\frac{\sqrt{2}}{3}$
2	$\frac{1}{3}$	0	$\frac{2}{3}$	0	0	$-\frac{\sqrt{2}}{3}$
3	$\frac{1}{3}$	0	$\frac{2}{3}$	0	0	$-\frac{\sqrt{2}}{3}$
4	$\frac{1}{3}$	$\frac{2}{3}$	0	$\frac{\sqrt{2}}{3}$	0	0
5	$\frac{1}{3}$	$\frac{2}{3}$	0	$\frac{\sqrt{2}}{3}$	0	0
6	$\frac{1}{3}$	$\frac{2}{3}$	0	$\frac{\sqrt{2}}{3}$	0	0
7	$\frac{1}{3}$	0	$\frac{2}{3}$	0	0	$\frac{\sqrt{2}}{3}$
8	$\frac{1}{3}$	0	$\frac{2}{3}$	0	0	$\frac{\sqrt{2}}{3}$
9	$\frac{1}{3}$	0	$\frac{2}{3}$	0	0	$\frac{\sqrt{2}}{3}$
10	$\frac{1}{3}$	$\frac{2}{3}$	0	$-\frac{\sqrt{2}}{3}$	0	0
11	$\frac{1}{3}$	$\frac{2}{3}$	0	$-\frac{\sqrt{2}}{3}$	0	0
12	$\frac{1}{3}$	$\frac{2}{3}$	0	$-\frac{\sqrt{2}}{3}$	0	0

Table C.1 Stress tensor components for each of the twelve monoclinic I defect orientations for stress along the <111> direction.

Acknowledgements

This work would have been absolutely impossible if not for the help of my friends and family Thanks to Professor Martin Henry for providing me with the opportunity for research in the semiconductor spectroscopy group I would like to thank Drs Enda McGlynn, Siobhán Daly, Kevin McGuigan and Tony Cafolla, my *foster* supervisors, whom I adopted!

Thanks to Professor Ed Lightowlers (RIP) and Dr Alexi Safanov for inviting me to KCL to use the uniaxial stress facilities and for providing several isotope samples

And, of course my many friends, past and present in DCU, CIT and at home in Wexford, several deserve special mention! Charles, Shane, Dirk, Pat, Fidelma, Simon, Conor, Pauline, Andy, Harvey, Josh, Ger, Eamonn B, Eamonn C, Aiden, The Cats, James, Wendy, Stephen, Anne, the gang in Booterstown, everyone who seemed interested in my work, even if they thought I was mad!

Special thanks to Catherine for all her encouragement and support during the long summer months

This thesis is dedicated to my family for all their love, support and constant encouragement I would like to thank all those who believed in me, as they never doubted that I would finally finish

Finally, I would like to thank Denis for all his support and encouragement whenever I strayed from track